Dissertation

submitted to the

Combined Faculties of the Natural Sciences and Mathematics

of the Ruperto-Carola-University of Heidelberg. Germany

for the degree of

Doctor of Natural Sciences

Put forward by

Ingo Martin, Deppner

born in: Hermannstadt/Sibiu, Romania

Oral examination: November 21, 2013

Development of a fully differential Multi-gap Resistive Plate Chamber for the CBM Experiment

Referees: Prof. Norbert Herrmann
Prof. Hans-Christian Schultz-Coulon

Entwicklung eines voll differentiellen Multi-gap Resistive Plate Chamber für das CBM Experiment: Die vorliegende Arbeit befasst sich mit der Entwicklung eines modernen Flugzeitzählers, eines MRPC (Multi-gap Resistive Plate Chamber) für das Compressed Baryonic Matter (CBM) Experiment. Eines der Hauptziele von CBM ist die Untersuchung des Phasendiagramms von stark wechselwirkender Materie bei großen baryonischen Dichten. Das CBM Experiment zeichnet sich dadurch aus, dass die möglichen Observablen mit einer Genauigkeit gemessen werden sollen, die alles bisherige übertrifft. Darum ist eine möglichst perfekte Teilchenidentifizierung notwendig. Die Schlüsselkomponente für diese Aufgabe für Hadronen ist eine 120 m^2 grosse Flugzeitwand. Diese ist unterteilt in eine Hoch-, Mittel- und Niedrigratenzone. In dieser Doktorarbeit werden Prototypen in Orginalgröße sowohl für die Mittel- als auch für die Niedrigratenzone vorgestellt. In Tests an Beschleunigern und mit Teilchen aus der kosmischen Höhenstrahlung konnte gezeigt werden, dass diese voll differentiellen Prototypen die geforderten Anforderungen wie eine Zeitauflösung von etwa 50 ps, eine Effizienz größer als 95 %, eine Ratenfestigkeit um 1 kHz/cm^2 und eine Granularitäten im Bereich von 25 - 50 cm^2 erfüllen. Basierend auf diesen Prototypen wurde im Rahmen der Arbeit die sogenannte "outer ToF-wall" von CBM entworfen.

Development of a fully differential Multi-gap Resistive Plate Chamber for the CBM Experiment: The subject of this thesis is the development of a modern time-of-flight detector, a MRPC (Multi-gap Resistive Plate Chamber) for the Compressed Baryonic Matter (CBM) experiment. The main goal of CBM is the investigation of the phase diagram of strongly interacting matter in the region of the highest baryon densities. In order to measure the necessary observables with unprecedented precision an excellent particle identification is required. The key element providing hadron identification in heavy ion reaction at incident energies between 2 and 35 AGeV is a 120 m^2 large Time-of-Flight (ToF) wall composed of MRPCs. The ToF-wall is subdivided in a high rate, an intermediate rate and a low rate region. In this thesis we present a full-size demonstrator for the intermediate rate region and for the low rate region. In-beam and cosmic ray tests demonstrated that these fully differential prototypes fulfill the necessary requirements which are a counter time resolution of about 50 ps, an efficiency above 95 %, a rate capability of about 1 kHz/cm^2 and a granularity between 25 - 50 cm^2. Based on these counters the so-called "outer ToF-wall" was designed in this work.

Contents

1 Introduction

1.1 The phase diagram of strongly interacting matter

Exploring the phase diagram of strongly interacting matter is one of the main research topics in nuclear physics worldwide. However, only very limited experimental knowledge is available about the bulk properties of this matter that can be found in nature e.g. in the center of large nuclei or in the interior of neutron stars. A sketch of the possible phase diagram of strongly interacting matter as function of the temperature T and the baryo-chemical potential μ_B including several partially speculative new phases and their boundaries is presented in Fig. 1.1. μ_B is the energy needed to add one baryon to the

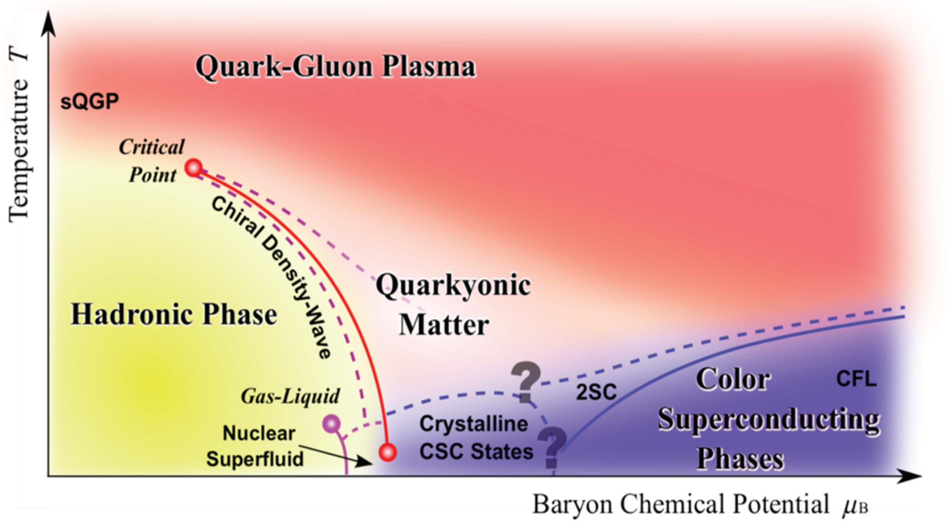

Figure 1.1: Sketch of the phase diagram for strongly interacting matter. Figure taken from [1].

system [2]. At high temperatures (T $\sim$ 160 MeV) and vanishing baryo-chemical potential lattice QCD predicts a smooth crossover between the hadronic phase (mixture of baryons, anti-baryons and mesons) and the so-called Quark-Gluon Plasma (QGP) where the quarks and gluons are de-confined creating a new phase [4; 5]. A transition from the QGP state to ordinary hadronic matter happened in the early universe, just a few microseconds after the Big Bang. Thus, intensive studies of this transition pursued at the Relativistic Heavy Ion

Collider (RHIC) and at the Large Hadron Collider (LHC) promise a better understanding of the evolution of our universe.
At larger baryo-chemical potentials lattice QCD calculations predict a critical endpoint, followed by a first-order phase transition from hadronic to partonic matter [6]. This phase transition line extends towards larger baryo-chemical potentials down to $T = 0$ MeV. However, it might well be that this line ends in yet another critical endpoint at very low temperatures (see Fig. 1.1) [1]. Other predictions assume that beyond the first-order phase transition there is a new phase called quarkyonic matter [7]. These three phases (hadronic matter, quarkyonic matter and QGP) would even form a triple point [8]. At moderate temperatures and extremely high baryo-chemical potential a so-called color superconducting phase (labeled CSC in Fig. 1.1) is predicted. However, from today's perspective it is not experimentally accessible in the laboratory. Further phases like a phase where the color degree of freedom couples strongly to the flavor degree of freedom (CFL in Fig. 1.1) are predicted at large baryon densities that might be present in the interior of neutron stars or in astrophysical events like the formation of black holes. The main goal of modern heavy-ion experiments at intermediate energies is to shed more light on the very interesting region of high net baryon densities.
As indicated above a unique opportunity to investigate certain regions of the QCD phase diagram and in particular the study of properties of strongly interacting matter under extreme conditions is offered by high-energy heavy-ion collision experiments [3]. The technique to reach high net-baryon densities at moderate temperatures is to collide heavy ions at moderate collision energies. The theoretical analysis of particle yields measured in heavy-ion collisions shows that the maximum net-baryon density at freeze-out is reached at about $\sqrt{s} = 8$ GeV corresponding to 30 AGeV beam energy for fixed target experiments. However, one should be aware that the freeze-out curve which can be derived from the

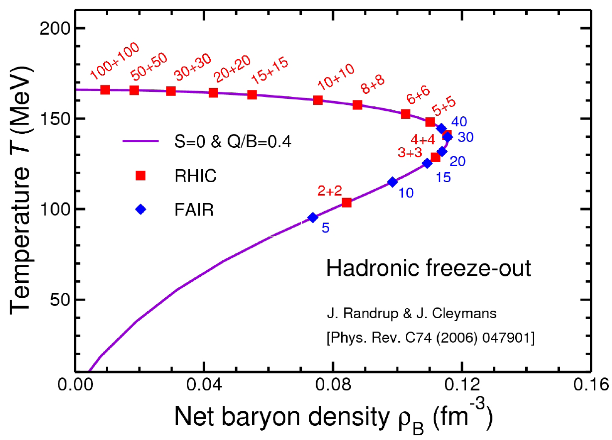

Figure 1.2: The hadronic freeze-out line in the plane temperature versus net-baryon density as obtained in the statistical model with the values of μ_B and T that have been extracted from the experimental data in Ref. [10]. The curve corresponds to Au+Au collisions. The symbols represent beam energies (in GeV) at either RHIC (total energy in each beam), or FAIR (kinetic energy of the beam for a stationary target) [3; 9]. Figure is taken from [11].

observed particle yields (see below) and the phase transition line are not the same thing.

The freeze-out line in the plane temperature versus net-baryon density is depicted in Fig. 1.2 [3; 9; 11]. The curve is obtained by investigating gold on gold collisions. The red points in the plot represent the conditions that can be reached by a beam energy scan from the STAR and the PHENIX collaborations at RHIC that is being performed in order to search for the QCD critical endpoint [12] (see also section 4.3). Similar studies are ongoing with the upgraded NA49 detector (NA61) at the CERN-SPS [13]. The blue points and labels represent the kinetic energy of the beams available at the Facility for Antiproton and Ion Research (FAIR) (see section 4.1). Also, at the Joint Institute for Nuclear Research (JINR) in Dubna a heavy-ion collider project (NICA) is planned with the goal to search for new phases of strongly interacting matter [3; 14].
Our current knowledge of the QCD phase diagram as function of temperature and baryo-chemical potential is illustrated in the left panel of Fig. 1.3 [17]. The data points corre-

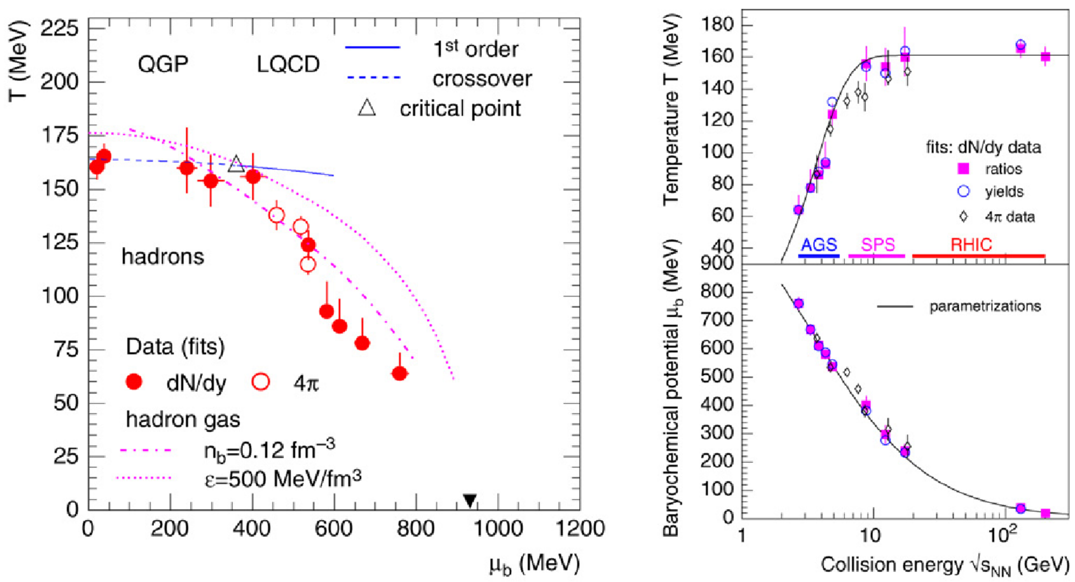

Figure 1.3: Left panel: Phase diagram of strongly interacting matter as function of temperature T and baryo-chemical potential μ_b. The data points represent freeze-out points obtained with a statistical model [178]. From lattice QCD the cross over (blue dashed line), a critical point (△) [6] and a first-order phase transition (blue line) are predicted. For more information see text. Right panel: Energy dependence of the freeze-out temperature and baryo-chemical potential [18]. For more information see text. Figure is taken from [17].

spond to chemical freeze-out and result from a statistical analysis of particle yield ratios measured in Pb+Pb and Au+Au collisions at the Schwerionen-Synchrotron (SIS) at GSI, the Alternating Gradient Synchrotron (AGS) at BNL, the Super Proton Synchrotron (SPS) at CERN and RHIC at BNL [18; 19]. The dashed-dotted line corresponds to a total baryon density of $n_b = 0.12$ fm^{-3} and the dotted line shows calculations of the freeze-out curve for a hadron gas at constant energy density of 500 MeV/fm^{-3}. Included in the plot are also the prediction of a specific LQCD calculation [6] for the critical point (triangle) and the trend of the subsequent first-order phase transition.
In the right panel of Fig. 1.3 the excitation functions of the temperature and the baryo-

chemical potential are shown as function of the collision energy. How the data points in these plots are obtained will be explained later. In the upper panel the data show a steep constant rise of the temperature up to $\sqrt{s_{NN}} \simeq 7 - 8$ [18] entering a plateau at a temperature of about 160 MeV. This behavior can be compared to the heating of a normal substance like water. Before the boiling point is reached the energy is used to heat up the system and the temperature rises. At the boiling point the entire energy is used to transfer the substance from one phase to an other while the temperature stays constant. For the QGP the energy is used to liberate quarks from their hadronic bags (deconfinement) and/or to dissolve the qqbar condensate over a larger spatial volume (chiral symmetry restoration). The experimentally obtained temperature of 160 MeV coincides with the critical temperature of the cross over calculated in lattice QCD. The baryo-chemical potential decreases all the way up to the top RHIC energies (lower plot). The data points in the left plot of Fig. 1.3 are the result of the combination of the two plots in the right panel of Fig. 1.3. The data points in the right panel are obtained by fitting particle yields or particle yield ratios measured in heavy ion collisions with the statistical (thermal) model. In the thermal model the particle density is given by [18]

$$n_i = \frac{N_i}{V} = -\frac{T}{V}\frac{\partial \ln Z_i}{\partial \mu} = \frac{g_i}{2\pi^2}\int_0^\infty \frac{p^2 dp}{\exp\left[(E_i - \mu_i)/T\right] \pm 1}, \tag{1.1}$$

with Z_i the partition function of the grand canonical ensemble for the particle species i. N_i denotes the number of particles in the volume V. $g_i = (2J_i + 1)$ is the spin degeneracy factor and $E_i = \sqrt{p^2 + m_i^2}$ is the total energy of the particle with momentum p and mass m_i. T is the temperature of the system. The chemical potential of a hadron i with baryon number B_i , the third component of the isospin I_{3i}, the strangeness S_i and the charmness C_i is given by $\mu_i = \mu_b B_i + \mu_{I_3} I_{3i} + \mu_S S_i + \mu_C C_i$. B_i, I_{3i}, S_i and C_i are the quantum numbers of the particles and μ_b, μ_{I_3}, μ_S and μ_C are the related chemical potentials of the system. The system has to obey the following conservation laws: $V\sum_i n_i B_i = N_B$, $V\sum_i n_i I_{3i} = I_3^{tot}$, $V\sum_i n_i S_i = 0$ and $V\sum_i n_i C_i = 0$. The net baryon number N_B and the total isospin I_3^{tot} of the system are input values which were chosen by [18] to be $N_B = 200$ and $I_3^{tot} = -20$ for central Au+Au or Pb+Pb collisions. The fit is typically applied to particle yield ratios where the volume of the system cancels out since it is in general not known. It is remarkable that the statistical model can fit nearly all possible particle yield ratios at a given collision energy with just two parameters, the temperature and the baryo-chemical potential. It can even predict the particle yield ratios starting at SIS energies all the way up to the top RHIC energies. Figure 1.4 demonstrates the capability of the thermal model to fit many particle yield ratios with just two parameters.
The excitation function of particle yields for Au+Au and Pb+Pb collisions is presented in Fig. 1.5. This plot summarizes most of the available particle yields measured at SIS, AGS, SPS and RHIC. At lower energies ($\sqrt{s_{NN}} < 10$ GeV) most of the particle yield data for rare particles like ϕ, hyperons (Ω, Ξ^-, Λ, $\overline{\Lambda}$) and even $\overline{p}$ have not been measured yet. In order to improve the situation high-luminosity experiments in the low-energy sector are needed. Tab. 1.1 summarizes the current and planned experiments and their limitations covering the low and intermediate energy region. The Compressed Baryonic Matter (CBM)

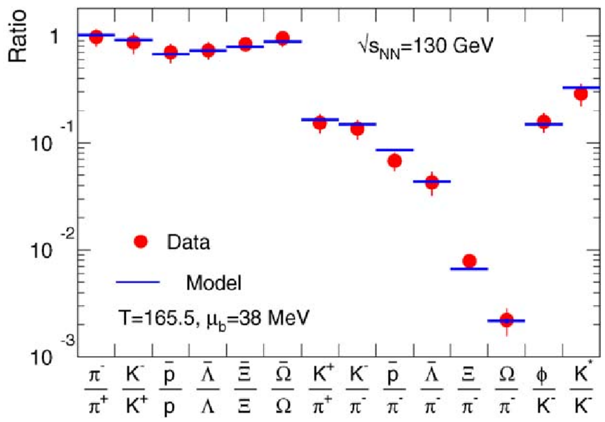

Figure 1.4: Measured particle yield ratios and the fit of the thermal model. Figure taken from [18].

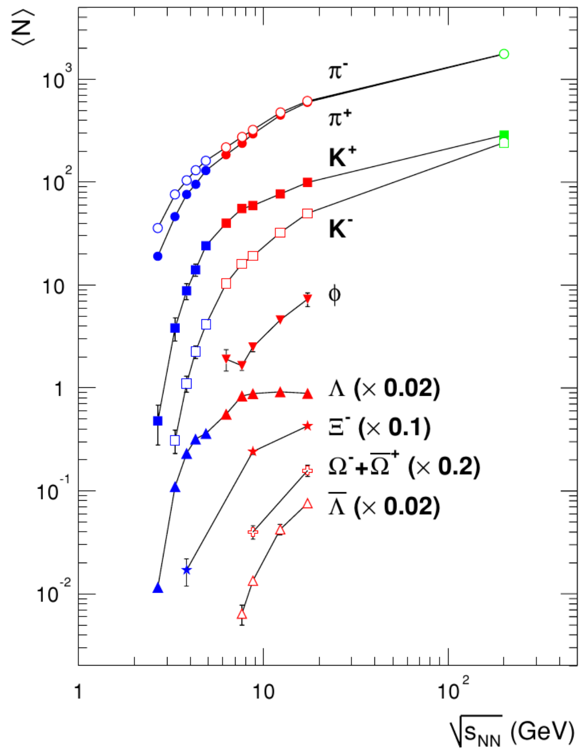

Figure 1.5: The total multiplicities of different particle species as a function of the center-of-mass energy $\sqrt{s_{NN}}$ as measured in central Au+Au/Pb+Pb reactions [20]. Figure taken from [20].

experiment for which the developments described in this thesis were done is special since it intends to measure excitation functions (from 2 to 35 AGeV) of yields and phase-space distributions of rare particles, in particular (multiple) strange particles and anti-particles, with unprecedented precision. These observables delivers information about the fireball dynamics and the nuclear matter equation of state over a wide range of baryon densities [17]. Hyperons can be identified by their weak decay topology: $\Xi^- \to \Lambda + \pi^-$, $\Omega^- \to \Lambda + K^-$ and $\Lambda \to p + \pi^-$. Since all decay products are identifiable via the time-of-flight method the signal to background ratio of the reconstructed hyperons can be improved substantially.
Another observable related to the equation of state of nuclear matter is the measurement of collective flow. The flow is driven by the pressure created in the early phase of the collision and carries information on the equation of state of dense matter [3]. In particular the measurement of elliptic flow v_2 as function of the transverse momentum p_t of various

Experiment	Energy range (Au/Pb beams)	Reaction rate Hz	Limitation by
STAR@RHIC BNL	$\sqrt{s}$ = 7 - 200 GeV	1 - 800	luminosity
NA61@SPS CERN	E_{kin} = 20 -160 AGeV $\sqrt{s}$ = 6.4 - 17.4 GeV	80	detector
MPD@NICA Dubna	$\sqrt{s}$ = 4.0 - 11.0 GeV	$\sim$ 1000	luminosity
CBM@FAIR Darmstadt	E_{kin} = 2 - 35 AGeV $\sqrt{s}$ = 2.7 - 8.3 GeV	$10^5 - 10^7$	detector

Table 1.1: Experiments investigating the high net-baryon density region in the QCD phase diagram, their energy range and the reaction rate which triggers the limitation. The reaction rate of CBM is orders of magnitude higher in comparison to the other experiments [15].

particles (mostly $\pi^{\pm}$, $K^{\pm}$ and $p^{\pm}$ but also rare particles) might shed light on the transition between hadronic and partonic phase. The scaling of v_2 with the number of constituent quarks is interpreted as a direct signature of partonic collectivity [3]. The identification of these various particles (hadrons) is done at CBM mainly by the time-of-flight method.
The investigation of the critical point and the first-order phase transition via event-by-event fluctuations of particle momenta and particle yield ratios (see section 4.3) is a major topic in the CBM physics program. Also in this case the time-of-flight information of the hadrons is the key element.
Exotic clusters like multi-strange hypernuclei are predicted to be formed in dense nuclear matter by coalescence. The finding of hyper-triton in Ni+Ni collisions at 1.91 AGeV by the FOPI collaboration [122] supports this coalescence scenario. The predictions of the thermal model for the yields normalized by the Λ-yield for different exotic multi-strange hypernuclei is shown in Fig. 1.6. The maximum yield is reached at a center-of-mass energy

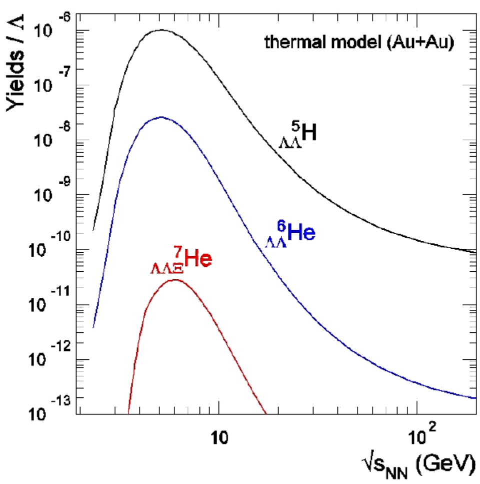

Figure 1.6: Energy dependence of multi-strange Λ hypernuclei yields relative to the Λ yields at midrapidity for central Au+Au collisions predicted by the thermal model. Figure taken from [3].

between 5 - 6 GeV i.e. in the energy range for which CBM is designed (cf. Tab. 1.1). Since strangeness is conserved in strong interactions the observation of anti-strange quarks in the form of K^+ - mesons guarantees the co-existence of a strange quark in the system [208]. Therefore, the reconstruction of the entire set of K^+ - mesons is of great interest in order

to enhance those events potentially containing multi-strange hyperons. The identification of K^+ - mesons via time-of-flight requires not only a very good time resolution but also a high reconstruction efficiency.
Further observables in CBM are for instance open and hidden charm production and dileptons stemming from low mass vector meson decay. More details about the physics program of CBM is presented in section 4.2.

1.2 Time-of-Flight (ToF) method

In general, particles are identified by their mass and electric charge [41]. The rest mass m_0 of a particle is connected to its momentum p and its time of flight t_{ToF} via

$$m_0 = \frac{p}{c}\sqrt{\frac{c^2 t_{ToF}^2}{L^2} - 1}, \tag{1.2}$$

with $\gamma = \frac{1}{\sqrt{1-\beta^2}}$, $\beta = \frac{v}{c}$ and $v = \frac{L}{t}$. L is the track length of the particle and c the speed of light. For particle identification typically m_0^2 is used (see section 4.5.1). The mass resolution is mainly dominated by the time-of-flight measurement (typical values for CBM: $\sigma_p/p \approx 1$ % and $\sigma_L/L \approx 0.1$ %). It is given by

$$\frac{\sigma_{m_0}}{m_0} = \left(\frac{E}{m_0}\right)^2 \frac{\sigma_{ToF}}{t_{ToF}}, \tag{1.3}$$

with $E^2 = p^2 + m_0^2 = \left(\frac{p t_{ToF} c^2}{L}\right)^2$ the energy of the particle.
If two particles A and B with masses m_A and m_B have the same momentum the time of flight difference can be calculated as [22]

$$|t_{ToF}^A - t_{ToF}^B| = \frac{L}{c}\left|\sqrt{1+\frac{m_A^2 c^2}{p^2}} - \sqrt{1+\frac{m_B^2 c^2}{p^2}}\right| \simeq \frac{Lc}{2p^2}|m_A^2 - m_B^2|. \tag{1.4}$$

Here the assumption is made that $p \gg mc$ leading to $\sqrt{1+(mc/p)^2} \approx 1 + (mc)^2/2p^2$. The separation power is given by [22]

$$n_{\sigma_{ToF}} = \frac{|t_{ToF}^A - t_{ToF}^B|}{\sigma_{ToF}} = \frac{Lc}{2p^2\sigma_{ToF}}|m_A^2 - m_B^2|. \tag{1.5}$$

σ_{ToF} is the resolution of the time-of-flight system. For particle identification a typical separation power of 3 is requested. From Eq. (1.5) it follows that the separation power improves linearly with a larger particle track length. In CBM, L is between 6 and 10 m (cf. chapter 6). However, kaons have a limited life time of $c\tau = 3.712$ m and therefore a shorter track length is favorable in order to detect as many kaons as possible. On the other hand, particles with a higher momentum have a longer path length before they decay due

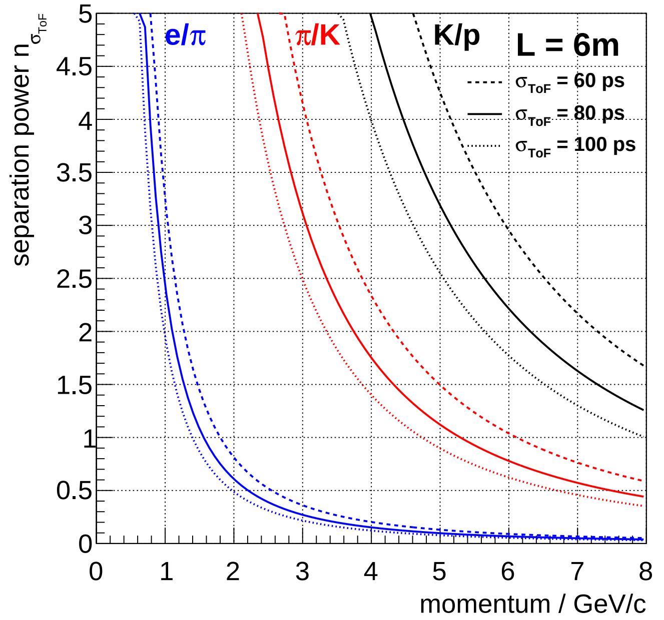

(a) Track length L = 6 m.

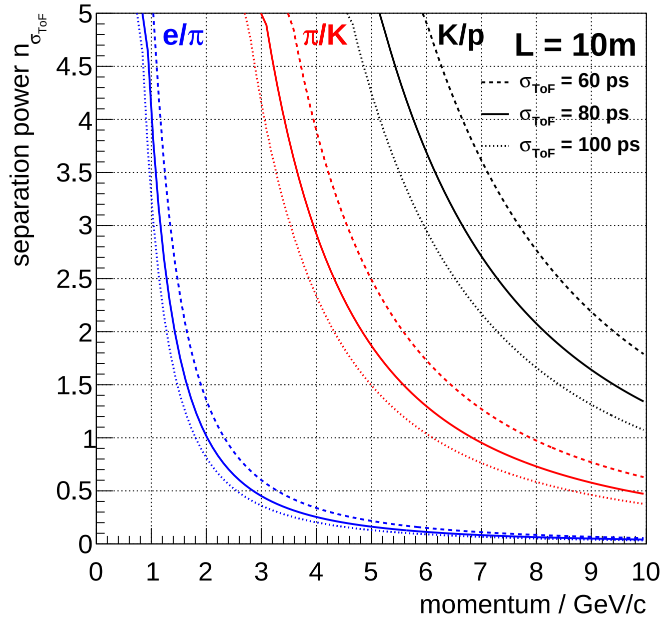

(b) Track length L = 10 m.

Figure 1.7: Particle separation power as function of the particle momentum for three different time resolutions (σ_{ToF} = 60, 80 and 100 ps) and for the particle combinations e/π, π/K and K/p. The momentum as well as the path length resolution are assumed to be infinitely good.

to the relativistic time dilation. All these effects need to be considered in order to find the optimal position of the time-of-flight detector. When designing an experiment also spatial constraints from other detector components have to be taken into account. Figure 1.7 shows the particle separation power as function of the particle momentum for three system time resolutions (σ_{ToF} = 60, 80 and 100 ps). The different colors represent the particle combinations e/π (blue), π/K (red) and K/p (black). The plots show that at a requested system time resolution of 80 ps a 3 σ separation between pions and kaons is reached at a momentum of about 3 GeV/c at L = 6 m and at about 4 GeV/c at L = 10 m. The π/K separation is most critical for the time-of-flight method since electrons are identified by other detector components. CBM intends to identify $\pi^{\pm}$, $K^{\pm}$, p, $\overline{p}$ and heavier fragments via the time-of-flight method.

Figure 1.8 shows the particle flux distribution on a virtual ToF wall placed 10 m downstream from the target. In this URQMD [23] simulation a 25 AGeV gold beam hits a gold target with an interaction rate of 10 MHz. From this plot one can estimate some of the requirements for the ToF-wall.

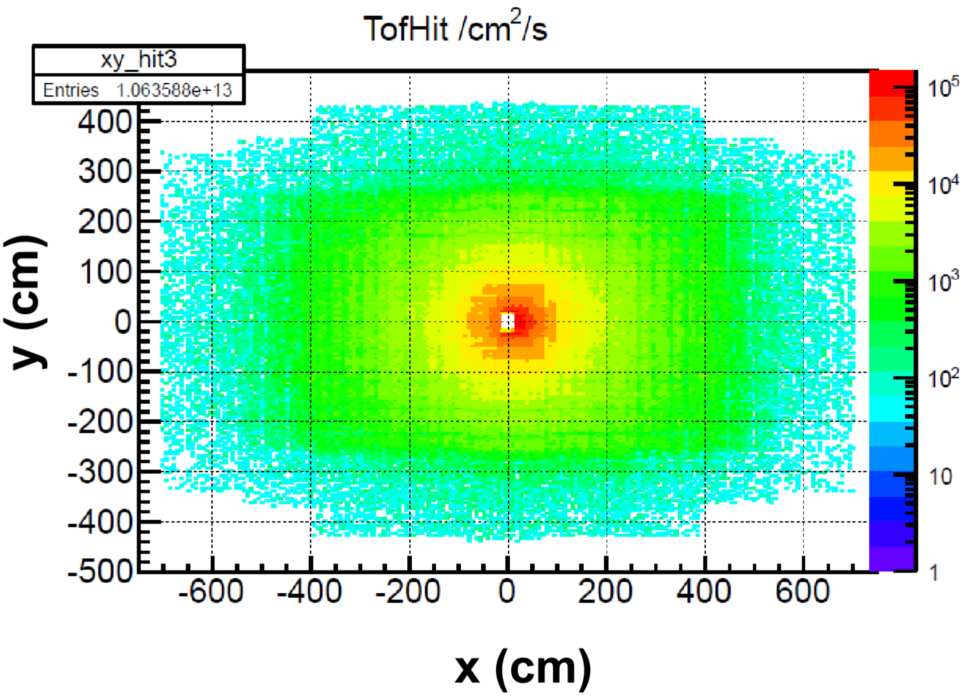

Figure 1.8: Particle flux at 10 m distance from the target reached in Au+Au collision at 25 AGeV in a fixed target experiment. The interaction rate is 10 MHz. Figure taken from [24].

The requirements are:

- Time resolution below 100 ps
- Efficiency above 95 %
- Granularity between few cm^2 and 1 dm^2

- Rate capability of 1 - 50 kHz/cm^2
- Total detector area about 120 - 140 m^2
- Number of channels about 100000

Plastic scintillators with Photomultiplier (PMT) readout which would fulfill the requirements cost about 1000 euro per channel which is simply not affordable. The only technique which is available at the moment in order to construct such a Time-of-Flight wall are Resistive Plate Chambers (RPC).

1.3 Resistive Plate Chambers

Resistive Plate Chambers (RPCs) are dedicated gaseous detectors for timing measurements and trigger applications. They consist of at least two parallel arranged planar electrodes forming a gas gap in which a uniform electric field of about 100 kV/cm is created. In the simplest case one electrode is made of a high resistive material with a bulk resistivity between 10^9 and 10^{12} Ωcm. A particle traversing the gas gap interacts with the detector gas and creates electron-ion pairs called clusters (cf. section 2.1). The energy loss per unit length of the particles in the gas is given by the Bethe-Bloch-formula (see appendix). Due to the extremely high electric field the electrons accelerate towards the anode until they gain enough kinetic energy to ionize other gas molecules and an avalanche process is developed. The positive ions drift in the opposite direction (towards the cathode) but with a much smaller drift velocity and therefore play a less important role in the avalanche process. The movement of the electrons induces a signal in the pickup electrodes (see section 2.4) which will be further processed by the front end electronics. The electrons reach the surface of the resistive plate while the positive ions still drift in the gap. The deposited charge Q_0 on the electrode surface will drift through the resistive plate with resistivity ρ. The charge on the surface follows the time dependent equation

$$Q(t) = Q_0 \mathrm{e}^{-t/\tau} \tag{1.6}$$

with $\tau = \rho\varepsilon_0\varepsilon_r$. ε_0 is the dielectric constant and ε_r is the relative permittivity of the resistive material. Therefore RPC are by construction limited in their rate capability (see section 2.7). During the avalanche process also photons are produced which can trigger secondary ionizations. These ionizations again develop avalanches and a so-called streamer might be formed (see section 2.3). The streamer probability can be controlled by the amount of photon quencher gas (iso-butane) in the gas mixture, by the gap size and by the applied electric field. In the worst case a streamer can develop into a spark. The working principle of an RPC is sketched in Fig. 1.9.

The history of RPC dates back to 1948 with the development of Parallel Plate Counter (PPC) [25]. These detectors had parallel arranged metal plates which created discharges at the place where a charged particle traversed the gap. Thus, the whole capacitance was discharged delivering very large signals. Due to the large capacitance that got discharged the operation in spark mode led to a limited rate capability of a few Hz/cm^2.

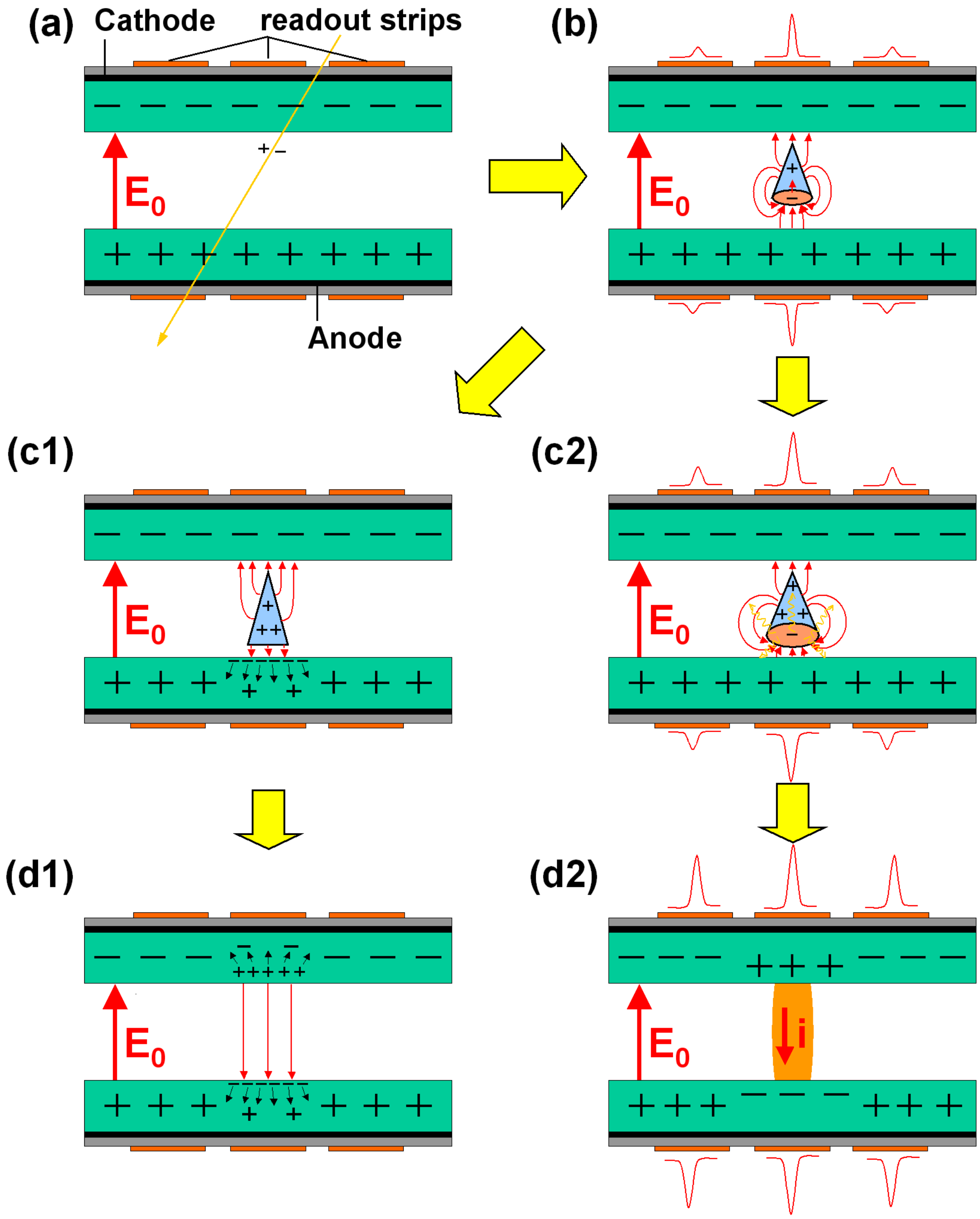

Figure 1.9: Working principle of an RPC. (a) A traversing particle (thin yellow arrow) ionizes the gas in the gap. (b) Electrons and ions drift towards the electrodes developing an avalanche and inducing a signal in the readout electrode. (c1) Since the drift velocity of the ions is much smaller than for the electrons their contribution to the signal is negligible. (d1) The charges are deposited on the surface of the resistive material building up an opposite electric field. This temporarily leads to a blind spot in the counter which is limiting the rate capability. (c2) At certain conditions and with a certain probability an avalanche can develop into a streamer (d2) leading to very large signals in the readout electrode.

With the development of the so-called Pestov counter in 1971 [26] this problem became partially solved. The electrodes of this counter consist of a resistive material with bulk resistivity of about 10^9 Ωcm. Therefore, the sparks discharge the electrodes only locally while the rest of the surface remains active. Additionally, new gas mixtures containing photon quenchers were developed. Thereby time resolutions of about 50 ps were reached. The Pestov spark counter operates at electric fields of about 500 kV/cm having gap sizes of about 0.1 mm. The conditions are such that essentially every avalanche develops into a spark. These sparks are the main reason for the limited rate capability rendering them obsolete for modern experiments. The Pestov Spark Counters (PSC) and their difficulties are discussed in more detail in section 3.2.
In the early 80is the Parallel Plate Avalanche Chambers (PPAC) were developed. PPACs are single-gap detectors, working in avalanche mode with multiplication factors of about 5×10^4 [27; 28]. Due to the small charges involved a rate capability up to 10^7 Hz/cm^2 was reached. The electrodes consist of plastic or ceramic plates onto which a metallic foil is glued. The gap sizes are between 0.5 - 2 mm. Time resolutions of about 250 ps were obtained [27]. A moderate efficiency ($\sim$ 80 %) for minimum ionizing particles and a small signal to noise ratio limits the applicability of this technology in high energy experiments.
The first RPC was presented by R. Santonico und R. Cardarelli in 1981 [29]. A schematic view of the RPC structure is presented in Fig. 1.10. It consists of two parallel arranged

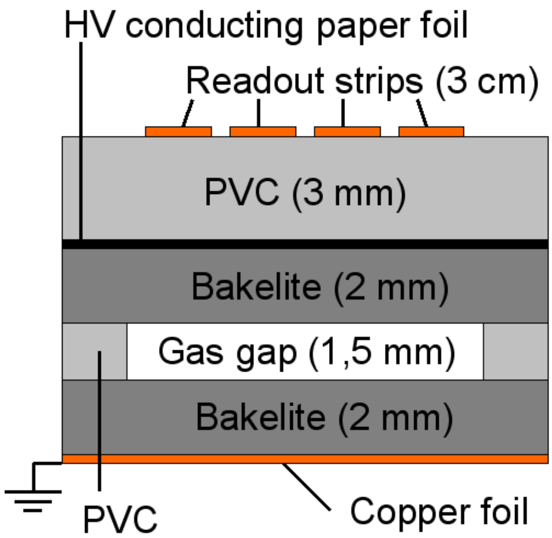

Figure 1.10: Schematic view of the first RPC developed by R. Santonico und R. Cardarelli.

Bakelite® plates of 2 mm thickness separated by a polyvinyl chloride (PVC) spacer forming a gap of 1.5 mm. From the outer side one Bakelite® plate is covered by a copper foil which is grounded while the other plate is covered by a low resistive paper (1 M$\Omega/\square$) on which the high voltage (HV) is applied. The signal readout strips are separated by a PVC plate of 3 mm thickness. For actual counters this structure was mirrored at the ground electrode so that a 2-gap RPC was formed. The gas mixture at that time consisted of 50 % argon and 50 % butane. This type of RPC was operated in the streamer mode.

Therefore, signal amplitudes between 200 and 400 mV were reached allowing for operation without preamplifiers. However, large signals infer a large charge flow in the resistive plates. In combination with the bulk resistivity of Bakelite® between 10^9 to 10^{10} Ωcm a rate capability of a few hundred kHz/cm^2 is achieved. A time resolution in the order of 1 ns and an efficiency of 98 % was obtained making them attractive for trigger application. Nowadays this type of RPC is called trigger RPC and is widely used in many particle and heavy ion experiments e.g. ATLAS [30], CMS [31], Alice [32], PHENIX [33], BaBar [34], ARGO-YPJ [35], OPERA [36]. Trigger RPCs operate at an electric field of about 50 kV/cm and have a typical gap size of 2 mm. A common gas mixture is 96.7 % $C_2F_4H_2$ / 3 % $i-C_4H_{10}$ / 0.3 % SF_6. Figure 1.11 shows the transverse view of the ATLAS muon spectrometer with the indicated RPC barrel covering a surface of about 3650 m^2. It comprises 596 RPCs with a sensitive area of 7300 m^2 and 355000 readout channels. In Fig. 1.12 a cross section of the ATLAS RPC barrel is depicted.

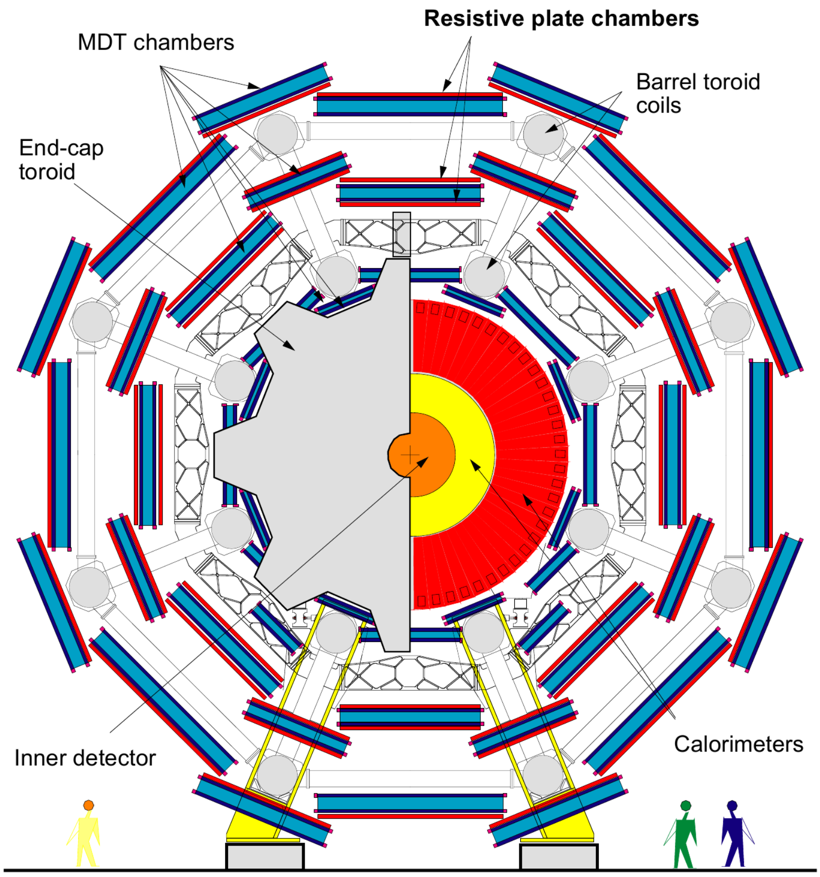

Figure 1.11: Transverse view of the ATLAS muon spectrometer. MDT stands for Monitored Drift Tubes. Figure taken from [37].

In 1995, a wide gap RPC with gap sizes between 6 - 8 mm was presented [39]. The gap sizes were increased in order to maximize the efficiency and signal amplitude. This RPC was operated in avalanche mode. However, in the wide gap the avalanches can grow until

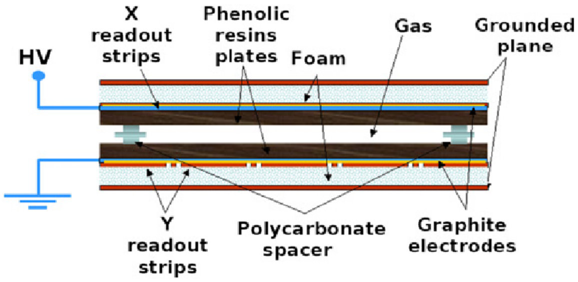

Figure 1.12: Structure of the ATLAS RPC. Figure taken from [38].

large streamers occur. Therefore, the same group introduced one year later the first multi-gap RPC (MRPC) [40]. The gap is subdivided by several floating resistive plates so that the avalanche will grow until the electrons arrive on one of the intermediate plates [41]. This design combines the good attributes of the wide gap RPC (good efficiency) and the narrow gap RPC (streamer free operation, better time resolution).
It was found that the gap size is related to the time resolution. Therefore, it is no surprise that the first timing RPC presented by Fonte, Smirnitski and Williams in the year 2000 [51] had a gap size of 0.3 mm and a time resolution of 107 ps. A further novelty was the use of glass as resistive plate. A schematic view of the RPC structure is shown in Fig. 1.13 The RPC is composed of two cells with 2 gaps each. In this device a glass plate is placed

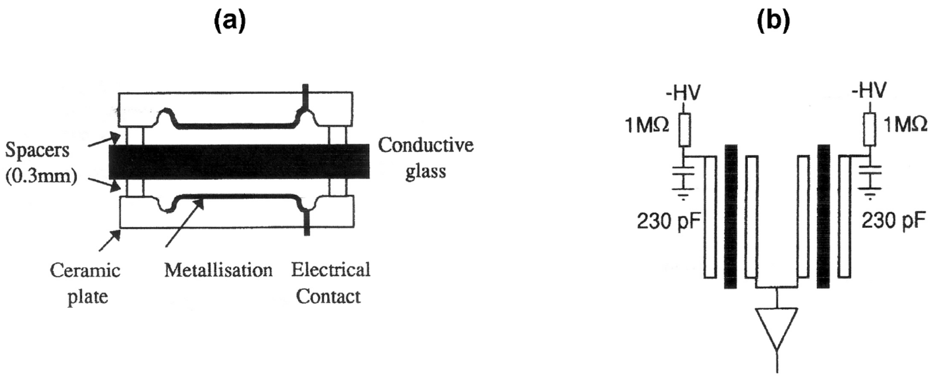

Figure 1.13: Schematic view of the first timing RPC. (a) Structure of one cell. (b) two of such cells are forming the RPC. Figure taken from [51].

between two metalized ceramic plates so that only one side of the gap faces the resistive plate. On one metalized surface the high voltage is applied and on the other the signal is read out. This alternating structure (metal - glass -metal) is nowadays used only in the HADES timing RPC design [43].
More common are MRPCs where the gaps are formed by equal glass plates (cf. Fig 1.14). Two types of MRPCs have been established: MRPCs with single ended readout (Fig. 1.14a) and MRPCs with differential readout (Fig. 1.14b). Furthermore, one distinguishes between a single stack configuration where the opposite electrodes are placed on top and on the bottom of the glass stack and a double stack configuration where one electrode is placed in the middle of the stack and the other electrode is placed on top and on the bottom of the

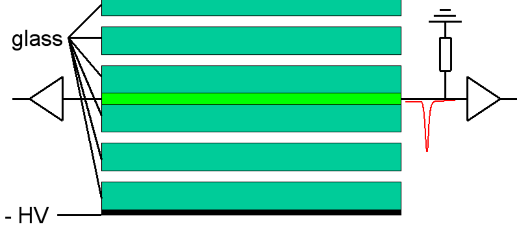

(a) Double stack with single ended readout.

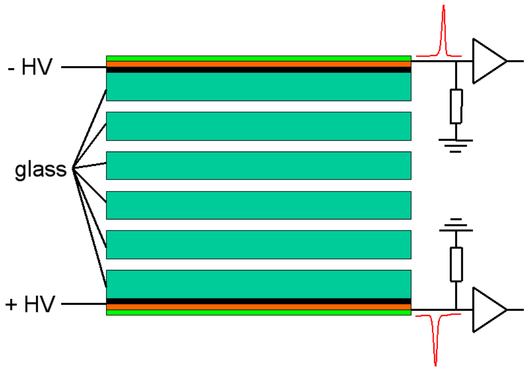

(b) Single stack with differential readout.

Figure 1.14: Structure of a multi-gap RPC.

stack. Both variations can be either single ended or differential. Experiments using timing MRPCs as time-of-flight detectors are among others FOPI (see section 3.2), ALICE [79], STAR [45], HARP [46]. The biggest system is realized by the ALICE collaboration with a total active area of about 160 m^2 and about 160000 readout channels. Future experiments utilizing MRPCs as time-of-flight detector are CBM (see this thesis) and e.g. LEPS2 [47]. Tab. 1.2 comprises the most important operating parameters of trigger-RPCs and timing-RPCs.

RPC-type	trigger-RPC	timing-RPC
operation mode	streamer mode	avalanche mode
signal charge	50 pC - few nC	< 5 pC
number of gaps	1 - 2	4 - 10
gap size	1,5 mm - 2 mm	150 - 300 μm
electric field strength	20 - 50 kV/cm	80 - 110 kV/cm
resistive material	Bakelit®	glass
efficiency	about 99%	> 99 %
time resolution	about 1 ns	40 ps - 100 ps
rate capability	few hundred Hz/cm^2	1 - 100 kHz/cm^2
gas mixture $C_2H_2F_4/SF_6/i-C_4H_{10}$	e.g. ATLAS Exp. 96,7%/0,3%/3%	e.g. FOPI Exp. / CBM Exp. (80%/15%/5%) / (85%/10%/5%)

Table 1.2: Difference between trigger-RPCs and timing-RPCs.

1.4 Outline of the thesis

This thesis contains seven chapters describing the development of an MRPC prototype for the CBM experiment. Chapter 2 summarizes the physics of RPCs. It contains theoretical estimations about the time resolution, efficiency and rate capability. Chapter 3 explains briefly the FOPI experiment and continues with a description of the FOPI multi-strip MRPC. The investigation of some RPC parameters was part of this thesis and is therefore discussed in more detail. Chapter 4 contains information about the CBM experiment and its physics program. One of the main goals of CBM is the study of the critical point via event-by-event fluctuations. The π/K-ratio fluctuation depends critically on the particle identification capability. A feasibility study of π/K-ratio fluctuations with CBM was performed via a small Monte Carlo toy model as part of this thesis. Chapter 5 describes the development of several MRPCs for the low and intermediate rate region of CBM. This chapter focuses on the design of the MRPC, the various test setups and the obtained results. The design of the outer Time-of-Flight wall including the MRPC modules discussed in chapter 5 was an additional part of this thesis and is presented in chapter 6. The thesis is closed by a discussion and an outlook in chapter 7.
Some of the results are published in [91; 195].

2 Detector physics of Resistive Plate Chambers

This chapter addresses the physical background of RPCs. The topic has been widely investigated amongst others by [48–55]. However, here we concentrate mainly on the work of [56; 57; 59; 60].
To introduce the coordinate system and some variables used in this chapter Fig. 2.1 shows a cutout of an MRPC with two resistive plates (in this case glass plates) having a thickness b. They are separated by the distance d representing the gas gap. Across the gap an extremely uniform electric field $\vec{E}$ pointing in $-z$ direction is created.

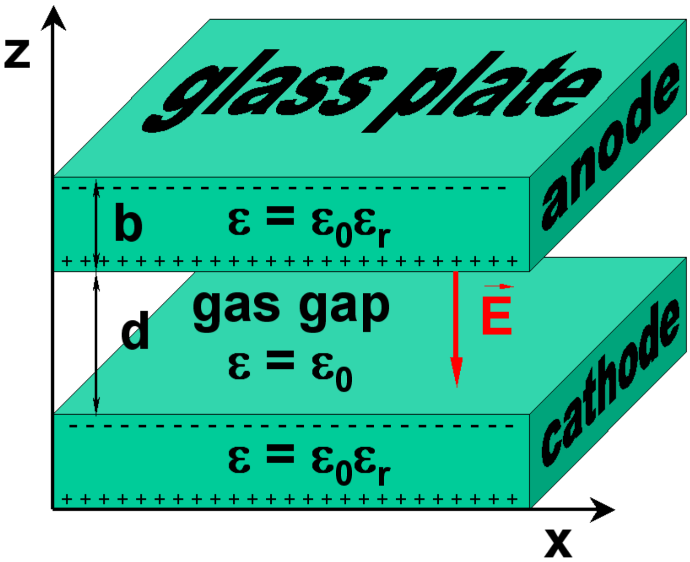

Figure 2.1: Simple structure of an RPC gap with glass as resistive plates. It is used to introduce some variables and the coordinate system.

The chapter is structured in the following way. In section 2.1 the primary ionization process is discussed followed by the description of the avalanche development in an RPC gap (section 2.2). Such avalanches can advance to streamers. This process is briefly addressed in section 2.3. The process of signal induction together with an estimation of the weighting field is investigated in section 2.4. A theoretical estimation of the intrinsic time resolution and the efficiency is given in section 2.5. The topic of section 2.6 is the signal propagation in a typical strip electrode of an RPC. The chapter is closed by elaborating possibilities to increase the rate capability of RPCs.

2.1 Primary ionization

A charged particle traversing an RPC ionizes the detector gas located in the gaps. The ionization process creates pairs of electrons and ions called clusters. The number of electrons and ions in a cluster and the total number of clusters in all gaps is related to the total charge of the readout signal.
The ionization cross section σ as function of the velocity of a high energy particle is given by [56; 61]:

$$\sigma(\beta) = K_1 z^2 \left(M^2 x_1 + C x_2\right) \tag{2.1}$$

with

$$K_1 = 4\pi \left(\frac{\hbar}{m_e c}\right)^2 = 1,874 \cdot 10^{-20}\ \mathrm{cm}^2 \quad , \quad x_1 = \beta^{-2} \ln\left(\frac{\beta^2}{1-\beta^2}\right) - 1 \quad , \quad x_2 = \beta^{-2}.$$

M^2 and C are gas dependent constants (e.g. for iso-butane: $M^2 = 14,19 \pm 0,20$ and $C = 141,9 \pm 0,6$ [61]) and z is the charge of the particle in multiples of the elementary electric charge e. $\hbar$ is the reduced Planck constant, m_e the electron mass and c the speed of light. The velocity of the particle enters in Eq. 2.1 through $\beta = v/c$. From the density ρ and the atomic mass number A of the gas the mean free path λ of the particle can be calculated:

$$\lambda = \frac{A}{\rho N_A} \cdot \frac{1}{\sigma(\beta)} \tag{2.2}$$

Here $N_A = 6.02214179(30) \times 10^{23}\ \mathrm{mol}^{-1}$ is the Avogadro constant [62]. The average number of ionizations (clusters) per unit length $\overline{n}$ is given by the reciprocal of the mean free path,

$$\overline{n} = \lambda^{-1}. \tag{2.3}$$

This quantity can be modeled by using the program HEED [63]. Figure 2.2 shows the modeled average number of clusters as function of $(\gamma - 1)$ for iso-butane, methane and typical gas mixtures for timing and trigger RPCs. The simulated values for the average number of clusters per mm for methane and iso-butane agree quite well with measurements quoted in [61] (solid lines). The gas mixture $C_2H_2F_4/i\text{-}C_4H_{10}/SF_6$ 85%/5%/10% typically used for the RPCs described in this thesis. It delivers on average 7.5 clusters per mm with minimum ionizing particles. This corresponds to an average distance between two clusters of $\lambda = 133\ \mu$m, i.e. 1.65 clusters on average per 220 μm gap or 13.2 clusters within 8 such gaps. The distance between the clusters is distributed exponentially. The probability to find the first cluster between position z and $z + dz$ is [57]:

$$P(z) = \lambda^{-1} \exp\left(-\frac{z}{\lambda}\right) \tag{2.4}$$

Assuming that the ionization probability does not depend on the previous ionization the probability to find the n-th cluster between z und $z + dz$ can be calculated by integrating the single probabilities as following [57]:

$$\begin{aligned} P_{clu}(n,z) &= \int_0^z \int_0^{z_{n-1}} \cdots \int_0^{z_2} P(z_1)P(z_2 - z_1)\cdots P(z - z_{n-1})dz_1 dz_2 \cdots dz_{n-1} \\ &= \frac{z^{n-1}}{(n-1)!\lambda^n} \exp\left(-\frac{z}{\lambda}\right) \end{aligned} \tag{2.5}$$

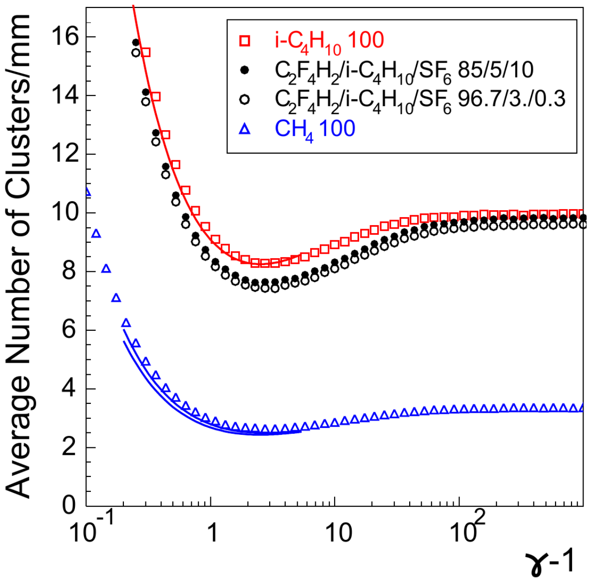

Figure 2.2: Average number of clusters per mm as function of $\gamma - 1$ predicted by HEED for typical gases used in gaseous detectors. The temperature of the gas was set to $T = 296.15$ K and the pressure to $p = 1013$ mbar. The gas mixture $C_2H_2F_4/i\text{-}C_4H_{10}/SF_6$ 85%/5%/10% is used for the RPCs in CBM. Solid lines correspond to measurements taken from [61]. Figure is taken from [56].

The number of electrons per cluster are distributed as shown in figure 2.3 [56]. The

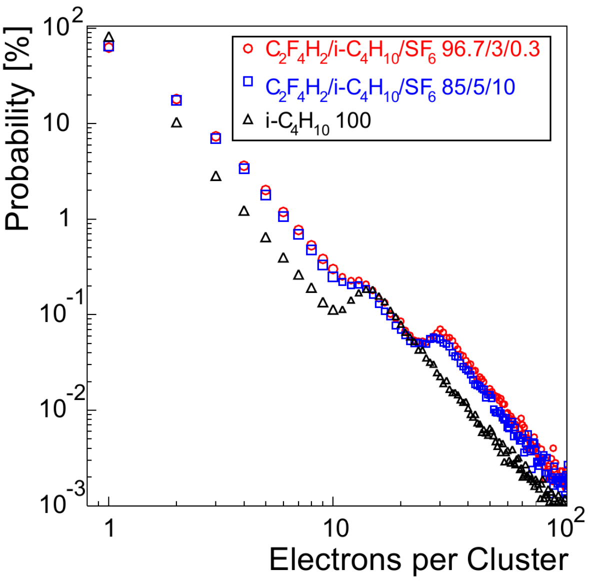

Figure 2.3: Distribution of electrons per cluster (cluster size distribution) as predicted by HEED for two gas mixtures and iso-butane. The simulations were carried out with 120 GeV muons for the 0.3 % SF_6 mixture and with 7 GeV pions for the 10 % SF_6 mixture and iso-Butane. The temperature of the gas was set to $T = 296.15$ K and the pressure to $p = 1013$ mbar. Figure is taken from [56].

dependence is roughly $1/n^2$ and the mean cluster size is about 2.6 electrons for the timing RPC mixture. To calculate the mean cluster size the maximum number of electrons was fixed to 500 [56].

A second type of particles which can cause an avalanche inside a gap are delta electrons created when the initial particle crosses solid material in front of the gas gap. FLUKA [64] simulations showed that for a 7 GeV pion crossing a 3 mm aluminum plate the probability that the pion is accompanied by at least one charged particle is only 4.92 % [57].

2.2 Avalanche dynamics

After an electron-ion-pair is created in the gas gap they start drifting towards the electrodes. The electrodes create the homogenous electric field $\vec{E}$. A typical value for $|\vec{E}|$ in a timing RPC is 100 kV/cm. The kinetic energy of the electron and the ion gained in the field passing a distance δz is:

$$T_{el.} = e_0 \cdot |\vec{E}| \cdot \delta z \tag{2.6}$$

with $e_0 = 1,6022 \cdot 10^{-19}$ C the unit charge.
Due to the huge mass difference the velocity of the positive ions is in comparison to the electron velocity negligibly small. Within about 100 nm the electron gains enough energy (1 eV) to ionize other gas molecules and the acceleration process starts again until the electron hits another molecule and so on. Averaging over many collisions the electron moves with a constant drift velocity v_D which depends proportionally on the applied electric field and inverse-proportionally on the gas density. Figure 2.4 depicts the drift velocity as function of the electric field calculated with the program MAGBOLTZ [65]. For timing RPCs drift velocities between 200 μm/ns and 250 μm/ns are predicted. During the drift, every electron

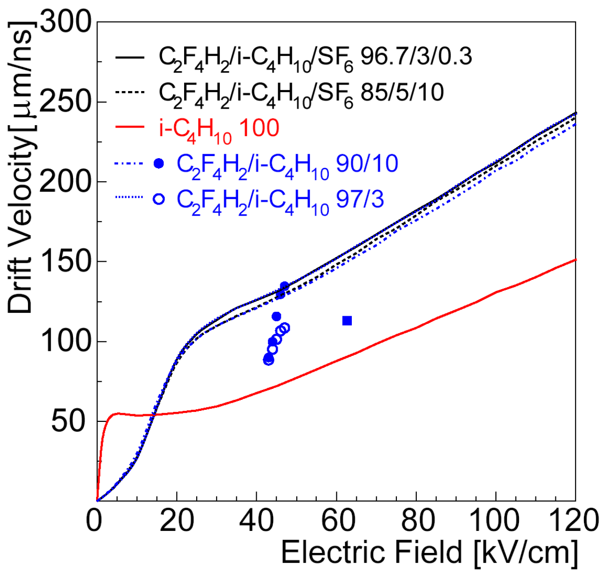

Figure 2.4: Drift velocity as function of the electric field calculated with MAGBOLTZ for different gas mixtures and iso-Butane. The temperature of the gas was set to T = 296.15 K and the pressure to p = 1013 mbar. The circles show measurements from [66] for two different gas mixtures, the squares show measurements from [67] for $C_2H_2F_4/i\text{-}C_4H_{10}/SF_6$ 96.9%/3%/0.1%. The Figure is taken from [56].

creates with a certain probability a further electron ion pair. This fact is expressed in the so called Townsend coefficient α. Starting with n electrons at position z, the probability to have $n+1$ electrons at position $z+dz$ is given by $n\alpha\ dz$ [57]. At the same time, the electron can be attached to a gas molecule forming a negative ion. The probability for this process to happen is given by $n\eta\ dz$ with the attachment coefficient η. For the average number of electrons $\overline{n}$ and the average number of positive ions $\overline{p}$ the following relations hold:

$$\frac{d\overline{n}}{dz} = (\alpha - \eta)\,\overline{n} \quad , \quad \frac{d\overline{p}}{dz} = \alpha\overline{n}. \tag{2.7}$$

With the boundary conditions $\overline{n}(0) = 1$ and $\overline{p}(0) = 0$ and the assumption that α and η stay constant, the solution of these differential equations is given by [57]:

$$\overline{n}(z) = e^{(\alpha-\eta)z} \quad , \quad \overline{p}(z) = \frac{\alpha}{\alpha-\eta}\left(e^{(\alpha-\eta)z} - 1\right) \tag{2.8}$$

The average number of electrons follows an exponential function depending on the effective Townsend coefficient $\alpha_{eff} = \alpha - \eta$. For timing RPCs $\alpha_{eff} \approx 110\ mm^{-1}$ and it increases linearly with the applied electric field. A calculation of α and η with the program IMONTE [68] as function of the electric field is shown in Fig. 2.5. For an electric

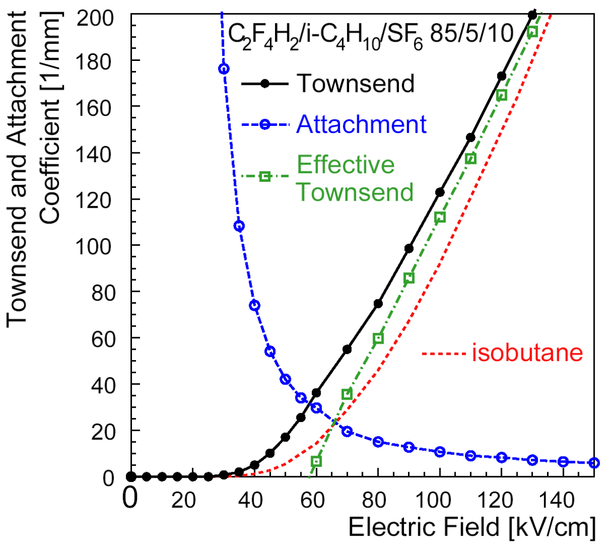

Figure 2.5: Townsend and attachment coefficient for the gas mixture $C_2H_2F_4/i\text{-}C_4H_{10}/SF_6$ 85%/5%/10% and iso-butane as function of the electric field calculated with IMONTE. The temperature of the gas was set to $T = 296.15$ K and the pressure to $p = 1013$ mbar. The Figure is taken from [56].

field of about 60 kV/cm, a gas temperature of $T = 296.15$ K and a gas pressure of $p = 1013$ mbar the Townsend coefficient has the same value as the attachment coefficient, i.e. the avalanche stops growing. This effect becomes important when the number of electron-ion-pairs in the avalanche is so large that the electric field that the charge are creating diminishes the external field. It is called space charge effect and will be discussed later on. Note that the effective Townsend coefficient can become negative when the field in the gap is below 60 kV/cm. In this case the electrons become strongly attached to the ions. The probability $P(n,z)$ for an avalanche triggered by a single electron to contain n electrons after a distance z is given by [57]:

$$P(n,z) = \begin{cases} k\frac{\overline{n}(z)-1}{\overline{n}(z)-k} & \text{if } n = 0, \\ \overline{n}(z)\left(\frac{1-k}{\overline{n}(z)-k}\right)^2\left(\frac{\overline{n}(z)-1}{\overline{n}(z)-k}\right)^{n-1} & \text{if } n > 0. \end{cases} \tag{2.9}$$

with $k = \eta/\alpha$. The variance $\sigma^2(z)$ of the distribution is given by [57]:

$$\sigma^2(z) = \left(\frac{1+k}{1-k}\right)\overline{n}(z)(\overline{n}(z)-1) \tag{2.10}$$

Both variance and distribution $P(n,z)$ depend not only on α_{eff} like the average number of electrons but also on k. As shown in [56; 57] the attachment coefficient plays a substantial

role in the avalanche development. However, in the literature [49] also the Furry law and the Polya distribution are used to determine the probability to find n electrons after a path length z. The Furry law and the Polya distribution do not contain the attachment coefficient.
The space charge which is created by the cloud of electrons and ions can be calculated by assuming that the charges form a sphere of radius r_S. Then the field E_r of this charged sphere at its surface is [56]:

$$E_r = \frac{e_0 n}{4\pi\varepsilon_0 r_S^2}, \tag{2.11}$$

with e_0 the unit charge, n is the number of charges and ε_0 the dielectric constant in the vacuum. Taking the example shown in figure 2.7a where the sphere of the cloud has a radius of about $r_S = 0.03$ mm and contains about $n = 0.75 \times 10^6$ electrons, the field strength becomes $E_r = 1.2$ kV/mm which is about 10 % of the external field. Figure 2.6 depicts a snapshot of a simulated avalanche after 0.5765 ns duration [56]. The avalanche

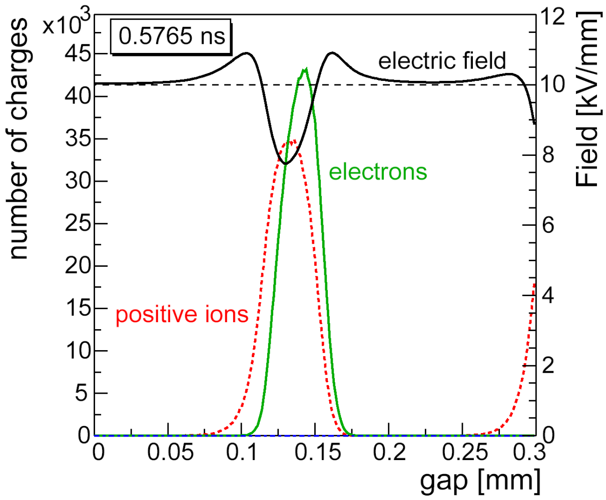

Figure 2.6: Snapshot of a simulated avalanche after a duration of 0.5765 ns. The electron (green line) and the ion distribution (red dashed line) modify the electric field (black line) locally and therefore change the effective Townsend coefficient in this region. For more detailed information see [56]. Figure is taken from [56].

is simulated within a gas gap of 0.3 mm which is subdivided into 500 steps. The electron distribution which is represented by the green line drifts towards the right side. The positive ion distribution is marked with the dashed red line. The black line denotes the electric field in the gap. A cloud of electrons which already reached the electrode on the right side sits on the surface of the resistive material and lowers the electric field together with the positive ions in front of the electrode. The electrons and ions in the middle of the gap amplify the electric field at the edges of the cluster and diminish it in the center of the cluster. With a progressing avalanche the field can be lowered to a value such that the effective Townsend coefficient becomes negative and the electrons get attached. During the drift of the electrons towards the electrode they additionally perform a motion in transversal direction. The reason for this transversal drift is the thermal motion with an average kinetic energy of about $\varepsilon = \frac{3}{2}kT = 40$ meV [193] and the repulsive forces of the other charges. k is the Boltzmann constant and T the temperature of the gas. The density distribution of the charge cloud in transversal direction corresponds to a Gaussian function with a width depending on time t. The width in x and y direction is given by $\sigma_{x,y} = \sqrt{2Dt}$ with the diffusion coefficient D. In z-direction the diffusion coefficient D_z differs due to the electric field from the transversal diffusion coefficient D. Figure 2.7 depicts two snapshots taken at $t = 0.5$ ns and $t = 0.65$ ns of the electron density in a simulated avalanche that moves toward the electrode on the right side. The 0.3 mm wide gap is filled with the standard gas mixture and the electric field across the gap is 93 kV/cm. From this figure the radius of an avalanche and the diffusion can be estimated. The charge deposition area on the glass plate is from the same magnitude whereby an estimation about rate capability can be done (see sec. 2.7). More detailed information about this figure can be found in [56].

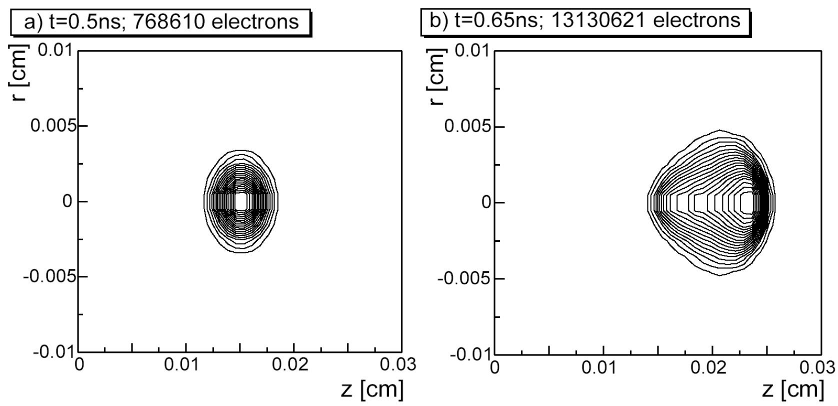

Figure 2.7: Snapshot of electron density distributions in an avalanche taken at $t = 0.5$ ns and $t = 0.65$ ns. The avalanche in (a) contains about 8×10^5 electrons. 0.15 ns later (b) the number of electrons augmented to about 1.3×10^7. The density is not symmetric any more due the distorted electric field. More detailed information can be found in [56]. Figure is taken from [56].

2.3 Streamers

At very high fields and under certain conditions the avalanche can transform into a luminous filament between the electrodes [60] called streamer. A streamer develops typically when the avalanche reaches a size of about 10^8 electrons (Raether condition) and the self-field of the avalanche is comparable to the external field [60]. The propagation velocity of streamers was measured to be significantly higher than the drift velocity of the normal avalanche [56; 69]. Streamers are generated by short-range UV photons which are created in the avalanche process and emitted spherically. These photons can either ionize the gas in the region where the external field is strongly enhanced (cf. figure 2.8) and thus generate new avalanches especially in the ion tails or knock out electrons from the cathode surface generating new avalanches as well. Due to a certain number of avalanches contributing to the creation process a streamer mechanism is rather slow. The experimental characteristic of a streamer is a large current signal following after a so-called precursor pulse which is

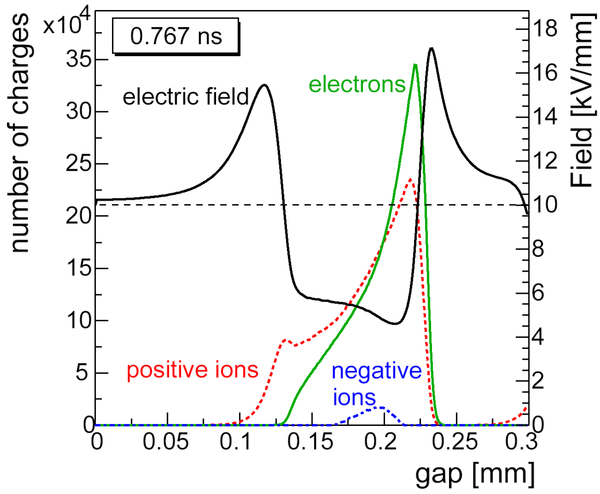

Figure 2.8: Snapshot of a simulated avalanche after a duration of 0.767 ns. The electron (green line) and the ion distribution (red dashed line) modify the electric field (black line) significantly. In front of the electrons and in the ion tail the field is enhanced by more than 50 % allowing for photon induced ionization. For more detailed information see [56]. Figure is taken from [56].

generated by the original avalanche. The delay of the streamer signal to the precursor pulse can vary between 10 - 100 ns. The magnitude, however, is about 100 times higher. This high charge deposition in the resistive plates reduces the electric field in the gap which leads to temporary inefficiency in this particular place. This inefficient spot is reflected in a reduced rate capability of the counter. Furthermore, streamers evoke a huge readout strip multiplicity due to the low preamplifier threshold which is required by the avalanche mode [56]. Therefore, in practice streamers are strongly suppressed by adding the photon quencher SF_6 to the gas mixture (5 - 15 %). The streamer probability in timing RPCs is below 1 ‰. However, for trigger RPCs operating in the streamer mode the appearance of streamers is enforced. In this case, where a good timing plays a minor role, one profits from the huge signals which can be fed into discriminators without amplification.

2.4 Signal induction

The current induced in an electrode by a moving charge q can be calculated with the Shockley - Ramo theorem [70; 71]:

$$i(t) = \vec{E}_W \cdot \vec{v}_D(t) q(t), \tag{2.12}$$

with $\vec{E}_W$ being the so-called weighting field and $\vec{v}_D(t)$ the drift velocity of the charge carriers. As already mentioned, the ion drift velocity is in comparison to the drift velocity of the electrons negligibly small. Therefore only electrons contribute to the fast signals in RPCs. In an RPC the electrons move parallel to the electric field in z-direction and the above equation can be simplified to [57]:

$$i(t) = \frac{E_W}{V_W} v_D(t) e_0 n(t), \tag{2.13}$$

with $n(t)$ the number of electrons created in an avalanche. If n_{cl} is the number of clusters / avalanches which occur in the active RPC volume the total induced current is the sum of all currents originating from individual clusters:

$$i(t) = \sum_{j=1}^{n_{cl}} i(t)_j. \tag{2.14}$$

The weighting field E_W is the electric field in the gap if the electrode is put to the potential V_W and the other electrodes are all grounded. V_W is typically set to 1 V. The weighting field can be calculated analytically for a 1 gap RPC (2 glass layers + 1 gap layer). However, the formulas become quite complex [56; 72]. For a RPC with many gaps the weighting field was calculated as quoted in [73; 74]. Figure 2.9 shows the calculated weighting field E_W for a narrow strip RPC with 2 × 4 gaps developed by the FOPI collaboration and a wide strip RPC with 2 × 2 gaps developed by Fonte [75]. For the wide strip RPC the

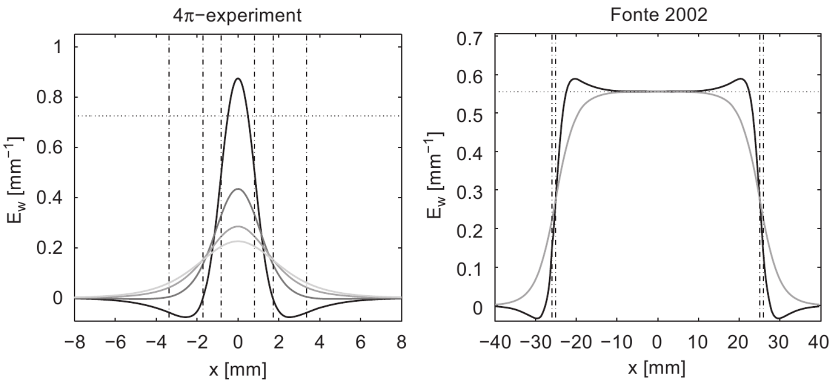

Figure 2.9: Weighting field profiles across the strips (x coordinate) evaluated at the center of each gap, for the FOPI-RPC (left) and the Fonte-2002 RPC prototype (right). The gray color gradient reads from black (gap closest to the readout strip) to light gray (gap furthest from the readout strip). The dashed lines indicate the strip geometry. The Figure is taken from [74].

weighting field is almost constant across the strip and almost the same in every gap. The value in the center of the electrode can be calculated by considering an RPC as a capacitor with $N = 2n + 1$ layers (n gaps and $n + 1$ glass plates) of thickness d_i and permittivity ε_i applying the following conditions [57]:

$$\sum_{i=1}^{N} E_i d_i = V_W, \qquad E_i \varepsilon_i = E_j \varepsilon_j, \tag{2.15}$$

with neighboring layer indices i and j. Assuming an RPC with n equal gaps with a gap size d and a permittivity $\varepsilon \approx 1$ and $n + 1$ equal glass plates with thickness b and permittivity $\varepsilon_r \approx 8$ the equations 2.15 become:

$$V_W = (n + 1) E_P b + n E_W d, \qquad E_P \varepsilon_r = E_W$$

, with E_P the electric field across the glass plate and E_W the electric field across the gap. V_W is the potential between the electrodes. The combination of both equations leads to an expression for the weighting field:

$$\frac{E_W}{V_W} = \frac{\varepsilon_r}{(n+1)b + nd\varepsilon_r}. \tag{2.16}$$

This formula holds for a strip of infinite width. For CBM a 8n gap RPC with a gap size of $d = 0.22$ mm and glass plates with a thickness of $b = 0.5$ mm is considered (cf. section 5.4 and 5.5). The corresponding weighting field is about 0.43 mm^{-1}. Figure 2.10 shows the weighting field calculated with equation 2.16 as function of the gap number n for the CBM prototype. The variation of the weighting field with the gap number for gap sizes bigger than 6 is not so strong any more. A decrease of the induced charge due to the lowering of the weighting field by adding one more gap is counterbalanced by an increase of the induced charge due to the increase of the number of clusters. The variation of the

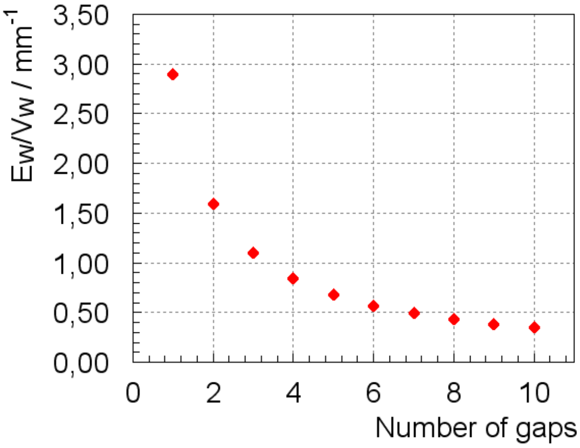

Figure 2.10: Weighting field calculated with equation (2.16) as function of the number of gaps.

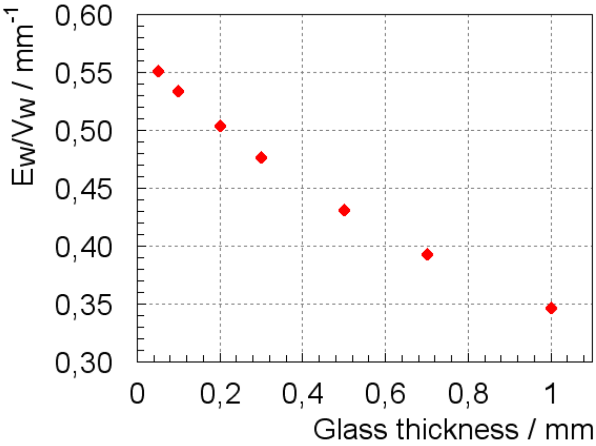

Figure 2.11: Weighting field calculated with equation (2.16) as function of the glass thickness b.

weighting field with the resistive plate (glass) thickness for an 8 gap RPC is depicted in Fig. 2.11. The plot suggests to minimize the plate thickness in order to increase the induced current. However, the gain would be only 24 % if one reduces the plate thickness from 0.5 mm to 0.1 mm.
In order to obtain an estimate of the current induced in the RPC the electric field and thus the drift velocity is assumed to be constant ($v_D(t) = v$). The number of electrons in the avalanche $n(t)$ can be approximated after some initial fluctuations by:

$$n(t) = n_{av}\mathrm{e}^{(\alpha-\eta)vt}, \tag{2.17}$$

leading to an induced current of [57]:

$$i(t,z) = \frac{E_W}{V_W} e_0 v n_{av} \mathrm{e}^{(\alpha-\eta)vt} \Theta\left(\frac{d-z}{v} - t\right) \tag{2.18}$$

for an avalanche starting at z in a gap of size d. n_{av} is the average number of electrons in a cluster. The largest part of the induced signal is due to the exponential growth at the very end of the avalanche development [76]. Assuming that the distance between individual clusters is exponentially distributed like

$$P(\Delta z) = \frac{1}{\lambda} e^{-\Delta z/\lambda}, \tag{2.19}$$

it can be shown after some lengthy calculation (see [57]) that the average signal of an RPC is given by:

$$\bar{i}(t) = \frac{E_W}{V_W} v e_0 n_{av} \mathrm{e}^{(\alpha-\eta)vt} \left(\frac{d - vt}{\lambda}\right) \times \Theta\left(\frac{d}{v} - t\right) \tag{2.20}$$

with the Theta-step function $\Theta(x)$. The average induced charge $\overline{Q}_{ind}$ can be calculated via the integral of the induced current.

$$\overline{Q}_{ind} = \int_0^T \bar{i}(t) dt \tag{2.21}$$

T is the total time of the signal. For timing RPCs a typical mean value for T is about 1 ns [76]. Since nowadays mostly the Time-over-Threshold (ToT) of a signal is measured instead of the charge the preamplifier has to be fast enough in order to handle those signals.

2.5 Intrinsic time resolution and efficiency

In this subsection a theoretical derivation of the time resolution and efficiency for a one gap RPC is presented. Further, the assumption is made that a single primary electron created somewhere in the gap starts an avalanche.

Intrinsic time resolution

The induced current $i(t)$ and the probability to find the amplitude A is according to equation (2.18) given by [57]:

$$i(t) = A \cdot \mathrm{e}^{(\alpha-\eta)vt}, \qquad P(A) = \frac{1}{A_{av}} \mathrm{e}^{-A/A_{av}}. \tag{2.22}$$

The amplitude A is exponentially distributed around an average amplitude A_{av}. Setting a threshold amplitude A_{thr} to the RPC signal the crossing time is given by:

$$i(t) = A \cdot \mathrm{e}^{(\alpha-\eta)vt} = A_{thr} \quad \rightarrow \quad t(A) = \frac{1}{(\alpha-\eta)v} \ln \frac{A_{thr}}{A}. \tag{2.23}$$

The time distribution $P(t)$ for a given threshold is given by [57]:

$$\begin{aligned} P(t) &= \int_0^\infty \frac{1}{A_{av}} \mathrm{e}^{-A/A_{av}} \delta\left(t - \frac{1}{(\alpha-\eta)v} \ln \frac{A_{thr}}{A}\right) dA \\ &= (\alpha-\eta)v \cdot \frac{A_{thr}}{A_{av}} \exp\left(-(\alpha-\eta)vt - \frac{A_{thr}}{A_{av}} \mathrm{e}^{-(\alpha-\eta)vt}\right), \end{aligned} \tag{2.24}$$

with $\delta(x)$ the Dirac delta function. This integration step is described in detail in the appendix. A different threshold amplitude leads only to a time shift. Therefore, the shape of the distribution is independent of the threshold and the average amplitude [57]. Time shifting the maximum of the distribution to zero leads to:

$$\begin{aligned} P(t) &= (\alpha-\eta)v \cdot F((\alpha-\eta)vt) && (2.25)\\ \text{with} \qquad F(x) &= \exp\left(-x-\mathrm{e}^{-x}\right). && (2.26) \end{aligned}$$

$F(x)$ is the so called Landau function. The variance $\sigma(F)$ of the Landau function is:

$$\sigma(F) = 1,28255 \tag{2.27}$$

The intrinsic time resolution of a one gap RPC is given by [77]:

$$\sigma_{RPC} = \frac{1,28255}{(\alpha-\eta)v} \tag{2.28}$$

This equation implies that the intrinsic time resolution of an RPC depends basically only on the effective Townsend coefficient $\alpha-\eta$ and the drift velocity v and not on the preamplifier threshold. This fact was confirmed both in simulations [57] and in the experiment [78]. However, in the derivation of equation (2.28) no space charge effects were considered [56]. Typical values for a timing RPC result in a theoretical time resolution of about 45 ps for a one gap RPC. The naive scaling with $1/\sqrt{n}$ for multi-gap RPCs, however, does not work because the timing in the MRPC is dominated by the gap with the largest signal. The largest signal gives the earliest threshold crossing time. The measurement of the earliest time has a larger r.m.s. than the average of n time measurements [57]. In simulations - using the above formalism - a time resolution of about 25 ps for an 8 gap RPC was achieved [57]. A similar value was measured with a 10 gap RPC [79]. However, most results reported in the literature include the jitter of the full electronics chain so that a statement about the pure counter time resolution is difficult. Typical values including the electronics time resolution are in the order of 50 - 70 ps [80–83].
The world record regarding time resolution measurements with an MRPC reported in the literature [84] is 20 ps for a 24 gap RPC with an applied field of 135 kV/cm across the gap.

Efficiency

Assuming again an avalanche originating from a single electron and starting at position z in the gas gap the induced charge can be calculated by [57]:

$$Q_{ind}(z) = \frac{E_W}{V_W}\frac{e_0}{\alpha-\eta}\mathrm{e}^{(\alpha-\eta)(d-z)} - 1. \tag{2.29}$$

d is the size of the gap. The weighting field is kept constant, i.e. space charge effects are not included. Assuming further that the RPC is efficient when the induced charge is larger than a threshold charge Q_{thr} the position where the threshold charge is reached is given by:

$$z_0 = d - \frac{1}{\alpha-\eta}\ln\left(1+\frac{V_W}{E_W}\frac{\alpha-\eta}{e_0}Q_{thr}\right). \tag{2.30}$$

Since the avalanche starts typically with one electron a substantial part of the gap delivers no signal above threshold. Using typical numbers for the weighting field and the effective Townsend coefficient for an 8 gap RPC with a gap size of $d = 0.22$ mm an avalanche induces about 1 fC after a drift length of 0.12 mm. Assuming a typical threshold of 10 - 40 fC the avalanche has to start at least 0.14 - 0.15 mm above the resistive plate. Taking more than one cluster per gap into account the efficiency for one gap is according to [57] approximately given by:

$$\varepsilon = 1 - \mathrm{e}^{-(1-\frac{\eta}{\alpha})\frac{d}{\lambda}} \left(1 + \frac{V_W}{E_W}\frac{\alpha - \eta}{e_0} Q_{thr}\right)^{\frac{1}{\alpha\lambda}} . \tag{2.31}$$

However, this formula is calculated assuming a readout of the charge only on one electrode. For a differential readout twice the induced charge is available. On the other hand a strip counter is mostly read out on both strip ends which halves the signal again. Plugging in typical numbers for a multi-gap timing RPC and a threshold charge of 40 fC, equation (2.31) delivers an efficiency of about 35 % per gap. This low efficiency is mainly caused by the fact that the avalanche needs a certain distance to develop before the gap becomes efficient. The scaling of the efficiency for n gaps is given by $1-(1-\varepsilon)^n$ with the deficiency $1-\varepsilon$ of one gap. With the efficiency calculated for one gap an 8 gap RPC has still an efficiency of 97 %. In reality, the efficiency is even higher because the induced charge of every gap contributes to the total induced charge and therefore the sum of all gaps counts. Efficiencies around 99 % and better are found in the literature [135].

2.6 Signal propagation

This subsection describes the propagation of the signal after induction. The RPC signal has a typical width of 1 ns. Thereby, for strip counter (strip length between 30 to 50 cm) it is shorter than the signal propagation time. In this case the read out electrodes have to be treated as a multi-conductor transmission line [59]. An avalanche induces a signal somewhere in the electrode i.e. it acts as a current source. The pulse propagates in both directions of the strip towards the end. In order to avoid reflections on the strip ends the counter has to be terminated properly [59]. Generally, the strip width is homogeneous and much smaller than its length (see figure 2.12). Therefore the electrode can be treated as

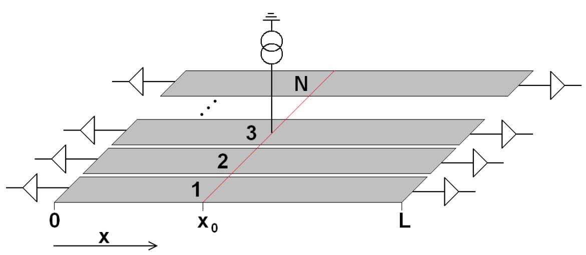

Figure 2.12: Sketch of a two dimensional multi-conductor transmission line which is similar to an RPC electrode. A current is injected in strip 3 at position $x = x_0$. The pulse propagates towards the strip ends where it is read out by preamplifiers.

a two dimensional N-conductor transmission line. Such a system can be described by the following telegraph equations in the Transversal ElectroMagnetic (TEM) approximation [59]:

$$\frac{\partial}{\partial x}\vec{U}(x,t) = -\hat{\mathbf{R}}\vec{I}(x,t) - \hat{\mathbf{L}}\frac{\partial}{\partial t}\vec{I}(x,t) \tag{2.32}$$

$$\frac{\partial}{\partial x}\vec{I}(x,t) = -\hat{\mathbf{G}}\vec{U}(x,t) - \hat{\mathbf{C}}\frac{\partial}{\partial t}\vec{U}(x,t), \tag{2.33}$$

where

$$\vec{I}(x,t) = \begin{pmatrix} I_1(x,t) \\ \vdots \\ I_N(x,t) \end{pmatrix} \quad ; \quad \vec{U}(x,t) = \begin{pmatrix} U_1(x,t) \\ \vdots \\ U_N(x,t) \end{pmatrix}$$

are the currents and the voltages of a system for N individual strips. $\hat{\mathbf{R}}$, $\hat{\mathbf{L}}$, $\hat{\mathbf{G}}$, $\hat{\mathbf{C}}$ are $N \times N$ matrices representing the resistance, inductance, transconductance and capacitance per unit length. These matrices are assumed to be independent of the frequency. This assumption is correct for frequencies below a few GHz. Assuming further a lossless electrode which is mostly justified in case of an RPC electrode the matrices $\hat{\mathbf{R}}$ and $\hat{\mathbf{G}}$ are zero and the coupled differential equation from above can be simplified to:

$$\frac{d^2}{dx^2}\vec{I}(x,t) = \hat{\mathbf{C}}\hat{\mathbf{L}}\frac{d^2}{dt^2}\vec{I}(x,t) \tag{2.34}$$

$$\frac{d^2}{dx^2}\vec{U}(x,t) = \hat{\mathbf{L}}\hat{\mathbf{C}}\frac{d^2}{dt^2}\vec{U}(x,t) \tag{2.35}$$

Considering a signal induced in strip n at position $x = x_0$ acting as a current source $I^0(x = x_0, t)$ the general solution of the equation above is [59]:

$$\vec{I}(x,t) = \frac{1}{2}\hat{\mathbf{T}}\left(\begin{pmatrix} t_{1n}^{-1}I^0\left(t - \frac{x-x_0}{v_1}\right) \\ \vdots \\ t_{Nn}^{-1}I^0\left(t - \frac{x-x_0}{v_N}\right) \end{pmatrix} - \begin{pmatrix} t_{1n}^{-1}I^0\left(t + \frac{x-x_0}{v_1}\right) \\ \vdots \\ t_{Nn}^{-1}I^0\left(t + \frac{x-x_0}{v_N}\right) \end{pmatrix}\right) \tag{2.36}$$

$$= \vec{I}(x,t)^+ - \vec{I}(x,t)^- \tag{2.37}$$

and

$$\vec{U}(x,t) = \frac{1}{2}\hat{\mathbf{Z}}_C\hat{\mathbf{T}}\left(\begin{pmatrix} t_{1n}^{-1}I^0\left(t - \frac{x-x_0}{v_1}\right) \\ \vdots \\ t_{Nn}^{-1}I^0\left(t - \frac{x-x_0}{v_N}\right) \end{pmatrix} + \begin{pmatrix} t_{1n}^{-1}I^0\left(t + \frac{x-x_0}{v_1}\right) \\ \vdots \\ t_{Nn}^{-1}I^0\left(t + \frac{x-x_0}{v_N}\right) \end{pmatrix}\right) \tag{2.38}$$

$$= \hat{\mathbf{Z}}_C\left(\vec{I}(x,t)^+ - \vec{I}(x,t)^-\right) \tag{2.39}$$

$$= \vec{U}(x,t)^+ - \vec{U}(x,t)^- \tag{2.40}$$

with

$$\hat{\mathbf{T}}^{-1}\left(\hat{\mathbf{C}}\hat{\mathbf{L}}\right)\hat{\mathbf{T}} = \hat{\mathbf{v}}^{-2} \quad \text{and} \quad \hat{\mathbf{Z}}_C = \sqrt{\hat{\mathbf{L}}/\hat{\mathbf{C}}} = \hat{\mathbf{L}}\hat{\mathbf{T}}\hat{\mathbf{v}}\hat{\mathbf{T}}^{-1} \tag{2.41}$$

and

$$\hat{\mathbf{v}}^{-2} = \begin{pmatrix} \frac{1}{v_1^2} & \dots & 0 \\ \vdots & \ddots & \vdots \\ 0 & \dots & \frac{1}{v_N^2} \end{pmatrix} \quad \text{and} \quad \hat{\mathbf{v}} = \begin{pmatrix} v_1 & \dots & 0 \\ \vdots & \ddots & \vdots \\ 0 & \dots & v_N \end{pmatrix} \tag{2.42}$$

The matrix $\hat{\mathbf{T}}$ contains the normalized eigenvectors of the matrix $\hat{\mathbf{C}}\hat{\mathbf{L}}$. The matrix elements $1/v_i^2$ are the eigenvalues of the matrix $\hat{\mathbf{T}}$. $\hat{\mathbf{Z}}_C$ is the so-called characteristic impedance matrix. T_{nm}^{-1} are the elements of the matrix $\hat{\mathbf{T}}^{-1}$. The solutions of the telegraph equation show a current running symmetrically in both directions from point x_0. They also show that a pulse running along one conductor is a superposition of N times the same pulse-shape $I_0(t)$ running with N different velocities v_i. Therefore, one finds signal dispersion even for a lossless transmission line which is called modal dispersion [59]. For RPC electrodes of less then 1 m length modal dispersion is negligibly small. The strip ends are terminated with the input resistance of the preamplifier defining together with the resistance between strips the load impedance matrix $\hat{\mathbf{Z}}_P$. The voltage measured by the preamplifier is:

$$\vec{U}(0,t) = \hat{\mathbf{Z}}_P \vec{I}(0,t) \quad \text{and} \quad \vec{U}(L,t) = \hat{\mathbf{Z}}_P \vec{I}(L,t). \tag{2.43}$$

The effect of the boundary is that the voltage pulses are reflected according to:

$$\vec{U}(0,t)^{\pm}_{refl} = \hat{\mathbf{\Gamma}}_P \vec{U}(0,t)^{\mp},$$

where $\hat{\mathbf{\Gamma}}_P$ is the reflection coefficient matrix at the line ends [59]. It is defined as:

$$\hat{\mathbf{\Gamma}}_P = \left(\hat{\mathbf{Z}}_P - \hat{\mathbf{Z}}_C\right)\left(\hat{\mathbf{Z}}_P + \hat{\mathbf{Z}}_C\right)^{-1}. \tag{2.44}$$

The total voltage on the strip ends is:

$$\vec{U}(0,t) = \vec{U}^- + \vec{U}^+_{refl} = \left(\mathbb{1} + \hat{\mathbf{\Gamma}}_P\right)\vec{U}^- \tag{2.45}$$

$$\vec{U}(L,t) = \vec{U}^+ + \vec{U}^-_{refl} = \left(\mathbb{1} + \hat{\mathbf{\Gamma}}_P\right)\vec{U}^+ \tag{2.46}$$

Assuming a small dispersion, i.e. the $v_i = v$ which is typically the case for short strips (below 1 m), the voltage measured by the preamplifier is [59]:

$$\vec{U}_{meas}(t) = \vec{U}(0,t) \tag{2.47}$$

$$= \hat{\mathbf{Z}}_P\hat{\mathbf{Z}}_C\left(\hat{\mathbf{Z}}_P + \hat{\mathbf{Z}}_C\right)^{-1} \times \left(0,\dots,0,I^0\left(t - \frac{x_0}{v}\right),0,\dots,0\right)^T \tag{2.48}$$

Defining the matrix $\hat{\mathbf{M}} = \hat{\mathbf{Z}}_P\hat{\mathbf{Z}}_C\left(\hat{\mathbf{Z}}_P + \hat{\mathbf{Z}}_C\right)^{-1}$ the cross talk from strip n to strip m is given by $U_m/U_n = M_{mn}/M_{nn}$ [59]. In order to eliminate reflections $\hat{\mathbf{\Gamma}}_P$ has to become zero i.e. $\hat{\mathbf{Z}}_P = \hat{\mathbf{Z}}_C$. The diagonal elements of $\hat{\mathbf{Z}}_P$ can be adjusted by choosing the proper impedance of the preamplifier. The off-diagonal elements, however, can be adjusted only by interconnecting the strips with the proper resistors which introduces normally a large cross talk. A large cross talk leads first of all to a reduced signal on the main strip and thus decreases the signal to noise ratio which becomes especially important for signals which just cross the preamplifier threshold. Second, a large cross talk increases the number of fired strips which decreases the effective granularity and therefore reduces the double hit capability. Third, a large cross talk reduces the spatial resolution and fourth it increases the data rate which can become critical in a high-rate experiment like CBM. In practice, the strips are typically not interconnected to avoid the cross talk. Furthermore, the reflections stemming from the unmatched off-diagonal elements are typically small. Our approach was to adjust the strip impedance to 100 Ω by choosing the proper geometry of the RPC (strip width, gap between strips, number of gas gaps, gap size, glass size). In order to find the proper geometry of the RPC it was implemented in the APLAC simulation environment [85]. By injecting a pulse on the RPC electrode surface and by measuring the output signal on every strip end the geometry was modified until the reflection and cross talk was minimal.

2.7 Rate capability

In high-rate experiments like CBM the rate capability of the detectors is a key issue. However, an MRPC by construction is limited in rate capability due to the resistivity of the plates. The time interval needed for a localized discharge to recharge from the glass plate is given by

$$\tau = RC = \rho\varepsilon_0\varepsilon_r. \tag{2.49}$$

$R = \frac{\rho d}{A}$ is the resistivity, $C = \varepsilon_0\varepsilon_r\frac{A}{d}$ is the capacitance, ρ is the volume resistivity, d is the thickness, A is the surface and ε_r is the relative permittivity of the resistive plate. ε_0 is the dielectric constant. Typical values for float glass are $\rho \simeq 10^{12}$ Ω cm and $\varepsilon_r = 8$ leading to $\tau \simeq 1$ s. Assuming a charge spot on the glass surface of few hundred μm in diameter, float glass RPCs are limited to rates about 1 - 2 kHz/cm^2.
An analytical description of rate effects is based on the so-called DC model [86]. The average ohmic drop $\overline{I}R$ in the plate is related to the average voltage drop $\overline{V}_{drop}$ in the gap by [86]:

$$\overline{V}_{drop} = V - \overline{V}_{gap} = \overline{I}R = \overline{q}\phi\rho d. \tag{2.50}$$

V is the applied external voltage, $\overline{q}$ is the average charge of an avalanche and ϕ denotes the incident particle flux. Since V is a constant value the real voltage across the gap is $\overline{V}_{gap} = \overline{V}_{gap}(\phi\rho d)$. If the performance of the RPC is ruled by the average effective field $\overline{V}_{gap}$, then any RPC observable O is just a function of $f(\phi\rho d)$ [60]. This is the case for the efficiency. The time resolution, however, is related to the fluctuations of the field and therefore a second moment observable. Nevertheless, in first approximation the following relations for the time resolution and the efficiency hold:

$$\sigma_T = \sigma_0 + K_T\overline{q}\phi\rho d \tag{2.51}$$

$$\epsilon = \epsilon_0 - K_\epsilon\overline{q}\phi\rho d. \tag{2.52}$$

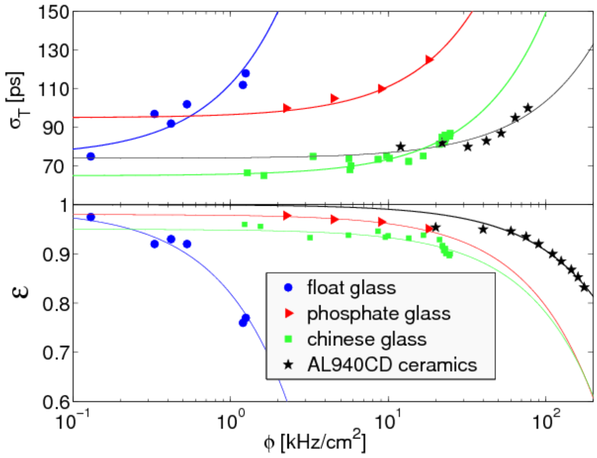

Figure 2.13: Behavior of efficiency and time resolution as function of the incident particle flux for [60] (○) , [88] (▷), [89] (□) and [90] (⋆) together with a linear fit according to equations (2.51) and (2.52). Figure is taken from [91].

K_T , K_ϵ are positive constants depending on the RPC multi-gap structure. This functional dependence has been used to fit some published data in Fig. 2.13. The second term in equations (2.51) and (2.52) determines how much the time resolution and the efficiency and thus the performance are deteriorated with the incident particle flux ϕ. One way to define the rate capability is by setting a limit at the deterioration of the resolution or the efficiency. In practice often a deterioration in time resolution of 20 ps or a drop in efficiency of 5 % is used [91]. According to the definition given above the rate capability can be improved by minimizing the slope $K_i\overline{q}\rho d$ of the functions given in (2.51) and (2.52). The average charge of an avalanche $\overline{q}$ can be decreased by lowering the gap size of the RPC while keeping the same field strength. However, this leads to smaller induced signals which decreases the signal to noise ratio. Modern RPCs are already optimized in terms of gap size.

Another attempt to increase the rate capability is to reduce the thickness of the resistive plate [92]. This is a reasonable approach for small area RPCs (few cm^2). However, large area RPCs suffer from the fragility of the material. Furthermore, these materials are often not produced in an industrial way which makes them very expensive. The minimal thickness for industrially produced float glass is about 0.4 - 0.5 mm.

Another possibility is to decrease the resistivity ρ by increasing the plate temperature. Non-metallic conductors generally follow the Arrhenius law [93] which for narrow temperature intervals is approximately given by:

$$\rho \cong \rho_{T_0} 10^{(T_0-T)/\Delta T}, \tag{2.53}$$

where T is the temperature, ρ_{T_0} the resistivity at the reference temperature T_0 and ΔT the temperature increase required for a resistivity decrease by one order of magnitude. This behavior was also observed in the case of float glass [87] (see Fig 2.14). By increasing the temperature by 25 °C the resistivity of the float glass changes by one order of magnitude. This change is reflected in the behavior of both, the time resolution and the efficiency, as function of temperature (cf. Fig. 5.39) leading to an improvement of the rate capability by one order of magnitude as well [93].

The most promising way to improve the rate capability is selecting materials with lower resistivity than float glass. During the last years two classes of materials were considered for

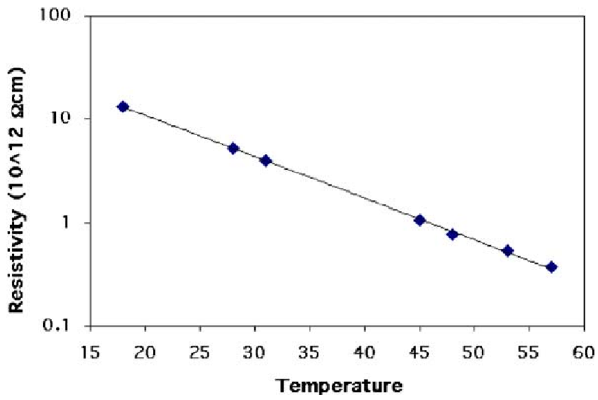

Figure 2.14: Resistivity of float glass as function of temperature. In the case of float glass $\Delta T \simeq 25$ °C. Figure is taken from [87].

high-rate RPCs: low resistive glass also called semi-conductive glass and ceramics. Known types of low resistive glass are: phosphate, silicate and borosilicate glass [88]. For ceramics the resistivity is even tunable in a certain range [94] by adjusting its composition. Table 2.1 lists some materials used for high-rate RPCs and their resistivity at 20 °C. Remarkably,

material	resistivity $\rho_{20°C}$ Ωcm
normal float glass	10^{13}
phosphate glass	10^{10}
silicate glass (Chinese glass)	10^{10}
AL940CD ceramics	10^{9}
Si_3N_4/SiC ceramics	tunable $10^{7} - 10^{12}$

Table 2.1: List of materials used for high rate RPCs and their resistivity at 20 °C. Values taken from [87–90; 94]

all these materials fulfill the Arrhenius law with $\Delta T \simeq 25$ °C. The resistivity of silicate glass, from now on called Chinese glass, as a function of the applied voltage for different temperatures is shown in Fig. 2.15. The resistivity for this kind of glass shows a constant behavior while other materials like phosphate glass show a slight degradation with the applied high voltage [88]. The Chinese glass was used as resistive material in one of the prototypes developed during this work. Figure 2.16 summarizes the various possibilities to increase the rate capability. It shows the measured rate capability (as defined above) as function of $1/\rho d$ for different resistive materials normalized to the typical value in float glass ($\rho_0 d_0 = 300$ GΩcm^2).

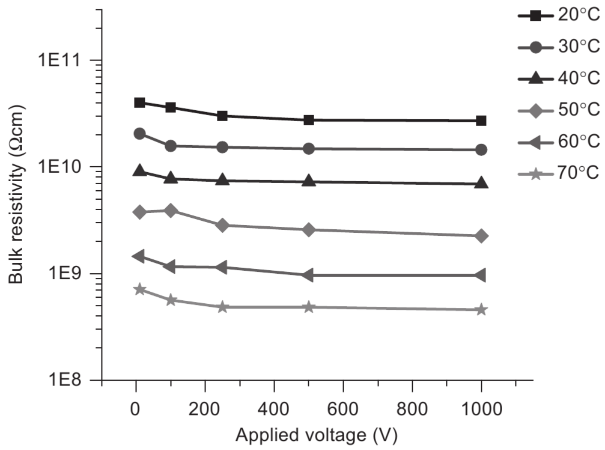

Figure 2.15: Resistivity of silicate glass as function of the applied voltage at various temperatures. By warming the glass by about 25 °C the resistivity can be lowered by one order of magnitude. Figure is taken from [89].

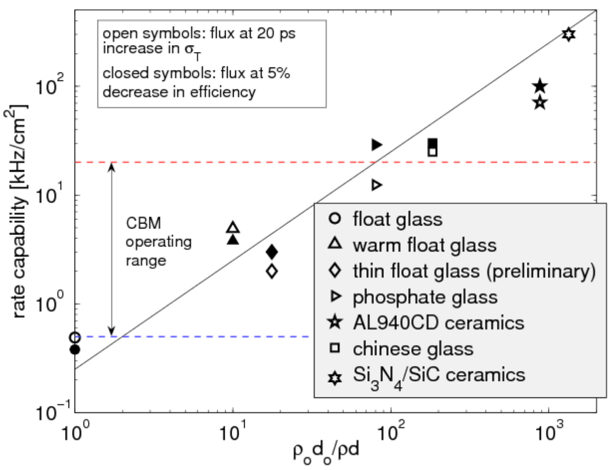

Figure 2.16: Measured rate capability (maximum operating flux) as function of $1/\rho d$ normalized to $\rho_0 d_0 = 300$ GΩcm^2 Data taken from [60] ($\circ$) , [93] ($\triangle$), [92] ($\diamond$), [88] ($\triangleright$) , [90] ($\star$), [89] ($\square$) and [94] ($*$). Figure is taken from [91].

3 The FOPI RPC barrel

The FOPI experiment is located at the SchwerIonenSynchrotron SIS18 at the GSI facility Darmstadt. It is a large-acceptance detector system designed to measure charged particles stemming from heavy ion collisions in the energy range up to 2 GeV per nucleon [95; 96]. The physics goal of FOPI is the study of fundamental properties of hadronic systems at finite temperatures and densities like the equation of state (EoS), the in-medium cross sections and the effective masses of the constituents [3]. The experimental program of FOPI comprises measurements of particle production [97–105], charged particle flow [97; 106–115], nuclear stopping [116–118], in-medium modification of strange particles [119; 120], as well as a search for kaonic clusters [121] and hypernuclei [122], to name the most prominent examples.

In this chapter we will briefly present the FOPI apparatus (section 3.1) followed by the description of the Multi-strip Multi-gap RPC (MMRPC) design and the Time-of-Flight barrel (section 3.2). The performance of the Time-of-Flight barrel is presented in section 3.3. The analysis of the behavior of the MMRPCs was a part of this thesis and will be discussed in more detail in section 3.4. Conclusion for the design of the next generation MRPCs will be presented in section 3.5.

3.1 The FOPI spectrometer

The FOPI detector is structured like most of the high energy and heavy-ion experiments in an onion shell fashion covering a solid angle of almost 4π [123] (see Figure 3.1). The target is surrounded by the so-called Central Drift Chamber (CDC). This detector component measures the tracks of charged particles. These tracks are bent if the particles traverse perpendicular to a magnetic field. The strength of the bending depends on the transverse momentum in the following way

$$\frac{p_t[GeV/c]}{|q|} = 0.3 \cdot B[T] \cdot R_C[m] \tag{3.1}$$

with p_t being the transverse momentum and q the charge of the particle, B the magnetic field and R_C the radius of the curved track. The CDC covers polar angles between $30° < \Theta_{Lab} < 150°$ and has a momentum resolution σ_{p_t}/p_t between 4 and 12 %. Another drift chamber covering the forward region ($7° < \Theta_{Lab} < 30°$) is called Helitron. Since both

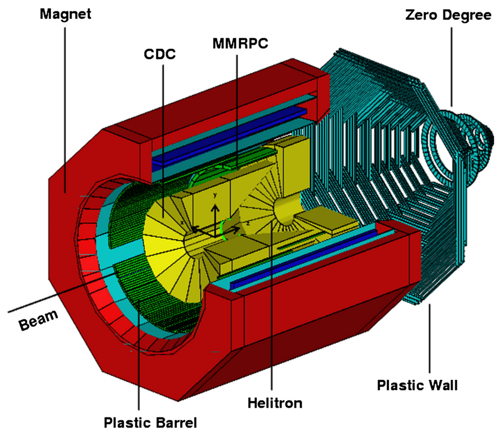

Figure 3.1: Layout of the FOPI spectrometer. For details see text. Figure taken from [140].

chambers are able to measure also the energy loss of the charged particles they can be additionally used for particle identification, especially for particles with low momenta. The CDC for example has a low transverse momentum acceptance of 70 MeV/c for pions and 120 MeV/c for protons. In figure 3.2 the energy loss $\log(dE/dx)$ is plotted versus the momentum p measured by the CDC. The lines denote the theoretical position of the various particles. With this PID method no kaons can be detected. In order to improve

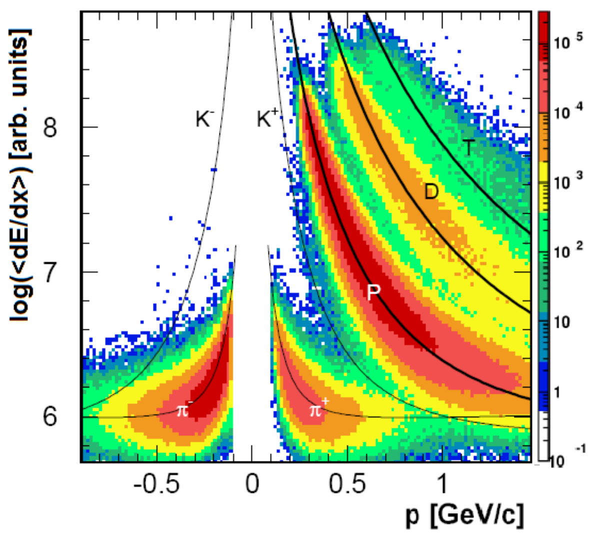

Figure 3.2: Energy loss vs. particle momentum measured in the CDC. The lines denote the theoretical position of the various particles. Figure taken from [115].

the particle identification capability 4 Time-of-Flight detection systems surround the drift chambers. The Zero-Degree Counter consists of 7 concentric rings of plastic scintillators measuring the Time-of-Flight of particles emitted under a polar angle between 1° and 7°. It is mostly used to determine the reaction plane. The plastic wall, covering almost the same polar angle as the Helitron, consist of 512 plastic scintillator bars with lengthes between 45 cm and 165 cm. The light pulse is read out on both sides via photomultipliers having a time resolution of about 200 ps. The position along the scintillator bar can be calculated with $x \propto (t_1 - t_2)/2$. A third scintillator sub system (Plastic Barrel) with a time resolution of about 300 ps is installed around the CDC having a polar angular acceptance of $50° < \Theta_{Lab} < 140°$. It allows for kaon identification in the momentum range from 0.1 MeV/c to 0.6 MeV/c. All scintillator sub systems are capable of measuring the energy loss ΔE of charged particles, thus allowing for an additional restricted particle identification on their own. In the most important region ($30° < \Theta_{Lab} < 52°$.), the mid-rapidity region (@ 2 $AGeV$), the FOPI collaboration installed in the upgrade phase III a Multi-strip Multi-gap Resistive Plate Chamber (MMRPC) barrel in order to separate kaons from pions and protons up to 1.2 GeV/c. The analysis of the features of the MMRPC is part of this thesis. Therefore, this detector will be explained in more detail in the following section. The CDC, Helitron, Plastic barrel and the MMRPC barrel are installed inside a superconducting solenoid magnet with a magnetic field strength of 0.6 T and a homogeneity of 1.5 %.

3.2 The FOPI MMRPC and the Time-of-Flight barrel

In this section we will describe the design of the MMRPC and the structure of the Time-of-Flight barrel developed by the FOPI collaboration.
Before describing the final performance, the development steps will be reviewed since the obtained results were quite interesting under detector-physical aspects. In the year 1998, the FOPI collaboration decided to upgrade their Time-of-Flight system in the midrapidity region with the requirement to have a time resolution below 100 ps in order to identify kaons up to a momentum of about 1 GeV/c. Due to some spatial constrains the counters including the electronics have to operate in the full magnetic field. At that time the solution of choice was the so-called Pestov spark counter [124], developed by Yu. N. Pestov in 1978 [125–127], which showed an excellent time resolution of $\sigma_t \approx 30$ ps [126]. The same type of counter was under investigation also in the ALICE collaboration [128; 129]. Figure 3.3 shows a sketch of a Pestov spark counter. The active volume is defined by an aluminum plate (cathode) and a special semi-conducting resistive glass plate ($\rho = 10^9 - 10^{10}$ Ωcm) called Pestov glass. This kind of glass is a unique product which needs to be polished from both sides, and therefore it is quite expensive. The gap between the two plates is 100 μm wide and supported by glass balls. On top of the glass a printed circuit board (PCB) serves as readout electrode (anode). The anode is segmented into 16 strips having an impedance of 50 Ohm each. The active area of the first prototype was 30 $\times$ 4 cm^2. The follow up prototype already had the dimension of a full-size prototype, namely 90 $\times$ 4 cm^2 (see Figure 3.3b). The Pestov spark counters have to be operated at a high gas pressure between 8 bars and 16 bars and at an extremely high electric field of about 400 kV/cm to 500 kV/cm. A typical gas mixture for Pestov counters (also used by other groups [126; 127]) being operated at 12 bars gas pressure consists of 9 - 10 bar argon, 1 - 2.5 bar iso-butane, 0.2 - 0.3 bar ethene and 0.1 - 0.3 bar 1,3-butadiene. The organic

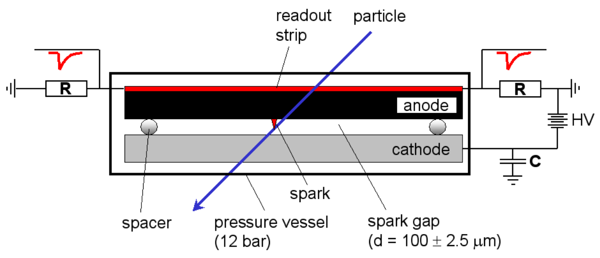

(a) Side view sketch of a single gap Pestov spark counter.

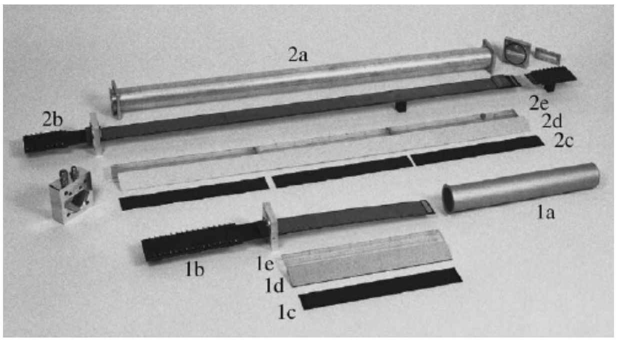

(b) Photograph: components of a 30 cm (1a - e) and of a 90 cm (2a - e) long counter. a: 1mm thick aluminum tubes, b: readout electrode, c: 30 cm long glass plates, d: aluminum cathode, e: extruded plastic profile to guide the gas flow. Figure taken from [124]

Figure 3.3: Pestov spark counter prototype for FOPI

gases were inserted as gamma quenchers. The whole structure was mounted within a 1 mm thick aluminum tube acting as a gas pressure vessel. The two prototypes were tested using heavy ion beams. The main results are summarized in Fig. 3.4 and in Fig 3.5. Figure 3.4 shows the time response function of the 90 cm long Pestov counter for various

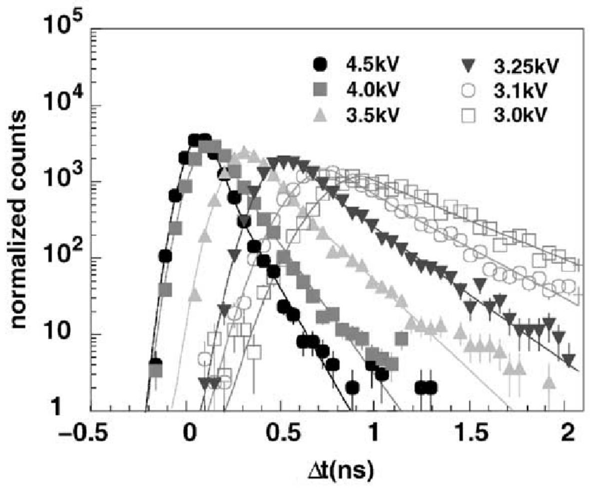

Figure 3.4: Time response function of the 90 cm long Pestov counter for various voltages across the gap, using a gas mixture of 9.23 *bar* neon, 2.4 *bar* iso-butane, 0.3 *bar* ethene and 0.07 *bar* 1,3-butadiene [124].

voltages across the gap starting at the threshold voltage of 3 kV. Below this voltage no sparks are observed. The efficiency which is at this voltage about 15 % rises towards higher voltages and reaches a plateau at about 4.2 kV. At this point the efficiency is 80 %. This rather low efficiency can be explained by the used gas mixture which was based on neon having a lighter mass number than the usually used argon. The time response function is in two aspects remarkable. First, the maximum of the curves is more and more delayed at lower voltages. The explanation is that with a lower electric field also the avalanche growth is diminished. It takes longer for the accumulated charge to develop a spark. Even more astonishing is the shape of the time response function showing a big tail towards delayed events. This tail depends mainly on the used noble gas and not so much on the gas pressure as can be seen in the plots of Fig. 3.5. In first order one would expect that a heavier noble gas increases the number of primary clusters created by a crossing particle. Based on reduced statistical fluctuations this would reduce the tails and improve the time resolution [124]. But the measurements show exactly the opposite. At that time it was explained by the difference in drift velocities of the electrons in the gases. A lower drift velocity leads to a larger avalanche delay and thus to larger tails. Additionally, one would

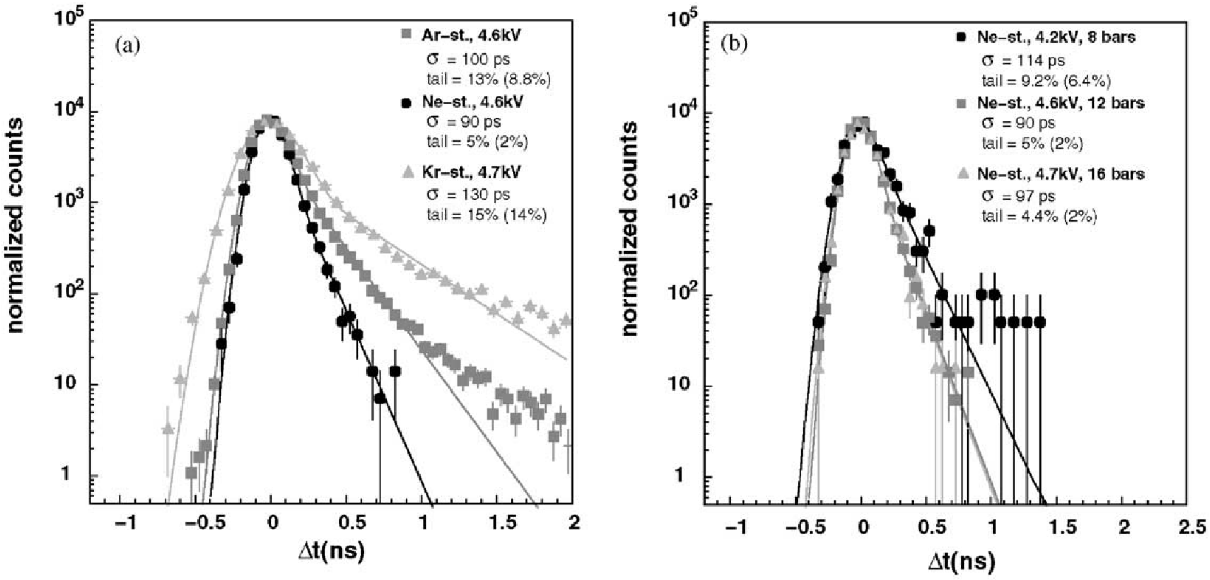

Figure 3.5: Time response function in dependence of the noble gases (left) and on the pressure (right). Figure taken from [124].

expect that at higher pressures, since the number of primary clusters is increased, the fluctuations are decreased and therefore the tails are reduced. On the other hand, at lower pressures, assuming a constant electric field, the drift velocity of the avalanching electrons is higher. It was argued that these two effects counter-balance and only a small change in the shape and in the amount of tails is observed in the time response function at different gas pressures. It was possible to model some of the observations made in these detector tests by simulating the avalanche dynamics including space charge-effects [130].
In conclusion, the most satisfying results regarding system time resolution (σ_t = 90 ps) and tail reduction ($\approx 1\%$) were obtained using neon as noble gas. However, the realization of a Time-of-Flight system made of Pestov spark counters is for the following reasons not trivial:

- Pestov spark counters need a specially manufactured glass. Therefore it is produced only in a small amount which makes it problematic to cover large area with it and thus extremely expensive

- the surface of the glass has to be polished with high accuracy therefore it is difficult to produce several glass plates with equal surface quality
- due to polishing the size of the counters is limited to a few dm^2
- spacing needs to be done with high precision
- the counters have to be operated at high gas pressure
- test results were not satisfactory (tales in the time response function, efficiency only 80 % for neon based gas mixtures)
- from today's perspective Pestov spark counters are not capable of operating under high rates which is a key issue for modern high energy and heavy-ion experiments.

With the development of resistive plate chambers and having experienced the limitations of the Pestov spark counter the FOPI collaboration decided in 2001 to develop a completely new configuration of a glass resistive plate chamber [131]. However, for the first MMRPC prototype many technical properties and components of the Pestov counter were adopted. For example, both electrodes could be reused. The structure of the counter is depicted in Fig. 3.6. The readout electrode is placed now in the center. From both sides, a stack of 2

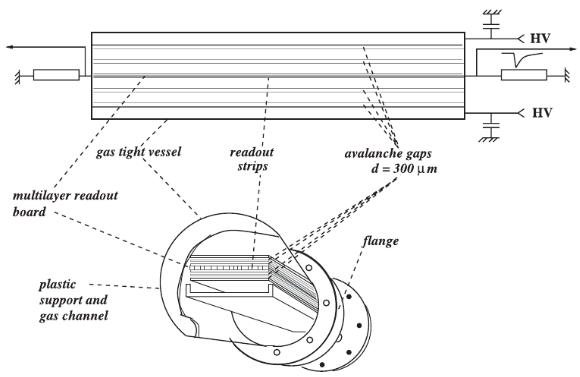

Figure 3.6: Schematics of FOPIs first MMRPC prototype [131].

glass plates and the HV-electrode are staggered around the readout electrode forming 2 × 2 gaps of 0.3 mm width (see Fig. 3.6). This double-stack configuration allows to operate the counters at a quite moderate high voltage of 7 kV. The gap size is realized by ordinary fishing lines which makes the construction of the counter considerably easier. Due to a completely new gas mixture (see chapter 2) this counter operates in the so-called avalanche mode suppressing strongly streamers and sparks. In this operation mode a Gaussian-shape time response function without any tails was observed [132]. A tolerable disadvantage of this operation mode are the rather small and fast signals (few mV and rise time about 200 ps) which have to be amplified by preamplifiers with a bandwidth of about 1 GHz. The FOPI collaboration decided to develop their own customized electronics including a time-to-digital-converter (TDC) and a charge-to-digital converter (QDC) [133]. Further development steps comprised the optimization of the strip-to-gap pitch, the gap size, the number of gaps, the glass thickness, the development and design of super modules, the integration in the existing experiment and so forth [134; 135]. One of the major R&D efforts was the adjustment of the counter impedance to 50 Ω.

3.2.1 The FOPI MMRPC

In this subsection we will describe the final version of the FOPI Multi-strip Multi-gap Resistive Plate Chamber.
Figure 3.7a depicts a cross section of the FOPI MMRPC. The anode is made of a standard 0.6 mm thick double-sided printed-circuit board (PCB) having 16 strips of the size 900×1.64 mm^2 on both sides which are plated through at the ends. The gap between the strips is 0.9 mm (pitch of 2.54 mm) which results in a total width of 46 mm including 2 grounded strips. At both ends of the strips thin transmission lines lead the signals to a special 50 Ω impedance matched connector. In order to keep the 50 Ω impedance over the full counter, capacitor blocks are glued on the part between strips and connector (see Fig. 3.7b). Five normal float glass plates are placed on top of and below the anode forming a 2×4 gap double-stack configuration. The gap size of 220 μm is ensured by commercial fishing lines. On the outer sides of the two outermost glass plates self-adhesive copper foils are glued serving as cathodes (see Fig. 3.7a). A high voltage of about 10 kV is applied forming an electric field of about 110 kV/cm. Finally, the whole stack is mechanically stabilized by two 3 mm thick support plates [136].

3.2.2 The FOPI MMRPC ToF-barrel

Five of the counters described in the previous subsection are grouped together in a gas-tight carbon fiber box of 0.6 mm wall thickness. This device is called a super module (SM). The counters are arranged in a way that two layers are formed. The top layer consists of three counters and the bottom layer of two RPCs covering the non-active area between the detectors in the top layer (see Fig. 3.8). The front faces of the box are closed by aluminum flanges through which the capacitor blocks of individual counters protrude. O-rings around each capacitor block keep the SM gas-tight [136]. One of the flanges additionally has a feed through for gas (inlet/outlet) and a high voltage connection. All five counters within the SM are powered by one single HV channel via a filter/divider circuit inside the box [136]. The carbon fiber box is screwed via four legs on a 10 mm thick aluminum plate. In between, the electronic cards are mounted (cf. Fig. 3.8). 20 cm long shielded cables connect the

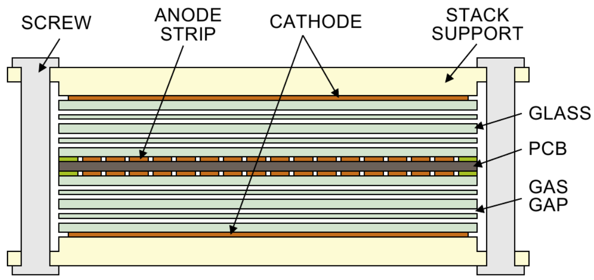

(a) Cross section of the FOPI MMRPC.

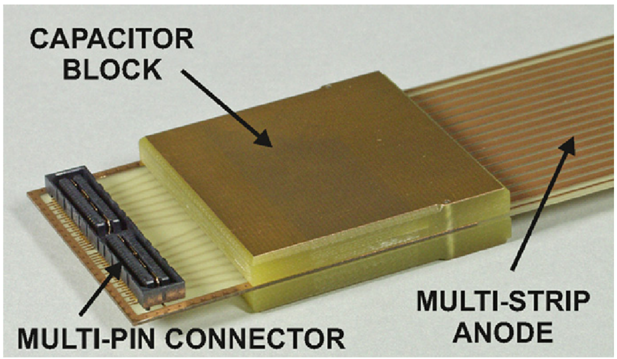

(b) Photograph of the readout electrode with capacitor block and multi-pin connector. The capacitor block has two functions: 1. It keeps the impedance of the signal transmission line at 50 Ω. 2. It penetrates the end flange of the super-module box and assures in combination with an O-ring the gas tightness

Figure 3.7: FOPIs MMRPC [136]

RPCs to the preamplifier cards. In order to minimize signal losses and signal deterioration the preamplifier cards are mounted as close as possible to the detectors.

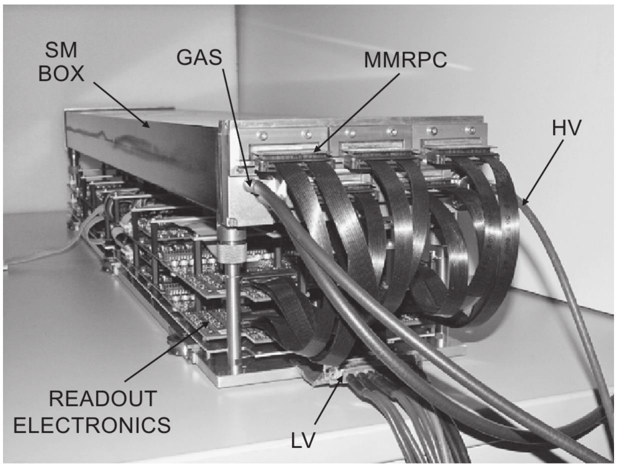

Figure 3.8: A single super module mounted with the readout electronics underneath [136].

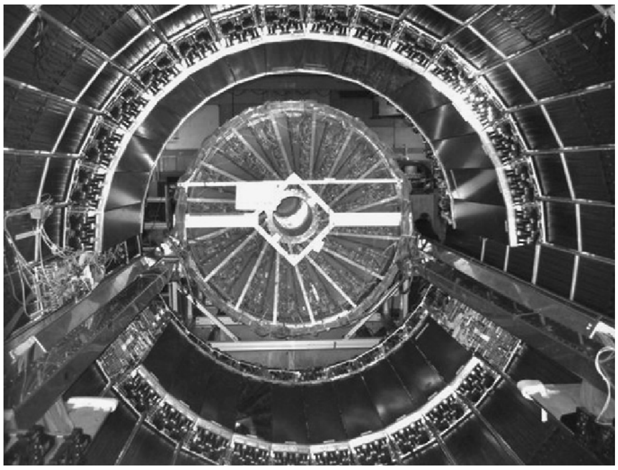

Figure 3.9: Photo of the MMRPC barrel from FOPI

30 of these super modules were arranged side by side forming two cylindrical half shells with a radius of 94 cm. Due to space constraints imposed by the CDC mechanics these two shells could not be combined to a full circle. Figure 3.9 shows a photograph of the MMRPC barrel inside the magnet. In this picture only 26 SMs are installed. Since the counters are read out from both sides the full barrel comprises 4800 timing channels and 2400 charge channels (from 2400 individual strips).

3.3 Performance of the FOPI MMRPC-barrel

This section contains the calibration method for the MMRPC ToF barrel followed by a discussion about time and spatial resolution. Finally, the particle identification capability will be demonstrated.
The first calibration step is the conversion of the data from TDC bins/channels to time. This can be done by dividing the total number of bins by the clock cycle time (40 MHz corresponding to a cycle time of 25 ns). The problem here is the temperature dependence of the effective range in the Time-to-Amplitude-Converter (TAC) chip of the TDC. At higher temperatures the time per bin shrinks so that more bins fit within the cycle time. The variation with temperature is neglected in the first calibration step. In the second calibration step the signal height dependence on the time of flight caused by the leading edge discriminator is corrected (see also Appendix). This procedure is called walk or slewing correction. The time of flight t_{ToF} is defined as:

$$t_{ToF} = t_{RPC} - t_{reference}. \tag{3.2}$$

$t_{reference}$ is the reference time stemming in detector tests typically from two plastic scintillator placed in front of and behind the RPC or from a second RPC used as reference. In the real experiment the reference time is delivered in the case of the FOPI experiment by the start counter. The RPC time t_{RPC} is calculated by taking the mean of the timing signals from both strip sides. In FOPI the walk correction is done for every individual strip using the charge information delivered by fast pions (v_{pion} > 25 cm/ns) identified by the CDC. The method how the correction is applied is called bin-by-bin method. First, profile histograms of the dependencies are created (for instance t_{ToF} vs. charge Q). They carry information about the mean time of flight $\bar{t}_{ToF}$ per changing bin (cf. fig 3.10a). For each event, the corresponding $\bar{t}_{ToF}$ from the profile histogram is subtracted from the actual t_{ToF}. Thus, $\bar{t}_{ToF}$ for each charge bin is shifted to 0. Since the correction causes dependencies on other variables this method has to be applied iteratively. However, this elegant correction method has the disadvantage that it can only be applied if enough statistics are available in every bin (at least 10 counts per bin). Figure 3.10 shows the charge Q dependence of the time of flight for two individual strips (one outer and one inner strip of the counter) before correction (a) and after correction (b).

The next calibration step refers to the intrinsic integral non-linearities in the TAC chip. The bin size of the individual TAC channels is not equal in time. The effect from these non-linearities on the time of flight distribution can be seen in Figure 3.11a. It shows a general trend starting from a positive dt crossing the zero line somewhere in the middle. In addition, a second dependence is superimposed which we call wiggles. These wiggles are shown in figure 3.12 with a resolution of 4 TAC bins per histogram bin. The non-linearity dependence is corrected for with the bin-by-bin method explained above. Due to a lack of statistics a single correction histogram is used for 32 TAC chips/time channels which corresponds to a full counter.
In order to improve the Time-of-Flight resolution further one has to correct also for other

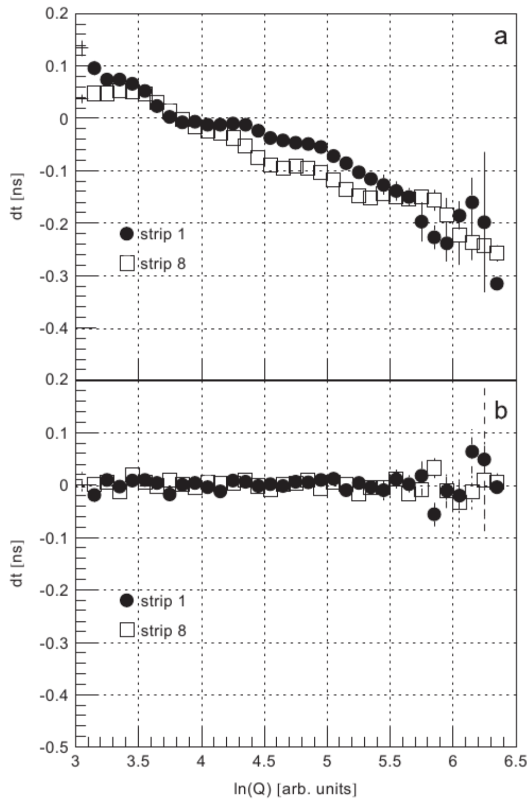

Figure 3.10: Charge Q dependence of the time of flight dt caused by the leading edge discriminator. The full dots refer to a side strip and the open squares to an inner strip in an MMRPC. They differ only slightly. The upper panel shows the dependence before correction and the lower panel afterwards. Figure taken from [136]

.

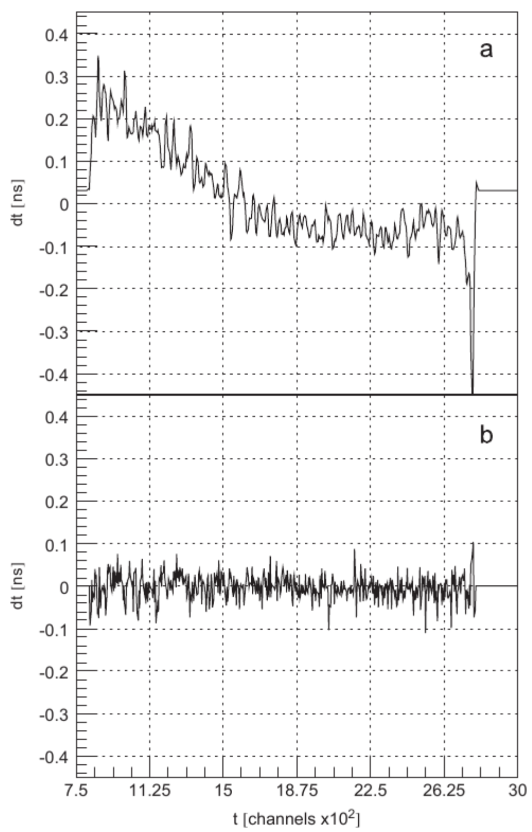

Figure 3.11: (a) Effect of the non-linearities of a TAC chip on the time of flight. Due to the substructure it is called wiggles. (b) After correcting the wiggles the effect is minimized. Figure taken from [136]

.

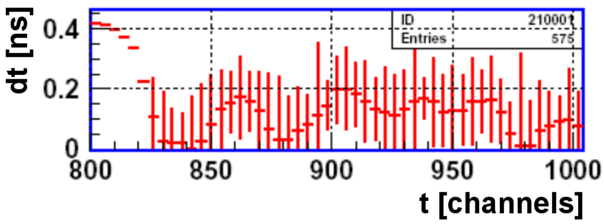

Figure 3.12: Nonlinearities of a TAC chip. The resolution is 4 TAC bins per histogram bin. The correction of these nonlinearities is called "wiggle correction" due to its shape. Only a small region is shown, out of in total $\sim$ 3000 channels.

variables like the position along the strip, the azimuthal angle distribution, the start time, the energy loss in the CDC, particle track parameters, and many more.
In addition, also the start counter has to be corrected in a similar way. After calibrating the time information from both sides of the counter, the charge information of each strip and the corrected reference time are available. From the individual times one calculates the corrected mean time $\bar{t}_{cor}$ of the strip by

$$\bar{t}_{cor} = \frac{1}{2} \cdot (t_l - cor_{t_l}(a, b, \ldots) + t_r - cor_{t_r}(a, b, \ldots)) - cor_{l+r}(d, e, \ldots), \tag{3.3}$$

with t_i representing the raw times of both sides of the strip (l $\widehat{=}$ left, r $\widehat{=}$ right), $cor_{t_i}(a, b, \ldots)$ the correction on the individual RPC raw times depending on the variables $a, b, \ldots$ and $cor_{l+r}(d, e, \ldots)$ the corrections which are common for both sides depending on other variables $d, e, \ldots$.

Also the position z_{cor} is calculated where the signal was created along the strip, using

$$z_{cor} = v \cdot \frac{1}{2} \cdot (t_l - cor_{t_l}(a, b, \ldots) - (t_r - cor_{t_r}(a, b, \ldots))), \tag{3.4}$$

with v representing the signal velocity (typically $0.5c - 0.66c$) and c the speed of light. z_{cor} gives the distance with respect to the center of the strip.
The next step in the analysis is the cluster formation. If a charged particle traverses a narrow strip RPC like the FOPI MMRPC, typically more than one strip show a signal (see section 3.4). A group of neighboring strips, firing simultaneously, form a so-called cluster. The total charge Q_{cl} of an N strips wide cluster is given by:

$$Q_{cl} = \sum_{st=1}^{N} Q_{st}, \tag{3.5}$$

with Q_{st} being the charges seen on the individual strips of a cluster. Sometimes also the mean cluster charge $\overline{Q}_{cl} = Q_{cl}/N$ is used. The mean time t_{cl} of an N strips wide cluster is calculated as follows:

$$\bar{t}_{cl} = \sum_{st=1}^{N} \frac{\bar{t}_{cor,st} \cdot Q_{st}}{Q_{cl}}. \tag{3.6}$$

The cluster mean time is weighted with individual strip charges. And finally the measured time of flight t_{meas} is given by

$$t_{meas} = \bar{t}_{cl} - (t_{ref} - cor_{ref}(x, y, \ldots)), \tag{3.7}$$

with the correction on the reference counter (start counter) $cor_{ref}(a, b, \ldots, x, y, \ldots)$ depending on the variables $a, b, \ldots, x, y, \ldots$.
Alternatively the time of flight can be calculated from the measured momentum p of the identified pions in the CDC by the following relation:

$$\frac{p}{m} = \beta\gamma = \frac{v/c}{\sqrt{1-(v/c)^2}}, \tag{3.8}$$

with m standing for the PDG pion mass, $\beta = v/c$, v for the pion velocity and c for the speed of light. The velocity of the pion can be related to the time of flight by calculating the particle's path s from the interaction point to the RPC. The calculated time of flight dt_{calc} is given by:

$$t_{calc} = \frac{s}{v} = \frac{s}{c} \cdot \frac{\sqrt{1+(p/m)^2}}{p/m}. \tag{3.9}$$

Since the pions move almost with the speed of light the error of t_{calc} is below 10 ps. In order to get the time of flight distribution one calculates $dt = t_{tof} - t_{calc}$. The plot in figure 3.13

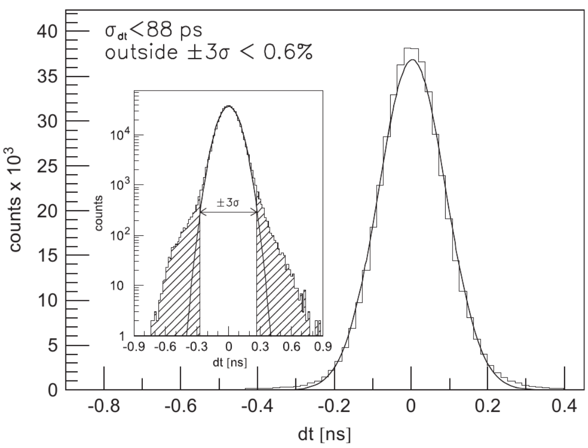

Figure 3.13: Time of flight distribution of the FOPI MMRPC barrel. The distribution is fitted with a Gaussian function delivering a σ_t below 90 ps. The inlet depicts the amount of tails (hatched area) outside 3σ. Figure taken from [136].

shows the time of flight distribution of fast pions (momentum $p > 0.5\ GeV/c$) obtained in a beam time colliding a ^{56}Ni beam of 1.91 $AGeV$ on a ^{56}Ni target. The distribution is fitted with a Gaussian delivering a full system time-of-flight resolution σ_{dt} of about 88 ps. The non Gaussian tails (outside of 3σ) are < 0.6 % (for comparison with Pestov spark counter, see section 3.2 or figure 3.5). The time resolution of the barrel $\sigma_{t(Barrel)}$ (since no reference time resolution is known) can be estimated only by taking particle tracks into account which traverse two overlapped RPC strips and create two clusters. However, this procedure is biasing the result in a sense that the overlapped strips always side strips of a RPC are. These side strips intrinsically have a worse time resolution in comparison to a strip in the middle as demonstrated in the following section. Nevertheless, an MMRPC barrel resolution of $\sigma_{t(Barrel)} \leq 70\ ps$ was obtained.

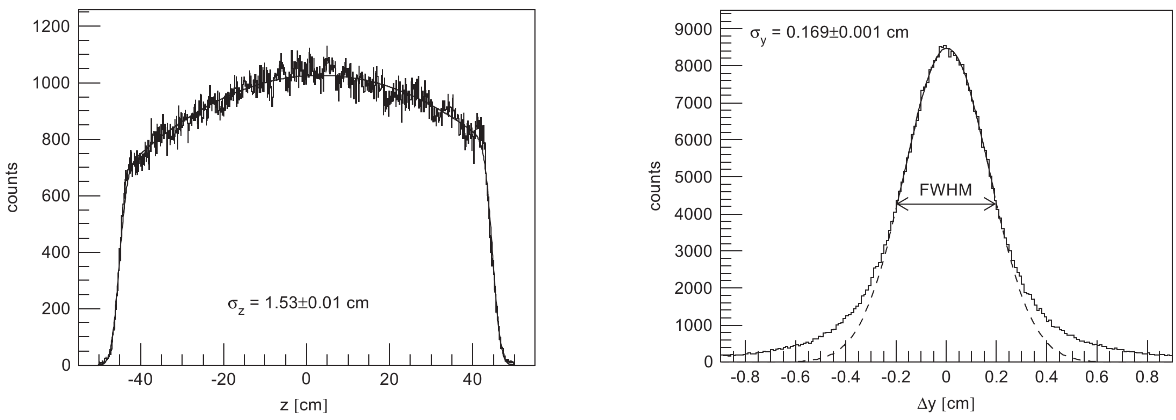

(a) Hit distribution in z-direction (along the RPC strip). The resolution σ_z is obtained by fitting the edges with error functions. Due to edge effects in the RPC this method delivers the worst estimation of σ_z.

(b) The hit position in y direction on the RPC surface is determined by weighting the individual strips in a cluster by their charge. Comparing this number to a theoretical position obtained by extrapolating a track in the CDC delivers the plot shown here. The sigma of the gauss fit corresponds to the resolution in Y-direction. The tails in the distribution originate from the extrapolation over a distance of 25 cm.

Figure 3.14: Spatial resolution of the MMRPC barrel [136].

To a cluster one can associate a position along the beam axis and along the azimuthal direction. The position along the beam axis z_{cl} is given by the weighted mean of the single strip positions:

$$\overline{z}_{cl} = \sum_{st=1}^{N} \frac{z_{cor,st} \cdot Q_{st}}{Q_{cl}}. \tag{3.10}$$

In order to determine the azimuthal position of a cluster the exact position of the counters has to be known, i.e. one can assign to each center of an RPC a polar angle. The center of a cluster, ranging from strip N to strip M with $N, M \in \{1, 16\}$ and $M \geq N$, is then given in terms of the mean strip $\overline{st}_{cl}$ by:

$$\overline{st}_{cl} = \sum_{st=N}^{M} \frac{st \cdot Q_{st}}{Q_{cl}} \tag{3.11}$$

The conversion to cm across the counter is:

$$y_{cl}\ [\mathrm{cm}] = 0.25 \cdot \overline{st}_{cl} - 2.16 \tag{3.12}$$

Once the variables Q_{cl}, t_{cl}, y_{cl} and z_{cl} of a cluster are calculated it is called an RPC hit. Figure 3.14a shows the hit distribution along the z position ranging from -45 cm to +45 cm (length of the detector). The resolution σ_z is derived by fitting error functions to the histogram edges. The result is $\sigma_z = (1.53 \pm 0.01)$ cm. For the determination of

these position resolutions all charged particles measured in the CDC and in the MMRPC Barrel were used [136]. However, the way the resolution σ_z is determined here implies edge, effects and the result can be regarded as a worst case limit. A second possibility to estimate the longitudinal resolution is multiplying the time resolution of the electronic components (jitter) with the signal propagation velocity. In this case we obtain $\sigma_z \approx 0.4\ cm$ which can be seen as the best case limit.
In order to obtain the spatial resolution in azimuthal direction the variable y_{cl} is compared to a virtual position on the RPC surface obtained by extrapolating a CDC track. The resulting distribution, shown in Fig. 3.14b, has a Gaussian shape with substantial tails resulting from multiple scattering and the extrapolation over 25 cm. Therefore, only the region above FWHM was fitted. The resolution is $\sigma_y = (0.169 \pm 0.001)$ cm which agrees with a limit get by the pitch of 2.54 mm [136]. The targeted goal for the upgraded FOPI spectrometer was a kaon identification up to a momentum of 1 GeV/c. With a flight distance from the target of about 1 m the necessary FOPI ToF-barrel time resolution has to be in the order of 100 ps. As shown in Fig. 3.13 this goal is reached and even surpassed. The actual particle identification capability is demonstrated in Fig. 3.15. In this histogram the momenta of each particle, derived from the CDC, are plotted against their velocity measured with the MMRPC. The different bands in the plot stem from the labeled particles. The K^+ can be separated from π^+ and protons up to momenta of 1.2 GeV/c. The anti-kaons (K^-) can be distinguished up to 0.8 GeV/c. The reason are the low statistics for K^-, about 100 times less then for the K^+ yield.

3.4 Characteristics of the FOPI MMRPCs

In order to gain the experience needed for the development of an RPC prototype for the CBM ToF-wall the existing MMRPC of FOPI was investigated in great detail. FOPI is the first experiment using a narrow-strip MRPC as time-of-flight detector. In the case of FOPI it is natural to use a narrow-strip configuration since a good position resolution in azimuthal direction was an requirement.
However, the narrow-strip technology has also some disadvantages. An avalanche created in an RPC induces on a surface (electrode) a charge pattern with a certain dimension. Therefore, in a narrow-strip RPC (strip size < 3 mm) the cluster size is typically several strips wide. In order to minimize this number FOPI uses a gas mixture with a large proportion of quencher gas. The exact gas mixture is 80 % tetra-fluorethan ($C_2H_2F_4$), 15 % sulfur-hexafluoride (SF_6) and 5 % iso-butane (C_4H_{10}). This gas mixture leads to a reduced amount of induced charge being distributed over several strips. Furthermore, the charge is divided in half since the strip is read out on both sides. Yet another half of the primary signal charge is lost due to the construction principle of the FOPI MMRPC. As described in subsection 3.2.1 signals in the FOPI MMRPC are read out only from the anode. The positive part of the signal is absorbed by the high voltage cathode. This type of counter is called single-ended. Hence, the signal is very small and requires dedicated electronics. Figure 3.16 shows the primary signal charge distribution. The charge ranges

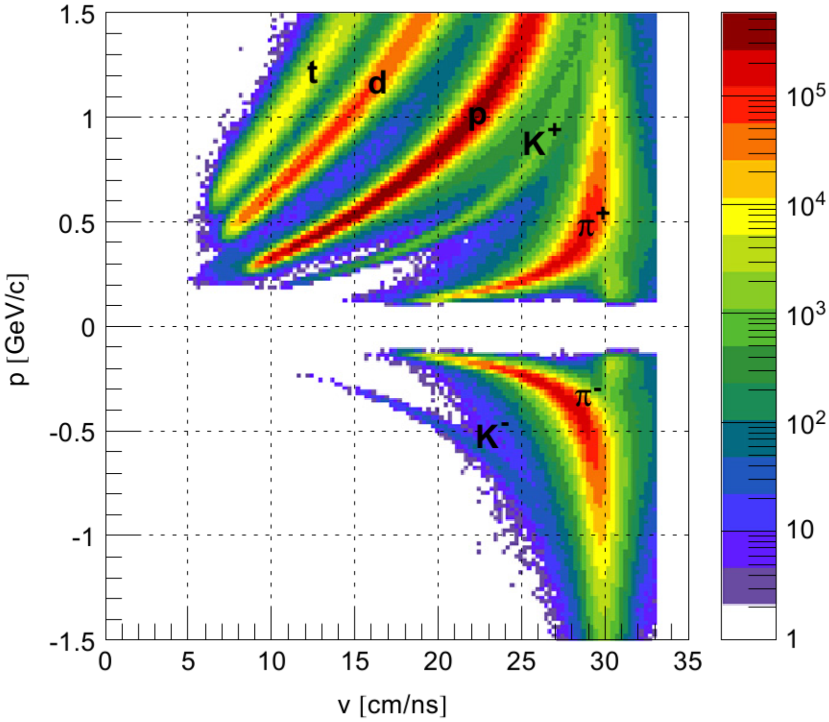

Figure 3.15: Particle identification capability of the FOPI spectrometer demonstrated in a momentum vs. velocity plot. The momentum p of the particles is measured by the central drift chamber. The velocity v is calculated by measuring the time of flight in the MMRPC. The bands in the plot are labeled with the corresponding particle species. Figure taken from [136].

from 30 fC to about 250 fC with a maximum at 50 fC. A typical primary signal, depicted in the inlet of Fig. 3.16, has an amplitude of a few mV and a rise of time less than 700 ps.

The charge Q_{cl} distribution of a cluster/hit plotted versus the energy deposition expressed

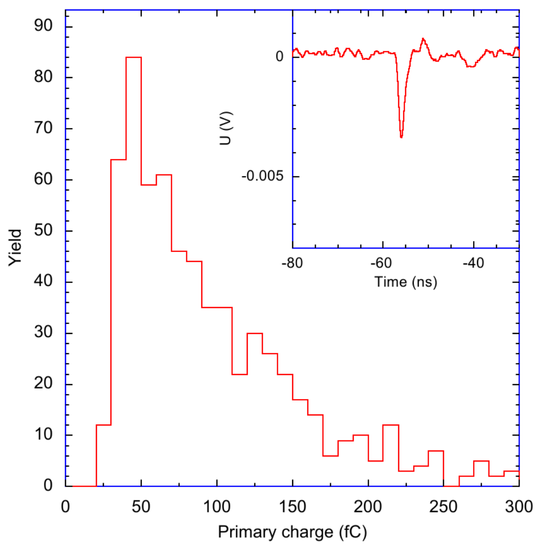

Figure 3.16: Primary charge distribution of a FOPI MMRPC strip. The mean charge is about 80 fC. The inlet shows the shape of a primary signal. the rise time is $< 700\ ps$. Figure taken from [135].

in $\beta\gamma$ [1] of the particles is depicted in Fig. 3.17. The quantity $\beta\gamma$ is obtained by the CDC. The mean of the cluster charge is indicated by the tiny black crosses imposed on the histogram. The vertical bars of these points denote the statistical error. Although the trend of the mean cluster charge is only a remanent of the Bethe-Bloch formula, since the preamplifiers have no linear amplification, it nevertheless shows an increase towards small $\beta\gamma$. Above $\beta\gamma = 2$ all particles are minimum ionizing. The missing data points at $\beta\gamma = 3.9$ are an artifact of the calibration procedure. As shown in the previous section

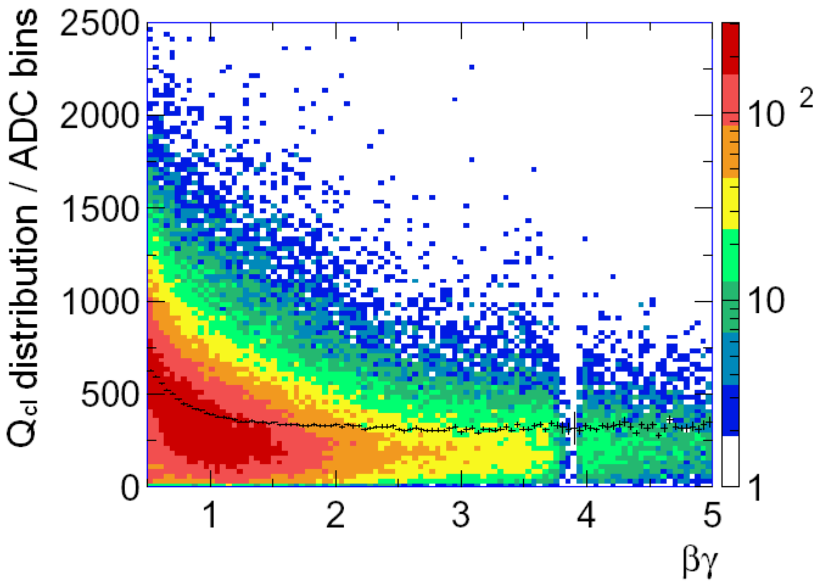

Figure 3.17: Cluster charge Q_{cl} distribution vs. the energy deposition expressed in $\beta\gamma$. The black crosses overlaid in the histogram denote the mean of the charge distribution. For more information see text.

(cf. Eq. (3.11)), every cluster can be assigned to a certain mean strip. Therefore one can plot for every strip a cluster charge distribution and determine its mean. This is of particular interest because one can see differences between strips positioned in the center of a counter and side strips, i.e. one can check for edge effects. Figure 3.18 shows the mean cluster charge plotted against the strip number for minimum ionizing particles (crosses) and all charged particles with $0.5 < \beta\gamma < 5$ (stars). For all strips, the mean cluster charge arising from minimum ionizing particles is about 80 % of the total mean cluster charge. However, it is not constant over the full counter. In the center, the data show a plateau like structure with a maximum on strip 9. Towards the side strips (considering the three outermost strips), the mean cluster charge continuously drops to about 55 % of its maximum value. The main reason for this drop is a purely geometrical effect (cf. Fig. 3.21). Avalanches arising on the edge of a counter induce a charge only to the side where the pickup electrode is located. In addition, the electric field gets slightly distorted on the counter edge because the strip width is only half in comparison to the distance between the

[1] $\beta = v/c$ and $\gamma = \left(1 - \beta^2\right)^{-\frac{1}{2}}$ with v representing the particle velocity and c the speed. of light

two electrodes creating the field. The grounded strip next to the last active strip prevents that the field gets fully distorted. For a narrow-strip design such an additional grounded strip is absolutely essential. The fact that the charge drops nearly to 50 % at the edges leads to the assumption that the mean of the charge distribution within a cluster increases linearly with the number of strips forming the cluster. This behavior is indeed observed and shown in Fig. 3.19. This plot indicates also that the number of strips forming a cluster (cluster size) can go up to 14 even if such big clusters are very rare. The question is how physically meaningful clusters with cluster sizes larger than 8 or 10 strips are.
The average cluster size of minimum ionizing particles ($\beta\gamma > 2$) plotted as function of the

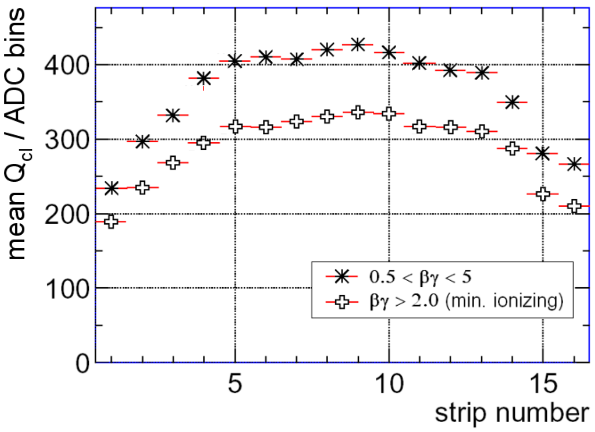

Figure 3.18: Mean cluster charge vs. RPC strip of minimum ionizing particles (crosses) and all particles (stars). The mean cluster charge for minimum ionizing particles is $\approx 60\%$ of the total charge.

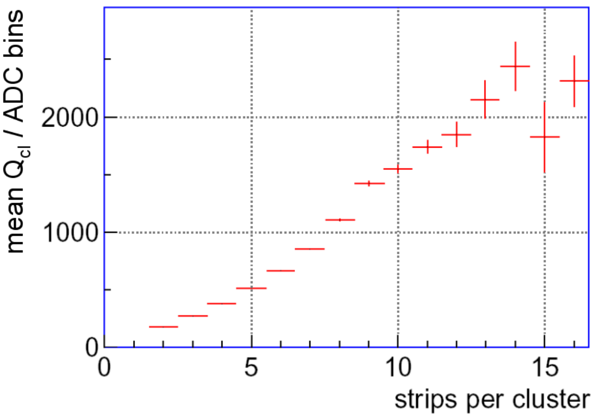

Figure 3.19: Mean cluster charge vs. strips per cluster. The error bars represent the statistical error.

strip number is depicted in Fig. 3.20. The trend is similar to the one observed in Fig. 3.18. A wide plateau across the counter ranging from strip 4 to strip 13 has a constant mean cluster size of 4.2. Towards the sides it drops to 2.8 due to the argument mentioned above. A sketch of this pure geometrical effect is shown in Fig. 3.21. For all particles, the average of the cluster size in the plateau is 4.6 [136] dropping to the sides in the same manner as in the case of minimum ionizing particles. From these results we can conclude that on average a measurable charge is induced on a spot of about 10 to 12 mm in diameter. Therefore, the width of a strip electrode for a newly developed RPC should be of the same

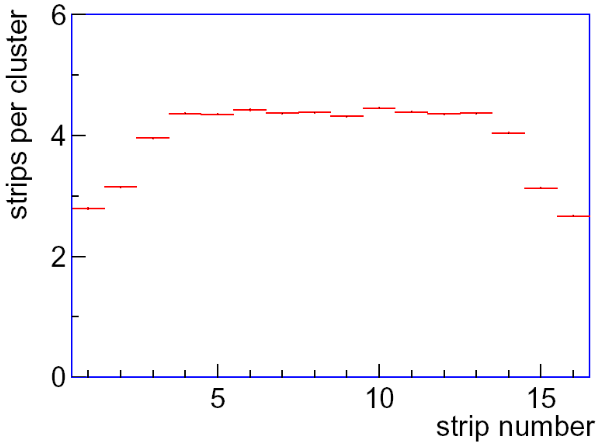

Figure 3.20: Mean cluster size vs. RPC strip of minimum ionizing particles ($\beta\gamma > 2$). The error bars indicating the statistical error are too small to be visible.

order if no further constraints like an improved lateral spatial resolution are formulated. The two most important parameters characterizing an RPC are its efficiency and its time

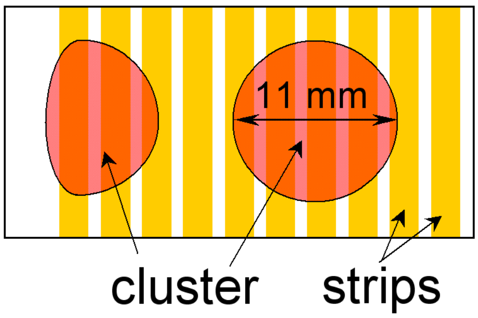

Figure 3.21: Sketch of the geometrical effect responsible for the drop in mean cluster size.

resolution. These parameters are typically measured during the development phase with cosmics and more likely in test beams. However, in most of the cases the measurements are not carried out under full battle conditions i.e. under conditions like in a real experiment. Often it is even not possible to simulate such conditions. Therefore, the results obtained in such test experiments generally overestimate the performance of the counters embedded in a system. As an example the efficency and the time resolution of the FOPI MMRPC evaluated during a test beam time with protons is shown in Fig. 3.22. In this test two counters were positioned in a row so that the proton beam (energy of 2 GeV) could traverse. The flux was approximately 100 Hz/cm^2. Since the beam diameter measured only a few cm the counter was not fully illuminated. The behavior of an RPC under such conditions is called spot response.

Under this condition the efficiency (full circles) rises continuously with the electric field across the gap reaching a plateau at nearly 100 % at an electric field strength of about 107 kV/cm. A field of 110 kV/cm corresponds to 9.6 kV electric tension applied on the cathode and is the normal working voltage during all experiments. The combined time resolution of two counters is presented in the same plot (Fig. 3.22) and is symbolized by the open squares. It improves towards higher electric fields reaching a minimum value of 85 ps for the nominal working field. Assuming that both counters perform equally the

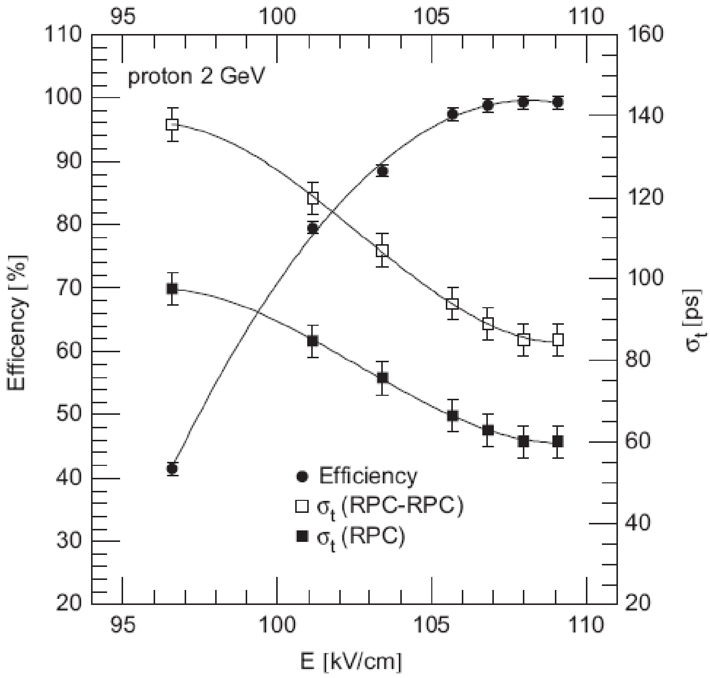

Figure 3.22: Efficiency and time resolution of the FOPI MMRPC measured in a direct proton beam (spot illumination). Open symbols represent the combined resolution of two overlapping MMRPCs, closed symbols show the individual contribution of each detector and the efficiency. The error bars are dominated by estimated systematic errors and hence equal for all points. Curves are eye-guides [136]. For more information see text.

combined time resolution can be divided by $\sqrt{2}$ in order to obtain the time resolution of the individual counter. A time resolution σ_t of 60 ps per counter, indicated by the full squares, was obtained in this test. These results agree quite well with the system time resolution presented in section 3.3 (cf. Fig. 3.13).
However, the 88 ps system time resolution was obtained only under certain cut conditions, e.g. only clearly identified pions with momenta above 0.5 GeV/c were used, the particle track given by the CDC has to match the RPC. The question is what one would find for the global efficiency and time resolution of the time-of-flight system. This question is not so easy to answer at this point since these two variables were not investigated within this work. At least an estimate can be done. Figure 3.23 shows the local efficiency obtained for the Time-of-Flight barrel allowing only for emitted particles with tracks within a polar angle range of $32° \leq \theta \leq 50°$ and an azimuthal angle range of $60° \leq \phi \leq 170°$. The RPCs have an acceptance of $30° \leq \theta \leq 52°$, i.e. edges are not included. The azimuthal angle ϕ was chosen to have no missing super module in that acceptance. Apart from that, the data sample contains all identified particles with momenta $0.4 \leq p \leq 2$. The mean efficiency is about 80 %. Towards larger polar angles θ the efficiency drops to 70 % (Fig. 3.23a). This behavior is not yet understood. The regular wiggles in ϕ (Fig. 3.23b) indicate the individual super modules (SM). The minima correspond to the SM edges where the barrel has no acceptance. An explanation for the reduced overall efficiency can be limitations in the matching algorithm. The global efficiency was estimated to be in the order of 60 % [137]. In this case no acceptance cut was applied (full counter acceptance

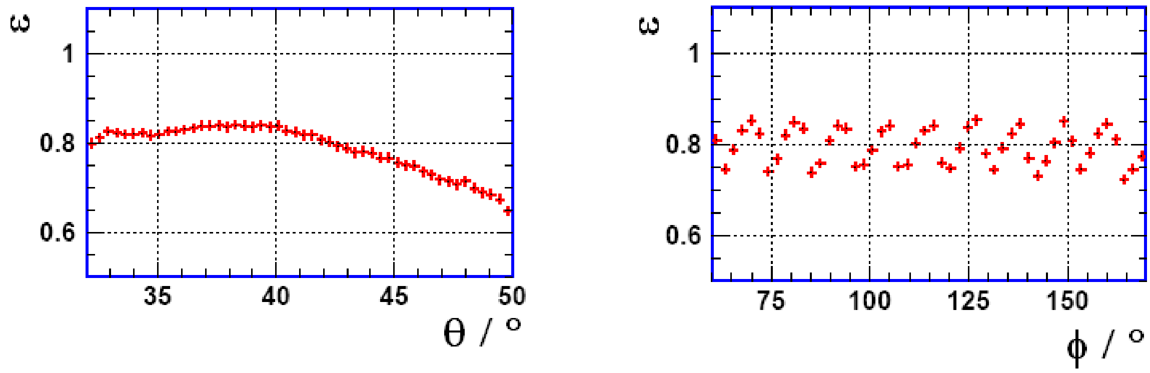

(a) ε vs. polar angle. The drop towards bigger angles is not yet understood.

(b) ε vs. azimuthal angle. The wiggles indicate the individual super modules.

Figure 3.23: Local efficiency ε of MMRPC barrel. [137]

and full azimuth). The missing super modules are the main reason for the reduction of the efficiency.

In order to get an estimation of the counter resolution during this experiment particle tracks were selected which traverse the edge strips of two RPCs within one SM. These particles create a cluster in every counter with its own cluster mean time (see section 3.3). Subtracting these two mean times from each other yields a time distribution Δt which can be fitted by a Gaussian function. The time resolution is given by the Gaussian variance σ obtained from the fit. The time distribution Δt is presented in Fig. 3.24. The fit delivers

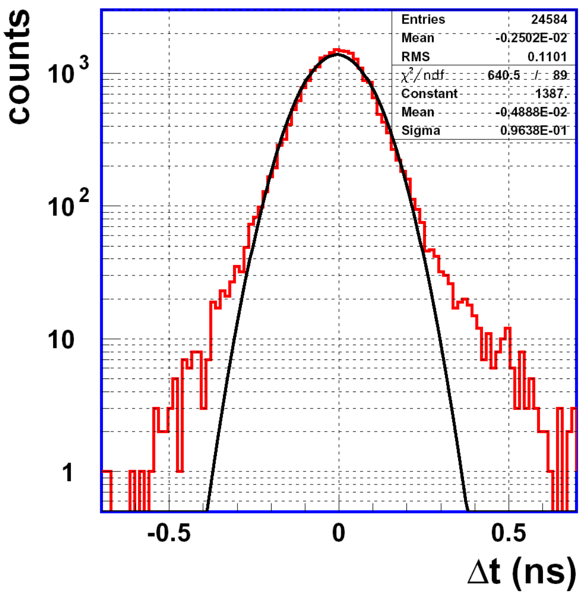

Figure 3.24: Time distribution Δt of two overlapping RPCs within a SM measured during a production run. A Gaussian fit delivers a combined time resolution of 96 ps. A single counter time resolution of 68 ps can be extracted. Plot taken from [137]

a time resolution of $\sigma_t = 96$ ps leading to a single-counter resolution of 68 ps. These numbers are slightly higher than the results shown in Fig. 3.22. One reason may be that the counter was fully illuminated (no spot response). An even more likely reason is the use of side strips in the RPC for these measurements (edge effects). A cluster generated on the counter edge has a smaller cluster size (cf. Fig. 3.20). Hence, less strips deliver timing information from the same avalanche. In addition, side strips have less charge, i.e. lower pulse heights, which causes a decreasing signal to noise ratio. Figure 3.25 shows the system time-of-flight resolution and the so-called intrinsic time resolution versus the strip number. The time-of-flight resolution is on average 88 ps (see also Fig. 3.13). However, it is not uniformly distributed over the full counter. Strips positioned in the center of the electrode have a lower time resolution ($\approx$ 83 ps) than outlying strips ($\approx$ 93 ps). This behavior can be explained by the intrinsic time resolution of the counter. The intrinsic time resolution is the RMS value of the distribution of the single strip times, labeled $\bar{t}_{cor}$ in section 3.3, forming a cluster. The more strips contribute to a cluster the more information is available about the times and therefore the intrinsic time resolution drops. Exactly this trend is observed in the intrinsic time resolution $\sigma_{cluster}$ plotted versus the strip number of the RPC (Fig. 3.25) and versus the number of strips per cluster (Fig. 3.26). The smallest value for the intrinsic time resolution obtained for the inner strips is about 30 ps. This resolution corresponds to the electronics time jitter reported in [133]. The plot in Fig. 3.26 also shows that beyond a cluster size of 8 strips there is no further gain in the intrinsic time resolution. The last subject which will be discussed in this section is the position

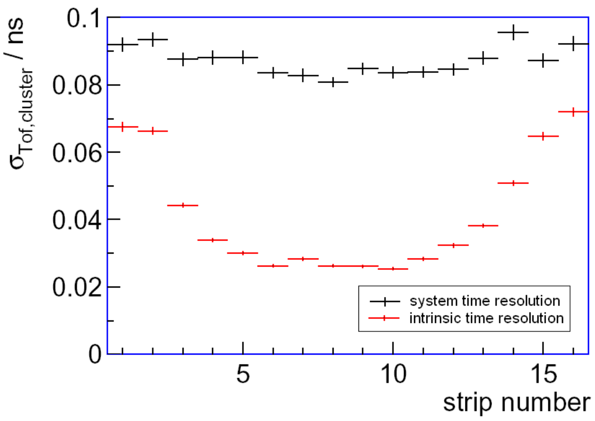

Figure 3.25: Time-of-flight resolution σ_{Tof} (black data points) and intrinsic time resolution $\sigma_{cluster}$ (red data points) as function of the RPC strip number. The side strips show a worse time of flight resolution due to edge effects. The intrinsic time resolution has a plateau in the middle of the RPC reflecting the electronics time contribution of about 30 ps. For more information see text.

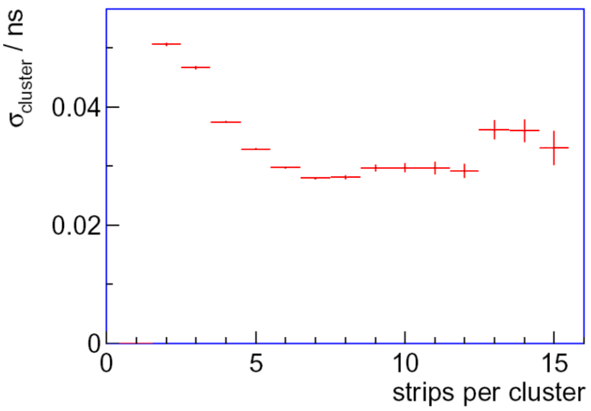

Figure 3.26: Intrinsic time resolution $\sigma_{cluster}$ dependence on the cluster size (strips per cluster). The drop in the intrinsic time resolution results from the fact that bigger clusters deliver more time information since the same avalanche is detected by more channels.

dependence of the timing response along the counter. These dependencies are depicted in Fig. 3.27. The behavior of dt shows a maximum in the center of the counter superimposed by a wiggle like structure. The wiggles reflect mechanical irregularities within the detector originating most probably from the bars across the counter. These bars are needed to fix the detectors to the main frame in the super module. It may be that these bars exert a pressure on the counters which leads to a small compression in the affected location. In this compressed region the electric field is slightly higher and therefore the timing response is changed.

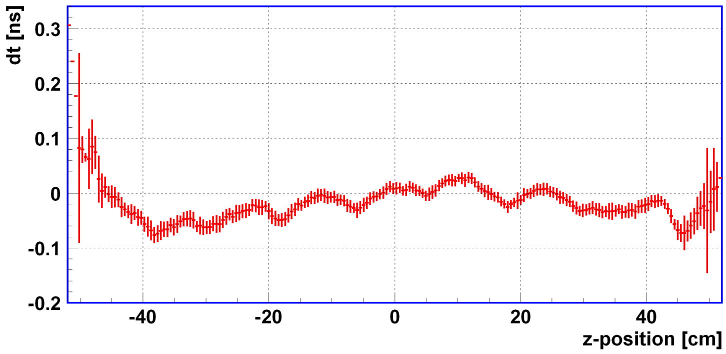

Figure 3.27: Position dependence of the timing response dt along the MMRPC. The wiggles are presumably caused by bars fixing the counter to the super module frame.

3.5 Conclusions for the CBM MMRPC and time of flight barrel

The FOPI collaboration developed and operated very successfully their MMRPC Time-of-Flight barrel. The targeted goal in terms of system time resolution was reached and even surpassed. A K^+ identification up to momenta of 1.2 GeV/c was demonstrated. In case of FOPI it was mandatory to design a narrow strip configuration since an excellent azimuthal spatial resolution was required. The strip pitch of 2.54 mm in combination with the number of glass plates and gaps was chosen in order to adopt the counter to a 50 Ω impedance. Matching all components to the same impedance minimizes reflections of the signals leading to a stable behavior of the counter. This becomes especially important for CBM since a free running data acquisition is under consideration. Therefore we will follow the same philosophy constructing counters. However, an average cluster having a size on the order of 1 cm implies a strip width with similar dimensions. The advantage in comparison to the narrow strip solution would be a signal 5 times larger. Taking a fully differential design the charge accumulated on both electrodes would be 10 times larger. This would allow for more robust electronics by which also the probability of channel losses would be minimized leading in the end to a higher global efficiency. A higher global efficiency can be additionally reached by overlapping counters and avoiding uncovered

areas. This motivates to construct the detector surfaces as big as possible. A second argument are edge effects. As shown in the previous section edge effects have a large impact on counter performance. On the other hand a big counter needs robust mechanics which can influence the time response and supplementary act as an absorber material.
The fact that the results of the counter performance also changed between detector test and real experiment implies that a spot response is not sufficient for evaluating the physics performance. Therefore, CBM prototypes need to be tested in heavy-ion beams.

4 The Compressed Baryonic Matter (CBM) Experiment

The Compressed Baryonic Matter (CBM) Experiment will be one of the major scientific activities at the Facility for Antiproton and Ion Research (FAIR) in Darmstadt [16]. The goal of CBM is to explore the phase diagram of strongly interacting matter in the region of the highest baryon densities including the study of the equation-of-state of nuclear matter at high densities and the search for the deconfinement and chiral phase transitions [138; 139]. The apparatus is designed in a way that it can measure bulk observables with large acceptance and simultaneously rare probes such as vector mesons or charmed particles.

This chapter is structured in the following way. First, the Facility for Antiproton and Ion Research will be briefly described in section 4.1. In section 4.2 the research program of CBM will be outlined. One of the main topics of the CBM research program is the measurement of event-by-event fluctuations. The investigation of this subject is partially part of this thesis and will be discussed in more detail in section 4.3. In Section 4.4 the concept of the CBM apparatus will be delineated. The requirements of the Time-of-Flight-wall as well as the hadron identification capability will be presented in section 4.5.

4.1 The Facility for Antiproton and Ion Research (FAIR)

Figure 4.1 depicts the future international Facility for Antiproton and Ion Research (FAIR) together with the existing GSI facility. It will provide unique research opportunities in the fields of nuclear, hadron, atomic and plasma physics [140]. Two synchrotrons with magnetic rigidities of 100 Tm and 300 Tm (SIS100/SIS300) deliver primary proton/heavy-ion beams with a kinetic energy of:

$$E/A = \sqrt{(0.3[\mathrm{GeV/Tm}] \cdot B \cdot r \cdot Z/A)^2 + m^2} - m, \tag{4.1}$$

with Z and A being the charge and atomic number of the ion, $B \cdot r$ the rigidity, and m the mass of the nucleon.

beam ion	Z	A	E/A GeV SIS100	E/A GeV SIS300
p	1	1	29	89
d	1	2	14	44
Ca	20	40	14	44
Ni	28	58	13.6	42
In	49	115	11.9	37
Au	79	197	11	35
U	92	238	10.7	34

Table 4.1: Ion species and their kinetic energy per nucleon for a beam rigidity of 100 Tm at SIS100 and 300 Tm at SIS300. Table taken from [3].

The maximum beam energies reached at SIS100 and SIS300 for typical ion species are listed in table 4.1. The minimum available ion beam energy is about 2 AGeV [3]. In addition

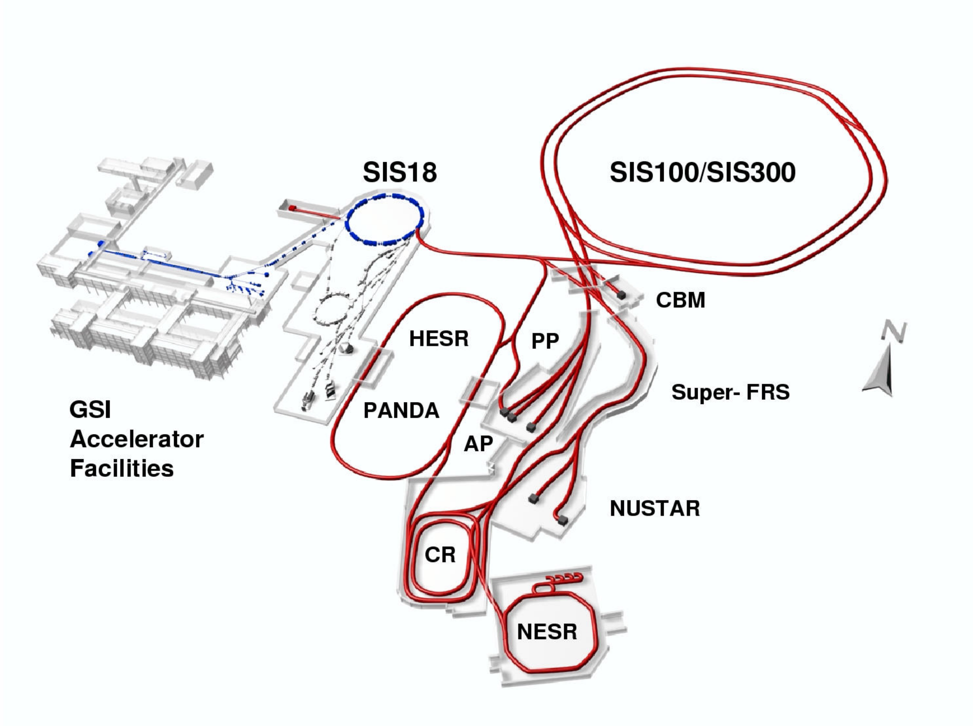

Figure 4.1: Layout of the Facility for Antiproton and Ion Research (FAIR) [140].

to SIS100/300 FAIR comprises the Superconducting Fragment Separator (Super-FRS), a storage ring for anti-protons (High-energy Storage Ring HESR), the Collector Ring (CR), and the New Experimental Storage Ring (NESR). The beam extracted at the CBM cave will reach intensities up to 10^9 Au ions per second, the highest beam intensities reached so far in this energy range. SIS100 will be operational in the year 2018. A few years later SIS300 will begin operations in the so-called phase II.

4.2 The research program of CBM

The CBM research program comprises a comprehensive scan of observables, beam energies and collision systems. The observables include low-mass dilepton pairs, charmonia and open charm, but also collective flow of rare and bulk particles as well as correlations and fluctuations. The experimental goal is to measure these rare probes with unprecedented precision in spite of the very low multiplicities [3].
Figure 4.2 depicts three snapshots of the time evolution of the reaction with two colliding uranium nuclei at a laboratory beam energy of 23 AGeV calculated with the UrQMD transport code [16; 23]. In the first snapshot the Lorentz-contracted nuclei are almost fully

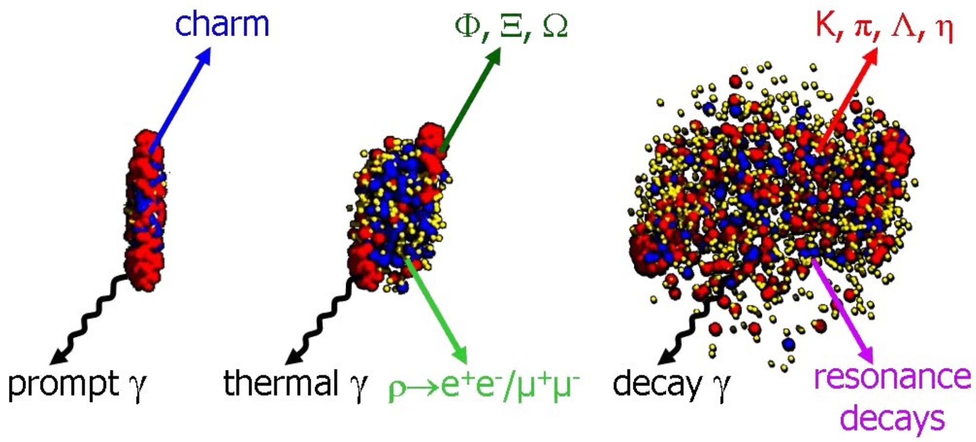

Figure 4.2: Evolution of a heavy-ion collision. The colliding system consist of two uranium nuclei at 23 AGeV. Figure taken from [16].

overlapped. In this early stage of the collision particles containing charm quarks (D mesons, J/ψ) are produced. Hence, the measurement of these particles delivers information about the dense fireball. Prompt photons which are directly produced by parton-parton collisions are also emitted in the very beginning. During the reaction vector mesons (ω, ρ and ϕ) are constantly produced by $\pi\pi$ annihilation. These particles mainly decay again to $\pi\pi$ but also in a small fraction (Branching Ratio (BR) between 10^{-4} - 10^{-5}) to e^+e^- and $\mu^+\mu^-$ (rare probes). The dileptonic decay offers the possibility to look into the fireball since leptons are not affected by final-state interactions [16]. Also multi-strange hyperons like Ξ and Ω are interesting probes of the hot and dense nuclear matter. During the evolution of the collision thermal photons are emitted. Measuring these photons allows to estimate the temperature of the fireball in the different evolution steps. In the third snapshot the freeze-out of the so-called bulk particles like Λ, K, π, p ... is displayed. Later on, no new particles are created. The physics interest of CBM is to measure and characterize such a heavy ion collision especially in the time interval where the nuclear matter is highly compressed.
One observable which is generated in the early stage of the collision is the collective flow (directed and elliptic flow [141]). With the measurement of the collective flow of hadrons, since it is driven by the pressure inside the fireball, one can study the equation of state

of dense nuclear matter. The goal of CBM is to measure with a high accuracy the collective flow of hadrons as function of the incident beam energy and different system sizes. Measuring excitation functions of flow also has a discovery potential for a first order phase transition [142]. The signature is the diminishing of flow at an energy density where the phase transition is supposed to happen.
Another observable that is sensitive to the equation of state is the yield of multi-strange hyperons in particular at low collision energies. At subthreshold energies, Ξ and Ω hyperons are produced in sequential collisions (coalescence model) involving kaons and Λs and are therefore sensitive to the density in the fireball.
The measurements of the excitation function of yields, spectra and flow of strange and charmed particles as well as lepton pairs is sensitive to the phase transition from hadronic to partonic matter. In particular particles containing charm quarks are created in the early phase of the collision and, hence, probe the highly compressed baryonic matter [3]. Measuring the cross section and momentum spectra of charmed particles (open and hidden charm) opens up the opportunity to study the charm production mechanism and charm propagation in the dense nuclear matter created at FAIR energies.
A new field of interest is the measurement of single and double hyper nuclei (e.g. ${}^{3}_{\Lambda}$H, ${}^{4}_{\Lambda}$H, ${}^{5}_{\Lambda}$He, ${}^{4}_{\Lambda\Lambda}$H, ${}^{5}_{\Lambda\Lambda}$H, ${}^{6}_{\Lambda\Lambda}$He, ${}^{6}_{\Lambda\Xi}$He, ${}^{7}_{\Lambda\Lambda\Xi}$He, $\cdots$) as well as heavy multi-strange objects (e.g. $\{\Xi^-, \Xi^0\}$, $\{2\Lambda, 2\Xi^-\}$, $\{2\Xi^-, 2\Xi^0\}$, $\{2n, 2\Lambda, 2\Xi^-\}$, $\cdots$) in heavy-ion collisions. Theoretical models predict that these objects are produced in heavy-ion collisions via coalescence with maximum yields in the energy region of SIS100 [143; 144]. The CBM experiment is due to its high interaction rate well suited to measure these aforementioned objects.
The CBM collaboration is also interested in studying the in-medium properties of hadrons which are modified by the restoration of chiral symmetry in dense baryonic matter. Especially convenient for this purpose is the measurement of low-mass vector mesons (ω, ρ and ϕ) decaying into dilepton pairs. Leptons are penetrating probes carrying undisturbed information from the dense fireball.
Another penetrating probe are photons which are emitted from the early fire ball. They will be measured by CBM as well.
One of the main pillars in the CBM physics program is the search for the critical point in the phase diagram of strongly interacting matter via event-by-event fluctuation measurements. In order to measure fluctuations on an event basis an excellent hadron identification is required. The feasibility study of event-by-event fluctuations with the CBM detector is part of this thesis and, therefore, this topic will be discussed in more detail in the following section.

4.3 Event-by-event fluctuation of the K/π ratio

Fluctuations and correlations are important characteristics of any physical system [145]. The original motivation for event-by-event (E-by-E) studies in ultra-relativistic heavy-ion collisions has been to find indications for distinct event classes. In particular it was hoped that one would find events which would carry the signature of the Quark Gluon Plasma [146]. Fluctuations are closely related to phase transitions. The well known phenomenon of critical opalescence is a result of fluctuations at all length scales due to a second order phase transition [145]. If the colliding system experiences strong density fluctuations due, e.g., to droplet formation in a first-order phase transition, all fluctuations can be enhanced substantially [147]. Considering the richness of the QCD phase diagram the study of fluctuations in heavy-ion physics should lead to a rich set of phenomena and is an essential tool for the experimental exploration of the QCD phase diagram [145; 148]. A prominent example where the measurement of correlations has lead to a scientific breakthrough are the fluctuations of the cosmic microwave background radiation [145; 149]. Fluctuations have contributions of different nature [146]:

1. Quantum fluctuations:
    - they arise if the specific observable does not commute with the Hamiltonian of the system under consideration. These fluctuations probably play a smaller role for the physics of heavy-ion collisions [145].

2. "Trivial" fluctuations:
    - statistical fluctuations due to a finite number of events
    - volume fluctuations due to the variation of the impact parameter

    These fluctuations add to the dynamical fluctuations.

3. Dynamical fluctuations:
    - density fluctuations which are controlled by the compressibility of the system
    - net electric charge fluctuations: these fluctuations are a direct probe for the existence of a QGP [145].
    - transverse momentum fluctuations: they reflect the energy fluctuations, which should show a peak close to the QCD phase transition, where the specific heat has a maximum [145].
    - particle / particle ratio fluctuations: particle ratio fluctuations are not effected by the volume fluctuations [146].

The problem is to dig out the interesting and dynamically relevant E-by-E fluctuations, to e.g. allow for the search for a possible critical point and for a first order co-existence region in the QCD phase diagram [3].

4.3.1 Fluctuation in the grand canonical ensemble

In a system in thermal equilibrium with i conserved quantities the grand canonical partition function is given by:

$$Z = \mathrm{Tr}\left[\exp\left(-\beta(H - \sum\nolimits_i \mu_i Q_i)\right)\right], \tag{4.2}$$

where $\beta = 1/T$ represents the inverse temperature, H is the Hamiltonian of the system, and Q_i and μ_i denote the conserved charge and the corresponding chemical potential. For a three flavor QCD $i = 3$ representing the three quark flavors up, down and strange. Alternatively, typically the strangeness S, the baryon number B and the electric charge Q are used.
The free energy is related to the partition function via:

$$F = -T \log Z. \tag{4.3}$$

The statistical density matrix is given by:

$$\rho_G = \frac{1}{Z} \exp\left[-\beta(H - \sum\nolimits_i \mu_i Q_i)\right], \tag{4.4}$$

and the moments of the operator A in the grand-canonical distribution:

$$\langle A^n \rangle_G = \mathrm{Tr}(\rho_G A) \tag{4.5}$$

For a thermodynamical system, typical fluctuations are Gaussian [148] and are characterized by the variance defined by:

$$\langle \delta A^2 \rangle = \langle A^2 \rangle - \langle A \rangle^2. \tag{4.6}$$

In the case of a grand-canonical ensemble, the mean and the fluctuations of quantities which characterize the thermal system, such as the energy or the conserved charges, can be expressed in terms of appropriate derivatives of the partition function [148]. The mean of the energy $E = \langle H \rangle$ and the conserved charges $\langle Q_i \rangle$ is given by:

$$E = -\frac{\partial}{\partial \beta} \log Z \tag{4.7}$$

$$\langle Q_i \rangle = T \frac{\partial}{\partial \mu_i} \log Z \tag{4.8}$$

The variance (fluctuations) of the energy and the conserved charges are:

$$\langle \delta E^2 \rangle_G = -\frac{\partial^2}{\partial \beta^2} \log Z = -T^3 \frac{\partial^2}{\partial T^2} F = T^2 C_V \tag{4.9}$$

$$\langle \delta Q_i^2 \rangle_G = T^2 \frac{\partial^2}{\partial \mu_i^2} \log Z = -T \frac{\partial^2}{\partial \mu_i^2} F = VT\chi_i, \tag{4.10}$$

with C_V the heat capacity for constant volume V and the susceptibility χ_i defined as:

$$\chi_i = \frac{T}{V} \frac{\partial^2}{\partial \mu_i^2} \log Z = -\frac{1}{V} \frac{\partial^2}{\partial \mu_i^2} F. \tag{4.11}$$

The charge susceptibility characterizes the response to a change in chemical potential. In order to avoid volume fluctuations one needs to study observables which are independent of the volume of the system. Among others the ratio of particle multiplicities has this property [148]. The particle ratio R is defined for two particle species N_1 and N_2 as:

$$R = \frac{N_1}{N_2} \tag{4.12}$$

The fluctuations of this ratio (δR) are then given by [145; 146; 150; 151]:

$$\frac{(\delta R)^2}{\langle R\rangle^2} = \frac{\langle(\delta N_1)^2\rangle}{\langle N_1\rangle^2} + \frac{\langle(\delta N_2)^2\rangle}{\langle N_2\rangle^2} - 2\frac{\langle \delta N_1 \delta N_2\rangle}{\langle N_1\rangle\langle N_2\rangle} \tag{4.13}$$

The last term in equation (4.13) takes into account the corelation between the particles type 1 and type 2 [146]. This term is also responsible to cancel out all volume fluctuations [150].

4.3.2 Particle ratio fluctuation measurements at NA49 and STAR

The measurements of the K/π fluctuations by the NA49 collaboration [152] at CERN were the first E-by-E fluctuation measurements in a heavy-ion experiment [145]. These measurements were performed with central Pb + Pb collisions at a beam energy of 158 GeV per nucleon. The observed fluctuations were with $2.8\% \pm 0.5\%$ rather small [152]. Later on, the NA49 collaboration measured with the same system the K/π and $(p+\overline{p})/\pi$ fluctuations at 20, 30, 40 and 80 GeV per nucleon [153]. The particles were identified by the dE/dx measurements in a TPC. The dE/dx resolution after corrections was about 3.9 %. The analysis of the data is described in detail in [153]. It results in a particle ratio distribution where the width of the distribution σ_{data} reflects the fluctuations in the data. The same analysis is done with a mixed event sample in order to determine the statistical fluctuations σ_{mixed}. The dynamical fluctuations σ_{dyn} of the particle ratio are calculated by:

$$\sigma_{dyn} = sign\left(\sigma^2_{data} - \sigma^2_{mixed}\right)\sqrt{|\sigma^2_{data} - \sigma^2_{mixed}|} \tag{4.14}$$

The dynamical fluctuations of the K/π and $(p+\overline{p})/\pi$ ratio measured by the NA49 collaboration are depicted in Fig. 4.3. The lower panel shows the $(p+\overline{p})/\pi$ fluctuations. The negative signal results mainly from the Δ-resonance decaying into pions and protons which increases the third term in equation 4.13. The data agree quite well with theoretical predictions from the Ultrarelativistic Quantum Molecular Dynamics (UrQMD) model [23; 154]. The upper panel depicts the K/π fluctuations measured by the NA49 collaboration (black full squares) and superimposed the data measured by the STAR collaboration at RHIC (green circles) available at that time. Above 20 GeV the data points measured by the STAR collaboration show a constant value of 4 %. The data measured by NA49 show, however, a steep increase of the K/π fluctuations with decreasing center of mass energy

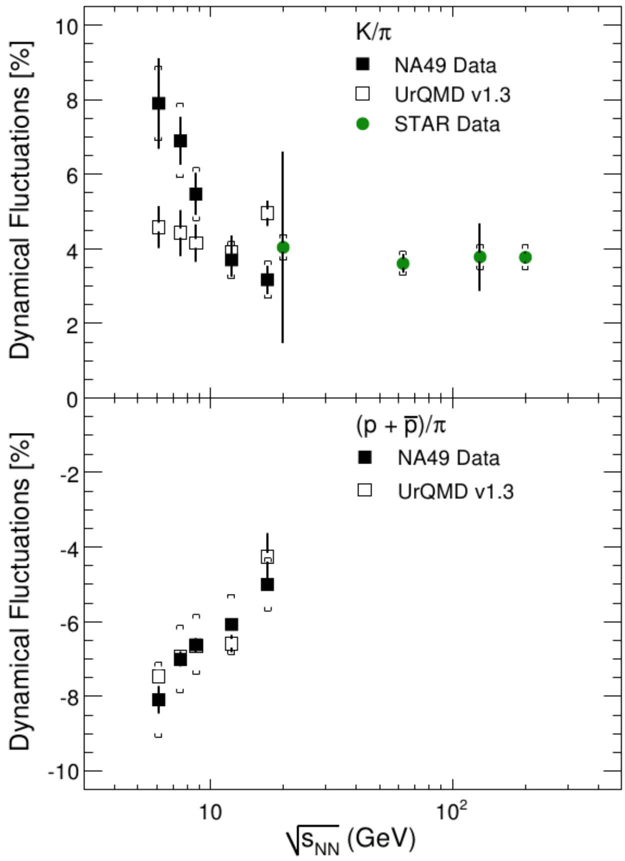

Figure 4.3: Energy dependence of the E-by-E dynamical fluctuations of K/π (upper panel) and $(p+\overline{p})/\pi$ (lower panel). Filled symbols show data, open symbols show calculations with the UrQMD transport code. Data from the STAR collaboration are taken from [156]. Figure taken from [153].

below 15 GeV. This rise coincides with the maximum of the inclusive K/π ratio [145; 155]. These results were considered as a first hint of the presence of a critical point and a first order phase transition. However, the UrQMD model cannot reproduce the results since it does not include phase transitions. In addition, the particle number ratio fluctuations scale roughly as the inverse of the accepted multiplicity. Consequently, the observed rise may partially be due to the change of the actual acceptance with beam energy, which is always the case in a fixed target experiment such as NA49 [145].
Partially inspired by the results of NA49 the STAR collaboration carried out an energy scan of Au + Au collisions from $\sqrt{s_{NN}} = 200\ GeV$ down to energies as low as $\sqrt{s_{NN}} = 7.7\ GeV$ and analyzed the data in terms of particle ratio fluctuations [156–158]. The STAR collaboration uses the variable ν_{dyn} to measure the particle number ratio fluctuations. For the K/π fluctuations ν_{dyn} is given by

$$\nu_{dyn,K/\pi} = \frac{\langle N_K(N_K-1)\rangle}{\langle N_K\rangle^2} + \frac{\langle N_\pi(N_\pi-1)\rangle}{\langle N_\pi\rangle^2} - 2\frac{\langle N_K N_\pi\rangle}{\langle N_K\rangle\langle N_\pi\rangle}, \tag{4.15}$$

where N_K and N_π are the number of kaons and pions in a particular event. Equation 4.15 can be generalized for other particle ratios. ν_{dyn} quantifies deviations in the particle ratios from those expected for an ideal statistical Poissonian distribution [158]. As derived in [158] ν_{dyn} and σ_{dyn} are connected via:

$$\nu_{dyn} = \sigma_{dyn}^2 \tag{4.16}$$

The particles for this analysis (π, K, p) were identified by the energy loss (dE/dx) in the TPC in the transverse momentum (p_T) range of $0.2 < p_T < 0.6$ GeV/c for pions and kaons and $0.4 < p_T < 1.0$ GeV/c for protons. At higher momenta up to 1.4 GeV/c for pions and kaons and 1.8 GeV/c for protons the particles were identified by measuring their time of flight with MRPC detectors. The increased particle detection efficiency in STAR in comparison to NA49 led to a smaller error in the data points. Figure 4.4 depicts the dynamical p/π fluctuations as function of the incident energy. The black stars are

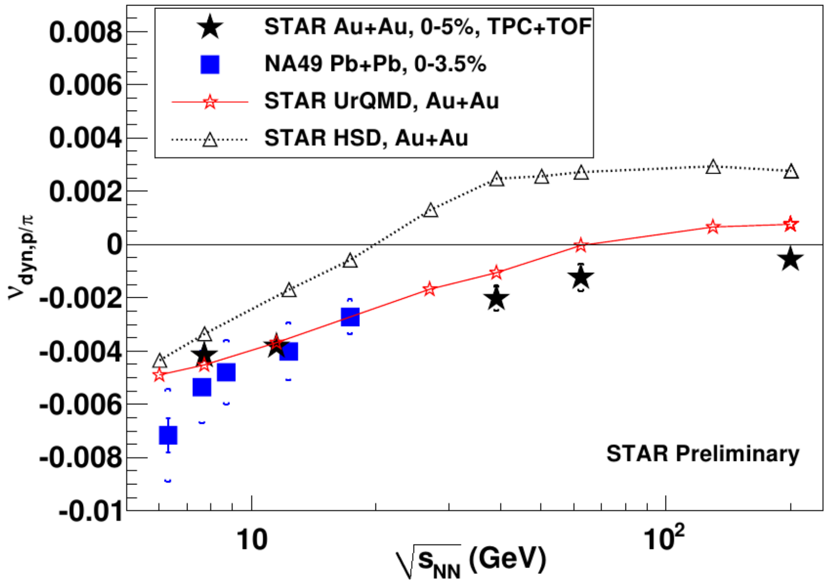

Figure 4.4: Fluctuation measurements of $\nu_{dyn,p/\pi}$ as function of the incident energy. The black stars represent measurements from STAR obtained in central 0 - 5 % Au+Au collisions. The results of the NA49 collaboration obtained in central 0 - 3.5 % Pb+Pb collisions are indicated by the blue squares. Model predictions from UrQMD and HSD using the STAR experimental acceptance are also included. Figure taken from [158].

the data points measured by the STAR collaboration and the blue squares are the data points from the NA49 experiment [153]. Additionally, two transport model predictions from UrQMD and the Hadron String Dynamic model (HSD) [159; 160] are superimposed using the STAR experimental acceptance. The data sets of both experiments show the same trend starting with large negative values at lower energies and then approach zero towards higher energies. At lower energies ($\sqrt{s_{NN}} = 7.7$ GeV and $\sqrt{s_{NN}} = 11.5$ GeV) there is an overlap between the two experiments. However, the slope of the excitation function from both experiments seams to differ. Measurements below $\sqrt{s_{NN}} = 7.7$ GeV would certainly help to resolve this discrepancy. The predictions of the UrQMD model agree widely with the data obtained at STAR whereas the HSD model calculations miss the data points over nearly the full energy range. The dynamical K/π fluctuations are displayed in Fig. 4.5. The results from NA49 represented by the blue squares are taken from [153]. In contradiction to NA49 results the data from STAR (black stars) do not show any dependence on the incident energy. Moreover, the UrQMD prediction follows the trend of the STAR data while the HSD model prediction follows the trend of the NA49 results. However, none of the models can describe the data satisfactorily, neither from STAR nor from NA49. New measurements in the energy range from $\sqrt{s_{NN}} = 3\ GeV$ to $\sqrt{s_{NN}} = 8\ GeV$ would help substantially to solve this puzzle.

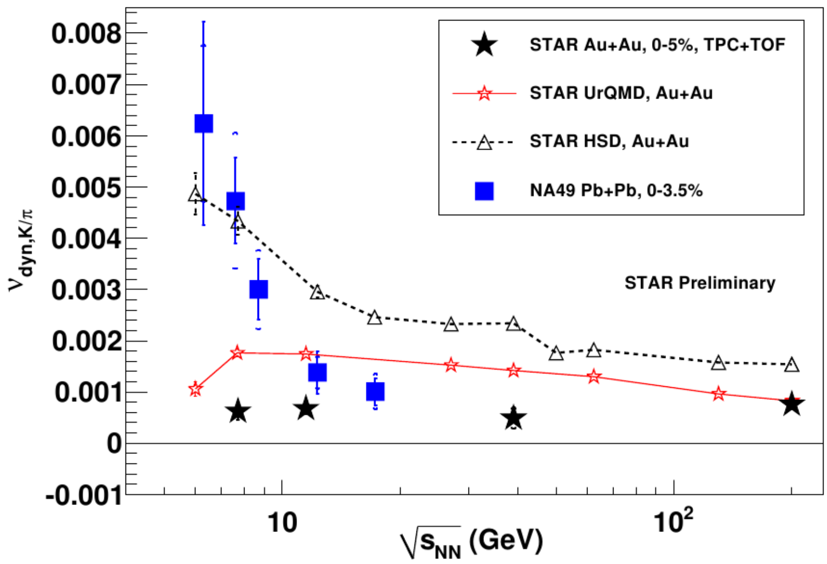

Figure 4.5: Fluctuation measurements of $\nu_{dyn,K/\pi}$ as function of the incident energy. The black stars represent measurements from STAR obtained in central 0 - 5 % Au+Au collisions. The results of the NA49 collaboration obtained in central 0 - 3.5 % Pb+Pb collisions are indicated by the blue squares. Model predictions from UrQMD and HSD using the STAR experimental acceptance are also included. Figure taken from [158].

4.3.3 K/π fluctuation measurements at CBM

As described in subsection 4.3.2 particle ratio fluctuations were measured in a wide energy range showing no evidence for a critical point or a first order phase transition. However, towards lower energies a discrepancy between the two available data sets generates some excitement. In order to shed more light on this difficult issue CBM intends to measure electric charge fluctuations, transverse momentum fluctuations and in particular particle number ratio fluctuations. Since hadron identification will be the main task of the Time-of-Flight detector a feasibility study regarding K/π fluctuations was performed. Therefore, a Monte Carlo toy model with the goal to estimate the error for $\nu_{dyn,K/\pi}$ was developed which will be described in the following.

The Monte Carlo toy model

The Monte Carlo toy model simulates the statistical fluctuations of the K/π ratio for minimum bias Au+Au collisions as function of the system energy, number of events and kaon detection efficiency. The structure of the Monte Carlo toy model as follows:

1. A table with the mean particle yields $\overline{N}_{Particle}(b=0)$ of K^+, K^-, π^+ and π^- for central Au+Au collisions at different center of mass energies $\sqrt{s_{NN}}$ is created. The values are extracted from the literature [20] (see Fig. 1.5). At this step the energy of the system can be selected.

2. A random impact parameter b according to the formula $b = b_{max}\sqrt{X}$ is generated. X is a random number between 0 and 1. The maximum geometrical impact parameter b_{max} for two colliding gold nuclei is 14 fm. The distribution of b is depicted in Fig. 4.6.

3. The mean particle yield is assumed to scale with the number of participants. It is calculated as a function of the randomly generated impact parameter by the following formula:

$$\overline{N}_{particle}(b) = \overline{N}_{Particle}(b=0) \cdot \left[1 - \left(3 - \frac{3}{\sqrt{2}}\right)\beta + \left(3 - \frac{6}{\sqrt{2}}\right)\beta^2 + \left(\frac{3}{\sqrt{2}} - 1\right)\beta^3\right] \tag{4.17}$$

with $\beta = b/b_{max}$. The equation (4.17) is taken from [161].

4. The total number of particles $N_{Particle}(b)$ in a single Au+Au event is generated randomly according to a Poisson distribution with the mean value $\overline{N}_{particle}(b)$. The K^+ multiplicity as function of the impact parameter of 10^6 Au+Au minimum bias events at 10 GeV center of mass energy is shown in Fig. 4.7.

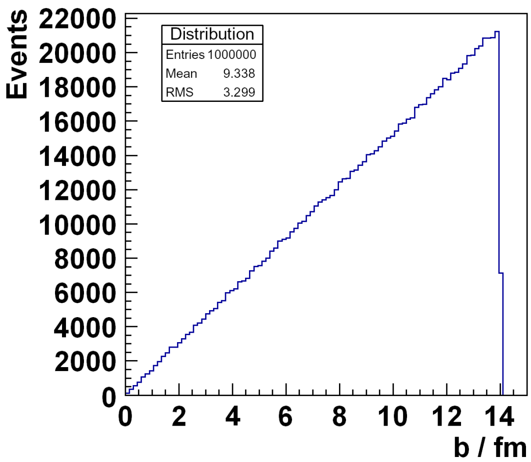

Figure 4.6: Impact parameter distribution of an Au+Au collision. The maximum impact parameter is twice the radius of a gold nucleus, $b_{max} = 14\ fm$.

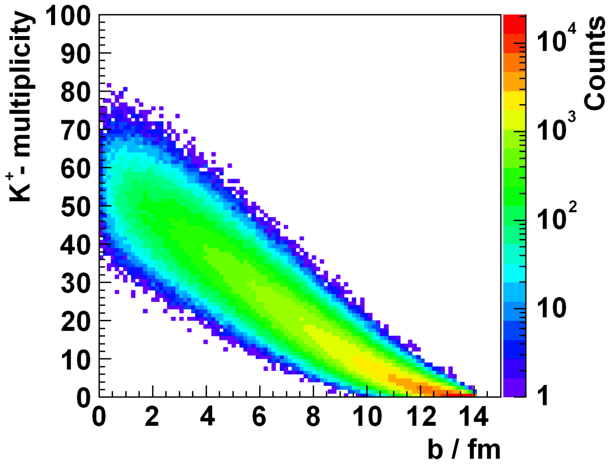

Figure 4.7: K^+ multiplicity as function of the impact parameter for 10^6 minimum bias Au+Au collisions. The center of mass energy is 10 GeV.

5. In a real detector only a fraction of the particles is detected. The number of detected particles $N_{Particle}^{detected}$ is generated randomly according to a binomial distribution $B(n, p)$ with $n = N_{particle}(b)$ and p being the particle identification efficiency. The $\pi^{\pm}$ efficiency was set to 0.8 and not changed. A typical value for the $K^{\pm}$ efficiency is 0.3 but since it is much smaller than the $\pi^{\pm}$ efficiency and dominates the fluctuations it was treated as a variable in order to investigate its influence on the statistical fluctuations. The determination of the number of detected particles per event, i.e. the procedure 1 - 5, has to be done for every particle species individually.

6. In order to get a data sample with a certain number of entries (N_{ev}) the algorithm loops N_{ev} times over the procedure 1 - 5 described above. At this point the number of events can be selected. The resulting particle multiplicity distributions for K^+, K^-, π^+ and π^- obtained for a center of mass energy of 4 GeV are presented in Fig. 4.8. 10^7 events were simulated. The blue histogram shows the distribution of all produced particles and the red histogram displays the detected particles.

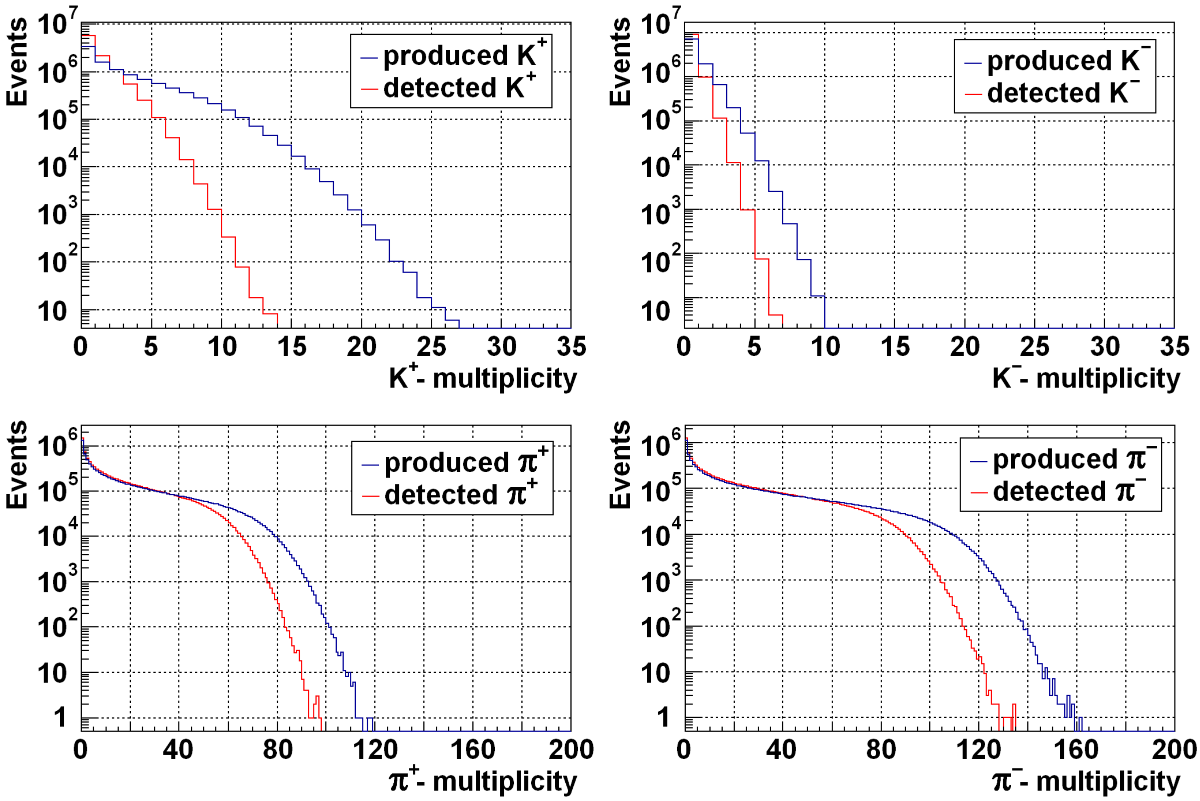

Figure 4.8: Particle multiplicity distributions for K^+ (upper left), K^- (upper right), π^+ (lower left) and π^- (lower right) for Au+Au minimum bias collisions at a center of mass energy of 4 GeV. The blue histogram shows the distribution of all produced particles and the red histogram displays the detected particles. The detection efficiency for pions is 80 % and for kaons 30 %. These numbers correspond to typical values for CBM.

7. Calculation of the statistical fluctuations quantity $\nu_{stat,K/\pi}$ via the formula:

$$\nu_{stat,K/\pi} = \frac{\langle N_K(N_K-1)\rangle}{\langle N_K\rangle^2} + \frac{\langle N_\pi(N_\pi-1)\rangle}{\langle N_\pi\rangle^2} - 2\frac{\langle N_K N_\pi\rangle}{\langle N_K\rangle\langle N_\pi\rangle}, \qquad (4.18)$$

with $N_K = N_{K^+} + N_{K^-}$ and $N_\pi = N_{\pi^+} + N_{\pi^-}$. N_i is the number of particles of species i detected in one event. $\langle\rangle$ denotes the average over the total number of simulated events.

8. The procedure 1 - 7 is repeated at least 2000 times in order to produce a $\nu_{stat,K/\pi}$ distribution which can be fitted with a Gaussian requiring the error of the width to be below 2 %. The width of the Gaussian fit provides the error of the statistical fluctuations, expressed as $\sigma_{\nu_{stat}}$.

Results

With the Monte Carlo toy model described above simulations were performed by varying the collision energy, the number of analyzed events and the kaon detection efficiency. The goal of these simulations is first to study the influence of these parameters on the uncertainty of the statistical fluctuations and second to estimate the values at which the uncertainty becomes small enough to see significant variations in the dynamical fluctuations. In order to detect dynamical fluctuations in the order of 10^{-3} the uncertainty of the statistical fluctuation should be below $5\cdot10^{-4}$. This value was estimated from Fig. 4.5. Figure 4.9 illustrates the uncertainty of the statistical fluctuations $\sigma_{\nu_{stat}}$ as function of the center of mass energy for $5\cdot10^6$ simulated events (black circles), for 10^7 events (red squares) and for $5\cdot10^7$ events (blue triangles). The kaon detection efficiency was set to 0.3. The red

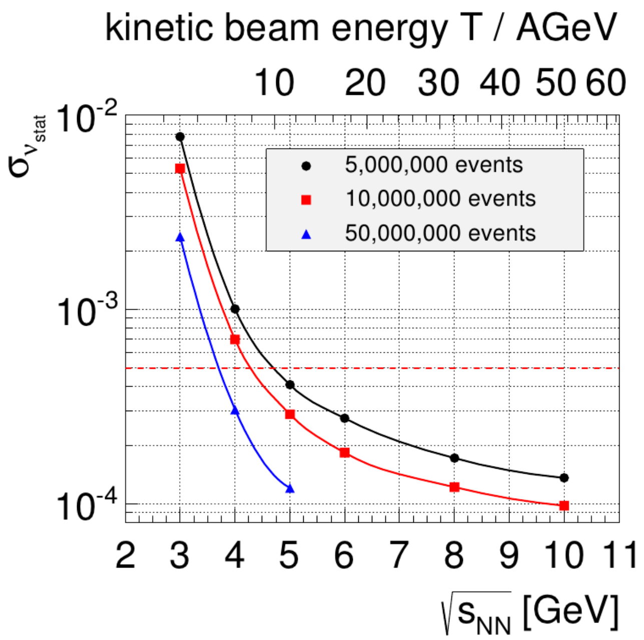

Figure 4.9: Uncertainty of the statistical fluctuations as function of the center of mass energy in an Au+Au collision. The black circles represent the simulated data with an event sample of $5\cdot10^6$ events, the red squares are related to 10^7 events and the blue triangles are obtained with $5\cdot10^7$ events. The red dashed line indicates the maximum value of the uncertainty of the statistical fluctuations in order to observe significant changes in the dynamical fluctuations.

dashed line indicates the threshold for the uncertainty of the statistical fluctuations mentioned above. $\sigma_{\nu_{stat}}$ increases fast with decreasing collision energy. It is mainly dominated by the $K^{\pm}$ yields since they are much lower than the $\pi^{\pm}$ yields. At about 5 GeV center of mass energy which approximately correspondents to the maximum SIS100 energy already $5 \cdot 10^6$ events are sufficient to achieve an uncertainty of the statistical fluctuations under the mentioned threshold. This corresponds to about 1 minute of data taking in CBM at 100 kHz archive rate. Totally different is the situation at 3 GeV. The uncertainty of the statistical fluctuations as function of the number of events simulated at a center of mass energy of 3 GeV is shown in Fig. 4.10. The kaon detection efficiency was kept at 0.3. $\sigma_{\nu_{stat}}$

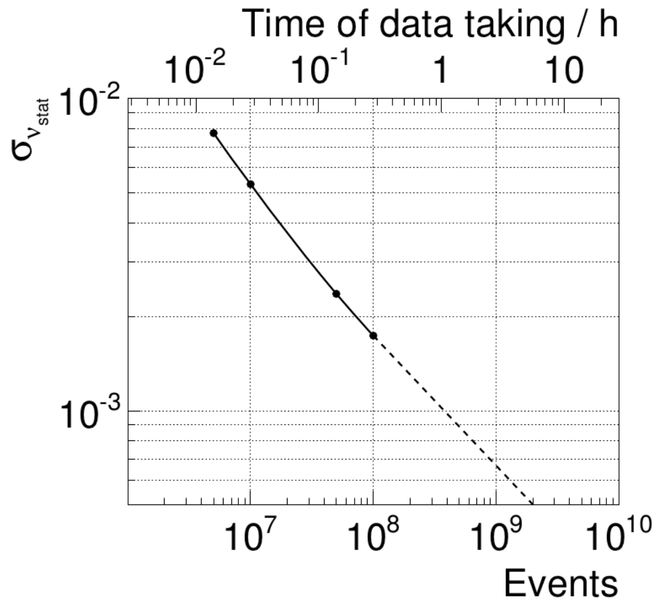

Figure 4.10: Uncertainty of the statistical fluctuations as function of the number of simulated events. The center of mass energy of the collision is 3 GeV. The pion detection efficiency is set to 0.8 while the kaon detection efficiency is 0.3. The black dashed line is an extrapolation of the data to the x-axis pointing to the minimum number of events in order to meet the uncertainty threshold.

decreases with growing statistics as expected. In order to get the necessary amount of events the data points were extrapolated to $\sigma_{\nu_{stat}} = 5 \cdot 10^{-4}$. The obtained value is $2 \cdot 10^9$. Assuming a data taking rate at 100 kHz about 5 hours are sufficient to obtain enough statistics at 3 GeV center of mass energy which corresponds to 3 GeV beam energy. For even lower energies (e.g. minimum SIS100 energy) it may take several days. $\sigma_{\nu_{stat}}$ depends also critically on the particle detection efficiency, in this case the kaon efficiency. In particular at low energies where the detection efficiency of the kaon drops due to the kaon decay it becomes difficult to measure the dynamical fluctuations. The behavior of $\sigma_{\nu_{stat}}$ as function of the kaon detection efficiency at a center of mass energy of 3 GeV is depicted in Fig. 4.11. The number of processed events is $5 \cdot 10^7$. However, the uncertainty of the statistical fluctuation is still huge especially for a decreasing kaon detection efficiency. A decrease of 10 % in efficiency almost leads to a doubling of the uncertainty of the statistical fluctuations. The plot in Fig. 4.11 demonstrates the importance of the particle detection efficiency of the Time-of-Flight wall for fluctuation measurements.

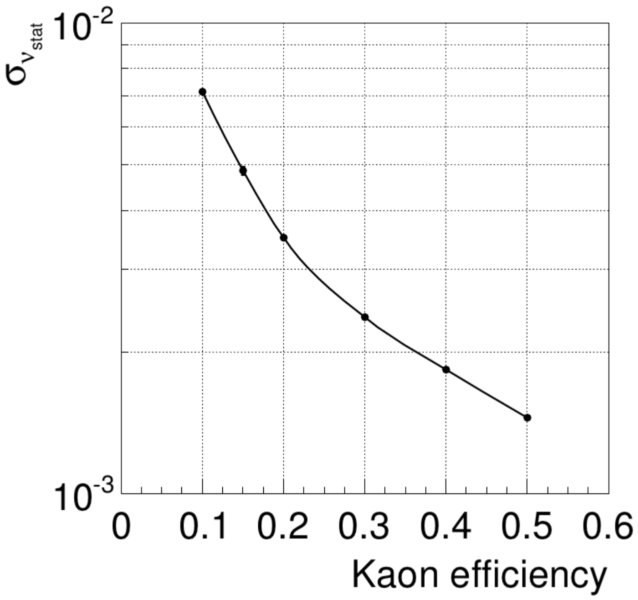

Figure 4.11: Uncertainty of the statistical fluctuation as function of the kaon detection efficiency.The center of mass energy of the collision is 3 GeV. The pion detection efficiency is set to 0.8. The number of simulated events is $5 \cdot 10^7$.

4.4 The CBM Detector concept

The CBM detector is designed as a multi-purpose device which will be able to measure hadrons, electrons and muons in heavy-ion collisions. Hardware development concentrates on highly granular, fast and radiation-hard detectors, on data-driven and fast read-out electronics, and on a high-speed data acquisition [3]. The conceptual design of CBM foresees two configurations. One setup is dedicated for measuring hadrons and in particular electrons and a second version is specified for measuring muons. The electron-hadron setup consists of a large acceptance dipole magnet, radiation-hard Silicon pixel/strip detectors for tracking and vertex determination (STS, MVD), a Ring Imaging Cherenkov detector (RICH) and Transition Radiation Detectors (TRD) for electron identification, Resistive Plate Chambers (RPC) for time-of-flight measurements, an Electromagnetic Calorimeter (ECAL) for photon identification, and a Projectile Spectator Detector (PSD) for centrality and reaction plane determination [3]. In the muon configuration the RICH is replaced by a Muon Chamber system (MuCh). In addition, some TRD stations removed from the beam line. Figure 4.12 and 4.13 depict the two versions of the CBM setup. The various subsystems are predestined to identify a specific type of particle. Tab. 4.2 lists the different particle types and the required detectors for identification. Hadrons are mainly identified via the time-of-flight method realized by the RPCs. In the following subsections the components of the CBM spectrometer are discussed in more detail starting with the components closest to the target.

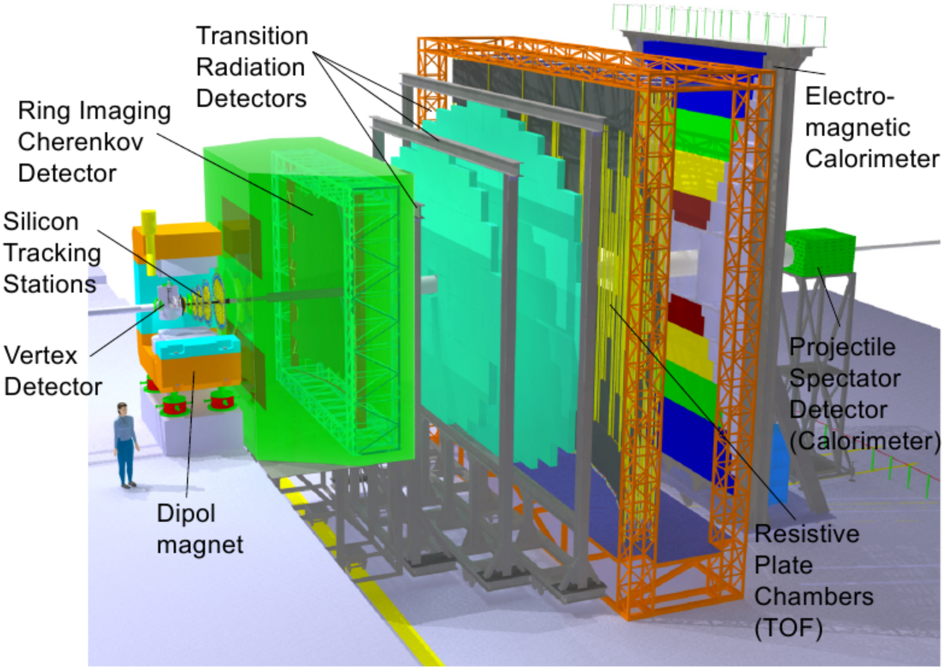

Figure 4.12: Conceptual design of CBM serving as combined e^+/e^-, γ and hadron spectrometer [162].

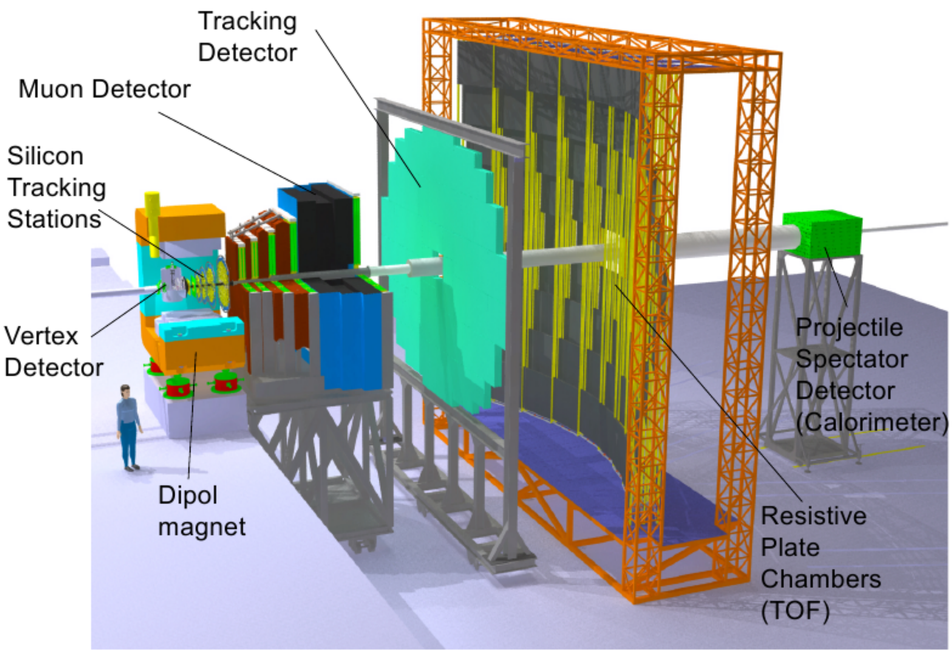

Figure 4.13: Conceptual design of CBM serving as μ^+/μ^- spectrometer [162].

Observable	MVD	STS	RICH	MuCh	TRD	RPC	ECAL	PSD
π, K, p		x	(x)		(x)	x		x
Hyperons		x			(x)	x		x
Open Charm	x	x	(x)		(x)	(x)		x
Electrons		x	x		x	x		x
Muons		x		x		(x)		x
Photons							x	x
Photons via $e^{\pm}$ conversion	x	x	x		x	x		x

Table 4.2: Observables and required detectors: Micro-Vertex Detector MVD, Silicon Tracking System STS, Ring Imaging Cherenkov detector RICH, Muon Chambers MuCh, Transition Radiation Detector TRD, timing Resistive Plate Chambers RPC, Electromagnetic Calorimeter ECAL, Projectile Spectator Detector PSD. Detectors marked as (x) can be used to suppress background. Table taken from [3].

4.4.1 The Dipole Magnet

The superconducting dipole magnet for the CBM experiment will provide a magnetic field integral of 1 Tm. The target is placed inside the magnet. The opening angle in horizontal direction is about $\pm 30°$ and in vertical direction about $\pm 25°$.

4.4.2 The Micro-Vertex Detector (MVD)

The goal of the Micro-Vertex Detector (MVD) is to determine the position of primary and secondary vertices with a resolution of about $50-100$ μm along the beam axis. This requires an excellent position resolution on the detection surface < 5 μm. Further requirements are a very low material budget (to minimize multiple scattering), radiation hardness above a dose of 10^{13} n_{eq} and a fast readout speed of about 10 μs. These requirements are met by Monolithic Active Pixel Sensors (MAPS). The MVD will consist of 3 layers of MAPS stations positioned at 5 cm, 10 cm, and 20 cm downstream of the target covering a polar angle of $\pm 25°$ [163; 164]. The MVD is placed in the vacuum.

4.4.3 The Silicon Tracking System (STS)

Behind the MVD station, between 30 cm and 100 cm downstream of the target, the Silicon Tracking System (STS) is positioned [165–167]. This detector unit consists of 8 tracking layers made of 300 μm thick silicon microstrip sensors. The stereo angle of these double-side sensors is 7.5°, the strip pitch is 58 μm and the strip length is between 20 mm and 60 mm. The typical hit resolution will be in the order of 25 μm. The STS provides the tracking and the momentum information of all charged particles. The momentum resolution Δp/p is in the order of 1 %. With 2.1 million channels the STS is the subcomponent with the largest channel number. Figure 4.14 shows a detailed view of the STS together with The MVD integrated in the magnet.

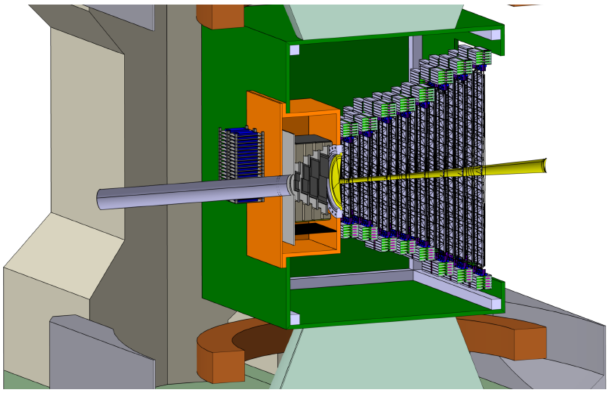

Figure 4.14: Detailed view of the STS together with MVD integrated in the magnet. Figure taken from [168].

4.4.4 The Ring Imaging CHerenkov detector (RICH)

In order to identify electrons and suppress pions up to a momentum of 10 GeV/c a Ring Imaging Cherenkov detector (RICH) with CO_2 as radiative material is under consideration. The required pion suppression for RICH is in the order of 500 – 1000. Taking the TRD (see subsection 4.4.6) into account the suppression factor can be enhanced to about 10^4. The length of the radiator is about 1.7 m. The created Cherenkov rings (diameter ~ 5 cm) are reflected by spherical glass mirrors (~ 12 m^2) onto two photodetector planes (2 $\times$ 0.6 m^2 each) consisting of 55000 Multi Anode Photo Multiplier Tubes (MAPMTs). In a central Au+Au collision at 25 AGeV about 100 rings have to be detected. The RICH detector is positioned behind the magnet (1.6 m downstream of the target). However, the photosensors are shielded by the magnet yoke. Illustrations and more details can be found in [169–172]

4.4.5 The Muon Chamber system (MuCh)

The Muon Chamber system (MuCh) is a complementary detector unit to the RICH. It is supposed to measure the decay of low-mass vector mesons and charmonium in the di-muon channel [173; 174]. The actual design of the final version foresees 6 hadron absorber layers made of iron with thicknesses of 3 $\times$ 20 cm, 30 cm, 35 cm and 100 cm [175]. Behind every layer a triplet of tracking chambers measures the tracks of charged particles. The hit density after the first absorber layer is around 3 MHz/cm^2 at 10 MHz interaction rate. In order to cope with such high rates straw tubes and chambers based on GEM technology are under consideration [176; 177]. The MuCh will have about 500000 channels.

4.4.6 The Transition Radiation Detector (TRD)

The Transition Radiation Detector TRD will provide electron and positron identification with a momentum p < 1.5 GeV/c ($\gamma \leq 1000$) and tracking of all charged particles. The required pion suppression is a factor of about 100 and the position resolution has to be in the order of $200 - 300$ μm [178]. The actual design foresees 3 TRD stations with 4+4+2 detector layers positioned at 5 m, 7.5 m and 9 m downstream of the target. The maximum rate on the first layer is about 100 MHz/cm^2 for a minimum bias Au+Au collision at 25 AGeV and 10 MHz interaction rate. The TRD is composed of about 700 detector modules covering an area of about 600 m^2 resulting in 740000 readout channels [179].

4.4.7 Resistive Plate Chambers (RPC)

The Time-of-Flight wall of CBM is composed of an array of Multigap-RPCs. Since this subcomponent plays a major role in this thesis it will be discussed more extensively in section 4.5 and chapter 6.

4.4.8 The Electromagnetic CALorimeter (ECAL)

In order to measure direct photons and neutral mesons (π^0, η) decaying into photons a shashlik type calorimeter placed at 12 m downstream of the target is under consideration. The design is based on the electromagnetic calorimeter used at the LHCb experiment [180]. It consists of lead and scintillator sheets of 1 mm thickness with cell sizes of 3 $\times$ 3 cm^2, 6 $\times$ 6 cm^2, and 12 $\times$ 12 cm^2.

4.4.9 The Projectile Spectator Detector (PSD)

The Projectile Spectator Detector (PSD) is a hadronic calorimeter measuring the energy of the projectile spectator nucleons and fragments. It will provide the information to compute the orientation of the reaction plane (required to study the collective flow) and for determining the collision centrality (important for the analysis of event-by-event observables). It comprises 45 individual modules with a surface of 20 $\times$ 20 cm^2. Each module consist of 60 lead/scintillator layers with a sampling ratio Pb:Scint of 4:1 grouped in 10 longitudinal sections. The energy resolution is about $55\%/\sqrt{E[GeV]}$.

4.4.10 Online event selection and data acquisition

The unique research program of CBM is based on the measurement of rare probes (see section 4.2) with high statistics. Therefore, it is designed such that it is capable to operate at interaction rates of 10 MHz producing about 10 kByte (100 GByte/s) of data per Au+Au collision at 25 AGeV minimum bias. Considering an archiving rate of 1 GByte/s (equivalent to an event rate of 100 kHz) a data reduction procedure has to be implemented. This is done in the First-Level Event Selector (FLES) where the data from the different sub-detectors are collected and a fast online event reconstruction is performed. The online identification of particles and the reconstruction of their tracks allow for a selection of interesting events. Since there is no hardware trigger involved a free streaming data acquisition is required. The data from every detector obtain a time stamp stemming from a clock which is synchronized with a common clock running at 156.25 MHz. Based on this time stamp information the data can be combined to an event.

4.5 The Time-of-Flight wall (TOF)

Hadron identification at CBM is provided by measuring the momentum and the time of flight of the respective particles. In order to separate kaons from pions up to a momentum of 4 GeV/c with a separation power of 3σ at 10 m distance from the target a system time resolution of 80 ps is necessary (cf. Fig. 1.7b). The existing conceptual design foresees a 120 m^2 ToF-wall composed of Multi-gap Resistive Plate Chambers (MRPC) covering a polar angular range from 2.5° to 25°. In the starting phase of FAIR (only SIS 100 available) the ToF-wall will be located most probably at 6 m downstream from the target. In the final setup of CBM the wall is positioned at 10 m (cf. chapter 6). A interaction rate of 10 MHz for the system Au+Au at 25 AGeV translates into an incident particle flux of around 20 - 50 MHz/cm^2 in the central region of the ToF-wall, dropping nearly exponentially to 500 Hz/cm^2 in the outermost region (see Fig. 4.15). A design occupancy of 5 % for the most central collisions in the aforementioned system leads, similarly, to very different counter granularities ranging from 4-6 cm^2 in the central part up to 50 cm^2 in the outer part. On one hand, this fact enforces the choice of a strip layout for the outermost part. On the other hand, the high channel density in the central part imposes naturally a need to develop a low-power and compact Front End Electronics, desirably at ASIC level. In total about 100000 readout channels are destined.
The ToF-wall is subdivided into three rate regions: the high rate region with incident particle fluxes above 8 kHz/cm^2, an intermediate rate region with fluxes between 1 kHz/cm^2 and 8 kHz/cm^2 and the low rate region with fluxes below 1 kHz/cm^2. The physical part of the high rate region is called inner ToF-wall. The outer ToF-wall comprises the intermediate and the low rate region. The design of the outer ToF-wall is part of this thesis and therefore will be explained in more detail in chapter 6.
The hadron identification capability of the CBM experiment is simulated in the CBMRoot simulation framework [181]. As event generator the UrQMD (version 1.3) [23; 154] code

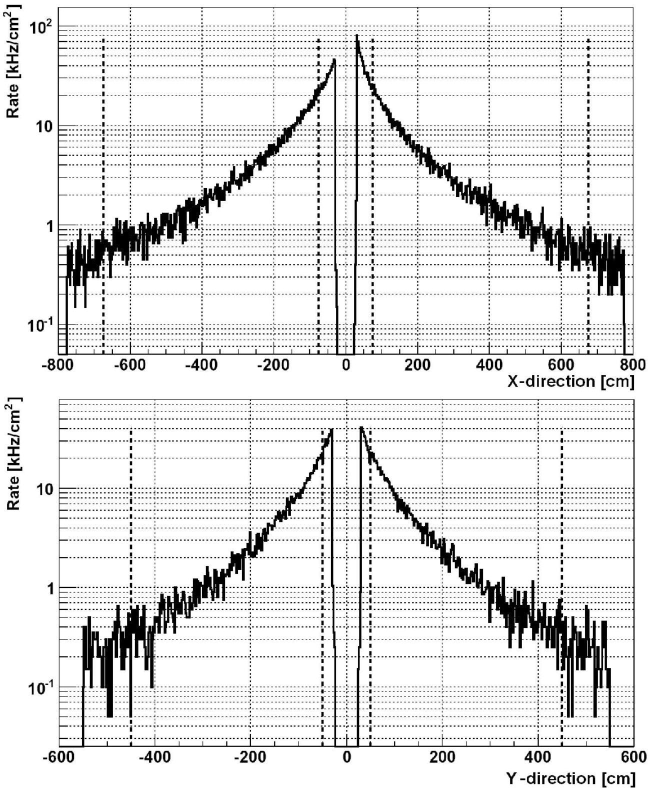

Figure 4.15: Simulated particle flux over the CBM ToF wall in x- and y-direction for the highest expected rate of Au+Au collisions at 25 AGeV. The x-axis is the direction of the magnetic field kick. The vertical dashed lines represent the detector acceptance. Figure taken from [91].

was used. Particles are propagated through the CBM detector model, shown in Fig. 4.12, using the transport code GEANT 3 [3; 182]. The simulations were performed with a planar ToF-wall. Results of the simulation are shown in the following subsection. A more realistic ToF-wall geometry is currently implemented in GEANT.

4.5.1 Hadron identification

The identification of pions, kaons and protons over a large phase space region is a prerequisite for a deeper understanding of the collision process [3].
Hadron identification in CBM is performed in several steps. First, the track of a charged hadron is reconstructed in the STS delivering simultaneously the momentum p of the particle. The track is extrapolated to the TRD adding the information to the track reconstruction. Then the track is matched to the nearest hit in the ToF-wall. Knowing the path length L and measuring the time of flight t the squared mass m^2 of the particle can be calculated via:

$$m^2 = p^2 \left(\frac{1}{\beta^2} - 1 \right), \tag{4.19}$$

with $\beta = L/ct$. In time-of-flight measurements the time resolution σ_t typically dominates the squared mass resolution σ_{m^2}. Therefore, the squared mass resolution σ_{m^2} can be calculated as follows:

$$\sigma_{m^2} = 2p^2 \frac{c^2 t}{L^2} \sigma_t. \tag{4.20}$$

Equation (4.20) states that the squared mass resolution is proportional to the square of the momentum leading to a reduced separation power and thus to a miss-identification of pions, kaons and protons above a certain particle momentum. The squared mass spectrum of reconstructed pions, kaons and protons in central Au+Au collisions at 25 AGeV beam energy for different momentum bins is shown in Fig. 4.16 [183]. For each momentum bin

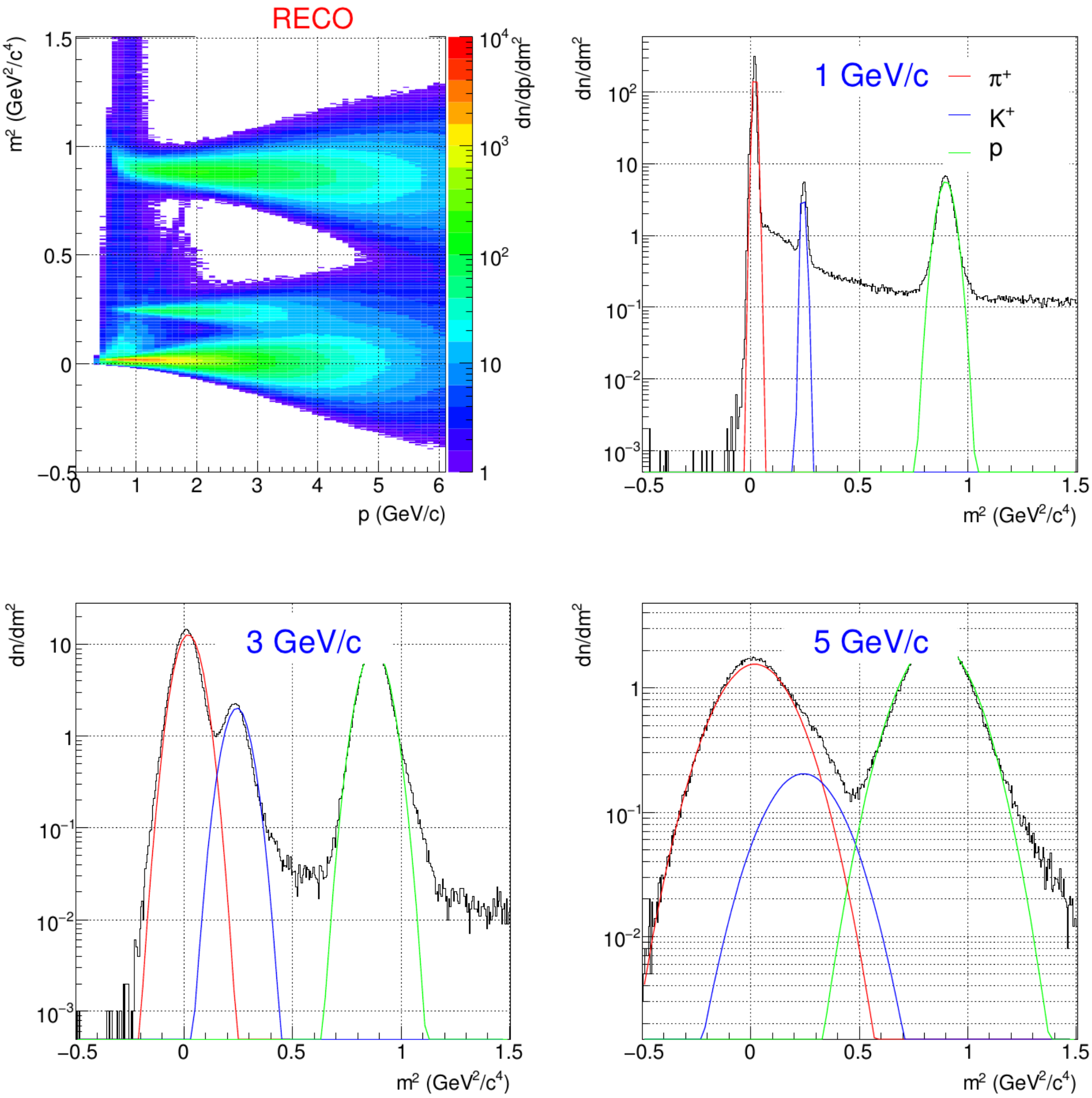

Figure 4.16: Upper left panel: Squared mass as a function of momentum assuming a time resolution of 80 ps. Other panels: mass spectra for momentum bins at $p = 1$, 3 and 5 GeV/c. Figure taken from [183]. For more information see text.

three Gaussians where fitted to the squared mass distribution. Since the squared mass resolution is independent of mass, the width of these peaks were kept the same. The position of each peak was fixed to the value of the nominal particle mass squared. In total there are 4 free parameters in the fit: the common width and three amplitudes [183]. The tails in the mass distribution at low particle momenta are caused by the energy loss of the low momentum tracks, ghost tracks, mismatches of tracks and ToF-hits as well as double hits in ToF [3]. For laboratory momenta up to 3 GeV/c pions, kaons and protons are well separated, for higher momenta the different yields can still be extracted from a statistical unfolding of the spectra. This technique will allow the extraction of $p_t - y$ spectra and a flow measurement at midrapidity up to transverse momenta of a few GeV/c [3]. The phase space distributions ($p_t - y$ distribution) of generated (top row), geometrically accepted (middle row) and identified (bottom row) pions, kaons and protons for Au+Au collisions at a beam energy of 25 AGeV is shown in Fig 4.18. The black lines indicate the detector acceptance. The ToF-wall was located at 10 m from the target. The kaon purity was required to be 50 % (with a $\pm\, 2\sigma$ cut) leading to a momentum cutoff at 5.0 GeV/c (red line). With momentum cutoffs at 4.2 GeV/c, 3.5 GeV/c and 2.2 GeV/c a purity of 90 %, 99 % and 100 % can be obtained, respectively [3]. Requiring a purity of 90 %, 38 % of the generated kaons are geometrically accepted and 18.4 % can be reconstructed and identified. The measurement of event-by-event particle ratio fluctuations requires kaon identification with high purity [3]. Therefore, it is unavoidable to develop RPC detectors with efficiencies as high as possible. Additionally, a shift of the ToF-wall towards the target should be considered in the design in order to further improve the detection efficiency of particles.

A preliminary plot of the squared mass distribution as function of the momentum simulated with a more realistic ToF-wall design is depicted in Fig. 4.17. The ToF-wall was positioned at 6 m downstream from the target. The collision system was Au+Au with a beam energy of 10 AGeV. The red lines represent the 2σ value of a Gaussian fit on the squared mass distribution of pions, kaons and protons. The plot shows that a 3σ separation between pion and kaons is ensured up to 3 GeV/c. The purity of particles obtained with a more realistic ToF-wall is not as good as the purity obtained with a planar ToF-wall. However, the particle identification algorithms are still work in progress and an improvement can be expected.

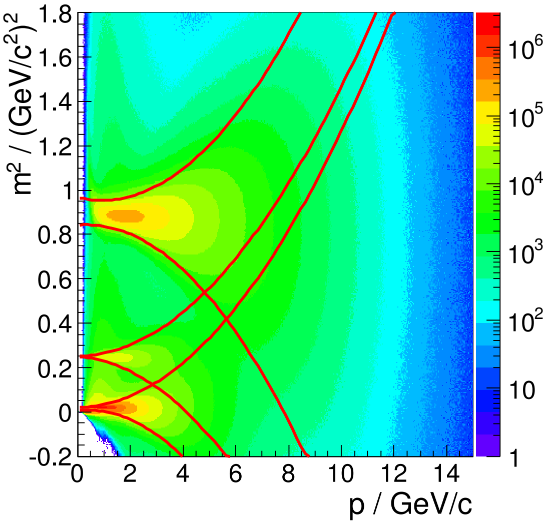

Figure 4.17: Squared mass distribution as function of the momentum simulated with a more realistic ToF-wall design. The red lines represents the 3σ value of a Gaussian fit on the certain particle species. Figure taken from [184].

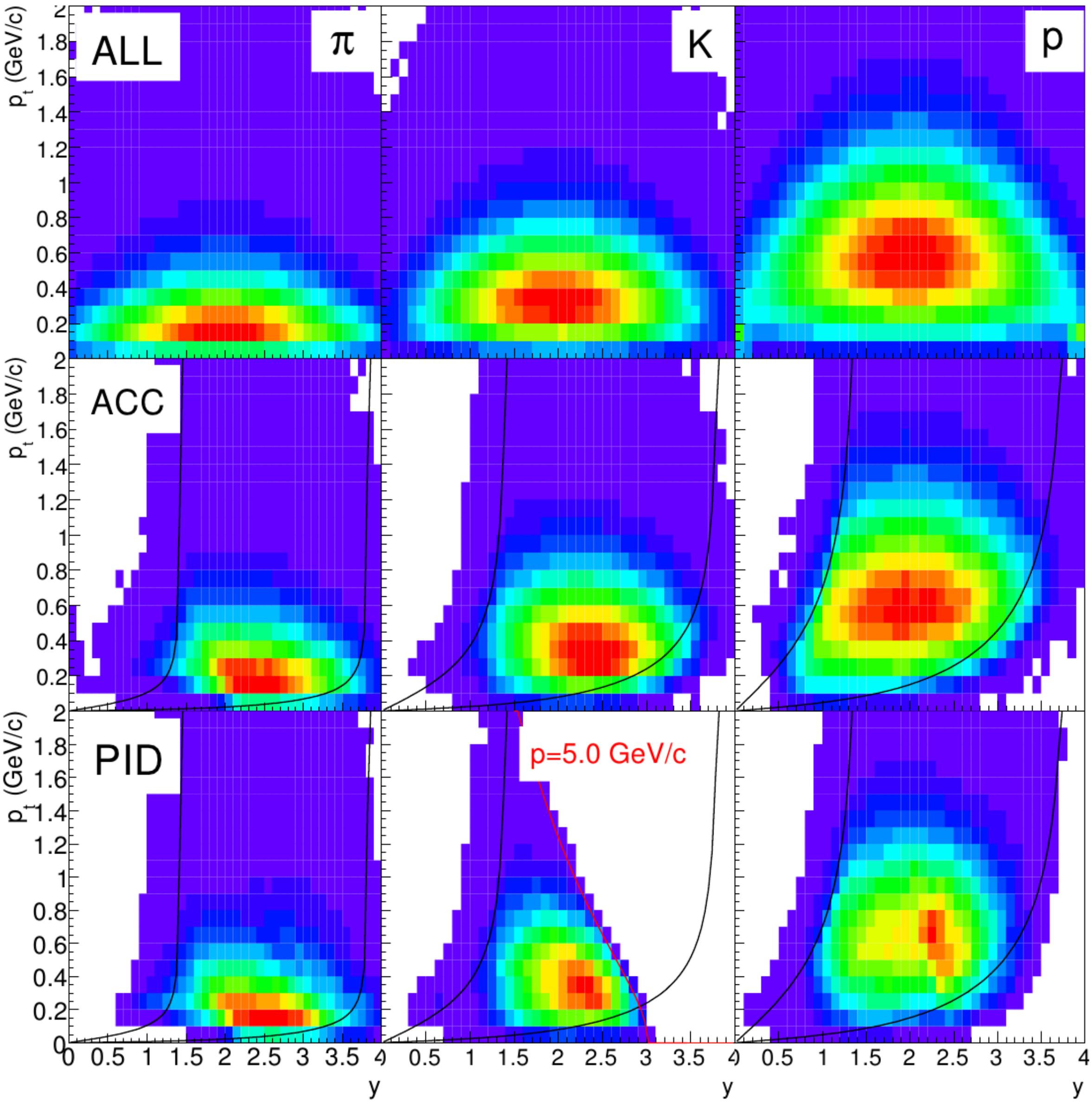

Figure 4.18: Phase space distribution ($p_t - y$ distribution) of generated (top row), geometrically accepted (middle row), and identified pions, kaons and protons (bottom row) for Au+Au collisions at a beam energy of 25 GeV. The z-axis is plot in a logarithmic scale The time resolution in this simulations is set to 80 ps. The black lines indicate the acceptance angle 2.5° and 25° Figure taken from [183], see also [3]. For more information see text.

5 A RPC-prototype for the CBM-ToF wall

This chapter comprises the development of Multigap-RPC prototypes for the CBM Time-of-Flight wall. In the development process several prototypes were constructed and tested. The test results and the experience gained from the previous prototypes inspires the development of the next generation detector. The realization and testing of these various prototypes is the main achievment of this thesis and will therefore be discussed in great detail.

In chapter 3 we studied the behavior of the FOPI MMRPC in order to gain as much input as possible for the new developments. In the conclusion section we were already able to give some indications regarding counter size, avalanche size and corresponding strip width, etc... In particular the philosophy of impedance matching that turned out to be of crucial importance of the operability of the FOPI detector is kept and extended. However, the whole design concept is changed and adapted to the requirements of CBM.

5.1 RPC requirements

The RPC design depends mainly on the requirements imposed by the CBM experiment. For the RPC they are:

- a counter time resolution in the order of 50 ps
- a counter efficency of better than 95 %
- a rate capability between 0.5 kHz/cm^2 - 25 kHz/cm^2 depending on the particle rate at this specific solid angle
- an occupancy smaller than 5 %
- a granularity of 4 cm^2 - 50 cm^2 depending on the particle rate at this specific place

This work is focused on the development of an MRPC for the low rate region with incident particle fluxes of maximum 1 kHz/cm^2. One of the prototypes fulfills the geometrical requirements of the intermediate rate region (granularity $\sim$ 25 cm^2). By applying small modifications this prototype can become a full-size demonstrator for the intermediate rate region.

5.2 Prototype RPC-P0

As a first step, we developed in cooperation with GSI Helmholtzzentrum für Schwerionenforschung GmbH in Darmstadt a so-called RPC-P0. This counter was developed in order to study different electrode configurations. Construction wise it is inspired by the FOPI MMRPC including the capacitor block techniques. The main difference to the FOPI-RPC is the design of the signal pickup electrode and the and consequently the size of the counter which is now 20×16.5 cm^2. The signal pickup electrode comprises 8 strips with a strip to gap ratio of 19.4 mm to 0.6 mm and a length of 20 mm. Four of the strips are subdivided into narrower strip of 1.9 mm which are interconnected on both ends (cf. Fig. 5.1). This

Figure 5.1: Left: Pickup electrode of RPC-P0. Bottom: The dark color denotes the metal part of the electrode. Four of the strips are sliced in sub-strips which are interconnected on both ends. In addition a ground guard is visible.

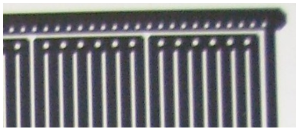

prototype has 4 gas gaps with a gas gap size of 220 μm. Figure 5.2 shows a photograph of the counter. First measurements were performed at GSI and results regarding efficiency

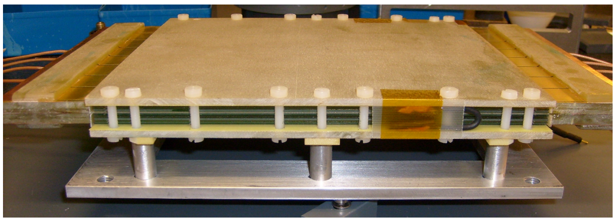

Figure 5.2: Photograph of the RPC-P0 RPC. The structure is similar to the MMRPC of FOPI. On the ends of the counter two capacitor blocks are glued onto the pickup electrode. In this case they act only as a feed through of the gas tight box.

are shown in Fig. 5.3. Data points labeled with strip 3 in the figure (black diamond) belong to a sliced strip and points labeled strip 4 (red triangle) belong to a full strip. From the data no difference is observed between these two kinds of strips. However, with this

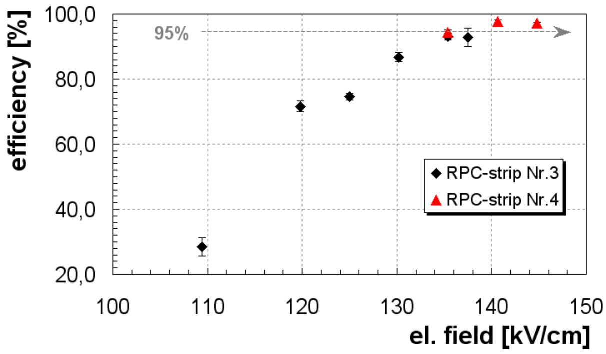

Figure 5.3: Efficiency of the RPC-P0. No difference is observed between a sliced strip and a full strip.

prototype we faced some new problems triggering new developments. One of the them was the gas tightness. The capacitor blocks on both ends of the RPC were penetrating the end flange of the gas box. On this feed through it was not possible to keep the box fully gas tight so that we always had an oxygen contamination in the counter gas. Unfortunately, the oxygen content in the gas was never measured. It was decided to implement the next prototype fully inside the gas box routing only the signals and the high voltage supply through the chamber wall. A second problem was the impedance matching. Since the width of the pickup electrode strip changed in comparison to the FOPI MMRPC but the RPC structure did not, the impedance went down due to the effective wide width of the strips from 50 Ω to roughly 20 Ω. This caused large reflections of the signals in the counter. The conclusion was that a larger strip width necessarily requires a different counter design. A third problem was the large amount of streamers measured in the test run. They were generated due to the enormous electric field applied that was necessary to obtain a reasonable efficiency. The amount of streamers lead to cross talk of about 40 %. Nevertheless, with this prototype we gained a lot of experience useful for developing the next generation of MRPC prototypes for CBM.

5.3 Prototype RPC-P1 - The next generation

In this section we will describe the first MRPC prototype developed at the Physikalisches Institut der Universität Heidelberg for the CBM experiment.

5.3.1 Construction principle

In order to study possible configurations of MRPCs for CBM a prototype of a Multi-strip MRPC with fully differential readout was developed. The differential readout has two advantages:

1. The charge of the signal is accumulated in both electrodes (anode, cathode) and hence twice as big as for a single ended readout.

2. The common pickup noise on both electrodes has typically the opposite polarity and cancels out in a differential preamplifier i.e. the counter is more stable with respect to DC offset variations.

A pictorial view of the cross section of this fully symmetric differential MRPC is shown in Fig. 5.4. The active area of the prototype is 28 x 16.5 cm^2. Its active volume is subdivided

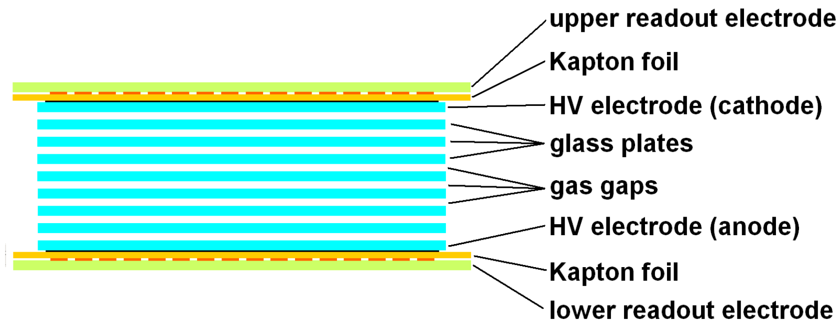

Figure 5.4: A pictorial view of the cross section of this fully symmetric differential MRPC. For more information see text.

by nine 0.55 mm thick float glass plates. The space between the glass plates is ensured by 220 μm thick fishing lines. The bottom and top glass plates are coated by an industrial spray called Licron® [185] forming a conductive layer (surface resistivity 100 $M\Omega/\square$). To this conductive layer the high voltage (HV) is applied via a copper strip running across the electrode (see Fig. 5.5b). The end of the copper strip is bent to the back side of the signal pickup electrode. The resistivity of the electrode is high enough to be transparent for fast signals (GHz) like the ones generated in an RPC. The two outermost layers are made of 4 mm thick PCBs which act as support for the MRPC and simultaneously as pickup electrode. They contain 16 readout strips with a width of 7 mm. The distance between the strips is 3 mm. The relatively large gap leads to reduced cross talk. With a pitch of 1 cm the electrode strips have a similar size like a typical cluster pattern created in the FOPI MMRPC (see section 3.4 or Fig. 3.21). Between the readout strips and the HV electrode 2 Kapton® foils of 75 μm thickness serve as isolation. The counter is embedded in a gas tight aluminum box with feed through for signals, HV and gas (see Fig. 5.6). Twisted pair cables of 110 Ω impedance are soldered to the signal pickup electrode. The other end of the cables is soldered to a 34 pin connector which is plugged to the feed through of the box.

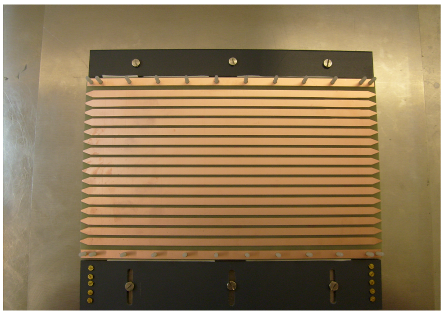

(a) Photograph of the signal pickup electrode. The width of the strips is 7 mm. The gap in between is 3 mm.

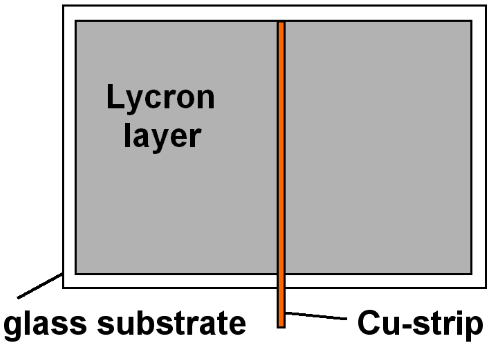

(b) Illustration of the high voltage electrode. A conducting layer is sprayed on a glass substrate. The HV is applied by the copper strip running across the counter.

Figure 5.5: Signal pickup and HV electrodes of the RPC-P1.

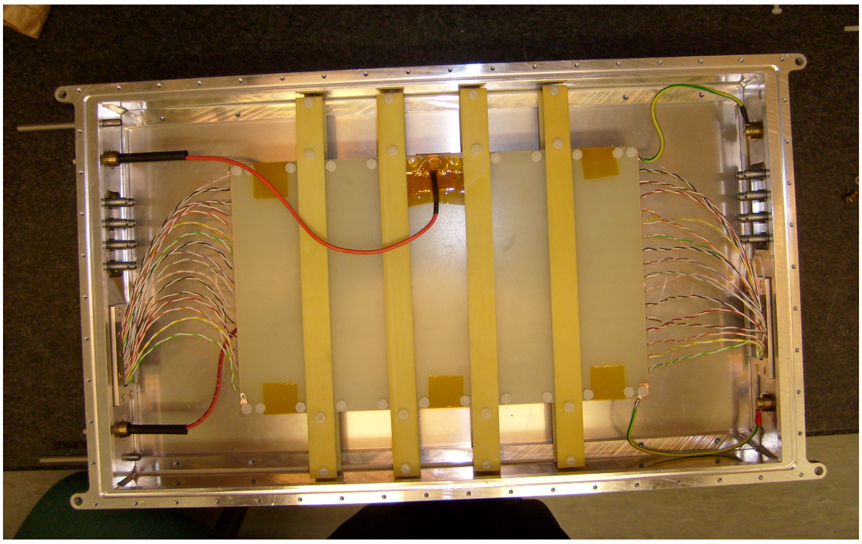

Figure 5.6: Photograph of the prototype 1 MRPC embedded in a gas tight aluminum box.

The strip configuration together with the total number of glass plates and gas gaps was simulated with APLAC [186] in order to obtain an impedance of 100 Ω. A good impedance matching with the Front End Electronics (FEE) is necessary in order to reduce signal reflections in the counter. Measurements with a time-domain-reflectometer show on average an impedance of about 80 Ω in the active area of the MMRPC (cf. Fig. 5.7). The reflectometer measurements show additionally the impedance of the signal path starting with a 50 Ω cable. The first jump in the impedance appears at the connector to the feed through. A second spike happens inside the box. At the soldering points the impedance reaches values of up to 140 Ω. At both ends of the twisted pair cable impedance spikes happen on the soldering points. These measurements demonstrate that the signal transmission lines from the detector to the preamplifier have to be treated in terms of impedance matching

equally careful as the detector itself. In the middle of the active RPC area the impedance has a dip generated by the copper strip in the HV electrode. This copper strip will be discussed in more detail in subsection 5.3.3.
Figure 5.8 shows an oscilloscope snap shot from a typical signal generated in the MRPC. The units in the graph are: x-axis → time in 2.0 ns/dev and y-axis → voltage in 10.0 mV/dev. The signal has an amplitude of 32 mV (compare to FOPI MMRPC, Fig. 3.16). The FWHM is about 500 ps and the rise time about 250 ps. After the signal reflections are visible with an amplitude below 10 mV. The reason is the impedance discontinuity between counter, cables and connections. The oscilloscope used for this measurement is a LeCroy Wavepro 7300A with 3 GHz bandwidth and 20 GS/s [187].

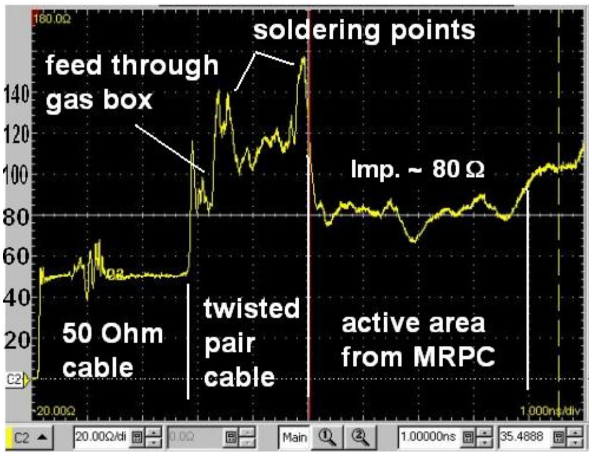

Figure 5.7: Impedance measurements with a time domain reflectometer. For more information see text.

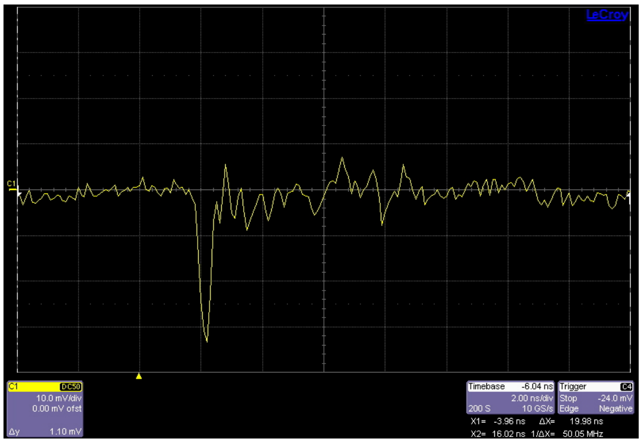

Figure 5.8: Oscilloscope snap shot of a typical signal from MRPC prototype 1. The signal has an amplitude of 32 mV, an FWHM of 500 ps and a rise time of about 250 ps.

5.3.2 Experimental setup

The prototype described in the previous section was tested in two different beam times. The first beam time was carried out in August 2009 at the SchwerIonenSynchrotron (SIS18) at GSI Helmholtzzentrum für Schwerionenforschung GmbH in Darmstadt. In this beam time a proton beam with a kinetic energy of 3.5 GeV was hitting a lead target producing a secondary particles which were used for the measurement. The setup was installed below the nominal beam height under a polar angle of 5°. The flux at this angle was approximately 100 Hz/cm^2. Several detectors were placed in the beam line starting with a pair of silicon strip detectors, a front scintillator, the Heidelberg RPC, 3 further RPCs from other groups, a rear scintillator, a further pair of silicon strip detectors and a final scintillator delivering the start signal of the data acquisition.
The silicon strip detectors were used in order to improve the spatial resolution of the

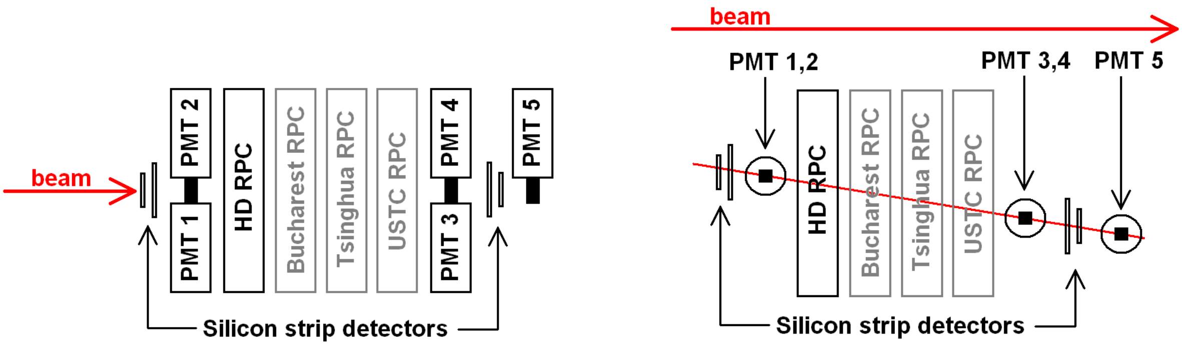

(a) top view **(b)** side view

Figure 5.9: Experimental setup used at GSI in August 2009

measurements. Since these silicon detectors were readout only on one side delivering information only in one dimension two of them were placed perpendicular to each other and form a pair of silicon strip detectors. The spatial resolution of this pair was about 100 μm in both directions. For more information about this type of silicon strip detector see [188]. The front and rear plastic scintillators had a size of 4 cm $\times$ 2 cm $\times$ 1 cm offering a trigger area of 8 cm^2. They were readout on both sides with photomultipliers (PMT) representing the reference system. The time resolution of the reference system was evaluated for each run individually. Figure 5.9 depicts a sketch ((a) top view and (b) side view) of the experimental setup. The trigger was formed by the coincidence of all photomultiplier signals delivering a gate signal for the Time to Digital Converter (TDC) and the Charge to Digital Converter (QDC). The signals from the RPC were amplified and discriminated by the so-called PADI II and PADI III chip [189–191] (see appendix B.6). This chip provids Time over Threshold (ToT) information, i.e. the output is an LVDS signal with the same width as the analog pulse at a given threshold. This information is used in the data analysis to correct for the charge dependencies of the timing distribution (walk) generated by the leading edge discriminator. The TDCs used during this test were not capable of measuring ToT. Therefore, an additional electronic card was produced in order to allow for ToT measurements. Unfortunately, this device did not work as expected such that only timing but no Tot information was available (the detailed electronic chain with all components is shown and explained in the appendix B.1).
The second beam test took place at the COoler SYnchrotron (COSY) at Forschungszentrum Jülich in November 2010. During this beam time protons of 3 GeV/c momentum were used. The beam was defocussed having a diameter of about 4 - 5 cm at the detector position. The setup was placed directly in the beam. The concept of the setup was similar to the one shown in Fig. 5.9. Only the type of detectors changed. Silicon strip detectors were not available for instance. In front, two scintillators provided the reference time. On the back side, a scintillator served as an additional trigger counter. All scintillators were read out by two PMTs each. The trigger was formed by the coincidence of the signals from PMT 3 to PMT 6 (cf. Fig. 5.10). The trigger scintillators had a size of 4 cm $\times$ 2 cm $\times$ 1 cm and a trigger area of 8 cm^2. Between the two beam times the RPC was slightly

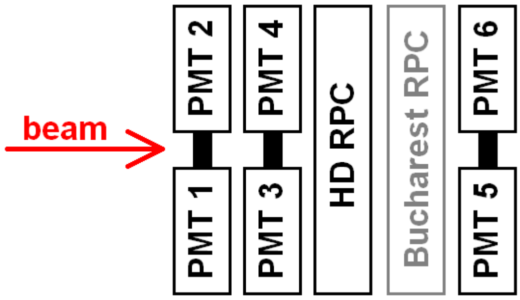

Figure 5.10: Experimental setup used at COSY in November 2010

modified. As demonstrated in section 5.3.3, the copper strip on the HV electrode (see Fig. 5.5b) generated a deficiency in the RPC at this position. Therefore, the strip was shortened in order to protrude only 1 cm inside the coated area. A second modification was exchanging the twisted pair cables connecting the RPC strips to the feed through inside the box. The new cables had a 100 Ω impedance and on the feed through side a non-soldered connector. Also, the electronic chain was exchanged completely (see appendix B.2). New PADI III preamplifier boards with individual channel threshold setting were implemented in the setup. The signals were digitized by a commercial TDC (CAEN V1290A see appendix B.7.1). In both beam tests a gas mixture of 85 % Tetrafluorethan ($C_2H_2F_4$), 10 % Sulfurhexafluoride (SF_6) and 5 % Isobutane (C_4H_{10}) was used. Note that in our case 5 % less quencher gas SF_6 is used in comparison to the FOPI MMRPCs. It was shown that a lower concentration of SF_6 improves the time resolution as well as the efficiency [192].

5.3.3 Test results

In this subsection we will show results obtained during the test beam times discussed in the previous subsection. The measured quantities are the efficiency, the time resolution and the cluster size as function of the applied high voltage/E-field on the RPC, as function of the threshold settings in the preamplifier and as function of the incident particle flux.

Efficiency

The Efficiency ε is defined as the number of detected events in the RPC N_{RPC} divided by the number of detected events in a reference counter N_{Ref} on a restricted common active area:

$$\varepsilon = \frac{N_{RPC}}{N_{Ref}} \tag{5.1}$$

The reference is in most cases the coincidence of the trigger counters since the trigger area (in our case 4 × 2 cm^2) is mostly covering the active area of the RPC under investigation. A coincidence of two scintillators placed in front and behind the RPC ensures that the particle crosses the active area of the RPC. But also a second RPC or a silicon strip detector could serve as reference if the path of the particle is known. In order to calculate the error of the efficiency one has to take into account that N_{RPC} and N_{Ref} are correlated and therefore the Bernoulli distribution holds [193]. The absolute error of N_{RPC} is given by:

$$\sigma_{N_{RPC}} = \sqrt{N_{Ref} \cdot \varepsilon(1-\varepsilon)} \tag{5.2}$$

The relative error of N_{RPC} normalized to N_{Ref} yields the error of the efficiency:

$$\sigma_{\varepsilon} = \frac{\sigma_{N_{RPC}}}{N_{Ref}} = \sqrt{\frac{\varepsilon(1-\varepsilon)}{N_{Ref}}} \tag{5.3}$$

It is always possible to cut on the reference without affecting the result.
Figure 5.11 shows the trend of the efficiency as function of applied high voltage for three different preamplifier threshold settings. The threshold of PADI III is applied after the amplification of the signal. The amplification has a gain of approximately 8 i.e. a set threshold of 70 mV corresponds to a discrimination value of 8.75 mV on the input signal. At a threshold of 70 mV only one data point was taken since the efficiency value was only 64 %. For the thresholds of 30 and 50 mV a voltage scan was performed. The rise of the efficiency as function of applied high voltage in this manner is typical for MRPCs (see for instance [135]). In our case the plateau starts at 11.5 kV and defines the nominal working voltage. For a threshold of 50 mV (30 mV) the maximal efficiency reached was 90 % (95 %), respectively. These measurements were performed at an incident particle flux of about 150 Hz/cm^2. These results demonstrate that a lower threshold setting is particularly important in order to fulfill the CBM ToF efficiency requirements. The attempt to lower the threshold even further failed due to the noise level. It was found out that the noise was mainly induced in the cables between gas box and preamplifier which allow for improvements as will be discussed later in section 5.4. The efficiency dependence on the incident particle flux for

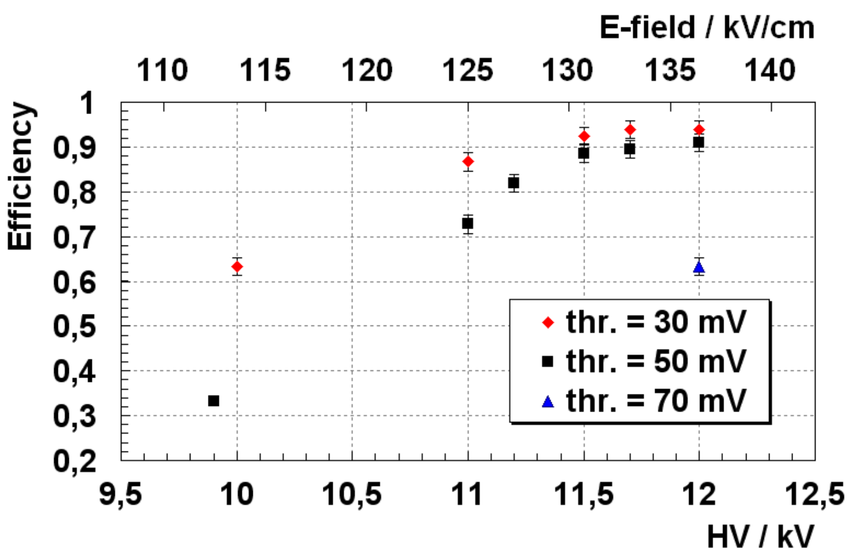

Figure 5.11: Efficiency of the RPC as function of the applied HV for three different preamplifier threshold settings.

50 and 70 mV threshold settings is depicted in Fig. 5.12. Unfortunately, no measurements

at 30 mV threshold were performed as function of the incident particle flux. The data in Fig. 5.12 show a degradation towards higher fluxes with a sharp bent at 1 kHz/cm^2 for 50 mV. The expectation is that at a lower threshold the efficiency stays even longer in a plateau. Measurements with the FOPI MMRPC showed an efficiency of 75 % at a flux of 3.5 kHz/cm^2 [135]. The rate capability of an RPC depends on the kind and the thickness of resistive material (see section 2.7), in our case float glass of 0.5 mm thickness was used. The conclusion is that at least efficiency wise a rate capability of 1 kHz/cm^2 to 1.5 kHz/cm^2 should be possible with float glass.

Making use of the very good spatial resolution of the silicon strip detectors it was possible

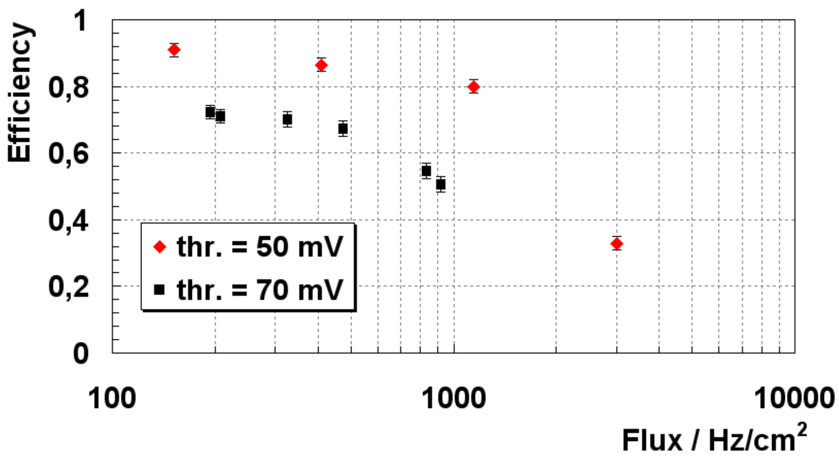

Figure 5.12: Efficiency of the RPC as function of the incident particle flux for three different preamplifier threshold settings.

to investigate the efficiency along and across the RPC strips in more detail. The area of investigation was 2 cm × 4 cm (trigger area) covering one strip fully and the two neighboring strips partially. Figure 5.13 depicts a sector of the pickup electrodes with the superimposed copper strip from the high voltage electrode and the trigger area. The

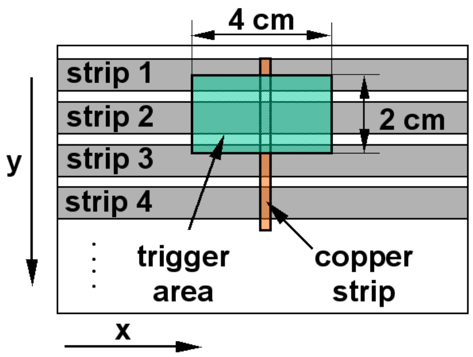

Figure 5.13: Pictorial view of a sector of the pickup electrodes with the superimposed copper strip from the high voltage electrode and the trigger area.

projection of the efficiency in x direction (along the strip) is shown in figure 5.14. During these measurements the high voltage electrode had a copper strip running across the surface

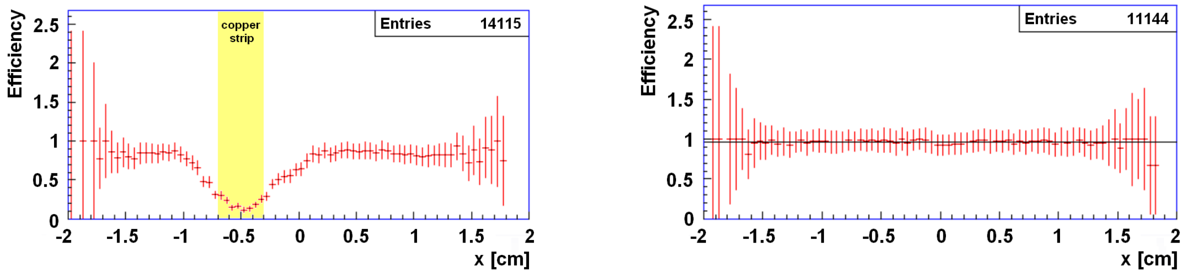

(a) The trigger window is overlapping the copper strip from the HV electrode.

(b) The trigger window is selecting a uniform active detector area

Figure 5.14: Efficiency along the readout strip.

(cf. Fig. 5.5b). Since copper is a very good conductor (electrical resistivity at 20 °C is 16.78 nΩm [194]) the signal is shielded by the copper strip and not detectable in the pickup electrode. The result is a dip in the efficiency on the counter where the strip is placed (see Fig. 5.14a). After this measurement the copper strip was partially removed from the active detector area. The same measurement was performed on an area without a copper strip. Figure 5.14b shows a flat distribution of the efficiency. The mean value indicated by the black line is about 95 %. The projection of the efficiency in y direction (across the strip) is shown in Fig. 5.15. The black data points correspond to the condition that strip 1 or strip 2 or strip 3 had a signal on both ends (total efficiency). The average value indicated by the arrow is about 95 %. In between the strips (white area in Fig. 5.15) the total efficiency is still about 92 %. The colored data points correspond to the individual strips. The efficiency of the fully covered strip (strip 2), represented by the red points, starts rising symmetrically before strips 1 and 3 end. In the middle of the gap an efficiency value of 75 % is measured. The efficiency plateau is reached 1 mm behind the border of strip 2. From the blue data points (strip 3) it is possible to estimate the cross talk of the counter by evaluating the efficiency after the drop in strip 1 and strip 2. It is in the order of 3 %. The measurement of the efficiency along and across the readout strips was performed at an incident particle flux below 100 Hz/cm^2. The applied high voltage on the counter electrodes was ±11.5 kV corresponding to a field of 130 kV/cm.

Time resolution

The time resolution is the most critical and the most important quantity of a Time-of-Flight detector. It specifies the accuracy how well a time period can be measured. For the RPC-P1 prototype only the strip time resolution is evaluated. Cluster building as for the FOPI counter (see section 3.3) was not performed yet and therefore no cluster mean time was constructed.
The calibration steps comprise the conversion of the TDC bins to time, the correction of walk cor_w and the correction of the integral non-linearities cor_n of the TDC with the bin-by-bin method explained in section 3.3. The average time of the reference system with

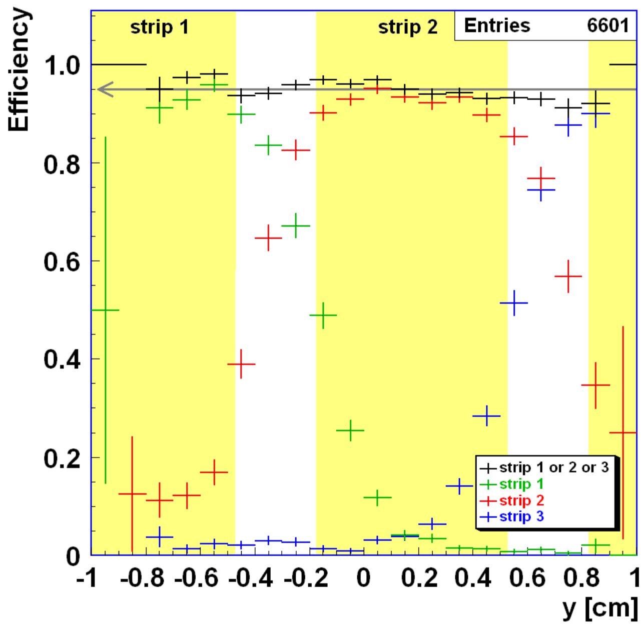

Figure 5.15: Efficiency across the read out strips. The black data points correspond to the condition that strip 1 or strip 2 or strip 3 had a signal on both ends. The colors green, red and blue correspond to the efficiency of the individual strip 1, 2 and 3.

N counters, in our case PMTs, is given by:

$$\bar{t}_{PMT} = \frac{1}{N} \sum_{i=1}^{N} (t_{PMT_i} - cor_{w,i} - cor_{n,i}) \tag{5.4}$$

with t_{PMT_i} being the raw times of the PMTs.
The average time of the RPC strip is given by:

$$\bar{t}_{RPC} = \frac{1}{2} (t_l - cor_{w,l} - cor_{n,l} + t_r - cor_{w,r} - cor_{n,r}) \tag{5.5}$$

with $t_{l,r}$ the raw times of both ends of the RPC strip.
In this analysis the time of flight t_{ToF} is calculated by taking the difference of the strip average time $\bar{t}_{RPC}$ and the average time $\bar{t}_{PMT}$ of 4 PMTs (labeled PMT1 to PMT4 in Fig. 5.10):

$$t_{ToF} = \bar{t}_{RPC} - \bar{t}_{PMT} \tag{5.6}$$

The error of t_{ToF} is given by:

$$\sigma_{t_{ToF}} = \sqrt{\sigma^2_{\bar{t}_{RPC}} + \sigma^2_{\bar{t}_{PMT}}} \tag{5.7}$$

with $\sigma_{t_{ToF}}$ the system time resolution, $\sigma_{\bar{t}_{RPC}}$ the RPC time resolution and $\sigma_{\bar{t}_{PMT}}$ the reference time resolution.
With this formula the RPC time resolution is calculated. The reference time resolution can be evaluated by calculating the time of flight between two scintillators. In the case with 2 scintillators readout on both ends $t_{ToF,PMT}$ is given by:

$$\begin{aligned} t_{ToF,PMT} &= \frac{1}{2} \sum_{i=1,2} (t_{PMT_i} - cor_{w,i} - cor_{n,i}) - \frac{1}{2} \sum_{i=3,4} (t_{PMT_i} - cor_{w,i} - cor_{n,i}) \\ &= \bar{t}_{PMT_{12}} - \bar{t}_{PMT_{34}} \end{aligned} \tag{5.8}$$

with

$$\begin{aligned}\bar{t}_{PMT_{12}} &:= \frac{1}{2}\sum_{i=1,2}\left(t_{PMT_i} - cor_{w,i} - cor_{n,i}\right)\\ \bar{t}_{PMT_{34}} &:= \frac{1}{2}\sum_{i=3,4}\left(t_{PMT_i} - cor_{w,i} - cor_{n,i}\right)\end{aligned} \tag{5.9}$$

The error of $t_{ToF,PMT}$ is given by:

$$\sigma_{t_{ToF,PMT}} = \sqrt{\sigma^2_{\bar{t}_{PMT_{12}}} + \sigma^2_{\bar{t}_{PMT_{34}}}} \tag{5.10}$$

On the other hand, one can calculate the error of $\bar{t}_{PMT}$ by rewriting $\bar{t}_{PMT}$ from (5.4) with $N = 4$:

$$\begin{aligned}\bar{t}_{PMT} &= \frac{1}{2}\left(\frac{1}{2}\sum_{i=1,2}\left(t_{PMT_i} - cor_{w,i} - cor_{n,i}\right) + \frac{1}{2}\sum_{i=3,4}\left(t_{PMT_i} - cor_{w,i} - cor_{n,i}\right)\right)\\ &= \frac{1}{2}\left(\bar{t}_{PMT_{12}} + \bar{t}_{PMT_{34}}\right)\end{aligned} \tag{5.11}$$

and the error of $\bar{t}_{PMT}$ is given by:

$$\begin{aligned}\sigma_{\bar{t}_{PMT}} &= \frac{1}{2}\left(\sqrt{\sigma^2_{\bar{t}_{PMT_{12}}} + \sigma^2_{\bar{t}_{PMT_{34}}}}\right)\\ &= \frac{1}{2}\sigma_{t_{ToF,PMT}}\end{aligned} \tag{5.12}$$

Note that $\sigma_{\bar{t}_{PMT}}$ is not the time resolution of a single PMT. It is the resolution of the mean time measured by 4 PMTs i.e. the time resolution of the reference system. Rearranging Eq. (5.7) and inserting Eq. (5.12) leads to the formula used for evaluating the RPC time resolution.

$$\sigma_{\bar{t}_{RPC}} = \sqrt{\sigma^2_{t_{ToF}} - \left(\frac{\sigma_{t_{ToF,PMT}}}{2}\right)^2} \tag{5.13}$$

$\sigma_{t_{ToF}}$ and $\sigma_{t_{ToF,PMT}}$ are determined by fitting a Gaussian to the t_{ToF} and $t_{ToF,PMT}$ distribution. The error of the RPC time resolution is calculated with the Gaussian error propagation rule:

$$\Delta\sigma_{\bar{t}_{RPC}} = \sqrt{\Delta\sigma^2_{t_{ToF}}\left(\frac{\partial\sigma_{\bar{t}_{RPC}}}{\partial\sigma_{t_{ToF}}}\right)^2 + \Delta\sigma^2_{t_{ToT,PMT}}\left(\frac{\partial\sigma_{\bar{t}_{RPC}}}{\partial\sigma_{t_{ToF,PMT}}}\right)^2} \tag{5.14}$$

The solution of equation (5.14) results to:

$$\Delta\sigma_{\bar{t}_{RPC}} = \frac{\sqrt{\left(\sigma_{t_{ToF}}\cdot\Delta\sigma_{t_{ToF}}\right)^2 + \left(\frac{\sigma_{t_{ToF,PMT}}\cdot\Delta\sigma_{t_{ToF,PMT}}}{4}\right)^2}}{\sigma_{\bar{t}_{RPC}}} \tag{5.15}$$

with $\Delta\sigma_{t_{ToF}}$ the error of the time of flight resolution and $\Delta\sigma_{t_{ToF,PMT}}$ the error of the reference time resolution. These values were obtained from a Gaussian fit to the t_{ToF} and

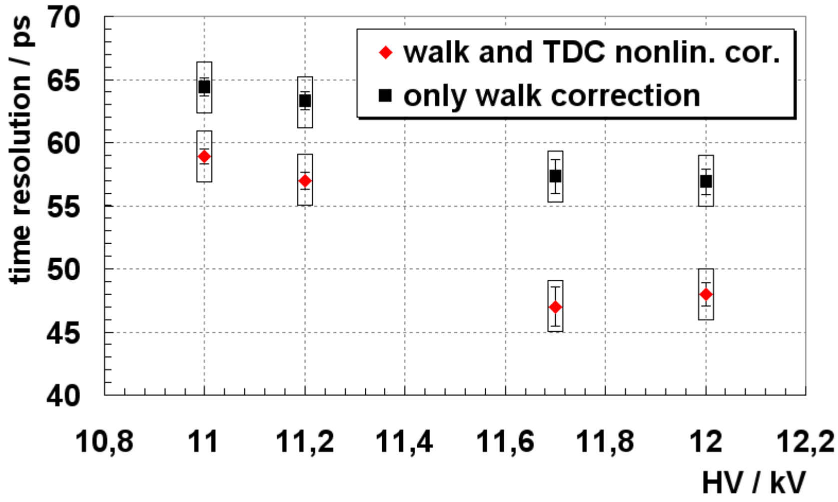

Figure 5.16: Time resolution of the RPC as function of the applied high voltage with all applied corrections (red data points) and with walk correction only (black data points). The bars represent the statistical error and the rectangles the systematic error. For more information see text.

$t_{ToF,PMT}$ distributions.
However, these errors are just statistical errors. The systematic error was estimated by comparing different runs and different readout strips performed under the same conditions. It is in the order of 2 ps. The RPC time resolution as function of the applied high voltage is depicted in Fig. 5.16. The red data points (diamonds) represent the time resolution evaluated with all mentioned corrections applied and the black data points (squares) represent the time resolution applying only the walk correction. The walk correction typically has a much larger impact on the result as the non-linearity corrections. Therefore, the nonlinearity correction is applied after the walk correction. On the level of 60 ps (without nonlinearity corrections) the non-linearity corrections can still improve the result by about 8 to 10 ps and hence become important. The statistical errors are in the order of 1 ps. This measurement was performed with a preamplifier threshold of 50 mV. The incident particle flux was ranging from 50 Hz/cm^2 to 200 Hz/cm^2. The time resolution improves with higher voltages. The same trend is also observed in Fig. 5.17 where the data from the previous plot are compared with data taken at a preamplifier threshold of 30 mV. The incident particle flux at 30 mV was between 20 Hz/cm^2 and 50 Hz/cm^2. The time resolution taken under the condition of 30 mV preamplifier threshold is about 10 ps higher as the one taken at 50 mV. This observation can be explained by the fact that at a preamplifier threshold of 30 mV the counter operates just above the noise level.
The rate dependence of the time resolution is shown in Fig. 5.18. The applied high voltage is 12 kV and the adjusted preamplifier threshold 50 mV. The incident particle flux varies only from 50 Hz/cm^2 to 380 Hz/cm^2, and a rise of the time resolution was observed! The Flux is determined by counting the particles traversing the first plastic scintillator in the setup (PMT1 and PMT2 in Fig. 5.10) between two trigger events. The time between the

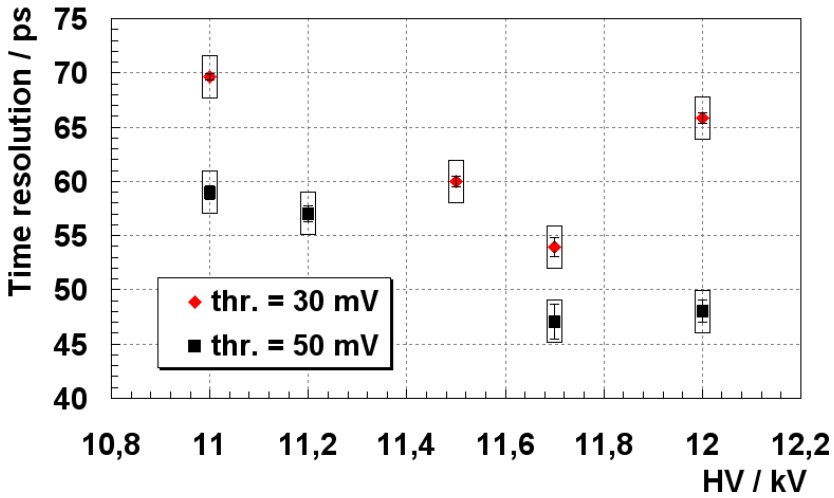

Figure 5.17: Time resolution of the RPC as function of the applied high voltage for different preamplifier thresholds. The bars represent the statistical error and the rectangles the systematic error.

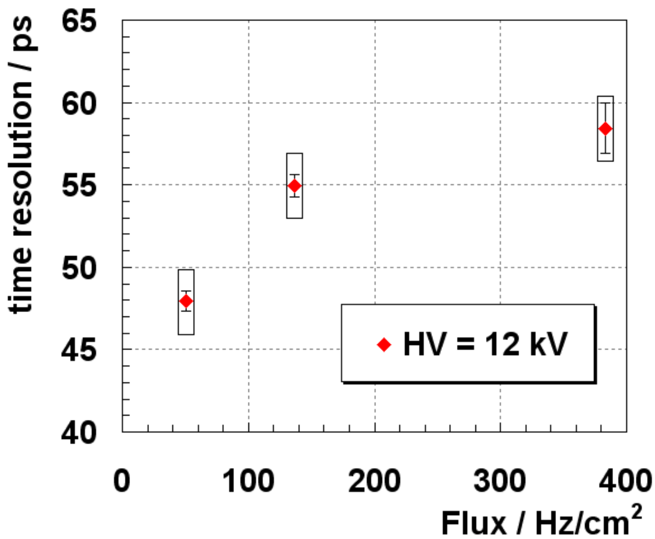

Figure 5.18: Time resolution of the RPC as function of the incident particle flux. The applied high voltage is 12 kV and the adjusted preamplifier threshold 50 mV.

trigger events is measured by a 10 MHz clock. The area of the plastic scintillator is 8 cm^2. The errors of the flux is estimated to be roughly 10 % since the beam intensity fluctuates (not shown in Fig. 5.18).

Mean Cluster size

The cluster size of a strip RPC is defined as the number of neighboring strips showing signals generated by a single avalanche. Hence it is an important parameter in determining the effective counter granularity. The typical cluster size distribution of prototype RPC-P1 is depicted in Fig. 5.19. The histogram shows how often one, two or more neighboring

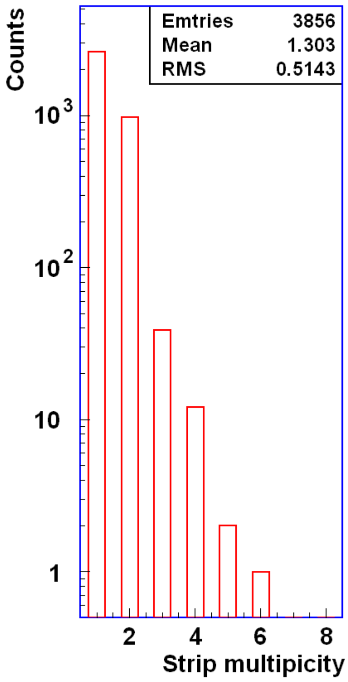

Figure 5.19: Cluster size distribution of a strip MRPC.

strips had a signal at the same time. In this special case the mean of the distribution was 1.30 and the RMS 0.51. The mean evaluated from such a distribution is in the following called the mean cluster size MCS and is calculated as follows:

$$MCS = \sum_{i=1}^{N} \frac{S_i \cdot n_i}{\sum_{j=1}^{N} n_j} \tag{5.16}$$

with S_i the strip multiplicity in bin i, N the total number of bins with entries (in our example $N = 6$) and n_i the number of entries for bin i in the strip multiplicity distribution. The statistical error of MCS can be calculated by the Gaussian error propagation function:

$$\Delta MCS = \sqrt{\sum_{i=1}^{N} \left(\frac{\partial MSC}{\partial n_i} \cdot \Delta n_i \right)^2} \tag{5.17}$$

with $\Delta n_i = 1/\sqrt{n_i}$ the statistical error of the measured entries for S_i.
The derivation of MCS with respect to n_i is:

$$\frac{\partial MSC}{\partial n_i} = \frac{S_i \cdot \sum_{j=1}^{N} n_j}{\left(\sum_{j=1}^{N} n_j\right)^2} - \frac{S_i \cdot n_i}{\left(\sum_{j=1}^{N} n_j\right)^2} - \sum_{k \neq i, k=1}^{N} \frac{S_k \cdot n_k}{\left(\sum_{j=1}^{N} n_j\right)^2}$$

Reducing further the fraction of term 1 and combining term 2 and term 3 yields to:

$$\frac{\partial MSC}{\partial n_i} = \frac{S_i}{\sum_{j=1}^{N} n_j} - \frac{MSC}{\sum_{j=1}^{N} n_j}$$

$$= \frac{S_i - MSC}{\sum_{j=1}^{N} n_j} \tag{5.18}$$

Finally, the statistical error is given by:

$$\Delta MCS = \sqrt{\sum_{i=1}^{N}\left(\frac{S_i - MSC}{\sum_{j=1}^{N} n_j} \cdot \frac{1}{\sqrt{n_i}}\right)^2}$$

$$= \frac{1}{\sum_{j=1}^{N} n_j} \cdot \sqrt{\sum_{i=1}^{N} \frac{(S_i - MSC)^2}{n_i}} \tag{5.19}$$

$\sum_{j=1}^{N} n_j =: E$ is the total number of entries in the histogram.
Since the total number of entries is typically much higher than 1000 the statistical error becomes very small. For the example shown in Fig. 5.19 the statistical error is about 0.0008. However, the MCS is measured on both sides of the readout strip and averaged. The discrepancy of these two measured values delivers an error used as statistical error. The mean cluster size depends on the applied high voltage, the preamplifier threshold, the incident particle flux, temperature, gas mixture and other constrains. During a beam time it is impossible due to this multi-dimensional parameter space to measure all dependencies in a systematic way. The procedure in most of the cases is to find a reasonable HV by performing a voltage scan. With a selected HV the further parameter are measured systematically one by one while keeping the others constant. However, the incident particle flux depends on the particle intensity delivered by the accelerator and can vary during the spill. The uncertainty of the flux was estimated to be about 10 %. The flux was determined for each setting as described above. Figure 5.20 depicts the mean cluster size as function of the incident particle flux. The differently colored data points belong to different preamplifier thresholds (red diamond $\widehat{=}$ 30 mV, black squares $\widehat{=}$ 50 mV and blue triangles $\widehat{=}$ 70 mV). The high voltage was set to $\pm$12 kV. The vertical bars represent the statistical error evaluated as described above. Systematic error bars are not shown since high voltage, threshold and temperature are well under control. The data show no significant difference in the mean cluster size between thresholds of 50 mV and 70 mV above 150 Hz/cm^2 and at HV = 12 kV. Only the slope of a fitted logarithmic function (not shown in the plot) is steeper for 50 mV in comparison to 70 mV. From the slope it is possible to estimate the systematic error for the mean cluster size plotted against other variables. The data point representing the measurement with a 30 mV threshold is slightly above a extrapolated line fitting the data points measured with a 50 mV threshold.

In order to investigate the behavior of the mean cluster size vs. the preamplifier threshold at 50 Hz/cm^2 a line was fitted to the data points corresponding to the 70 mV threshold. The value of this line at 50 Hz/cm^2 is taken as the 70 mV threshold data point at this flux. The data point for 30 mV is calculated in a similar way using the slope of the fitted line from the 50 mV data points. The result is presented in Fig. 5.21. The data show a decrease of the mean cluster size with higher applied thresholds. The uncertainty of the threshold setting is indicated by the width of the rectangle. However, the errors are quite large and no precise conclusions are possible.

The mean cluster size as a function of the applied HV is shown in Fig. 5.22. The threshold

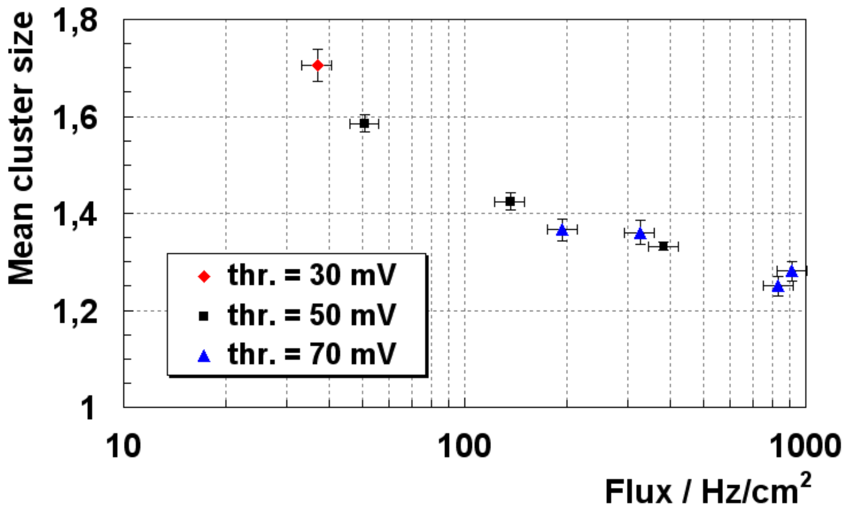

Figure 5.20: Mean cluster size as function of the incident particle flux for 30 mV, 50 mV and 70 mV preamplifier thresholds. The applied high voltage was set to ±12 kV. The error of the flux is estimated to be in the order of 10 %. The vertical bars represent the statistical error evaluated by averaging the mean cluster size obtained at both ends of the readout strips. For more information see text.

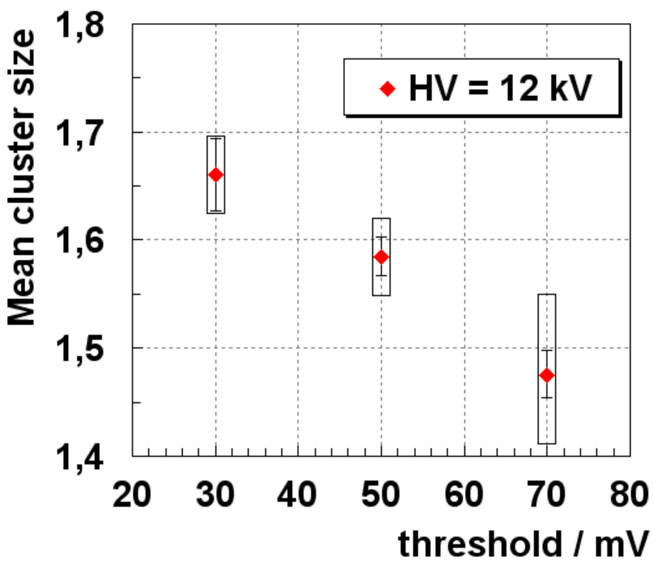

Figure 5.21: Mean cluster size as function of the applied preamplifier threshold. The vertical bars represent the statistical errors. The rectangles represent the systematic error taking also the uncertainty of the extrapolated data points into account. The width of the rectangle indicates the uncertainty of the threshold setting. For more information see text.

was set to 30 mV. The incident particle flux varied only from 19 Hz/cm^2 to 50 Hz/cm^2. The vertical bars represent the statistical errors, the rectangle the systematic errors. The systematical errors take into account the variation of the particle flux by estimating the error from the plot in Fig. 5.20. Although the errors are quite big a systematic rise in the mean cluster size as function of HV is observed. Whether the rise is linear with HV or of a higher order can not be determined yet. From this plot the conclusion regarding the occupancy is to operate the RPC on an HV level where the counter just enters the efficiency plateau.

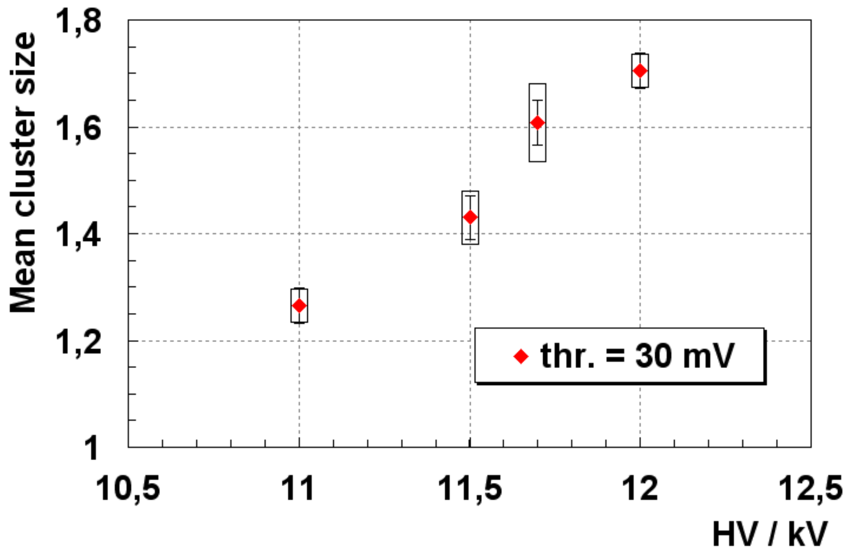

Figure 5.22: Mean cluster size as function of the applied high voltage. The preamplifier threshold in these measurements is set to 30 mV. The incident particle flux varied from 19 Hz/cm^2 to 50 Hz/cm^2 indicated by systematic errors. The statistical errors are represented by the vertical bars.

5.4 RPC-P2 - A full size demonstrator for the intermediate rate region

In the previous section it was demonstrated that the performance of the newly designed prototype (RPC-P1) fulfills the CBM ToF requirements up to an incident particle flux of 100 Hz/cm^2. However, this prototype consists of components which could still be improved. One Example is the HV electrode. At the prototype RPC-P1 the HV was applied by a copper strip which was glued by a conductive glue to the coated surface of the HV-electrode (cf. subsection 5.3.1). It turned out that this glue subjects aging effects. This glue losses its conductivity within half a year. A further weak point of RPC-P1 was the signal connection between the counter and the preamplifier.
In this section we will describe the layout of a subsequently developed prototype (RPC-P2) which fulfills the requirements of a full size demonstrator for the intermediate rate region of the CBM ToF wall. Experimental setups and results of in-beam tests are presented as well.

5.4.1 Construction principle

In order to approach a real size demonstrator for the low rate region a fully symmetric MRPC prototype with an active area of 32 $\times$ 27 cm^2 was developed [195]. Consequently, the number of strips was increased to 32. The inner structure of the counter (gap size, number of gaps, strip width, glass thickness and glass type) is identical to prototype RPC-P1. Modifications were done to the signal pickup electrodes, to the high voltage electrode and in particular to the signal transmission between strip and FEE. The pickup electrode is made of a 1.6 mm thick PCB containing strips of 27 cm length. Transmission lines with 50 Ω impedance with respect to ground starting from both ends of the strips guide the signals to the connectors (see Fig. 5.23). At the end of the transmission lines 200 kΩ resistors connected to ground prevent the pickup electrode to charge up i.e. every strip has a 100 kΩ connection to ground. The connector consists of 17 L-shaped pins where the even pins have contact to the transmission lines and the odd pins are connected to ground. Therefore, the cross talk is minimized. Alternatively, it is possible to connect either a twisted pair cable of 100 Ω impedance or the preamplifier card directly to the pickup electrode. The design of the high voltage electrode was changed completely (cf. Fig. 5.23). The Lycron® layer is now coated on the Kapton® foil facing the glass. The coating is done by spraying the Lycron® through a mask onto the Kapton® surface allowing for all possible geometrical shapes. On the side of the electrode a strip is coated where the HV is applied. This strip is bent to the backside of the counter and fixed with screws. A spring on which the HV cable is soldered presses on the coated surface. A photograph of the described electrodes is depicted in Fig. 5.23. On top, the HV electrode is visible and underneath the pickup electrode. In order to improve the mechanical stiffness two 6 mm

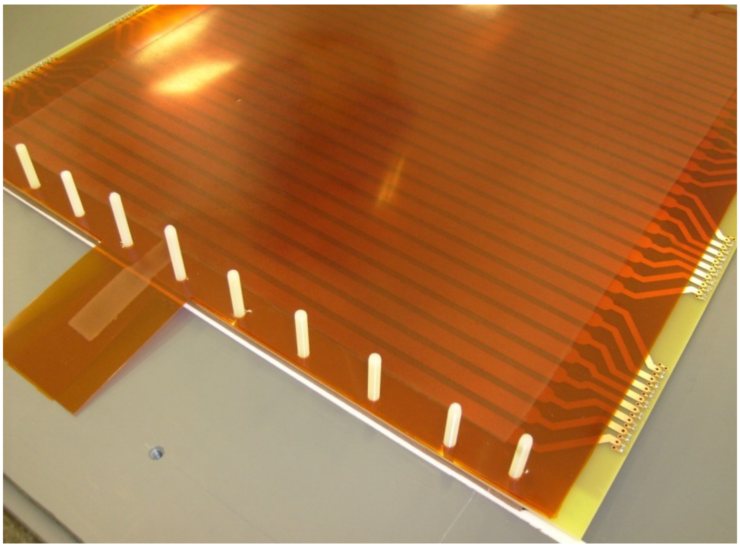

Figure 5.23: Photograph of the coated HV electrode. The pickup electrode is visible underneath the HV electrode.

thick honeycomb structured plates are placed on top of the pickup PCBs. All pieces of the RPC, beside the pickup electrode, were manufactured in the institute. The RPC was built in the clean room of GSI.

A photograph of the counter embedded in the gas tight aluminum box as it was used for in-beam tests is shown in Fig. 5.24. One preamplifier board on each side was connected directly to the pickup electrode (8 readout strips). The threshold of the preamplifier

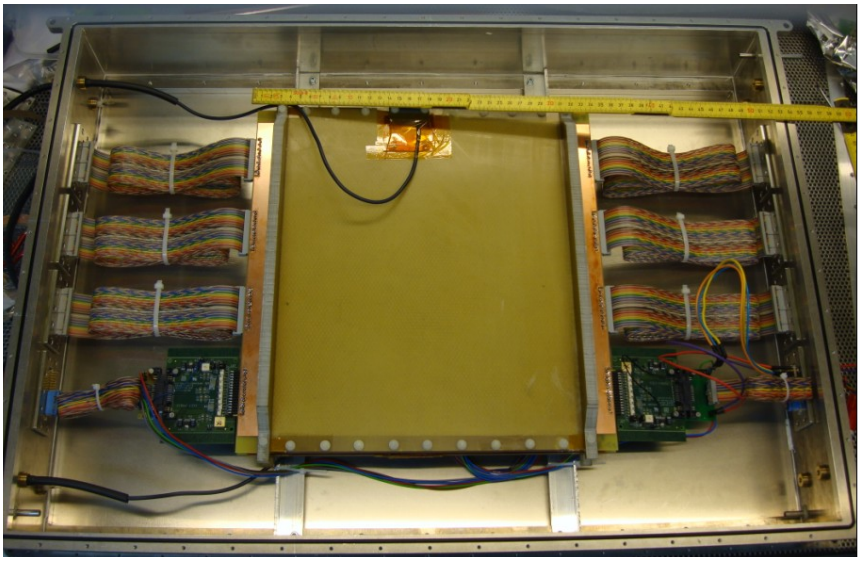

Figure 5.24: Photograph of the MRPC embedded in the gas tight aluminum box. The MRPC has connectors on the pickup electrode which allow to connect either a twisted pair cable or the preamplifier card.

was set from outside via Inter-Integrated Circuit interface (I^2C-interface). The threshold setting is common for all channels of the board. The variation is ± 1 mV. The signals from the remaining strips were routed outside the box via 100 Ω impedance matched twisted pair cables. Measurements with a time domain reflectometer (see Fig. 5.25) on strips connected via cables showed that the slightly changed geometry of the counter increased the impedance from 80 Ω to 93 Ω. In addition the spikes in the impedance (cf. Fig. 5.7) created by the soldering vanished mostly. Impedance peaks of 120 Ω are observed only

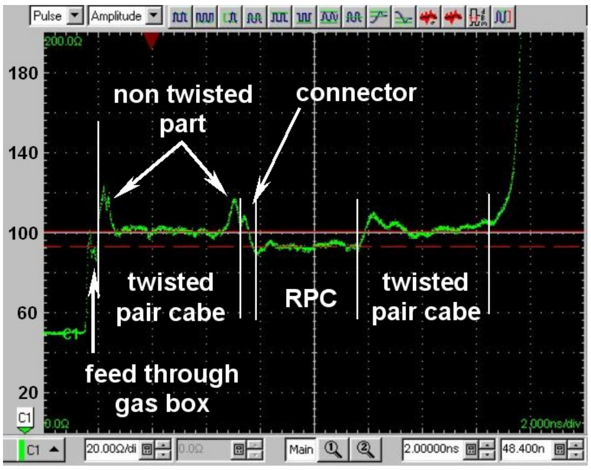

Figure 5.25: Impedance measurements with a time domain reflectometer. The impedance of the counter is 93 Ω. For more information see text.

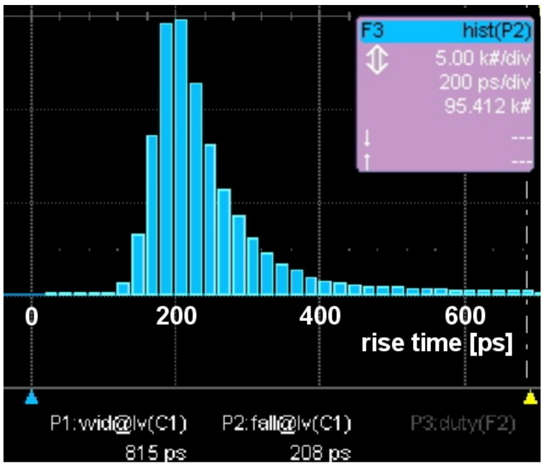

Figure 5.26: Signal rise time measurements with the oscilloscope. The distribution shows a maximum at about 200 ps.

at the non-twisted part of the cables. Measurements of the distribution of the signal rise time are shown in Fig. 5.26. The rise time of the signal is defined as the time which the signal needs to rise from 10 % to 90 % of its total hight. The maximum of the distribution is at 200 ps. The prototype RPC-P2 fulfills the geometrical requirements for a full-size demonstrator for the intermediate rate region. After performing two in-beam tests the normal float glass was replaced by a special low resistive glass in order to improve the rate capability. More information about this special glass produced in China can be found in [196]. Figure 5.27 depicts the opened counter during the assembling of the low resistive glass. Based on results obtained during the in-beam tests (see subsection 5.4.3) it was

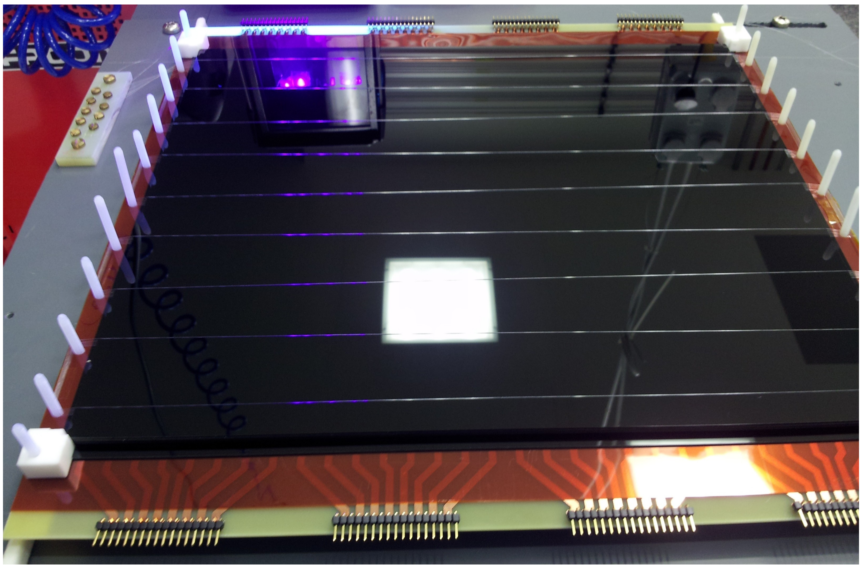

Figure 5.27: Photograph of the MRPC during the assembling of the low resistive glass. The vertical lines across the glass are the fishing line keeping the gap size of 220 μm fixed.

decided to implement the preamplifier cards inside the box connecting them directly to the readout electrode of the RPC. The preamplifier cards carrying the PADI VII discriminator are connected to a common base board. The base board distributes the power to the preamplifier cards and collects the signals. Additionally, it transmits the threshold settings via Serial Peripheral Interface (SPI). The RPC together with the FEE mounted in the box is depicted in Fig. 5.28. The counter as it is shown in Fig. 5.28 can be considered as a full-size prototype for the intermediate rate region.

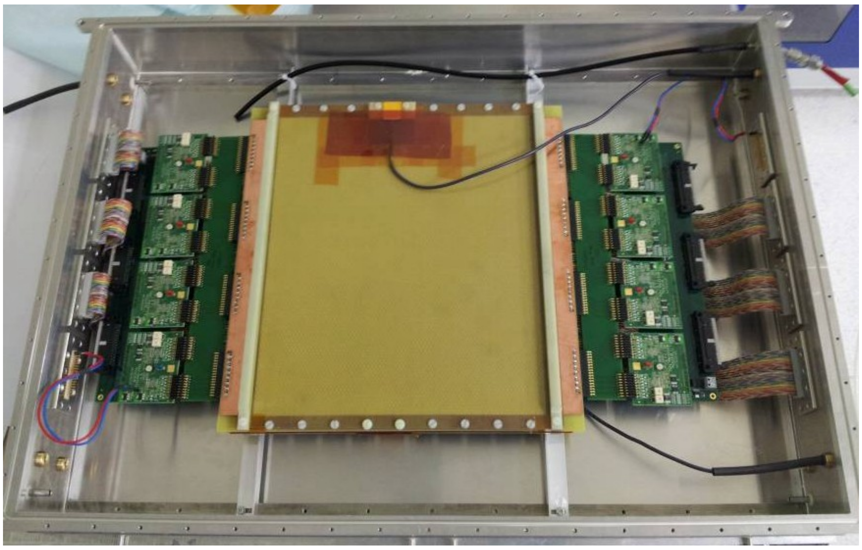

Figure 5.28: Photograph of the RPC-P2 prototype embedded in the gas tight aluminum box. The active area is 32 × 27 cm^2.

5.4.2 Experimental setup

With the prototype RPC-P2 three in beam test were performed, two before replacing the float glass by low resistive glass and one after.
The first in-beam test was carried out in June 2011 at SIS 18. Since this beam time was an experimental production run with pions at momenta of 1.7 GeV/c for FOPI the rate was small (few kHz) but stable over the whole beam time. The beam spot had a diameter of about 8 cm. In the setup a flux of about 50 Hz/cm^2 was measured. The structure of the setup was similar to the one used at COSY in November 2010 (see Fig. 5.10). This time, the RPC from Bucharest was used as a reference counter being positioned behind the Heidelberg RPC. The reference RPC is a high granular strip-MRPC with a strip pitch of 2.54 mm [197; 198]. Therefore, it was possible to investigate edge effects on our prototype. The trigger was formed by two plastic scintillators of the size 4 cm × 2 cm × 1 cm creating a trigger area of 8 cm^2. They were located in front of and behind the RPCs selecting particles which went through both counters. The electronic chain is presented in the appendix. The second beam test was performed in November 2011 at COSY with protons of momenta of 3.35 GeV/c. The goal of this test was to measure the performance of the RPC at different gas temperatures and at different rates. In order to warm up the gas the back plane of the gas box could be flushed by heated water. Inside the box the RPC was surrounded by 18 PT100 temperature sensors. Therefore, a full temperature control was guaranteed. Figure 5.29 shows the experimental setup used at COSY. The trigger was formed by the coincidence between the OR of the two front plastic scintillators and the plastic scintillator in the back of the setup. For the analysis a software coincidence of all 6 PMTs was requested. Because of a better performance the two front scintillators were used as reference for timing measurements [195]. Additional information about the

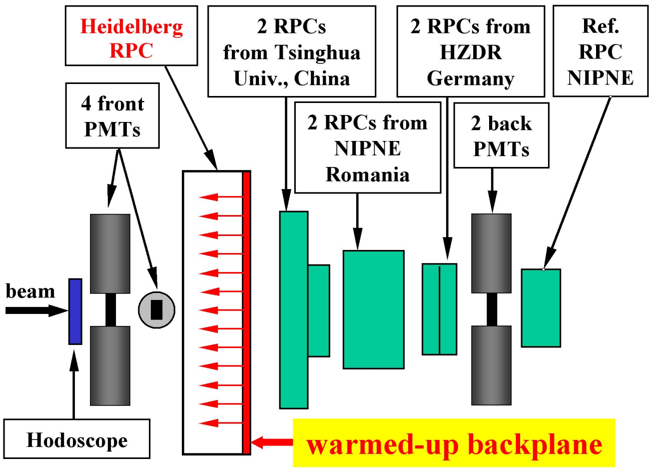

Figure 5.29: Experimental setup used at COSY in November 2011. The hodoscope deliver an information about the beam profile. The backplane of the Heidelberg RPC box was heatable [195].

beam position and profile was delivered by a hodoscope mounted in front of the scintillator. The granularity of this device i.e. the width of the scintillator fibers is 1 mm in horizontal and in vertical position.
After the upgrade with the low resistive glass the counter was tested in October 2012 at SIS 18. The goal was to perform an in-beam test at high rates with a fully illuminated counter simulating the conditions at CBM. This was possible due to a high intensity ^{56}Ni beam with momenta of 1.9 GeV/c bombarding a lead target and creating a spray of secondary particles. The setup consisted of a diamond start counter, two plastic scintillators, the RPC-P2 and the highly granular RPC from Bucharest described above. The Bucharest counter was used as the time reference. During this test many trigger conditions were used in parallel. One trigger was generated when the RPC-P2 delivered a signal on any strip, a second trigger was generated when the reference counter fired in coincidence with the start counter, a third trigger signal was created when the signal of the plastic scintillators coincided with the reference counter. The analysis of the data obtained in this beam time is still in progress. The main task is the development of new software regarding data calibration, cluster formation and time of flight calculation which can be generalized for the whole Time-of-Flight wall.

5.4.3 Test results

In this subsection the results obtained during the in-beam tests described in the previous subsection are presented. The measured quantities are the dark rate, the efficiency, the time resolution and the cluster size as function of the applied high voltage on the RPC, as function of the threshold settings in the preamplifier and as function of the incident particle flux in combination with the gas temperature. In particular, the difference between the results obtained with the preamplifier mounted inside and outside the box are discussed in detail.
In order to estimate the incident particle flux during the in-beam test at COSY the beam profile was measured with the hodoscope (see Fig. 5.30). The beam had an oval 2-dimensional Gaussian shape with the RMS values of RMS_x = 2.60 mm in x-direction

and $RMS_y = 5.87$ mm in y-direction. From these RMS values a beam cross section of about 0.4 cm^2 was calculated (indicated by the black ellipse in Fig. 5.30). The beam hit mainly one strip generating a so-called spot response. The incident particle rate was estimated using the scalers of the vertically positioned PMTs averaged over 200 triggers. The flux is calculated by the ratio of particle rate and beam cross section. Since the beam profile is not uniform over the full surface the calculated flux is rather an average.
The temperature was obtained by taking the mean of all 18 sensors. The RMS of the temperature values at 27 °C (room temperature) was 0.1 °C. The RMS is linearly increasing to 3 °C at 48 °C which is caused by a temperature gradient in vertical direction due to convection. However, the readout strips are positioned in horizontal direction and therefore operated at a constant temperature environment with an RMS of about 0.6 °C (evaluated with 6 sensors) [195].

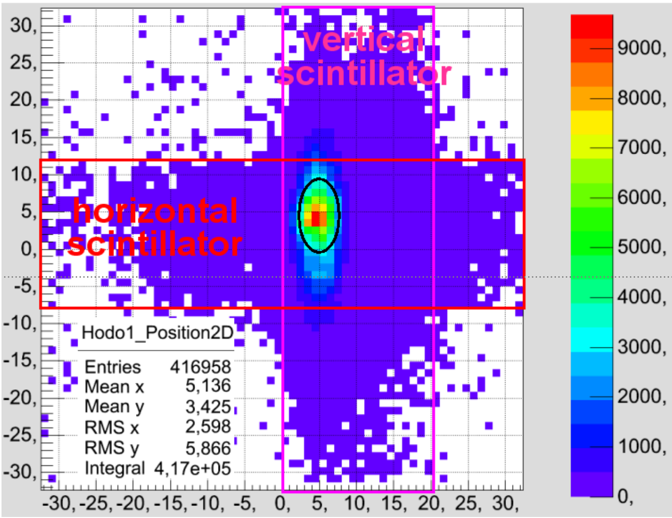

Figure 5.30: Beam profile measured by the hodoscope. The black ellipse indicates the RMS values of the Gaussian like beam profile. The area of the ellipse was used to calculate the incident particle flux.

Dark rate

The dark rate is the number of counts per second delivered by the RPC without a source normalized to a counter surface of 1 cm^2. The main contribution to the dark rate for a normally working RPC are the cosmic particles. However, impurities of the glass plates or dust particles in the gas gaps can increase the dark rate substantially. Therefore, a dark rate of a few Hz/cm^2 is desirable. Figure 5.31 depicts the dark rate as function of the applied high voltage of the prototype RPC-P2. Every data point was measured 10 times and averaged. The errors are calculated by the standard deviation of the mean value. At nominal working voltage ($\pm$11.3 kV) a dark rate of (0.72 $\pm$ 0.08) Hz/cm^2 was measured leading to a rate of 622 Hz for the full counter.

Efficiency

The efficiency and its statistical error are calculated according to (5.1) and (5.3) q. respectively. As reference, the coincidence of the plastic scintillators forming the trigger was

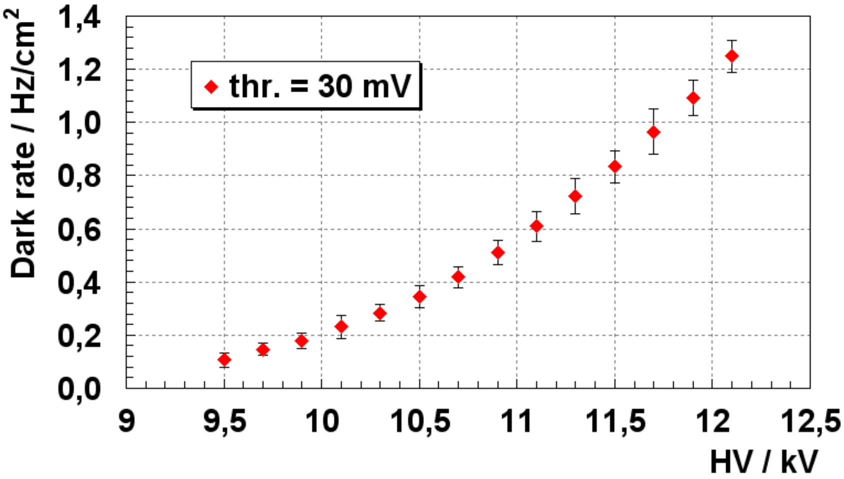

Figure 5.31: Dark rate as function of the applied high voltage. The preamplifier threshold in these measurements was set to 30 mV. The statistical errors are represented by the vertical bars. For more information see text.

used. The efficiency as function of the applied high voltage is shown in Fig. 5.32. The red data points (diamonds) represent the efficiency achieved with the preamplifier card connected directly to the readout electrode. The threshold was set remotely to 27 mV. The black data points (squares) represent the efficiency having the preamplifiers mounted outside the box. For these preamplifiers a threshold of 30 mV was used. The statistical and systematic errors are not visible since they are smaller than the symbols representing the data. Systematic errors are estimated to be about 1 %. The black data points can be compared to the results obtained for the prototype RPC-P1 described in section 5.3 (cf. Fig. 5.11 red diamonds). RPC-P2 reaches the 90 % level already at 10.8 kV in comparison to RPC-P1 where the 90 % level was reached at 11.2 kV. This can be explained by the improved signal transmission. An efficiency of 95 % was reached at 11.3 kV being the nominal working voltage. Efficiency measurements done with the electronics mounted inside show slightly better results even if one scales them to the same threshold. A threshold scan for the preamplifiers mounted inside is depicted in Fig. 5.33 (red symbols). The two black data points stem from the preamplifiers located outside. The preamplifiers mounted inside were much more stable in terms of pick-up noise from the environment. Therefore, it was possible to lower the threshold by almost 10 mV which is actually the bigger advantage. At a threshold of 23 mV an efficiency above 97 % was achieved. The applied high voltage during the threshold scan was 11.3 kV. These results triggered the decision to mount the front end electronics as close as possible to the readout electrode of the RPC.
Figure 5.34 illustrates the efficiency as function of the flux measured at four different gas temperatures (high voltage HV = 11.5 kV, preamplifier threshold Thr. = 30 mV). The statistical error is below 10^{-6}. The systematic error is due to the temperature uncertainty 0.3 % at 27°. It rises linearly to 1.7 % at 48°. At 27 °C the efficiency starts to decrease already at 1 kHz/cm^2 . At 2 kHz/cm^2, which can occur in the very innermost part of the

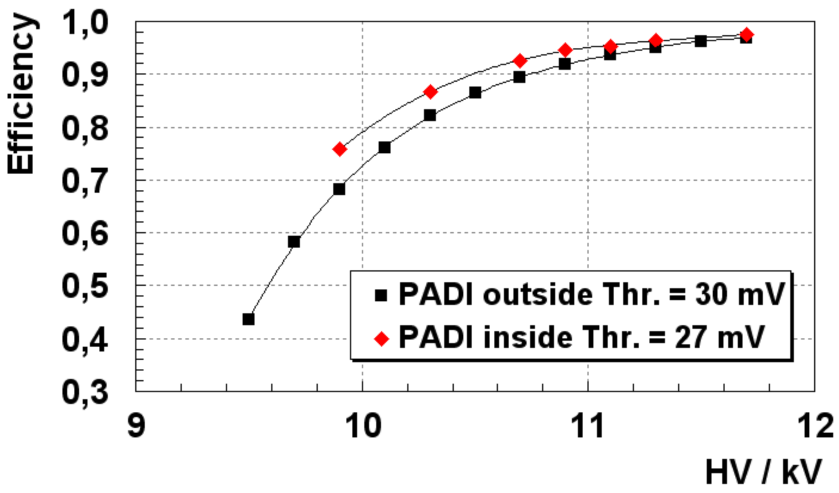

Figure 5.32: Efficiency of the RPC as function of the applied high voltage. The red (black) data points represent the efficiency obtained with the preamplifier mounted inside (outside) the box. The errors are smaller than the data symbols and therefore not visible. For more information see text.

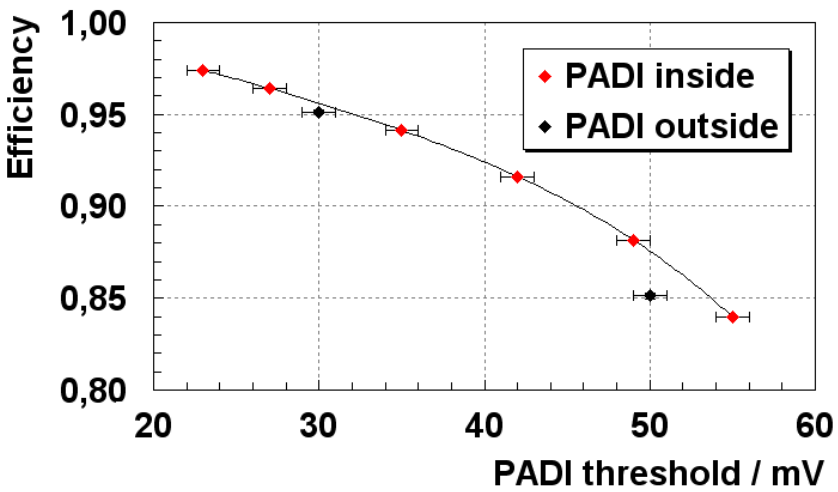

Figure 5.33: Efficiency as function of the preamplifier threshold.

low rate region, an efficiency of 85% is observed. Warming up the gas by 15 degrees seems to be sufficient to obtain a fully efficient counter. By warming up to 50 °C an efficiency of 90% is achievable for a particle flux of 15 kHz/cm^2. This result agrees with the well known fact that a temperature increase of 25 °C improves the rate capability by one order of magnitude (see section 2.7 or [87; 93; 195]).

Using the narrow strip prototype from Bucharest as reference (see subsection 5.4.2) edge effects can be investigated. Especially the efficiency on the border of the electric field region i.e. on the edge of the HV-electrodes is worthwhile to explore. The exact position

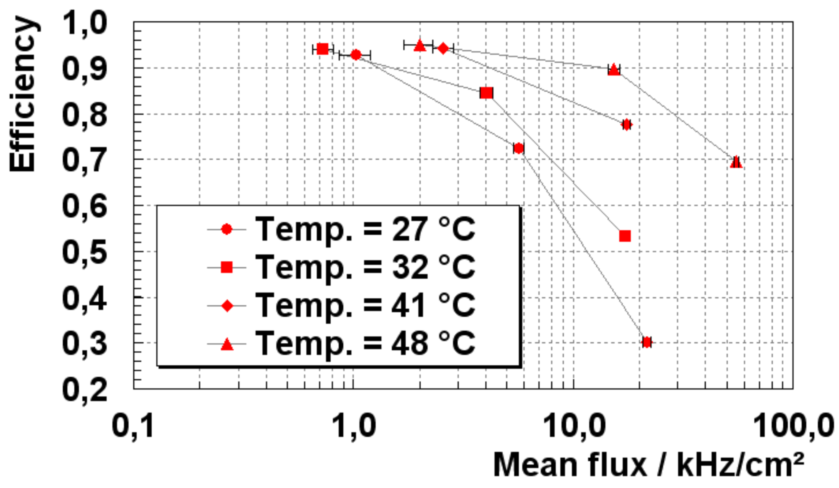

Figure 5.34: Efficiency as function of the incident particle flux measured at four different gas temperatures. The errors of the efficiency are not visible since they are smaller than the symbols.

of the reference counter with respect to the Heidelberg RPC is depicted in Fig. 5.35. The parts are drawn to scale to each other. The active area of the reference counter covered the end of the strips and beyond. The trigger area fully covered the active area of the reference counter. The efficiency was calculated by comparing the number of hits in every reference counter strip with the number of hits in the Heidelberg RPC. The result is shown in Fig. 5.36. The efficiency on top of the HV electrode is about 95 % indicated by the dashed arrow. 2 mm from where the HV electrodes end the efficiency starts to diminish. Within 5 mm corresponding to 2 strips of the reference counter the efficiency drops from 90 to 10 %.

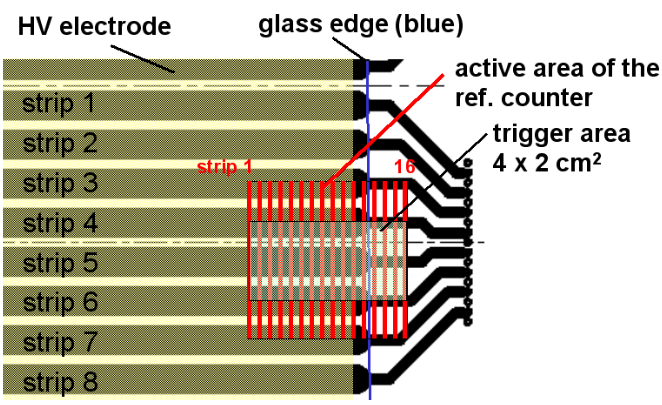

Figure 5.35: Pictorial view of the detector alignment used to study age effects. The active area of the reference counter covered the end of the strips and beyond. The trigger area fully covered the active area of the reference counter.

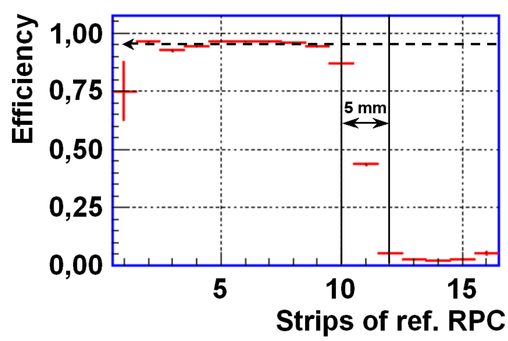

Figure 5.36: Efficiency of the test counter at the strip end. For more information see text.

Time resolution

First time resolution measurements of RPC-P2 were performed at SIS 18 at low particle fluxes (≈ 50 Hz/cm^2). At these particle fluxes a system time resolution of (72.3 ± 1.2) ps was measured taking only one strip of the reference RPC [197] and only one strip of the test RPC into account. Both detectors worked at their nominal voltage i.e. for the Heidelberg RPC HV $= \pm$ 10.3 kV. The preamplifiers used for these measurements were placed outside the box and the threshold was set to 30 mV. It was assumed that both detectors have the same resolution leading to a counter time resolution of (51.2 ± 0.9) ps. The time difference between the reference counter and the test MMRPC was calculated by:

$$dt = \frac{t_{HD,l} + t_{HD,r}}{2} - \frac{t_{ref,l} + t_{ref,r}}{2} \tag{5.20}$$

with $t_{HD,l}$ and $t_{HD,r}$ the time of the left and the right side of one Heidelberg RPC strip and $t_{ref,l}$ and $t_{ref,r}$ the time of the left and the right side of one reference RPC strip.
All times were corrected for walk and TDC nonlinearities. The time distribution dt is depicted in Fig. 5.37. The result obtained in this test beam time can be compared to

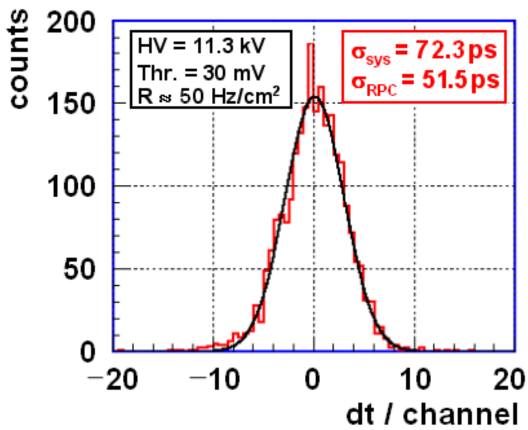

Figure 5.37: Time distribution between reference RPC and Heidelberg RPC. The system time resolution σ_{sys} is 72.3 ps. Assuming both detectors have the same time resolution the system time resolution can be divided by $\sqrt{2}$ leading to a counter time resolution σ_{RPC} of about 51.2 ps.

the results of RPC-P1. From Fig. 5.17 it is possible to get by interpolation the value of the time resolution for HV = 11.3 kV and at a threshold of 30 mV. It is about (63 ± 2) ps i.e. about 12 ps worse than the measured value of prototype RPC-P2. One difference is the used reference system. Before the plastic scintillators were used as reference and now an RPC. But this should not affect the results. RPC-P2 is more advanced in terms of impedance matching and signal transmission to the preamplifier. The noise level is a bit lower too. Unfortunately, no data regarding the time resolution with the preamplifier mounted directly onto the readout electrode were analyzed so far.
Figure 5.38 illustrates the RPC time resolution as function of the incident proton flux for different temperatures measured at COSY. The RPC time resolution and its statistical error are calculated according to Eq. 5.13 and 5.15, respectively. The systematic error is calculated from the uncertainty of the temperature. All timing signals involved are corrected for walk and for integral non-linearities of the TDC with the bin-by-bin method explained in section 3.3. The time resolution deteriorates as already indicated in the

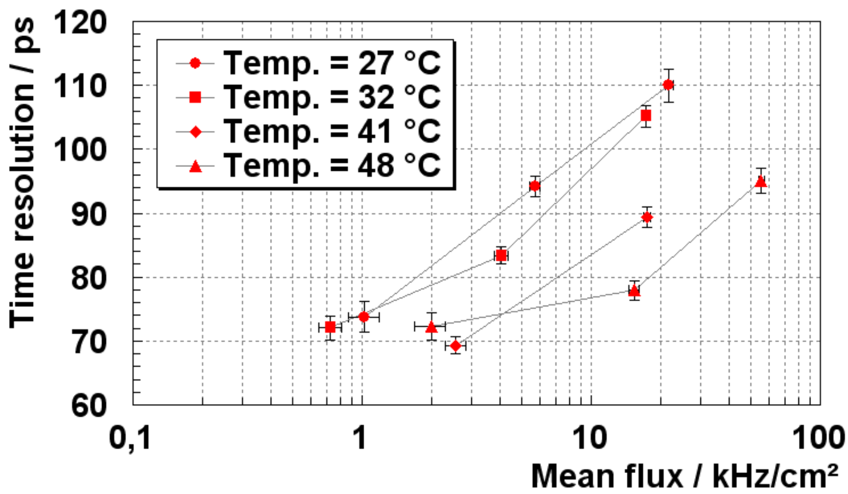

Figure 5.38: RPC time resolution as function of the incident particle flux measured for the gas temperatures ϑ = 27 °C (dots), 32 °C (squares), 41 °C (diamonds), 48 °C (triangles). The vertical error bars represent the sum of the statistical and the systematic error. The applied high voltage was set to $\pm$ 11.3 kV and the preamplifier threshold to 30 mV.

previous section with the flux in a logarithmic way but can be improved drastically by warming. This can be seen best from the data points between 15 kHz/cm^2 and 20 kHz/cm^2 (see also Fig. 5.39). This observation is supported by the so-called DC model for RPC signal generation where under the assumption specified in [86], the following expression for the time resolution σ_T can be obtained for moderate particle fluxes [91]: $\sigma_T = \sigma_o + K_T \bar{q} \phi \rho d$ (see section 2.7) A higher temperature leads to a lower glass resistivity [87] and therefore to a better time resolution. However, a time resolution better than 70 ps using the plastic scintillators as reference was not observed with any of the tested prototypes. On the other hand the lowest incident particle flux at room temperature was already above 700 kHz/cm^2. At the highest temperature the measurements start at 2.5 kHz/cm^2.
Figure 5.39 illustrates in a combined plot the efficiency and the RPC time resolution as function of the gas temperature. The data points in this plot were obtained at incident particle fluxes between 15 Hz/cm^2 and 22 Hz/cm^2. The systematic errors of efficiency and time resolution take the range of the incident particle fluxes into account. The vertical error bars represent the sum of the statistical and the systematic errors. Both the efficiency and the time resolution improve almost linearly with temperature. However, technically it is neither simple nor practicable to warm up 70 m^2 of the CBM ToF wall to 50 °C and to keep the temperature uniform and stable. In that sense warming can be an option for the low rate region where the flux does not exceed 2 kHz/cm^2.

Mean cluster size

In contrast to subsection 5.3.3 the mean cluster size is not calculated for both sides of a strip individually and averaged afterwards. Here, the calculation is done by taking only

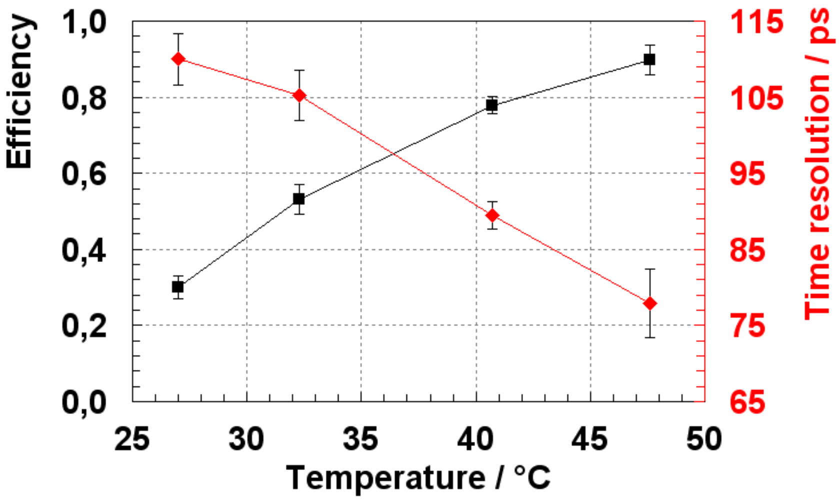

Figure 5.39: Efficiency and RPC time resolution as function of the gas temperature. The vertical error bars represent the statistical and the systematic errors. The applied high voltage was set to ±11.3 kV and the preamplifier threshold to 30 mV. The incident particle flux is between 15 Hz/cm^2 and 22 Hz/cm^2

strips into account which had a signal on both sides.

The same criteria will be applied later on when several strips form a cluster

Signals which are very small and do not pass both preamplifier thresholds because they are slightly different are ignored. The mean cluster size as function of the applied high voltage is shown in Fig. 5.40 for the preamplifier mounted outside the box (black squares) and for the preamplifier connected directly to the read out electrode (red diamonds). The incident particle flux is homogeneous and about 50 Hz/cm^2 for both data sets. The rise of the mean cluster size as function of the applied voltage is very similar for both preamplifier locations. However, the data sample with the preamplifier mounted inside the box is offset about 0.1. At the nominal working voltage (HV = ±11.3 kV), for example, the mean cluster size measured with the preamplifier outside the box is about 1.28 and for the preamplifier inside the box about 1.38. The effect caused by the different threshold settings is only about 40 % of the discrepancy. The main contribution (60 %) comes from the fact that the signal discriminated inside the box does not suffer from losses in the cable and on the connectors. This effect can be seen better in Fig. 5.41 where the mean cluster size is plotted as function of different threshold settings for the preamplifier mounted inside and outside the box. The trend line in Fig. 5.41 follows the function $f(x) = ax^b$. A lower threshold, which is favored in terms of efficiency, causes a bigger mean cluster size which can improve also the timing performance since the time of a single avalanche is measured on several strips. However, a bigger mean cluster size decreases the effective granularity of the counter.
A logarithmic behavior is observed in the mean cluster size dependence on the mean particle

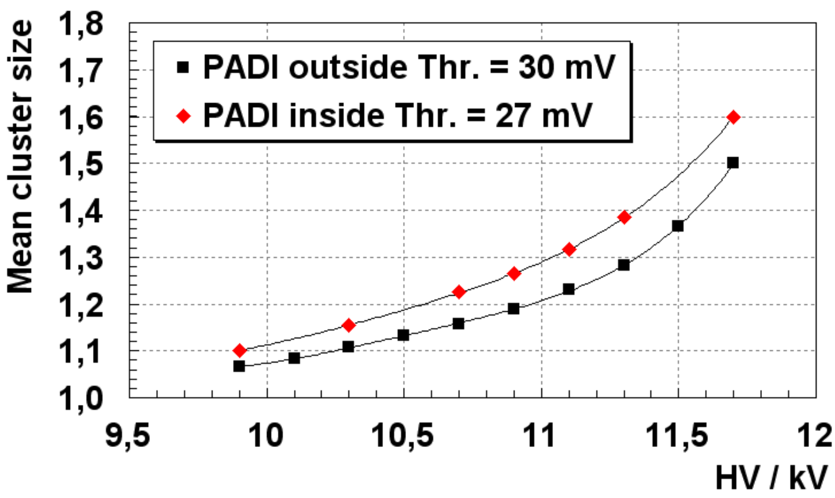

Figure 5.40: Mean cluster size as function of the applied high voltage. The red (black) data points represent the efficiency obtained with the preamplifier mounted inside (outside) the box. The errors are smaller than the data symbols and therefore not visible. For more information see text.

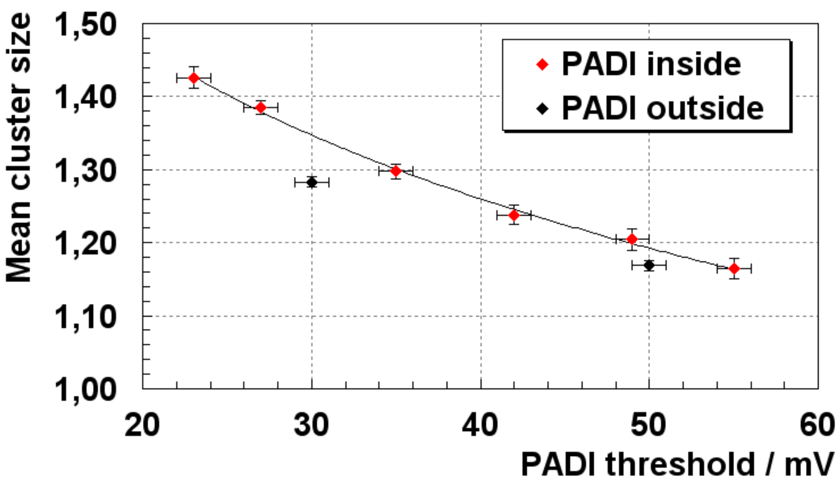

Figure 5.41: Mean cluster size as function of the preamplifier threshold measured with preamplifier connected directly to the readout electrode (red data points) and preamplifiers mounted outside the gas box. The trend line follows the function $f(x) = ax^b$.

flux shown in Fig. 5.42 for different gas temperatures. The MCS and the slope increases with rising temperature. It was shown [87] that the effective gap voltage scales linearly with temperature at constant gas pressure which leads to a higher average avalanche charge and therefore to a higher efficiency and mean cluster size. A similar result was also observed by [199]. The advantages in terms of efficiency and time resolution gained by warming are counterbalanced by the disadvantages resulting from an increased cluster size inducing not only a lower effective counter granularity (and therefore a reduced double hit capability)

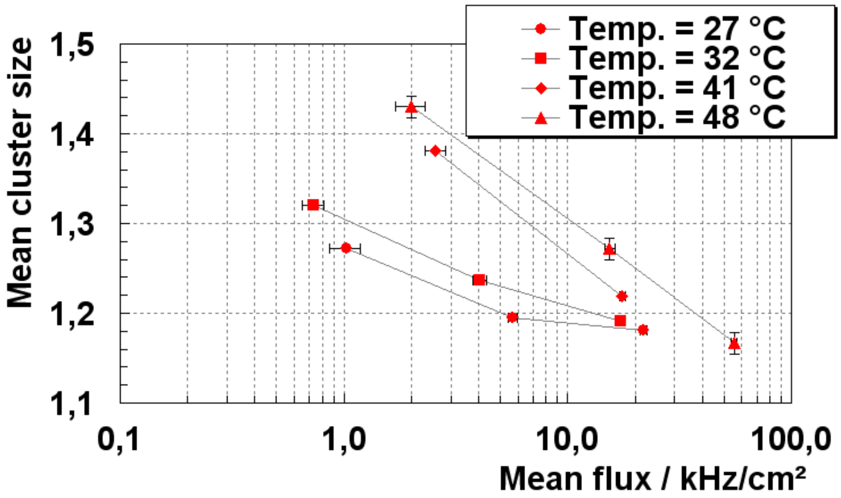

Figure 5.42: Mean cluster size as function of the incident particle flux for the gas temperatures ϑ = 27 °C (dots), 32 °C (squares), 41 °C (diamonds), 48 °C (triangles). The vertical error bars represent the sum of the statistical and the systematic error. The applied high voltage was set to ±11.3 kV and the preamplifier threshold to 30 mV.

but also a higher data rate [195].

5.5 RPC-P3 - A full size demonstrator for the low rate region

In the previous section the design of an MRPC prototype equipped with normal float glass was presented. The results obtained in the test beam times encouraged the decision to construct a full-size demonstrator for the low rate region. The low rate region has to cope with incident particle fluxes below 1 kHz/cm^2 hence normal float glass, which is about 100 times cheaper than semi-conductive glass, should be sufficient.

5.5.1 Construction principle

For the low rate region a full-size demonstrator (RPC-P3) with an active area of 53 cm × 52 cm was developed. The design of the MRPC did not change with respect to PRC-P2 described in section 5.4. Changes occur only due to the bigger size. The number of readout strips increased to 56 in order to maintain a multiple of 8 preamplifier channels. Therefore, the strip width changed to 7.6 mm and the gap between the strips to 1.8 mm. The impedance of this prototype was not measured. The signal pickup electrode is depicted in Fig. 5.43. On top of the signal pickup electrode the coated HV electrode is visible. Due to the large size the HV electrode has two redundant HV connectors. In a conventional

MRPC the fishing lines are placed on top of each other causing deficiencies up to 2 %. In order to diminish this deficiency the strategy how to arrange the fishing lines was changed in this prototype. The fishing lines are installed cross-wise (see Fig. 5.44) i.e. the fishing line on top of the first glass layer is arranged horizontally and on top of the second glass plate it is traced vertically. With this arrangement only the crossing points of the fishing lines contribute to the deficient area. It is assumed that the gas exchange inside the gap happens by diffusion. Therefore, the fishing line arrangement should not influence the gas quality.

The assembling of this prototype was done in the clean room at GSI. A photograph taken

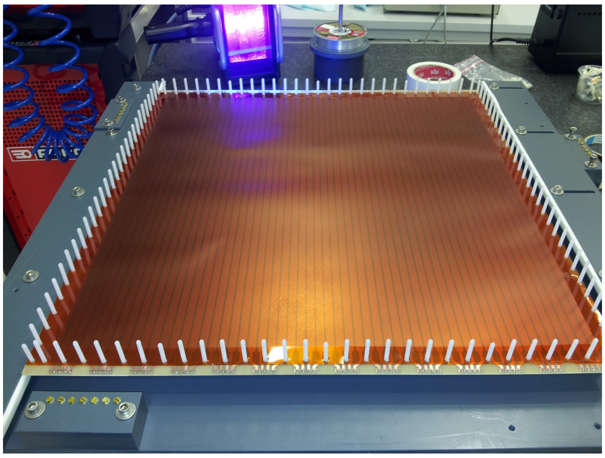

Figure 5.43: Signal pickup electrode and on top the HV electrode of the full size prototype for the low rate region.

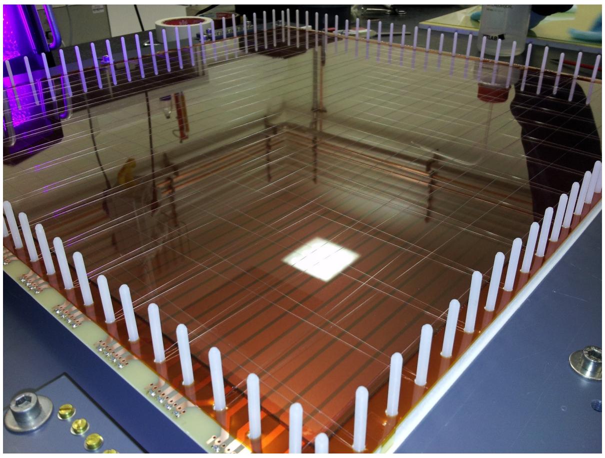

Figure 5.44: The counter during the assembling. The fishing line are installed cross-wise.

during the assembling is depicted in Fig. 5.45. In order to minimize bending and barreling honeycomb plates of 1 cm thickness were placed on top of the pickup electrodes. In addition, the whole structure was pre-stressed uniformly before screwing. After mounting the detector in the gas tight chamber the electronics are connected to the pickup electrode. Twisted pair cables of 100 Ω impedance transmit the discriminated signals to the feed through. A photograph of the counter mounted in the gas box is presented in Fig. 5.46.

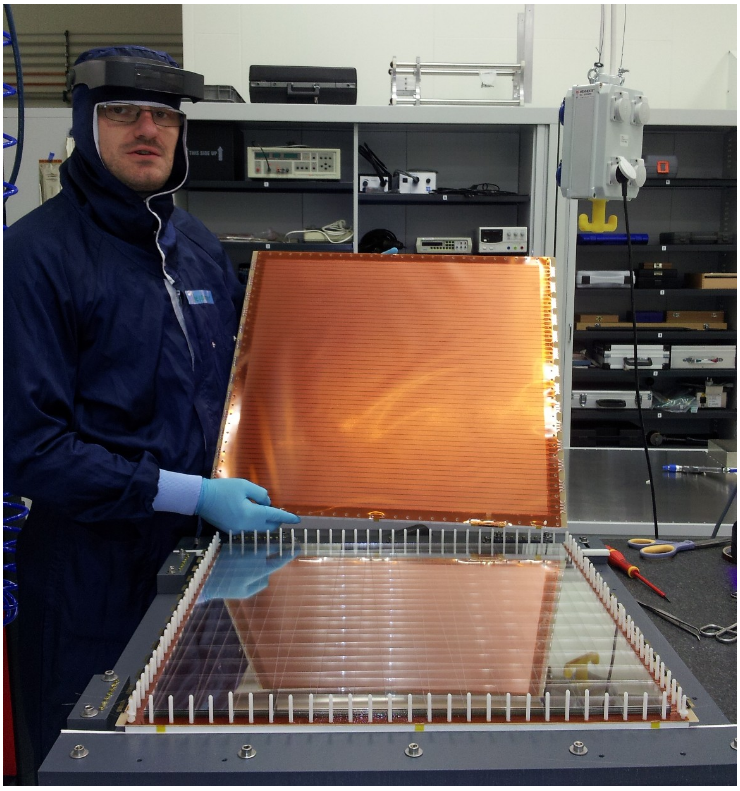

Figure 5.45: Photograph of the MRPC taken during the assembling.

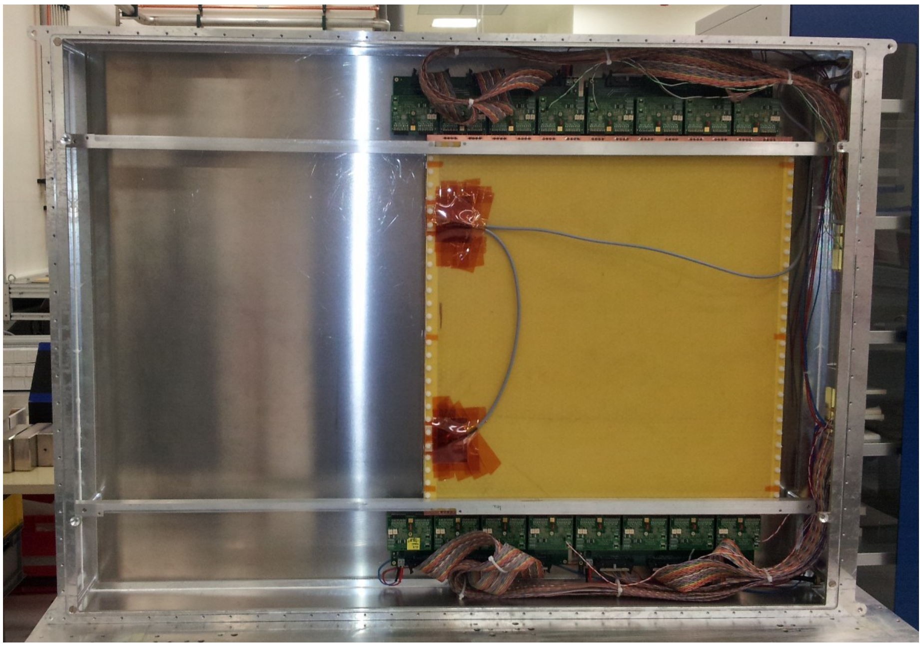

Figure 5.46: Photograph of the RPC-P3 prototype for the low rate region.

5.5.2 Results

First results with the prototype RPC-P3 were obtained with cosmic rays. The reference system consists of two plastic scintillators with the dimensions 8 $\times$ 2 $\times$ 1 cm^3 and 11 $\times$ 4 $\times$ 2 cm^3 placed on top and below the RPC chamber. Each scintillator was read out by two PMTs (Hamamatsu H 2431-50). The coincidence of all PMTs delivered the trigger signal. The time resolution of the reference system is determined as described in subsection 5.3.3. The time-of-flight distribution of the reference system is shown in Fig. 5.47. The Gaussian standard deviation of this distribution $\sigma_{t_{ToF,PMT}}$ corresponds to the time resolution of the reference system $\sigma_{\bar{t}_{PMT}}$ according Eq. (5.12). Throughout the whole analysis, a 3σ cut on the time-of-flight distribution measured by the PMTs was applied. Therefore, the range of the Gaussian fit was restricted to 3 sigma. The time resolution of the reference system is (54.8 $\pm$ 0.4) ps.

The time resolution of the RPC and its efficiency are derived from clusterized hits and thus from the full counter response with corrections for all known and measured dependencies (as described in section 3.3). The applied corrections are: timing corrections due to different signal path length, walk, integral nonlinearities of the TDC, corrections due to the incident angle of the particles, corrections due to the velocity spread of the particles. The time-of-flight distribution derived from the RPC is shown in Fig. 5.48. $\sigma_{t_{ToF}}$ is obtained by a Gaussian fit and amounts to (67.2 $\pm$ 0.5) ps. According to Eq. 5.13 and Eq. 5.15 the RPC time resolution is (39.0 $\pm$ 1.0) ps. Note that this value contains the jitter of the whole electronics chain. These measurements were performed at an applied high voltage

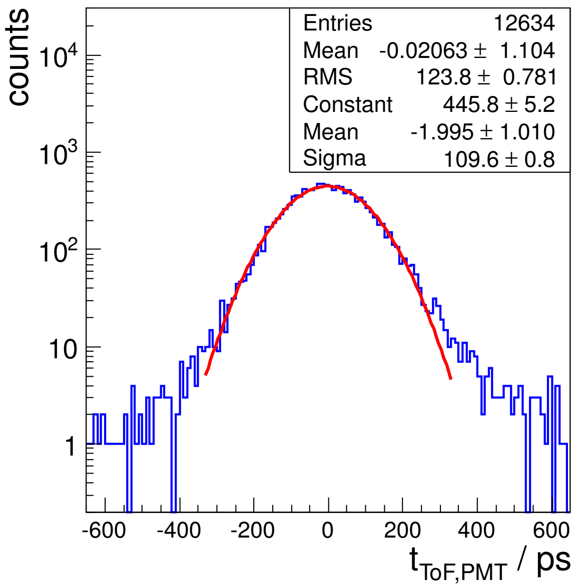

Figure 5.47: Time-of-flight distribution measured for the reference system. The Gaussian fit is represented by the red line. The range of the fit is 3 sigma. It amounts to (109.6 $\pm$ 0.8) ps.

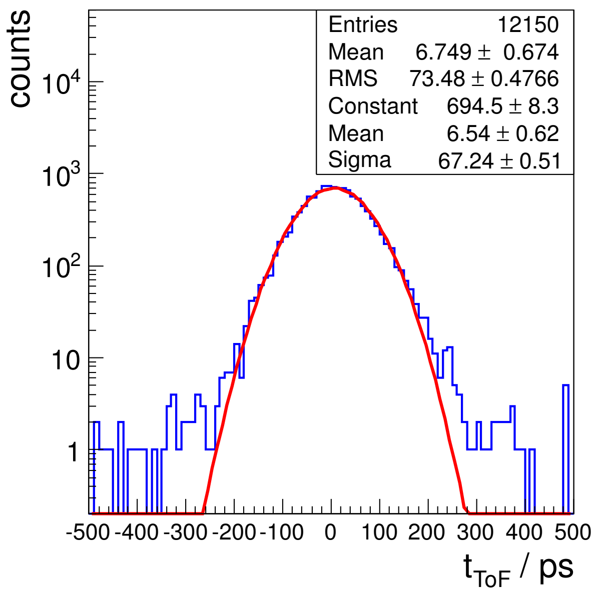

Figure 5.48: Time-of-flight distribution measured for the RPC system. The Gaussian fit is represented by the red line. Sigma amounts to (67.2 $\pm$ 0.5) ps.

of ±11 kV.
The efficiency is determined by dividing the number of clusters contributing to the time resolution (12151 events) by the number of coincidences within the 3σ cut of the reference system time-of-flight distribution (12333 events). One finds an efficiency of (98.5 ± 0.1) %. The error is calculated according to Eq 5.3 and represents the statistical error.
The distribution of the clusters on the RPC surface is shown in Fig. 5.49. The majority of

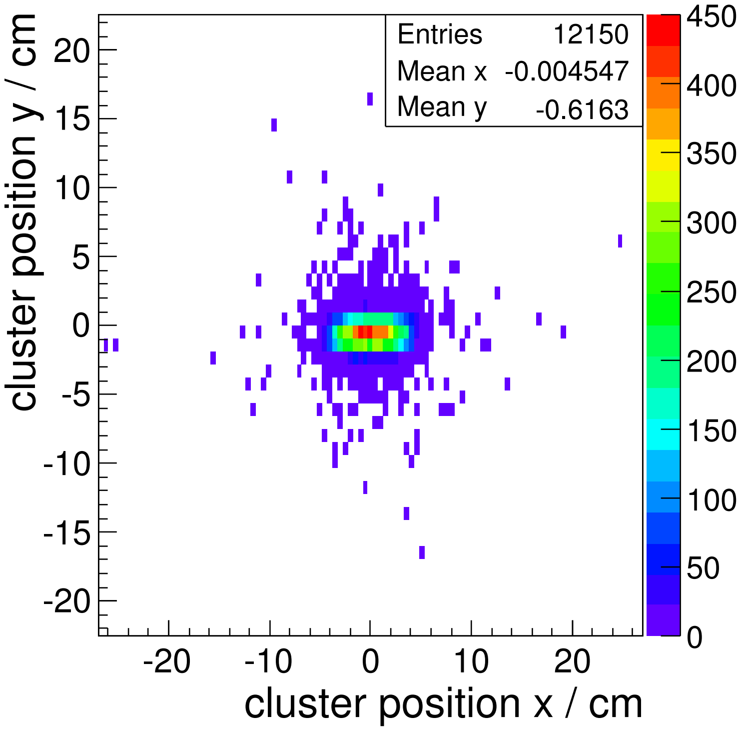

Figure 5.49: Spatial cluster distribution on the RPC surface. The plastic scintillator cover a surface of about 9.5×3 cm^2. The binning of the y-axis is given in units of the strip width.

the hits is located within the area which is covered by the plastic scintillators (on the RPC surface about 9.5×3 cm^2). The outliers accounting for of about 3 % of the hits stem from particles which are either scattered in the RPC or from a shower where the particle which triggered the system was not detected by the RPC. The mean cluster size at ±11 kV is about 1.39. The distribution of the cluster size is shown in Fig. 5.50. The cluster building algorithm does not only check if two neighboring strips have a signal. It also checks if the signals are correlated in space. The matching radius was set to 2.5 cm. The cluster multiplicity is depicted in Fig. 5.51. The mean of the cluster multiplicity distribution is about 1.26. In most cases ($>$ 90 %) only one cluster is created per event. However, a few events show cluster multiplicities of 10 or more clusters. The reason is that sometimes the system is triggered by a particle shower.
During the cosmic ray tests a second data point at ±10.2 kV was analyzed. The results

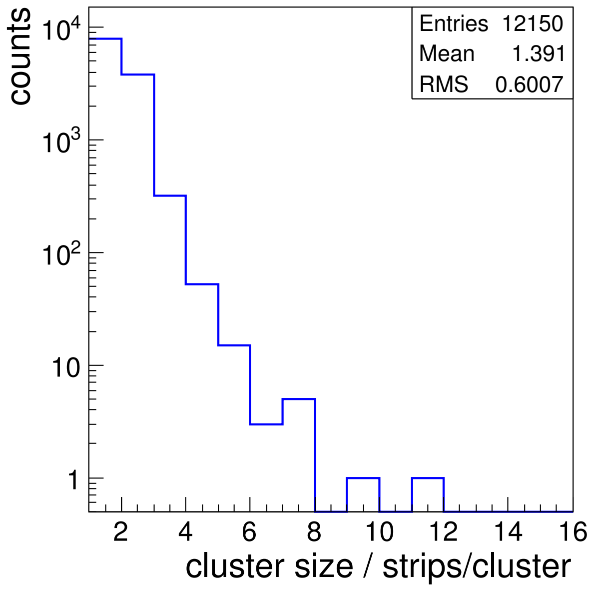

Figure 5.50: Cluster size distribution of the prototype RPC-P3. The applied high voltage is ±11.0 kV.

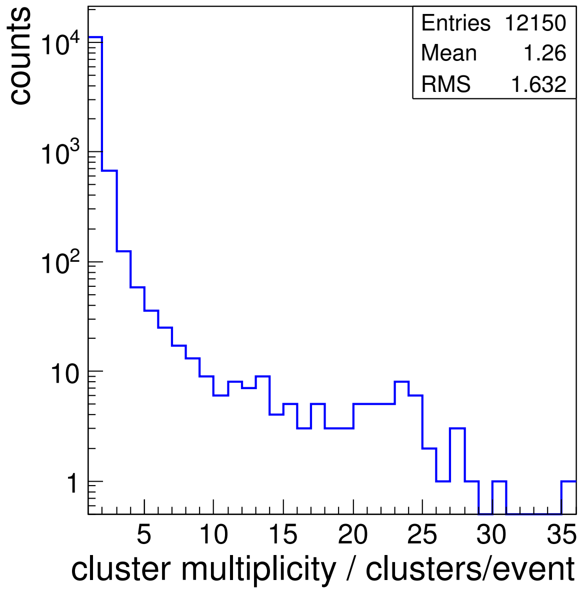

Figure 5.51: Cluster multiplicity distribution of the prototype RPC-P3. The applied high voltage is ±11.0 kV.

Applied high voltage	±10.2 kV	±11.0 kV
Efficiency	(94.4 ± 0.2) %	(98.5 ± 0.1) %
RPC time resolution	(43.5 ± 1.2) ps	(39.0 ± 1.0) ps
Mean cluster size	1.24	1.39
Mean cluster multiplicity	1.26	1.26

Table 5.1: Results obtained in the cosmic ray test for RPC-P3.

are summarized together with the data point taken at a high voltage of ±11.0 kV in Tab. 5.1

6 The outer Time-of-Flight (ToF) wall

In this chapter the CBM outer ToF-wall is presented. The development of its possible layout was part of this thesis including the design of the super module and the super module chamber.
The requirements will be briefly discussed in section 6.1. In section 6.2 the design of the super module chamber is presented, followed by the description of the super modules for the outer ToF-wall in section 6.3. The layout of the wall is described in section 6.4.

6.1 Experimental and technical requirements for the CBM ToF-wall

The experimental requirements for the ToF-wall imposed by the physics program of CBM were discussed in section 4.5. Here they will be briefly repeated. Additionally, technical requirements will be mentioned which are important for the engineering design. Of course, some of them - like the z-position of the wall - are also physically motivated e.g. by the decay length of the kaon.

- Experimental requirements for the ToF-wall:
  - system time resolution including start detector of about 80 ps
  - overall efficiency of 95 % or better
  - rate capability between 1 kHz/cm^2 and 50 kHz/cm^2
  - occupancy below 5 %
  - granularity between 4 cm^2 and 50 cm^2
- Technical requirements for the ToF wall:
  - the acceptance of the ToF-wall should be in the same order as for the other subcomponents i.e. an angular range of about 35° in x-position and of about 25° in y-position.
  - flexible and easily extendable construction, i.e. the wall should be constructed in a modular way.

- movable in z-direction from $z = 6$ m to $z = 12$ m. The final position of the ToF-wall will be at $z = 10$ m but for service reasons an adjustable range is necessary.
- with respect to the other subdetectors a planar design of the wall is favorable.
- the super module chambers should be easily and cheaply producable, mechanically stiff and simultaneously light.

The CBM Time-of-Flight wall is sub-divided in two parts: the so-called inner wall and the outer wall. The outer wall comprises the intermediate rate region with rates between 1 kHz/cm^2 and 8 kHz/cm^2 and the low rate region with rates below 1 kHz/cm^2. For both rate regions possible RPC layouts were presented in section 5.4 and section 5.5.

6.2 The super module chamber

The chamber housing the RPCs has to fulfill the following requirements. First of all, it needs to be gas-tight which is not trivial in combination with the other requirements. Requiring a maximum loss rate of 1 l gas per day and per super module the leakage rate should not extend $1.2 \cdot 10^{-3}$ Pa $\cdot$ m^3/s. In order to minimize multiple scattering and energy loss of the particles traversing the box the material budget of the box should be kept as small as possible. This implies a low-weight architecture which is also preferred in order to keep the total weight of the wall for stability reasons as small as possible. However, RPCs are composed mainly out of glass with a substantial weight. Therefore, the chamber has to be robust enough to carry the load without major deformation.
Figure 6.1 shows an explosive view of a possible design of a super module box. All pieces of the box are made of aluminum. The backbone of the box, carrying most of the load, are two rectangular frames which are mounted together via spacers in each corner forming a cuboid framework. The frames have a thickness of 8 mm. Into the inner side a groove is milled in which the side walls are glued. Additional grooves on the outer side help to close the box tightly with O-rings on the front and on the back side. Three of the side walls consist of only 1 mm thick blank aluminum sheets. This is especially important since the particles pass through this part of the super module at large angles and therefore penetrate more material. On the other hand, the walls are still strong enough to stabilize the whole construction. On the remaining side of the box a 10 mm thick plate incorporating all feed throughs is glued between the two frames. This side of the super module will be hidden behind the active zone of a SM in front (cf. section 6.4). The covers on both sides consist of 0.5 mm aluminum foil glued onto a 3 mm thick frame. In order to reduce the material budget even further the front aluminum foil can be replaced by a 75 μm thick poly-imide foil. The back side cover can be exchanged - if necessary - with a water-heated version. The flange-type feed throughs for control signals and detector output signals are realized by two multilayer PCBs with connectors soldered on both sides. Aluminum frames press the PCBs onto the surface of the 10 mm thick plate with an O-ring underneath. The total weight of the empty chamber is about 15 kg.

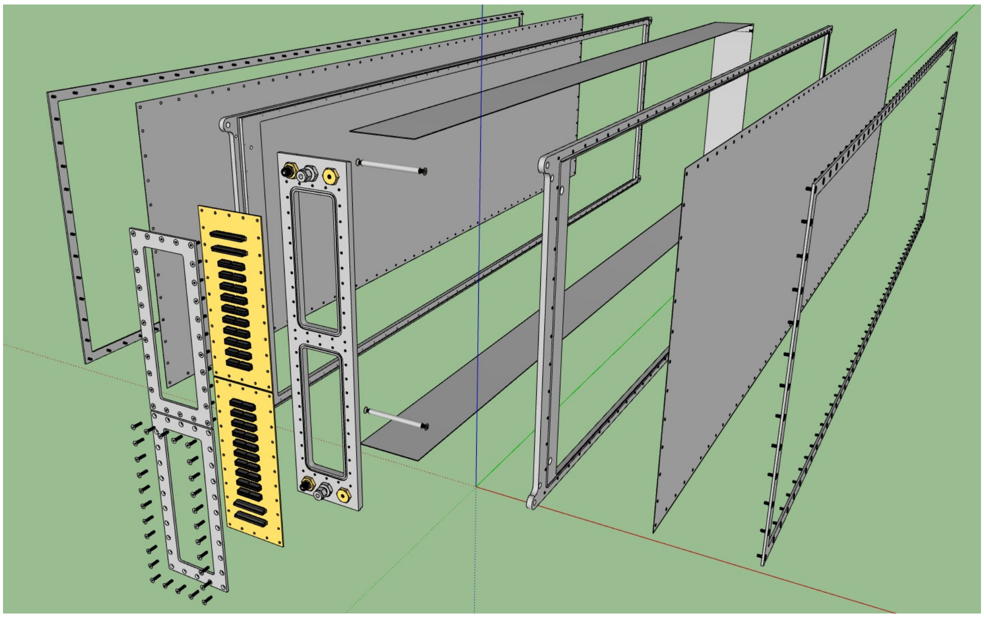

Figure 6.1: Explosive view of the super module chamber.

6.3 The Super Module (SM)

For the outer wall only two types of super modules (SM) are under consideration:

1. Type 1: SM size 180 cm × 49 cm × 10 cm
2. Type 2: SM size 180 cm × 74 cm × 13 cm

A small number of SM types reduces production costs and the complexity of the installation. Both SM types have the same design (see section 6.2). The SM of type 1 comprises 5 strip MRPCs with an active area of 27 cm × 32 cm each as described in section 5.4. The strips of the detectors are positioned vertically. The overlap between the counters is 2 cm corresponding to two strips. This is sufficient to avoid edge effects. The total active area of a super module is 27 cm × 152 cm. The forseen overlap with the neighboring super modules is 2 cm on each side. For a type 1 SM the staggering of the RPCs is done in two ways (cf. Fig. 6.2):

1. an alternating staggering (3 RPCs in front and 2 RPCs behind)
2. a roof-tile structured staggering (one side of the RPC is on top to the next coming RPC)

The reason for considering these two types of staggering which are depicted in Fig. 6.2 is given in section 6.4 where the general layout of the wall will be explained. The SM of type 2 comprises 3 strip MRPCs with an active area of 53 cm × 52 cm each as described in section 5.5. The staggering is done in a roof-tile fashion. The overlap between the

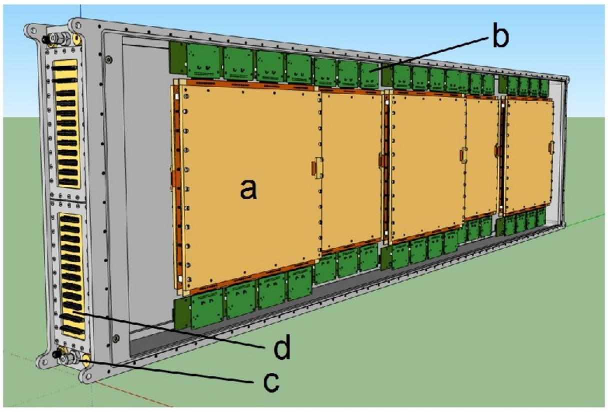

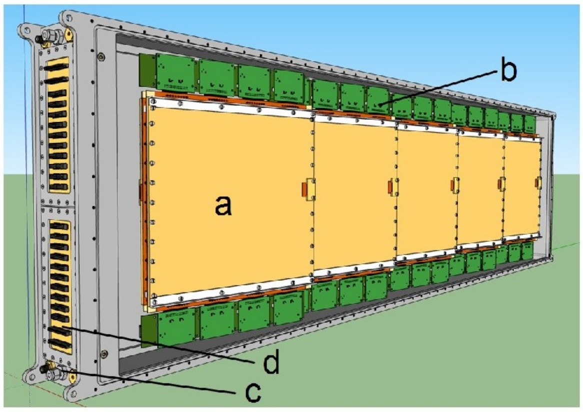

Figure 6.2: View of an opened Super Module of type 1: Single RPCs are denoted by (a), the preamplifier cards which are connected directly to the readout electrodes by (b), feed-throughs for HV, gas and low voltage by (c) and feed-through connectors for the signals by (d). The RPCs are staggered alternately on the left and in a roof tile fashion on the right picture.

RPCs is also 2 cm leading to a total active are of 53 cm × 152 cm. The overlap with the neighboring SMs is 3 cm in the horizontal and 2 cm in the vertical direction. The tilting angle of the RPCs in the type 1 SM is 8.7° and in the type 2 SM 7°. The layout of the type 2 SM is shown in Fig. 6.3. Figure 6.2 and 6.3 show also details such as

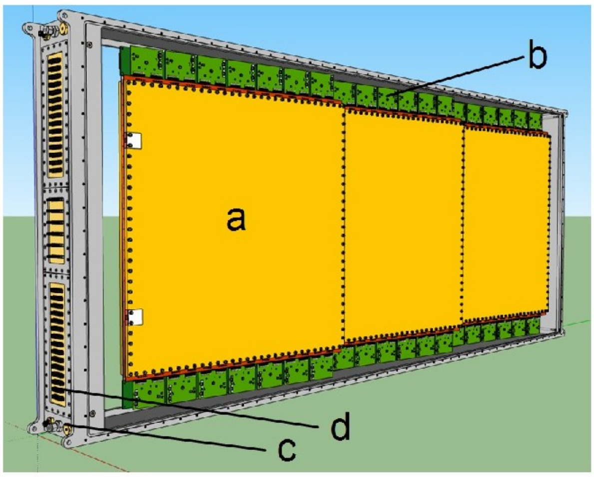

Figure 6.3: View of an opened Super Module of type 2: Single RPCs are denoted by (a), the preamplifier cards which are connected directly to the read-out electrodes by (b), feed-throughs for HV, gas and low voltage by (c) and feed-through connectors for the signals by (d). The RPC are staggered in a roof tile fashion.

the preamplifier cards (labeled (b)) with 2 PADI chips on board coupled directly to the readout electrodes of the RPC. The discriminated signals are collected on main boards (four preamplifier boards are connected to one main board) and transmitted via twisted pair cables (not shown) to the feed-through connectors (labeled (d)). More information about the preamplifier electronics can be found in the appendix. The Time-to-Digital Converters (TDCs) are plugged directly onto the connectors of the feed-through boards. As TDC either the GET4-ASIC (GSI Event-driven TDC with 4 Channels) [200] will be used or an FPGA-based TDC developed at GSI. Figure 6.4 shows a crate mounted onto a

	SM of type 1 (small SM)	SM of type 2 (big SM)
number of RPCs	5	3
number of strips	160	168
number of channels	320	336
number of PADI-boards	40	42
total active area	152 cm × 27 cm	152 cm × 53 cm
overlap	hor.: 2 cm, vert.: 2 cm	hor.: 3 cm, vert.: 2 cm
tilting angle of the RPCs	8.7°	7°
box size	180 cm × 49 cm × 10 cm	180 cm × 74 cm × 13 cm

Table 6.1: Numbers and dimensions of SMs and RPCs contained therein.

SM box which houses the directly connected TDCs. A data collector board combining all

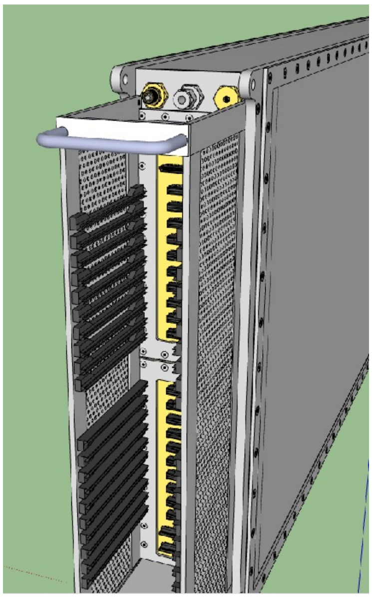

Figure 6.4: Crate mounted on a SM chamber to house the TDCs which are connected directly to the connectors of the feed-through PCB.

TDCs sends the data via an optical cable to an FPGA based pre-processing board. This solution decreases the amount of cables leaving the super module tremendously. Finally, a few additional cables are needed: 2 for the ±HV, 2 pairs for the low voltage supply (one for the Preamplifiers and a second one for the TDCs), two glass fiber cables for the data transfer and one glass fiber cable for the clock and threshold setting, etc. The total power consumption of one SM is about 75 W. The consumption of the preamplifier cards mounted inside the SM chamber contribute with 25 W. Table 6.1 summarizes the technical details of the two types of SMs.

6.4 The outer wall layout

A possible layout of the complete outer ToF-wall with the described two types of super modules is shown in Fig. 6.5 (the wall is positioned at 10 m). The empty rectangle in

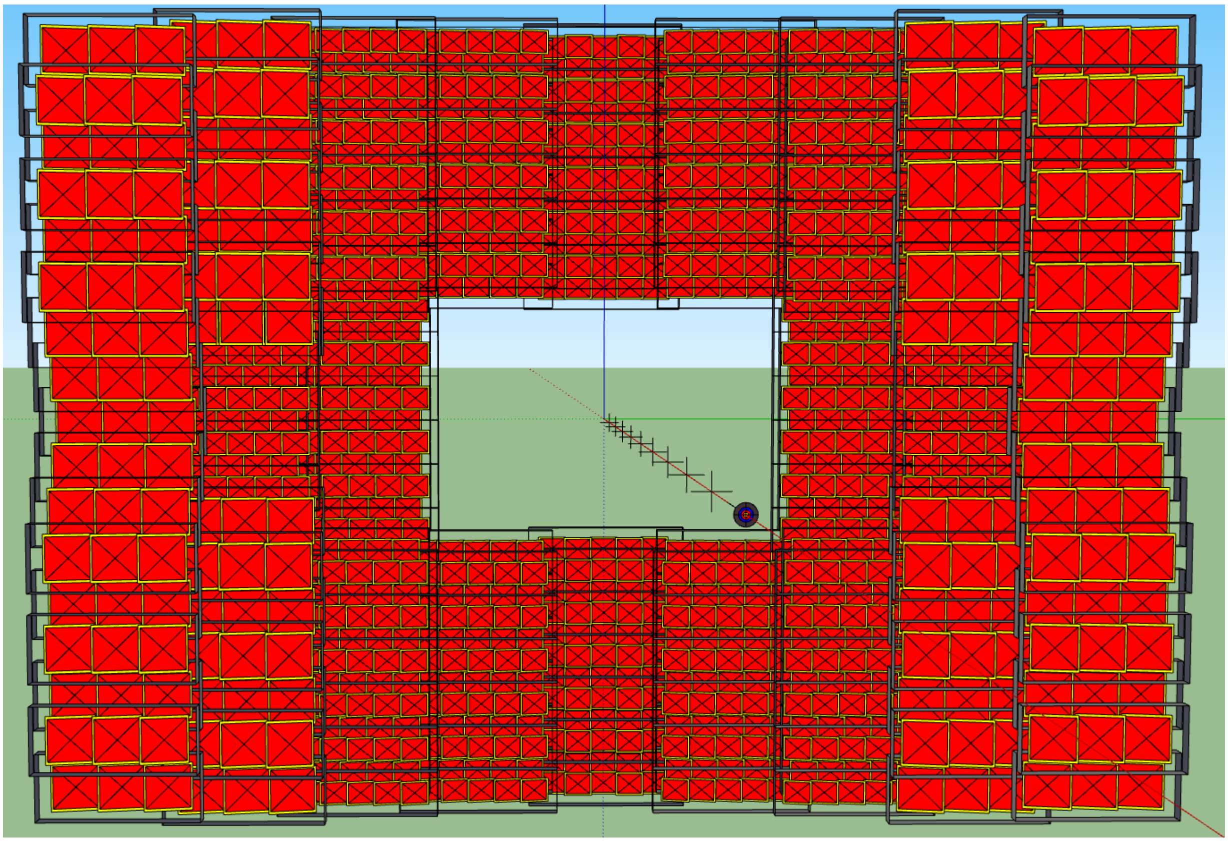

Figure 6.5: Layout of the outer ToF-wall for the final version of CBM. The red rectangle with a yellow frame represent the individual RPCs. They are grouped in super modules indicated by the gray rectangles. The hole in the center denotes the area of the inner wall. The circle represents the target 10 m away from the ToF-wall.

the center is the space where the inner wall will be located. The active area of each individual RPC is represented by a red rectangle with a yellow frame which denotes the overlapped area of the RPC. Either three or five RPCs are grouped in a frame (gray rectangles) representing the side walls of the super module type 1 and type 2, respectively. The main structure of the outer ToF-wall consists of nine columns composed of super modules from type 1 or type 2. The horizontal extention of the active area is about 12.15 m and the vertical extention is about 8.78 m. The hole in the center has the dimensions of 4.20 m × 2.80 m. In order to have an overlap between RPCs from different SMs, the SMs have to be staggered too (cf. Fig. 6.6). Since the wall is constructed symmetrically with the median lines serving as symmetry axes only a quarter of the wall is depicted. The super modules are staggered in a way that the overlap is guaranteed everywhere and

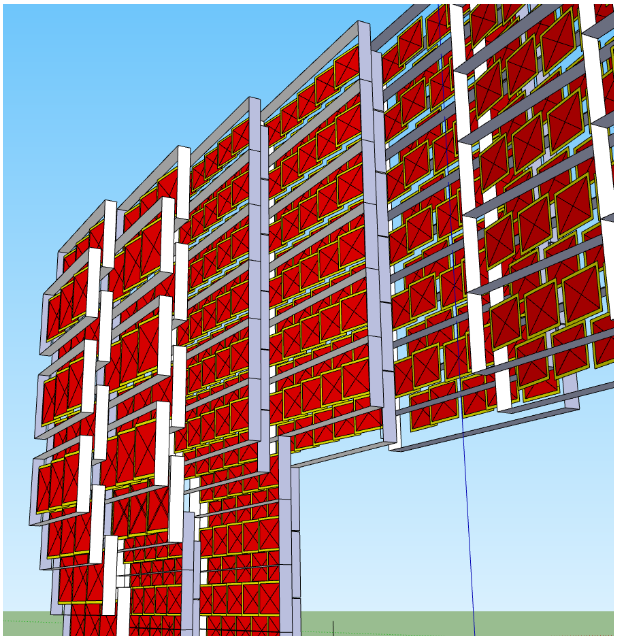

Figure 6.6: Oblique view of the outer ToF wall. From this view the staggering of the super modules is visible.

as homogeneous as possible. Due to the staggering the wall is almost flat (total thickness about 1.45 m) but has a spherical shape. From Fig. 6.6 it becomes also clear why the RPCs in the super modules of type 1 are staggered in two ways. The center column consists of SMs with alternatly staggered RPCs while the side columns consist of SMs with roof-tile staggered RPCs. The tilting angle of the RPC reduces the crossing angle of the incident particles in the side modules.
For the start version of FAIR with only the SIS100 in operation the ToF-wall will be placed closer to the target, in order to increase the kaon efficiency. Up to now the plan is to move the wall to a position 6 m downstream from the target. At this distance the ToF-wall would have a bigger acceptance than required. The idea is to build a start version with only 7 columns and 4 SMs less on top and on the bottom of the wall. The remaining modules would be staggered as shown above. For the default 10 m distance no major changes would be necessary. Only a small shift of some SMs in vertical direction needs to be carried out in order to compensate for the changed incident particle angle. Figure 6.7 visualizes the ToF-wall at both positions under consideration. In the 6m-version all RPCs in type 1 super modules would be equipped with low-resistive glass. The additional type 1 super modules in the 10m-version would consist of RPCs made of normal float glass since they cover the low rate region. The costs for low-resistive glass are about 100 times higher than for normal float glass. Figure 6.8a shows a fraction of the 6m-version wall through a small hole in the target. Shifting the wall to 10 m from the target without adjusting the vertical position of some super modules leads to so-called dead zones (areas without acceptance) shown in Fig. 6.8(b). In order to avoid such dead zones the suspension of the SMs should allow for vertical shifts. Table 6.2 recapitulates the technical data of the 6m- and the 10m-version of the wall. The 6m-version was elaborated in a more realistic setup. The super modules described in section 6.3 are mounted onto a frame made of industrial

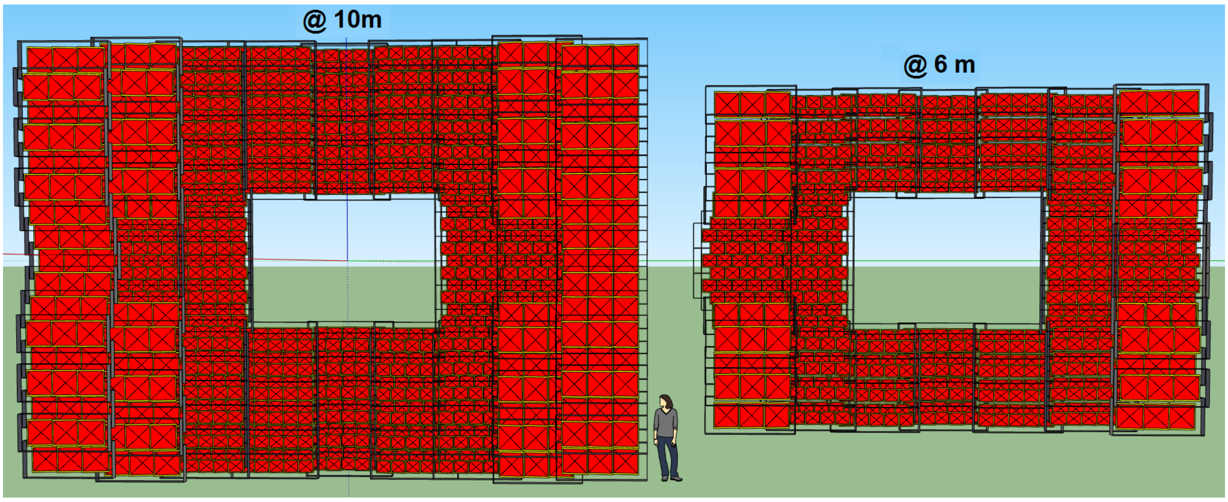

Figure 6.7: 10m- and 6m-version of the CBM outer ToF-wall in direct comparison. The 6m-version can be easily extended to the 10m-version by adding 4 rows of SMs on top and on the bottom and two more columns on the side.

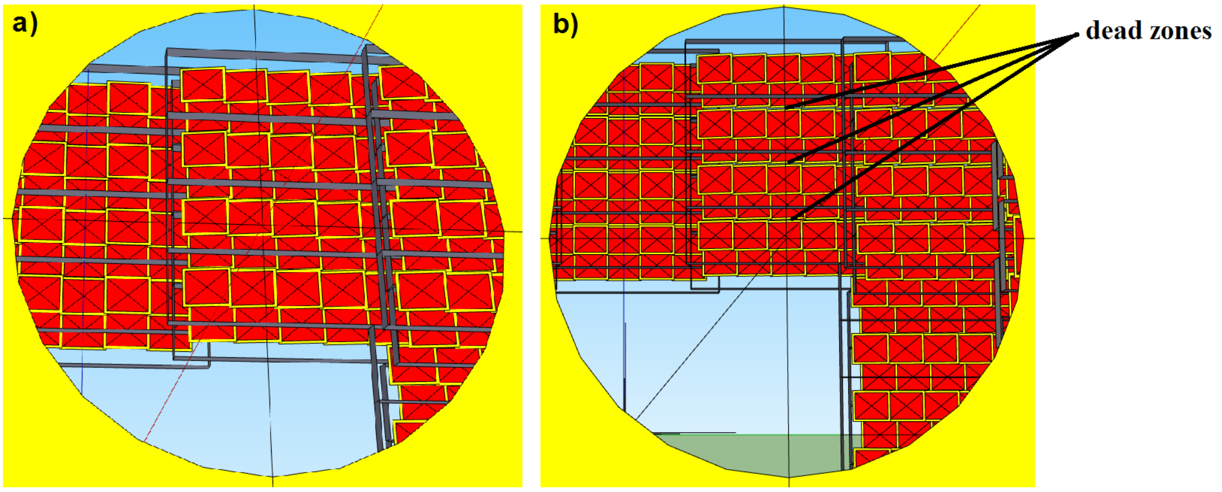

Figure 6.8: Outer Tof-wall seen through a small hole in the target. a) The wall is positioned 6 m from the target; the overlap in between RPCs is everywhere about 2 cm. b) Moving the wall to 10 m without vertically adjusting the SMs will result in dead zones.

aluminum profiles. The size of the frame is about 15 m $\times$ 10 m, as needed for the 10m-version. A sketch of the wall is presented in Fig. 6.9. Thick profiles with a radiation length of 30 % ($X_{0,Al} = 8.72$ cm) are used only for the outer frame and for only one vertical bar behind each column. These bars carry most of the load. The super modules are screwed on vertical thin profiles of 80 mm $\times$ 16 mm cross section with a typical radiation length of 6 %. These profiles have a groove where the SMs can be fastened allowing for easy vertical shifts (see figure 6.10). The SMs are mounted in a way that they can be easily removed

	6 m version	10 m version
horizontal width of the active area	≈ 9.55 m	≈ 12.15 m
horizontal opening angle	≈ 42 °	≈ 33 °
vertical width of the active area	≈ 6.78 m	≈ 8.78 m
vertical opening angle	≈ 29.5 °	≈ 23.7 °
total thickness without frame	≈ 107.5 cm	≈ 145 cm
number of type 1 (small) super modules	116	156
number of type 2 (big) super modules	20	62
number of RPC with low-resist. glass	580	580
number of RPC with float glass	60 big	120 small, 126 big
number of channels	43840	70752

Table 6.2: Wall dimensions, number of super modules and of RPCs for the 6m-version and the 10m-version of the CBM outer wall.

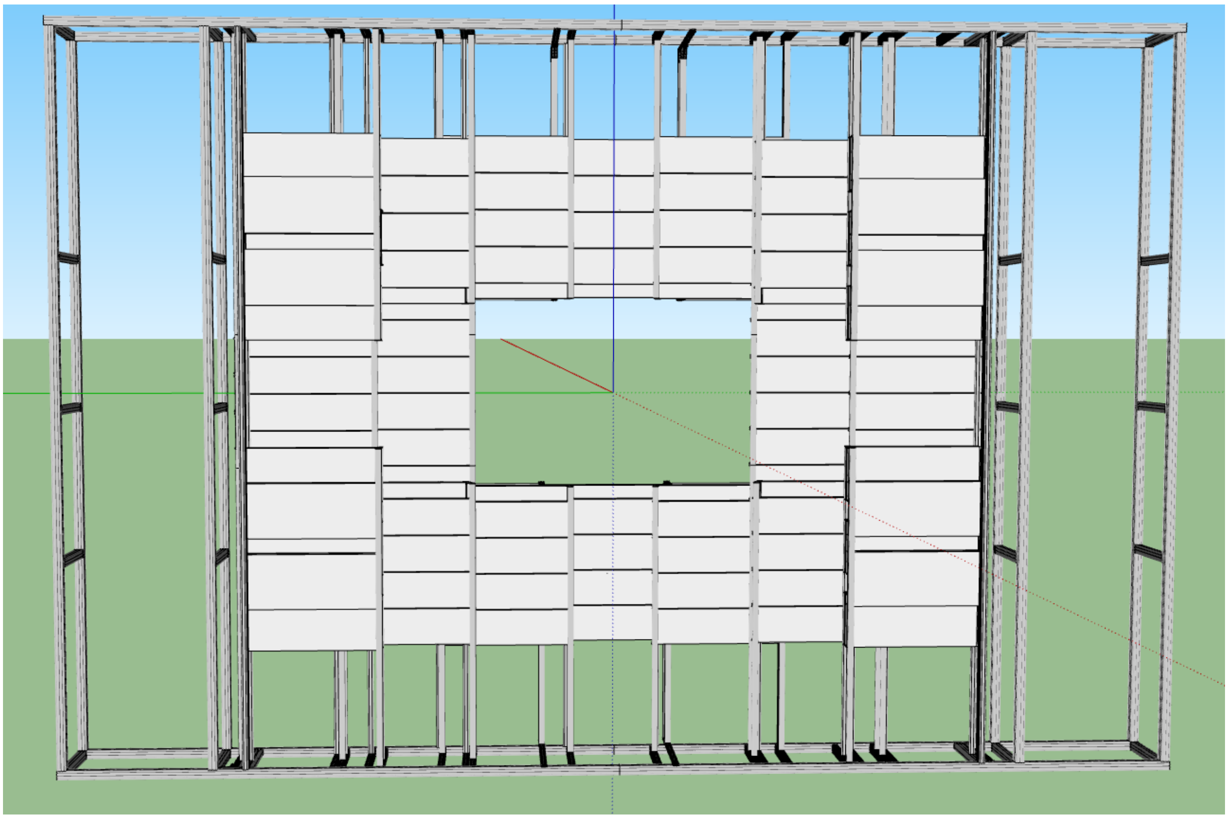

Figure 6.9: Sketch of the CBM outer ToF-wall elaborated in a more realistic setup.

or replaced without un-mounting other SMs. After unplugging the cables the SMs can be pulled out from the side like caskets. Figure 6.11 shows a side view of the rear of the wall, taken roughly at the height of a person's eye. The picture shows the mounted SMs without any infrastructure. All the connections to a SM are hidden behind another SM. Therefore, no infrastructure will cover the front of the active detector material. The total

Figure 6.10: Detailed view of the mounting procedure of the SM. By releasing the screws the SM can be shifted in vertical direction.

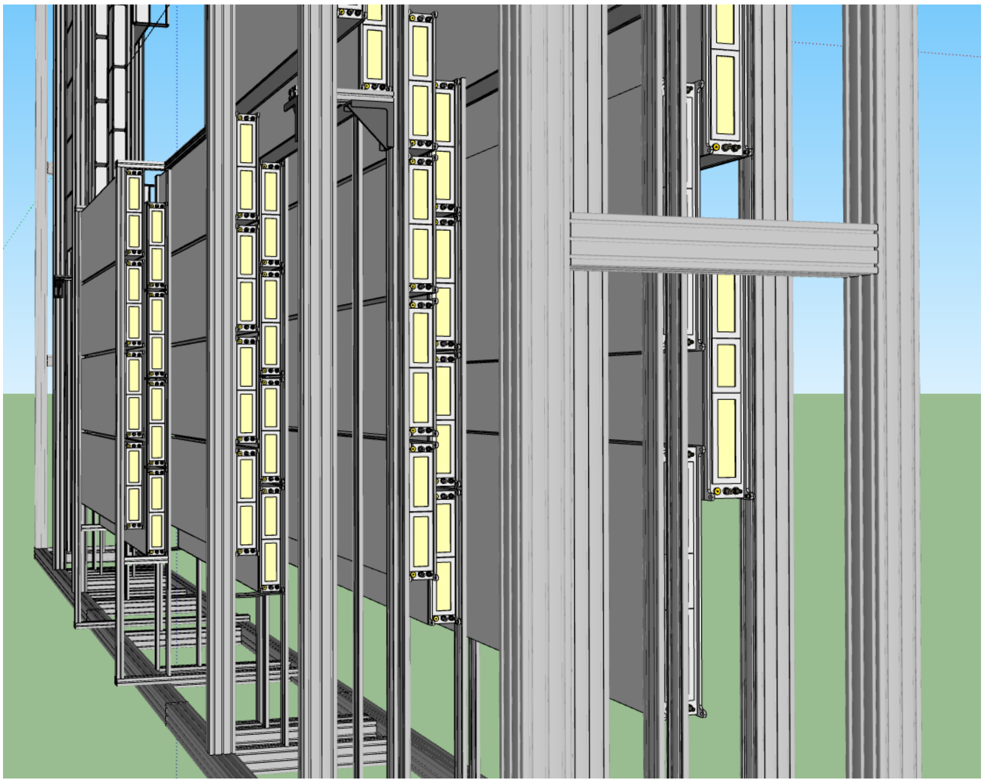

Figure 6.11: Back view of the setup. The infrastructure to the detectors is applied only from one side.

amount of material (only aluminum bars for mounting) in front of the active detector area was calculated to be about 150 kg. The total weight of the frame (without SMs) is about 2.5 t, about 80 % of which is concentrated outside the acceptance.

7 Conclusions and outlook

In this thesis the development of a Multi-gap Resistive Plate Counter (MRPC) prototype with a flexible granularity for the intermediate and the low rate region of the Compressed Baryonic Matter (CBM) experiment is presented. The CBM spectrometer is expected to be operational in the year 2018 at the facility for Anti-proton and Ion Research (FAIR) in Darmstadt, Germany. The physics goal of CBM is to explore the phase diagram of strongly interacting matter in the region of the highest baryon densities including the study of the equation-of-state of nuclear matter at high densities and the search for the deconfinement and chiral phase transitions. In particular the investigation of a speculated first order phase transition from hadronic to partonic phase which might end in a second order critical point is a main pillar of CBM. The signature of a critical point is among others the fluctuation of strangeness or baryon number. The strangeness fluctuation can be measured by evaluating the particle yield ratios of pions and kaons on the event-by-event bases. In this thesis it is demonstrated based on a Monte Carlo simulation program that CBM is capable to measure K/π-fluctuations with sufficient precision at energies starting from 3 GeV. Especially the kaon detection efficiency plays a crucial role for the necessary precision of the K/π-fluctuations determination.
The key element providing charged hadron identification at incident energies between 2 and 35 AGeV is a time-of-flight wall composed of MRPCs. The RPC-technology is nowadays an established gas counter detection principle to measure the time of flight of charged particles with an excellent time resolution, a high efficiency and granularity and simultaneously at low costs. The main goals of this thesis was the design and construction of a MRPC prototype and the evaluation of its detector characteristics as time resolution, efficiency and mean cluster size at different working conditions. The requirements of the counter were a granularity between 25 - 50 cm^2, a time resolution in the order of 50 ps, an efficiency better than 95 % and a rate capability of about 1 kHz/cm^2.
Since the FOPI collaboration installed and operated successfully such a RPC based time-of-flight system it was natural to start investigating the characteristics of the existing MRPC counters. These RPCs showed a time resolution of about 60 ps, a mean cluster size of about 4.2 and an efficiency close to 100 %. The peculiarity of these counters is their narrow strip design (2.54 mm) of the signal pickup electrode which matches in combination with the counter design almost perfectly an impedance of 50 Ω. The impedance matching to the front end electronics ensures a reflection free and extremely stable behavior. In prevision, that CBM will have a free streaming data acquisition, this philosophy was maintained in the development of our RPC prototypes.
Based on the experience gained with the FOPI MRPCs 3 prototypes were developed and tested. All prototypes have in common a fully differential layout with 8 gapes of 220 μm size. The readout electrode strips have a pitch of about 1 cm showing a mean cluster size

between 1.3 - 1.4 at nominal working condition. The length of the strips differs depending on the prototype between 27 and 53 cm. The measured quantities are the efficiency, the time resolution and the mean cluster size as function of the applied high voltage/E-field on the RPC, as function of the threshold settings in the preamplifier as function of the counter gas temperature and as function of the incident particle flux. The rate capability of the RPC is typically defined as the value of the incident particle flux at which the efficiency dropps by 5 % or the time resolution deteriorats by 20 ps.

The first prototype (RPC-P1) showed from in-beam measurements an efficiency of about 95 % at the nominal working voltage ($\pm$11.7 kV) and with a preamplifier threshold of 30 mV. With a higher threshold this efficiency value could not be reached. The nominal working voltage is defined as the electrical tension at which the counter efficiency reaches the plateau. The time resolution at nominal working voltage was about 50 ps at 50 mV preamplifier threshold and about 8 ps worse at 30 mV preamplifier threshold. A rate capability of about 1 kHz/cm^2 was derived from the results at 50 mV preamplifier thresholds. In conclusion RPC-P1 does not fully reach the requested requirements. The main reason was a non-perfect transmission of the signal between pickup electrode and the preamplifier. The signal is routed from the pickup electrode via a soldered twisted pair cable to the connector of the gas chamber feed-throughs and from there via twisted pair cables to the preamplifier which is located outside the gas chamber. In particular the cable between the connector of the gas chamber feed-throughs and the preamplifier introduced a large pickup noise. Measurements with a time domain reflectometer showed a counter impedance of 83 Ω. However, at the soldering points impedance peaks of about 150 Ω were reached leading to signal reflections in the counter. A further problem was the stability of the connection which applies the high voltage to the electrode.

The second prototype (RPC-P2) comprises improvements regarding high voltage electrode and signal transmission. With in-beam tests it was possible to show that RPC-P2 performed by far better than RPC-P1. In particular the mounting of the preamplifier directly to the readout electrode inside the gas box had a great advantage. The working voltage for the RPC-P2 prototype was reduced to $\pm$11.3 kV. The maximal value for the efficiency was about 96 % at $\pm$11.7 kV for the preamplifiers connected outside the box (threshold at 30 mV) and 97.5 % at $\pm$11.3 kV for the preamplifier connected inside the box (threshold at 23 mV). The possibility to operate the preamplifier inside the box at mutch lower thresholds is actually the great advantage. A counter time resolution at strip level of about 52 ps was measured taking another RPC as reference. However, this measurements were performed at a low rate of about 50 Hz/cm^2. At higher rates starting from 700 Hz/cm^2 a time resolution of about 72 ps was measured. The rate capability of RPC-P2 is similar to RPC-P1. It could be shown that warming the gas by 25 °C can improve the rate capability by one order of magnitude. In the case of CBM it is sufficient to warm only few modules which have a rate slightly above 1 kHz/cm^2 by few degree. It can be concluded that prototype RPC-P2 fulfills all imposed requirements. However, the granularity of RPC-P2 is matching the needs of the intermediate rate region of the ToF-wall. Therefore, the counter was equipped with low resistive glass expecting a rate capability higher than 20 kHz/cm^2. RPC-P2 can be seen as a full-size demonstrator for the the CBM-ToF wall in the intermediate rate region.

The third prototype (RPC-P3) is a full-size demonstrator for the low rate region. The preamplifiers are connected directly to the pickup electrode. With this prototype cosmic

ray test were performed. The results show a time resolution of about 40 ps and an efficiency of 98.5 % at an applied voltage of ±11.0 kV. These values are among the very best that have been obtained within the international collaborations attempt to optimize the MRPCs designs for future applications. Since the performance numbers depend to a large extend on the possible software corrections, they most likely apply also to the performance of RPC-P2. This, however, will have to be demonstrated. The time resolution and the efficiency is now derived from clusterized hits and thus from the full counter response with correction for all known and measured dependencies.
We can conclude that both prototypes (RPC-P2 and RPC-P3) are well suited to be implemented in the CBM ToF-system. A design of the outer CBM ToF-wall including these prototypes is presented. The counters were designed such that they can be grouped easily to super-modules (SM) having the proper overlap. A design of the outer part of the CBM-ToF wall was elaborated as part of this thesis and is currently used as a base input for a detailed engineering level description.
In the near future it is planned to build a complete SM with the final electronics chain including PADI preamplifier/discriminator in the gas volume and directly attached TDCs on the super modules. The SM will be tested in heavy-ion beams under conditions that will be chosen to match the final running condition within CBM. If the super module works successfully the counter design has a fair chance to be adopted in the CBM ToF-wall.

Publications

- I. Deppner et al., The CBM time-of-flight wall, *Nuclear Instruments and Methods in Physics Research A*, 661, 2012, 121-124

- I. Deppner, N. Herrmann, M. Ciobanu, J. Frühauf, M. Kis, P.-A. Loizeau, K. Wisniewski and C. Xiang, A glass type Multistrip-MRPC prototype for the low rate region of the CBM Time-of-Flight wall, *JINST*, 7, 2012 P10008, doi:10.1088/1748-0221/7/10/P10008

- A. Schüttauf, M. Ciobanu, K.D. Hildenbrand, M. Kiš, I. Deppner, N. Herrmann, Y.J. Kim, T.I. Kang, P. Koczon, X. Lopez, Y. Leifels, M. Petrovici, K. Piasecki, A. Reischl, W. Reisdorf, M.S. Ryu, V. Simion, N. Zernezki. X. Zhang, Multi-strip MRPCs for FOPI, *Nuclear Instruments and Methods in Physics Research A*, 602, 2009, 679-681

- J. Wang, Y. Wang, X. Zhu, W. Ding, Y. Li, J. Cheng, N. Herrmann, I. Deppner, Y. Zhang, P. Loizeau, P. Senger, D. Gonzalez-Diaz, Development of multi-gap resistive plate chambers with low-resistive silicate glass electrodes for operation at high particle fluxes and large transported charges, *Nuclear Instruments and Methods in Physics Research A*, 621, 2010, 151-156

- M. Kiš, M. Ciobanu, I. Deppner, K.D. Hildenbrand, N. Herrmann, T.I. Kang, Y.J. Kim, P. Koczon, Y. Leifels, M. Marquardt, M. Petrovici, K. Piasecki, M.S. Ryu, A. Schuttauf, V. Simion, J. Weinert, X. Zhang, A Multi-strip Multi-gap RPC Barrel for Time-of-Flight Measurements, *Nuclear Instruments and Methods in Physics Research A*, 646, 2011, 27-34

- M. Petriş, M. Petrovici, V. Simion, D. Bartoş, G. Caragheorgheopol, I. Deppner, K. Doroud, N. Herrmann, M. Kiss, P. Loizeau, Y. Zhang, M.C.S. Williams, Toward a high granularity and high counting rate, differential readout timing MRPC, *Nuclear Instruments and Methods in Physics Research A*, 661, 2012, 129-133

- M. Petrovici, M. Petriş, V. Simion, D. Bartoş, G. Caragheorgheopol, F. Constantin, L. Rădulescu, J. Adamczewski-Musch, I. Deppner, K. Doroud, N. Herrmann, S. Linev, P. Loizeau, M.C.S. Williams, High counting rate, two-dimensional position sensitive timing RPC, *JINST*, 7, 2012, P11003 doi:10.1088/1748-0221/7/11/P11003

A Formalism

A.1 The Bethe-Bloch Formula

Charged particles traversing a medium lose their kinetic energy by exciting and/or ionizing it. The Bethe-Bloch formula describes the mean energy loss of moderately relativistic ($0.1 \lesssim \beta\gamma \lesssim 1000$) charged heavy particles passing a medium [201]. It is given by:

$$-\left\langle \frac{dE}{dx} \right\rangle = \frac{Kz^2 Z\rho}{A\beta^2}\left[\frac{1}{2}\ln\frac{2m_e c^2\beta^2\gamma^2 T_{max}}{I^2} - \beta^2 - \frac{\delta(\beta\gamma)}{2}\right]. \tag{A.1}$$

$K/A = 4\pi N_A r_e^2 m_e c^2/A = 0.307075$ MeV g^{-1} cm^2 is a constant value including the classical electron radius $r_e = \frac{e^2}{m_e c^2}$. z is the charge of the incident particle and Z the atomic number of the medium nucleus. T_{max} is the maximal energy transfer in a single collision. For $M \gg m_e$ the relation $T_{max} \cong 2m_e c^2\beta^2\gamma^2$ holds. I is the mean ionization energy (≈ 10 GeV). The mean energy loss of charged particles in different materials is depicted in Fig. A.1. The energy fluctuations especially in thin absorbers or in gases can be approximated with a so-called Landau distribution.

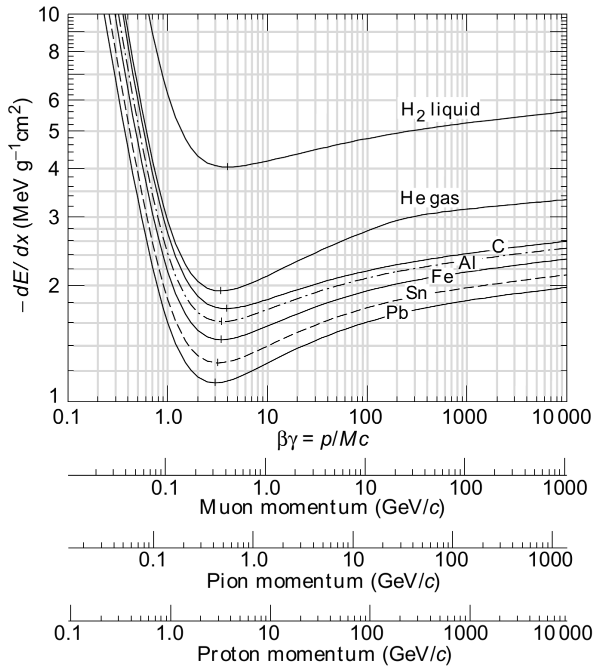

Figure A.1: Mean energy loss of charged particles due to excitation and/or ionization in different materials. Figure taken from [201].

A.2 Integration step for the time distribution at a given threshold

In this appendix the integration step of the threshold time distribution is shown. The integral from equation (2.24) is:

$$P(t) = \int_0^{\infty} \frac{1}{A_{av}} \mathrm{e}^{-A/A_{av}} \delta\left(t - \frac{1}{(\alpha-\eta)v} \ln \frac{A_{thr}}{A}\right) dA \tag{A.2}$$

with $\delta(g(A))$ the delta function. The function $g(A)$ is given by:

$$g(A) = t - \frac{1}{(\alpha-\eta)v} \ln \frac{A_{thr}}{A} \tag{A.3}$$

In order to carry out the integral the following two relations are used [202]:

$$\int f(x)\delta(x-a) = f(a) \tag{A.4}$$

$$\delta(g(x)) = \sum_{i=1}^{N} \frac{1}{|g'(x_i)|} \delta(x - x_i) \tag{A.5}$$

with $g(x_i) = 0$ and $g'(x_i) \neq 0$ $(i = 1, 2, \ldots, N)$. The zero crossing of the function $g(A)$ is given by:

$$t - \frac{1}{(\alpha-\eta)v} \ln \frac{A_{thr}}{A} \stackrel{!}{=} 0 \qquad \Rightarrow \qquad A_1 = A_{thr}\mathrm{e}^{-(\alpha-\eta)vt} \tag{A.6}$$

The first derivative of $g(A)$ is given by:

$$g'(A) = \frac{1}{(\alpha-\eta)v} \frac{1}{A} \tag{A.7}$$

$$g'(A_1) = \frac{1}{(\alpha-\eta)v} \frac{1}{A_{thr}} e^{(\alpha-\eta)vt} \tag{A.8}$$

using Eq. (A.5) the delta function $\delta(g(A))$ becomes:

$$\delta(g(A)) = (\alpha-\eta)vA_{thr}\mathrm{e}^{-(\alpha-\eta)vt}\delta(A - A_{thr}\mathrm{e}^{-(\alpha-\eta)vt}) \tag{A.9}$$

Inserting this expression in (A.2) leads to the final solution shown in section 2.5:

$$P(t) = (\alpha-\eta)v \cdot \frac{A_{thr}}{A_{av}} \cdot \mathrm{e}^{-(\alpha-\eta)vt} \int_0^{\infty} \mathrm{e}^{-A/A_{av}} \delta(A - A_{thr}\mathrm{e}^{-(\alpha-\eta)vt})\, dA \tag{A.10}$$

$$= (\alpha-\eta)v \cdot \frac{A_{thr}}{A_{av}} \cdot \exp\left(-(\alpha-\eta)vt - \frac{A_{thr}}{A_{av}}\mathrm{e}^{-(\alpha-\eta)vt}\right) \tag{A.11}$$

B Setup

In this appendix chapter the setups used in the various beam tests are presented. The used electronic compoments are discribed in section B.6 and B.7.

B.1 Electronics chain used in August 2009

The electronics chain used at GSI in August 2009 is depicted in Fig. B.1. The differential

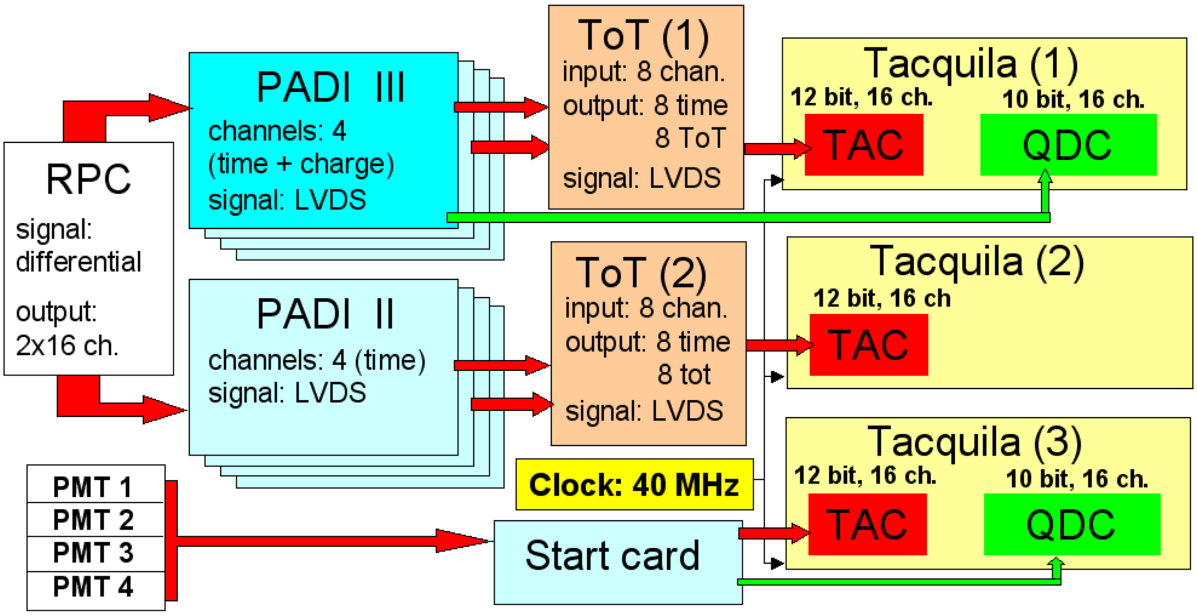

Figure B.1: Electronics chain used at GSI in August 2009.

signals from the RPC are amplified and discriminated by the PADI-ASIC (cf. section B.6). PADI III has in contrast to PADI II an analog output which was connected to the QDC of the Tacquila card. Therefore, it was able to compare the ToT distributions with the charge spectra from the QDC. The Tacquila card is a 16-channel TDC card combined with a QDC. This custom-built TDC with an intrinsic time resolution in the order of 12 ps [133] was designed for the MMRPC barrel in the FOPI experiment [203]. However, the Tacquila card is not capable of measuring differential signals. In addition, it cannot measure simultaneously the time from both edges of the discriminated signal. Therefore, a additional 8-channel electronic device was developed labeled ToT in Fig. B.1. This device splits the original signal, inverts one of them and converts both to NIM signals. However, during the detector tests this card did not perform satisfactorily. The signals from the photomultipliers (PMT) were plugged in a separate discriminator card labeled Start card in Fig. B.1. All Tacquila cards are synchronized by a 40 MHz clock.

B.2 Electronics chain used in November 2010

The electronics chain used at COSY in November 2010 is depicted in Fig. B.2. 16 (8 on

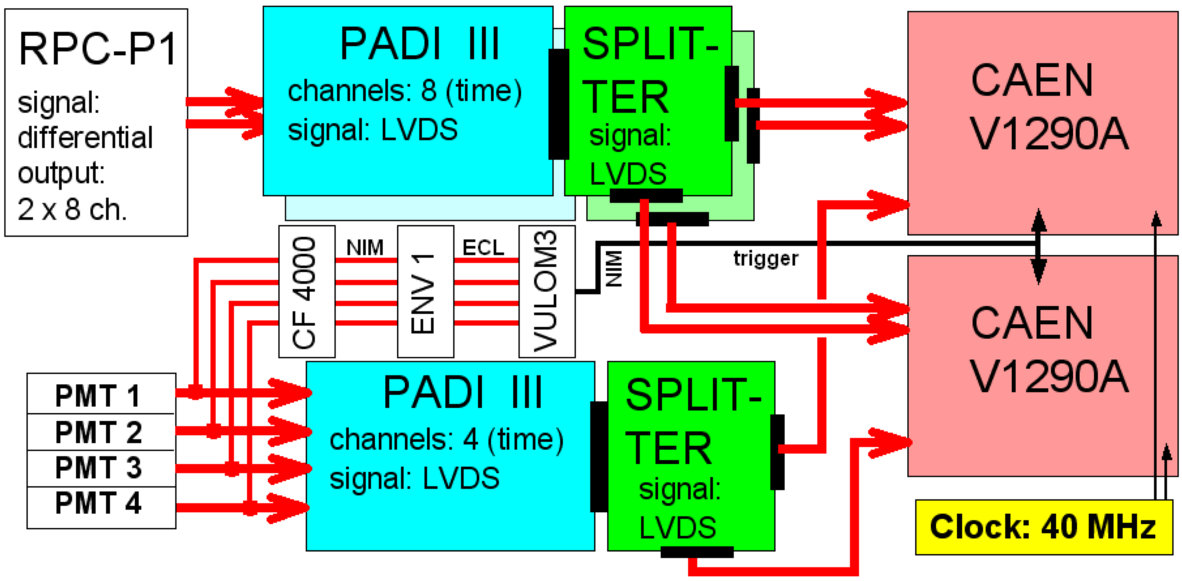

Figure B.2: Electronics chain used at COSY in November 2010.

each readout side) out of 32 RPC signals are routed in 2 PADI boards housing 2 PADI-ASICs each. After discrimination the signals are split by a splitter (13 ps jitter) and fed into two TDCs. One TDC measures the leading time and the other TDC the trailing time of the signal. This type of TDC (CAEN V1290A see appendix B.7.1) is able to measure leading and trailing edges simultaneously but only for signals larger than 10 ns. The PMT signals are split in an analog splitter. One analog signal is discriminated by the PADI-ASIC while the other signal is discriminated by a NIM constant fraction discriminator (CF 4000). The NIM signals are fed into the trigger module (VULOM3, VME-module developed at GSI [205]) after converting them to ECL signals (ENV1, VME-module developed at GSI [204]). The trigger was formed by the coincidence of all PMT signals. The discriminated PMT signals from PADI are split and fed into both TDCs as well.

B.3 Electronics chain used in June 2011

The electronics chain used at GSI in June 2011 is depicted in Fig. B.3.

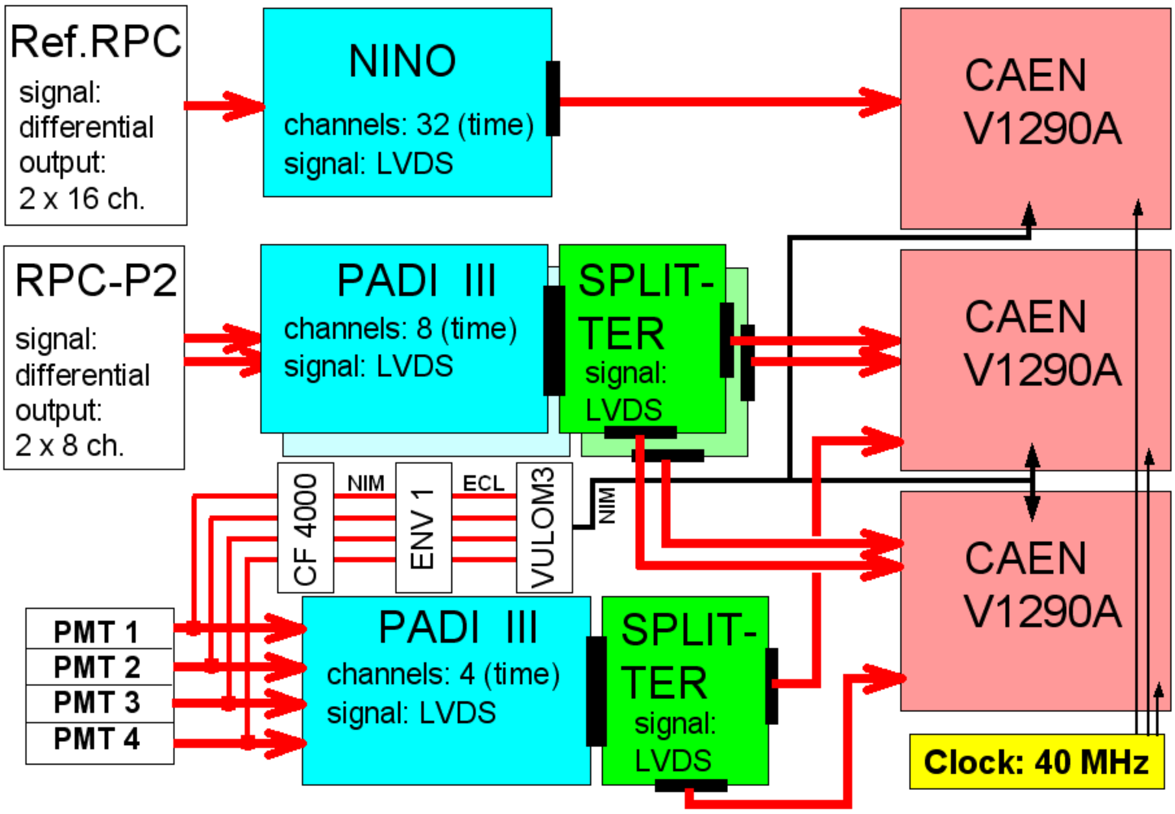

Figure B.3: Electronics chain used at GSI in June 2011.

The only difference to the setup used in November 2010 is the additionally implemented reference RPC. The preamplifier/discriminator ASIC used for the reference RPC is called NINO [206]. The NINO board has a stretcher included and therefore no splitter is needed. Both signal edges can be detected by the same TDC. All TDCs are synchronized by a common 40 MHz clock.

B.4 Electronics chain used in November 2011

The electronics chain used in November 2011 at COSY is essentially the same as the setup used in June 2011. Since several groups participated in this in-beam test the setup was extended to 8 TDCs.

B.5 Electronics chain used for cosmic ray test

The electronics chain used for cosmic ray tests in Heidelberg is depicted in Fig. B.4. The

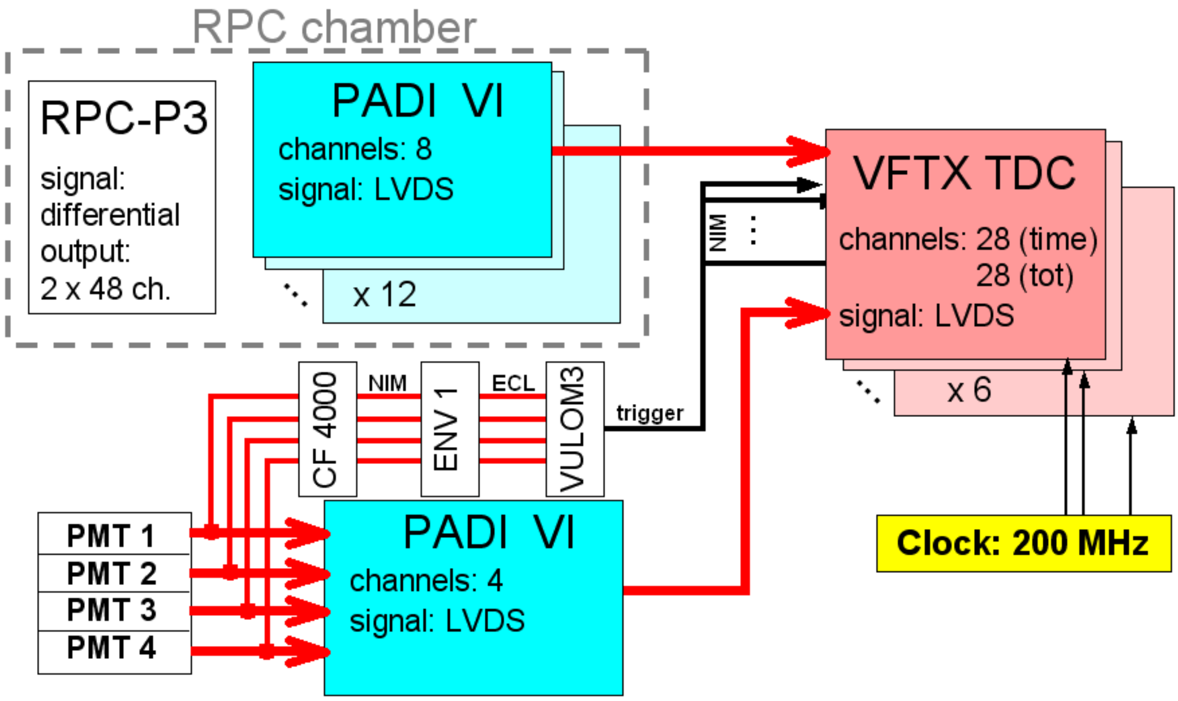

Figure B.4: Electronics chain used for cosmic ray test in Heidelberg.

trigger system is the same as explained in section B.2. The PADI preamplifier/discriminator are attached directly to the readout electrode inside the gas volume. The signals are routed to the FPGA TDC (cf. subsection B.7.2) called VFTX. The VFTX-module can measure both signal edges by splitting the signal internally. In total 6 TDCs are used. They are synchronized by a 200 MHz clock.

B.6 The preamplifier PADI

The PreAmplifier DIscriminator (PADI) chip is a 4-channel custom made ASIC in 0.18 μm CMOS technology. It is adapted to the following requirements given by the CBM MMRPCs:

- differential design with 100 Ω input impedance
- time jitter < 15 ps
- bandwidth > 300 MHz

- peaking time < 1 ns
- noise related to input $< 25\ \mu V_{RMS}$
- preamplifier gain of about 100
- comparator gain > 100
- DC feedback loop for offset/threshold stabilization
- threshold range related to input 0.5 - 10 mV

During the last years several development steps were performed [189–191; 207]. In the following only the PADI versions which were used in beam / cosmic ray test are presented.

B.6.1 PADI III

All PADI versions consist of a preamplifier stage (PA), a discriminator stage (DI), a buffer stage (source followers) to deliver the differential analog signal for monitoring tasks and the bias block supplying all needed biasing currents. Additionally, an OR-feature which allows to daisy-chain chips for trigger purposes was implemented. A PADI III block scheme is presented in Fig. B.5. The measured time resolution as function of the signal amplitude for

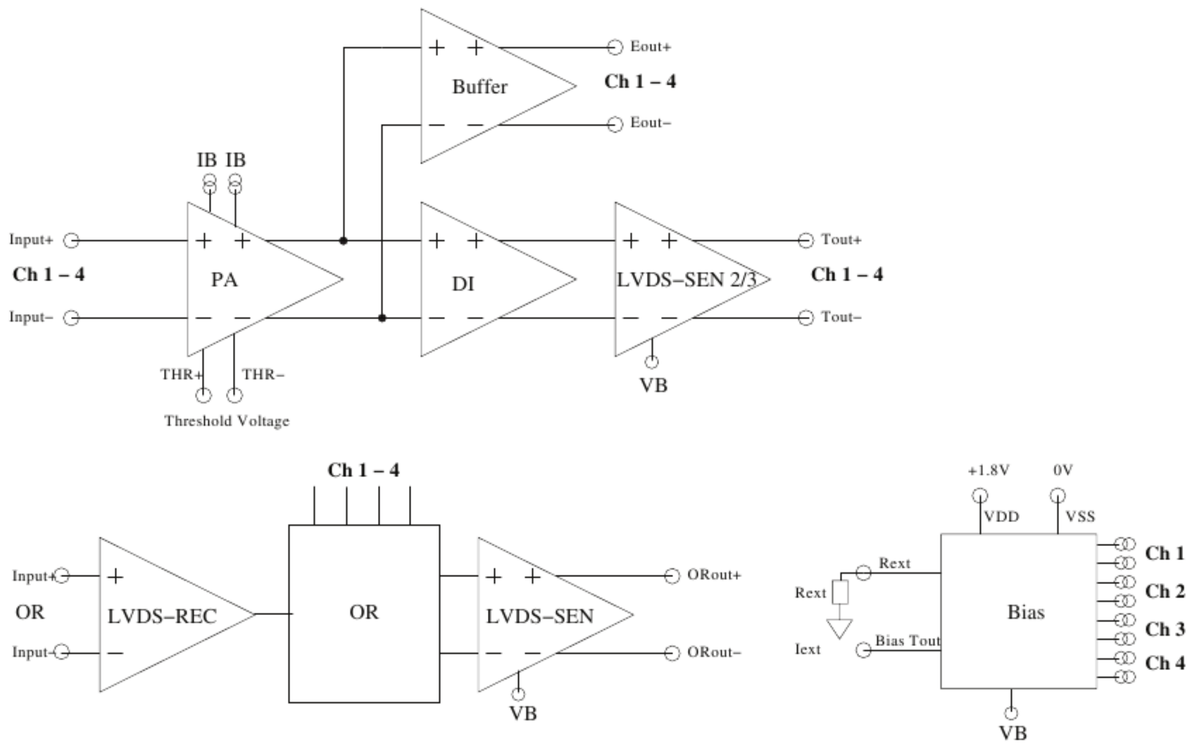

Figure B.5: PADI III block scheme. Figure is taken from [191].

different threshold voltages is shown in Fig. B.6. During the in-beam tests the threshold

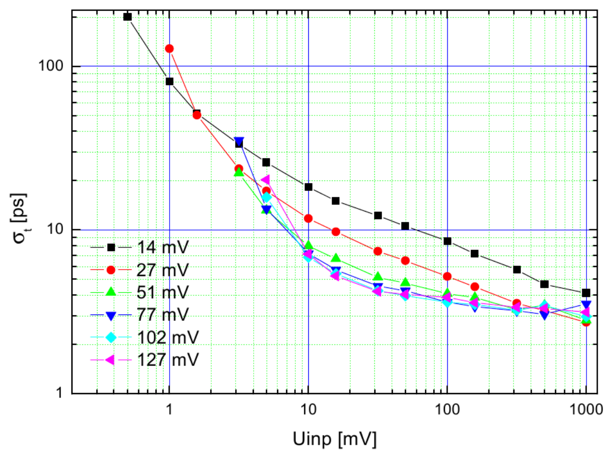

Figure B.6: Time resolution of PADI II/III as function of the input signal amplitude for different threshold voltages. Figure is taken from [190].

was adjusted to 30 mV and 50 mV (cf. section 5.3 and 5.4). Assuming a mean signal amplitude between 20 and 30 mV the time resolution of PADI III is below 10 ps. Note that the value given as threshold is not the real threshold value at the preamplifier input stage. It is the value of the base-line in the analog output.

B.6.2 PADI VI/VII

Based on CADANCE Monte-Carlo simulations the preamplifier scheme was changed (cf. Fig. B.7).

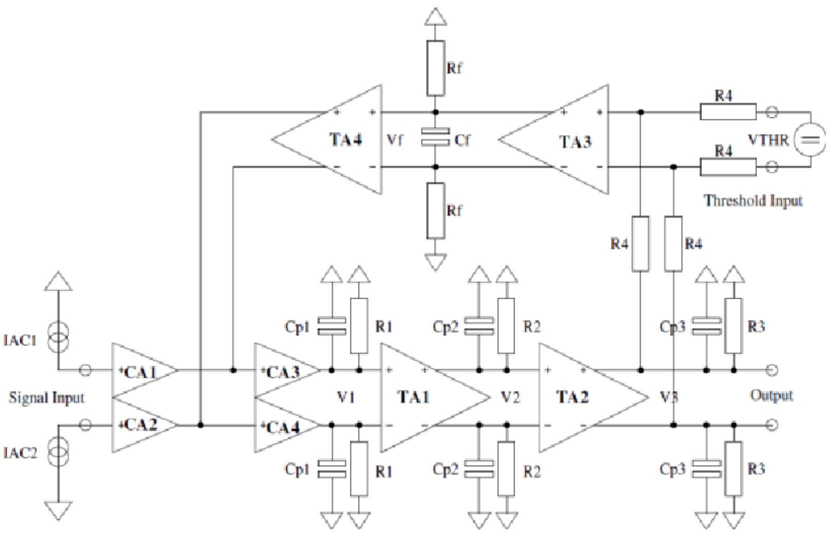

Figure B.7: Simplified AC scheme of the PADI VI preamplifier. Figure is taken from [207].

There is now a common feedback path for signals and threshold voltage. The whole design can be regarded as a fully-differential operational transconductance amplifier (OTA) with two inputs (V_{THR} and signal) and one output [208]. Only one current-biasing block sends a

current to each channel to set the input impedance. All other biasing voltages are generated at the channel level. The threshold voltage is determined by a DC bridge of 6 resistors. This bridge can be controlled internally by two 10-bit DACs or externally by a potentiometer. These soldering pads are common for all channels, hence all channel thresholds can be set by the potentiometer. The two DACs are commanded complementarily and the common-mode voltage is not affected by the DAC value. The interface was changed from I2C to SPI (Serial Protocol Interface) which is simpler and more robust [208]. The OR-facilities for trigger purposes and the buffer stage for monitoring were kept from the PADI III.
The time resolution as function of the input amplitude for different threshold settings is depicted in Fig. B.8. During the tests a threshold voltage of 200 mV was applied. The

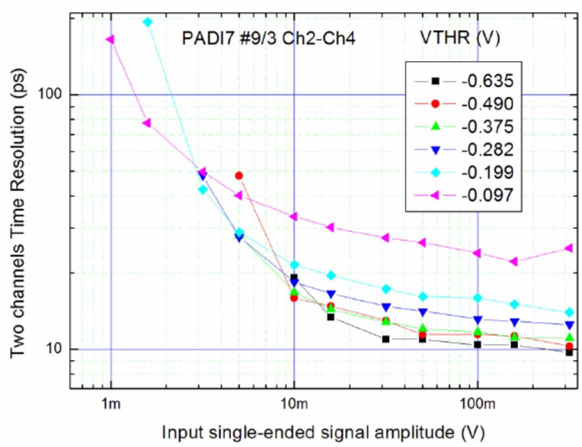

Figure B.8: Time resolution of PADI VI as function of the input signal amplitude for different threshold voltages. Figure is taken from [207].

main technical parameters of PADI III and PADI VI are summarized in Table B.1.

Parameter	Unit	PADI III	PADI VI
Time resolution @ 10 mV	ps	< 12	< 15
PA gain (single-ended input)		~ 86	> 100
PA bandwidth (at buffer output)	MHz	~ 300	> 300
Linear range	mV	$\sim \pm 3$	$\sim \pm 3$
Noise (at input)	μV_{RMS}	≈ 32	≈ 32
Cross Talk Rejection Ratio (CTRR)	dB	≈ 26 - 40	≈ 46 - 60
Common Mode Rejection Ratio (CMRR)	dB	> 40	> 40
Input impedance	Ω	≈ 48 - 58	≈ 50
Power consumption	mW/Ch	≈ 30	$\approx$

Table B.1: Main technical parameters of Padi III and PADI VI.

B.7 The Time-to-Digital-Converter TDC

During the detector tests two types of TDCs were used. A commercial high performance TDC from CAEN (model V1290A [215]) and a VPGA[1] TDC produced at GSI.

B.7.1 The CAEN V1290A TDC

The V1290A is a 32-channel multi-hit TDC, housed in a 1-unit wide VME (cf. C.3) 6U module [215]. The module accepts both ECL and LVDS inputs at 110 Ohm impedance. The channels can be enabled for the detection of rising/falling edges. However, this is only the case if pulses are not shorter than 10 ns. Therefore, in our setup two TDCs were used in order to measure the leading time as well as the trailing time. The time resolution is about 25 ps and the RMS resolution < 35 ps. The Integral Non-Linearities (INL) are smaller than 2.5 LSB (1 LSB = 25 ps) and the differential non-linearities are below 3 LSB. The INL curve can be corrected using a compensation look-up table (see Fig. B.10) [216]. The module has an internal clock (40 MHz) but can be daisy-chained with an external clock (40 MHz). The trigger window is programmable from 25 ns to 100 μs. The double hit resolution is 5 ns. For more information see [215]. Figure B.9 shows a picture of the HPTDC-board V1290A.

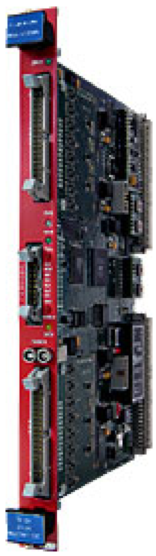

Figure B.9: Picture of a V1290A 32-channel multi-hit TDC with 25 ps time resolution developed by CAEN. Figure taken from [215].

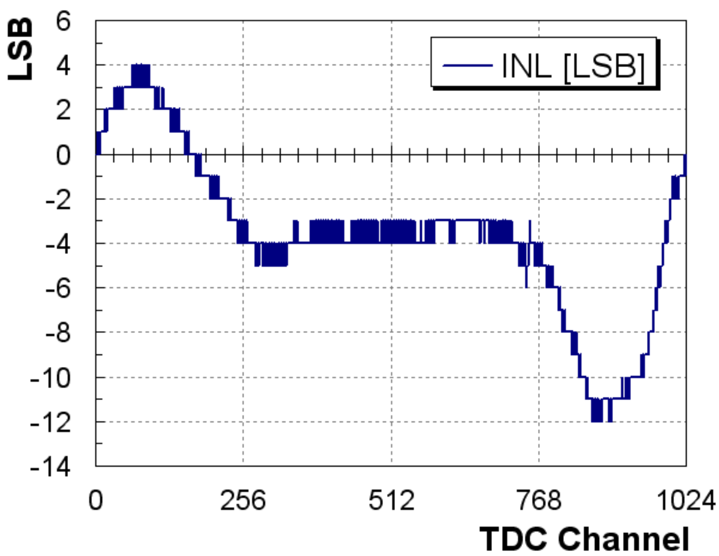

Figure B.10: A Integral Non Linearity (INL) look-up table from one cannel of the V1290A module.

[1]Field Programmable Gate Array

B.7.2 The FPGA TDC

A dedicated VME-module for time measurements called VFTX (VME-FPGA-TDC 10ps) has been developed at GSI Experiment Electronic Department [208]. It is based on an FPGA TDC using the Tapped-Delay-Line (TDL) method (see [217]). At the moment due to space constraints on the FPGA (Xilinx Virtex-4) the number of complete channels is limited to 28. Complete channels means in this context that the FPGA splits the signal internally and measures the time of the leading and trailing edge in separate channels (56 channels in total). In addition the time information of every signal is measured via two TDLs in order to improve the time resolution. Increasing the number of TDLs leads to an improvement of the TDC by $1/\sqrt{n}$ with n numbers of TDLs. Since the TDC implementation is just a VHDL-program it can be featured in different layouts e.g. a 16-channel TDC with 7 ps time resolution (only leading edge) or a 32-channel TDC with 10 ps time resolution (only leading edge). Each TDC board has an external clock input (200 MHz) allowing for synchronization. Pulser test measurements show a channel to channel resolution of about 10 ps on a single module and of about 12 ps between different modules. The intrinsic nonlinearities can be estimated from the bin-width of each bin shown in Fig. B.12. The time resolution as a function of the input signal height for different threshold

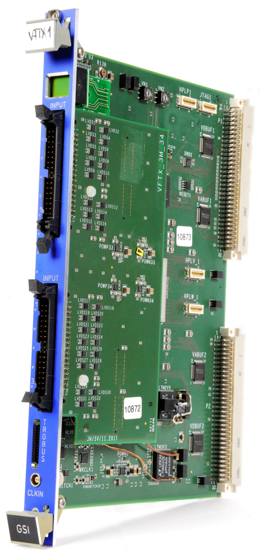

Figure B.11: The FPGA TDC module VFTX1 developed at GSI with 10 ps time resolution.

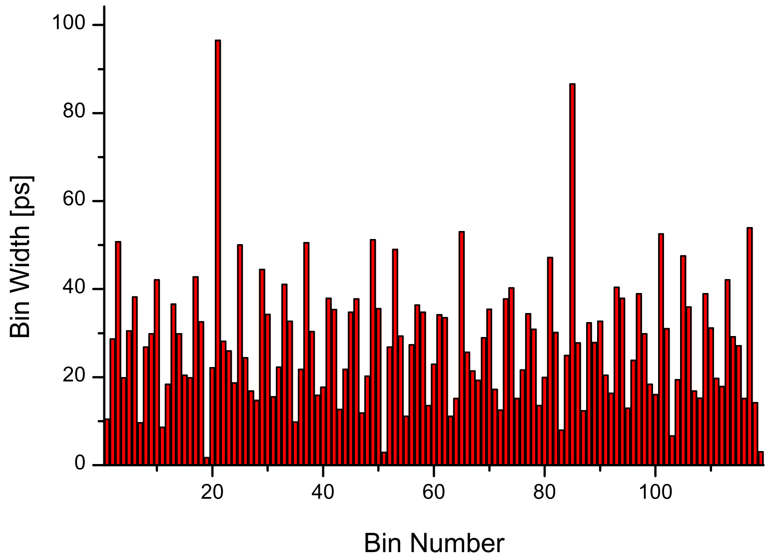

Figure B.12: Bin width plot of a region in the carry chain with two ultra wide bins at positions 21 and 85. Figure taken from [217].

settings with the combined system of PADI VI and VFTX-TDC is shown in Fig. B.13.

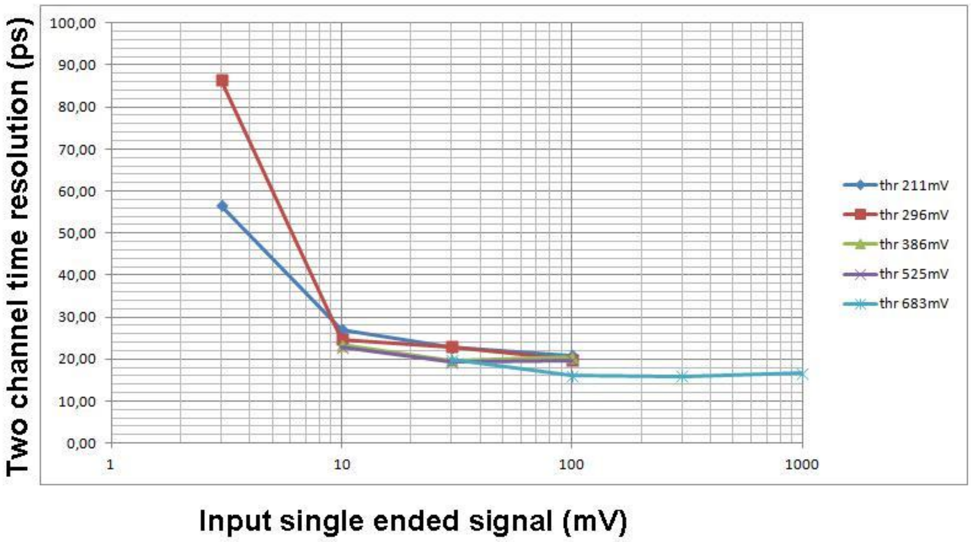

Figure B.13: System time resolution measurement with PADI VI and VFTX-TDC. In order to get the single channel resolution the result needs to be divided by $\sqrt{2}$.

The measurements were performed using a pulser signal which was split and fed into two different PADI channels.

C Keywords

In this appendix some of the keywords which appear in the thesis are discribed.

C.1 Time Walk

The time walk is a phenomenon appearing in leading edge dicriminators. The leading edge dicriminator reacts with a digital output signal when an analog signal crosses a certain threshold in its input channel. As can be seen in Fig. C.1 different signal amplitudes lead to a different release time of the discriminator called "walk". However, leading edge discriminators are commonly used in timing measurements due to their extremely fast reaction time. The walk effect can be corrected in the off-line analysis. A constant fraction discriminator (CFD) has the feature that its release time is independent of the signal amplitude. The analog signal is split into two signals with one them being attenuated and inverted. The second signal is delayed and added to the first one. The first zero crossing is used as release time. However, this procedure takes time which makes this type of discriminator slow in reaction time.

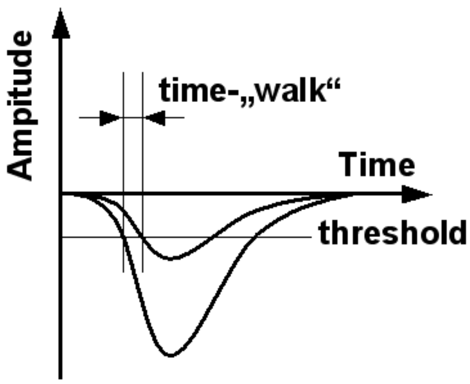

Figure C.1: Visualization of the walk effect emerging in a leading edge discriminator.

C.2 LVDS

Low-voltage differential signaling (LVDS) is an electrical digital signaling standard that can run at very high speeds over inexpensive twisted-pair copper cables [209]. It transmits information as the difference between the voltages on a pair of wires. The receiver is terminated by 100 - 110 Ω matching the impedance of the twisted pair cable. The voltage difference across the resistor is about 350 mV.

C.3 NIM and VME standard

The NIM standard

The Nuclear Instrumentation Module (NIM) standard defines mechanical and electrical specifications for electronics modules used in experimental particle and nuclear physics [210]. The frame housing these modules is called NIM-crate or NIM-bin. Additionally, the crate supplies ± 24, ± 12 and ± 6 volts DC power to the modules via a backplane. The modules operate with logic signals (NIM-signals) where the logic true is set to -0.8 V at an impedance of 50 Ω. Logic 0 corresponds to 0 V.
During the detector tests several NIM module were used among other constant fraction discriminators, Fan-in-Fan-outs and scalers. The NIM standard is widely replaced by the VME standard since the modules cannot communicate with each other through the crate backplane [210].

The VME standard

The VME standard was introduced in the early 80is as a computer bus standard. Later it was widely used for many applications [211]. VME is a high-speed and high-performance bus system with powerful interrupt management and multiprocessor capability [212]. The original standard was a 16-bit bus. The current VME64 includes a full 64-bit bus in 6U-sized cards and 32-bit in 3U cards [211]. Our data acquisition system is based on 6U-sized VME-modules.

C.4 I^{2}C

I^{2}C (Inter-Integrated Circuit) is a multimaster serial single-ended computer bus invented by Philips used for attaching low-speed peripherals to a motherboard, embedded system, cellphone, or other electronic devices [213]. I^{2}C is based on a master-slave-bus concept. The advantage of I^{2}C is that it needs only three lines to communicate. A bi-directional Serial Data Line (SDA), a Serial Clock Line (SCL) and a power supply line (V$_{dd}$). Modern I^{2}C interfaces are able to run with clock speeds up to 5 MHz. Typical voltages used are

+5 V or +3.3 V [213].
An I^2C interface was used in our setup in order to change the thresholds of the preamplifiers which were mounted inside the RPC chamber. However, the I^2C interface was connected to a normal PC and introduces a huge noise in the preamplifier. Therefore and for stability reasons it was decided to change to an SPI interface.

C.5 SPI

The Serial Peripheral Interface Bus (SPI) is a synchronous serial data link de facto standard, named by Motorola, that operates in full duplex mode [214]. It operates similar to the I^2C interfaces in the master slave mode but in this case the data line is not bi-directional. The SPI bus consist of at least 4 lines with a Serial-Data-Out-line (SDO), a Serial-Data-In-line (SDI), a Serial-Clock-line (SCK) and a Chip-Select-line (CS). Optionally a Chip-Select-line can be used for every individual SPI slave. The clock frequency can be freely chosen up to 1 MHz.
The SPI interface is the ideal communication system in order to set the threshold for several preamplifiers mounted inside the super module chamber. With the SPI interface integrated in the PADI VI chip it is even possible to set the threshold to every channel individually.

List of Figures

List of Tables

References

[1] K. Fukushima and T. Hatsuda, Rept. Prog. Phys. 74 (2011) 014001

[2] F. Schwabl, Statistische Mechanik, Springer-Verlag, 2 Auflage, 2004

[3] B. Friman, C. Höhne, J. Knoll, S. Leupold, J. Randrup, R. Rapp, P. Senger, The CBM Physics Book, Compressed Baryonic Matter in Laboratory Experiments, Springer Verlag, February 4, 2011

[4] A. Basavov et al., arXiv:1111.1710v1

[5] Y. Aoki et al., Nature 443 (2006) 675

[6] Z. Fodor and S.D. Katz, JHEP 0404 (2004) 050

[7] L. McLerran, R.D. Pisarski, Nucl. Phys. A 796 (2007) 83.

[8] A. Andronic et al., Nucl. Phys. A837 (2010) 65

[9] J. Randrup, J. Cleymans, Phys. Rev. C 74, 047901 (2006) 611, 612

[10] J. Cleymans, H. Oeschler, K. Redlich, S. Wheaton, Phys. Rev. C 73, 034905 (2006)

[11] J. Randrup, J. Cleymans, arXiv:0905.2824

[12] A. Schmah, arXiv:1202.2389v1

[13] A. Aduszkiewicz et al., Acta Physica Polonica B43 (2012) 635

[14] NICA White Paper, http://nica.jinr.ru/files/WhitePaper.pdf

[15] C. Höhne, Journal of Physics: Conference Series 420 (2013) 012016, doi:10.1088/1742-6596/420/1/012016

[16] P.Senger, Nucl. Phys. A, 862-863 (2011) 139-145

[17] P. Senger, Progress in Particle and Nuclear Physics 62 (2009) 375 - 380

[18] A. Andronic, P. Braun-Munzinger, J. Stachel, Nuclear Physics A 772 (2006) 167 - 199

[19] P. Senger, Journal of Physics, Conference Series 50 (2006) 357 - 360

[20] Ch. Blume, J. Phys. G: Nucl. Part. Phys. 31 (2005) 57 - 68

[41] M. C. S. Williams, J. Phys. G: Nucl. Part. Phys. 39 (2012) 123001 doi:10.1088/0954-3899/39/12/123001

[22] Ch. Lippmann, arXiv:1101.3276v4 [hep-ex] (2011)

[23] S. A. Bass et al., Progress in Particle and Nuclear Physics 41 (1998) 255 - 369

[24] N. Herrmann, Particle Detectors at their limits (Time Of Flight), IRTG spring school (2013)

[25] J. W. Keuffel, Phys. Rev., 73, 531 (1948)

[26] V. V. Parkhomchuck, YU. N. Pestov and N. V. Petrovykh, Nuclear Instruments and Methods 93 (1971) 269 - 270;

[27] V. Akimov et al., Nuclear Instruments and Methods in Physics Research A344 (1994) 120 - 124

[28] A.Arefiev et al. Nuclear Instruments and Methods in Physics Research A 348 (1994) 318 - 323

[29] R. Santonico and R. Cardarelli, Nuclear Instruments and Methods 187 (1981) 377 - 380

[30] G. Aielli et al., Nuclear Physics B (Proc. Suppl.) 158 (2006) 11 - 15

[31] C. Carrillo, Nuclear Instruments and Methodsin Physics Research A 661 (2012) 19 - 22

[32] M. Gagliardi, Nuclear Instruments and Methodsin Physics Research A 661 (2012) 45 - 49

[33] B. Hong, Nuclear Instruments and Methods in Physics Research A 602 (2009) 644 - 648

[34] G. Cavoto, Nuclear Instruments and Methods in Physics Research A 533 (2004) 46 - 49

[35] P.Camarri, NuclearInstruments and Methods in Physics Research A 602 (2009) 668 - 673

[36] A. Bertolin, Nuclear Instruments and Methodsin Physics Research A 661 (2012) 60 - 63

[37] ATLAS muon spectrometer technical design report CERN LHCC-97-22, ATLAS TDR 10, CERN, 1997

[38] G. Cattani, Nuclear Instruments and Methods in Physics Research A 661 (2012) 6 - 9

[39] I. Crotty, E. Cerron Zeballos, J. Lamas Valverde, D. Hatzifotiadou, M.C.S. Williams, A. Zichichi, Nuclear Instruments and Methods in Physics Research A 360 (1995) 512 - 520

[40] E. Cerron Zeballos, I. Crotty, D. Hatzifotiadou, J. Lamas Valverde, S. Neupane, M.C.S. Williams, A. Zichichi Nuclear lnstmmenu and Methods in Physics Research A 374 (1996) 132 - 135

[41] M. C. S. Williams, J. Phys. G: Nucl. Part. Phys. 39 (2012) 123001 (24pp) doi:10.1088/0954-3899/39/12/123001

[51] P. Fonte, A. Smirnitski, M.C.S. Williams, Nuclear Instruments and Methods in Physics Research A 443 (2000) 201 - 204

[43] D. Belver et al., Nuclear Instruments and Methods in Physics Research A 602 (2009) 687 - 690

[79] A. N. Akindinov et al., Nuclear Instruments and Methods in Physics Research A 533 (2004) 74 - 78

[45] F. Geurts et al., Nuclear Instruments and Methods in Physics Research A, 533 (2004) 60 - 64

[46] V. Ammosov et al., Nuclear Physics B (Proc. Suppl.) 158 (2006) 56 - 59

[47] N. Tomida et al., JINST 7 P12005 (2012), doi:10.1088/1748-0221/7/12/P12005

[48] M. Abbrescia et al.,Nuclear Instruments and Methods in Physics Research A 409 (1998) 1 - 5

[49] M. Abbrescia et al., Nuclear Instruments and Methods in Physics Research A 431 (1999) 413 - 427

[50] M. Abbrescia et al., Nuclear Physics B (Proc. Suppl.) 78 (1999) 459 - 464

[51] P. Fonte, Nuclear Instruments and Methods in Physics Research A 456 (2000) 6 - 10

[52] G. Aielli, Nuclear Instruments and Methods in Physics Research A 508 (2003) 6 - 13

[53] M. Abbrescia Nuclear Instruments and Methods in Physics Research A 533 (2004) 7 - 10

[54] A. Mangiarotti, P. Fonte, A. Gobbi Nuclear Instruments and Methods in Physics Research A 533 (2004) 16 - 21

[55] A. Mangiarotti et al., Nuclear Physics B (Proc. Suppl.) 158 (2006) 118 - 122

[56] Ch. Lippmann, Ph.D. thesis, Detector Physics of Resistive Plate Chambers, Johann Wolfgang Goethe Universität (2003)

[57] W. Riegler, Ch. Lippmann, R. Veenhof, Nuclear Instruments and Methods in Physics Research A 500 (2003) 144 - 162

[193] Claus Grupen, Teilchendetektoren, BI-Wissenschaftsverlag (1993)

[59] W. Riegler, D. Burgarth Nuclear Instruments and Methods in Physics Research A 481 (2002) 130 - 143

[60] D. González-Díaz, Ph.D. thesis, Santiago de Compostella, (2006)

[61] F. F. Rieke, W. Prepejchal, Phys. Rev. A6 (1972) 1507 - 1519

[62] P. J. Mohr, B. N. Taylor, and D. B. Newell, Rev. Mod. Phys. 80, (2008) 633 - 730

[63] I. Smirnov, Heed, program to compute energy loss of fast particles in gases, Version 1.01, CERN.

[64] A. Fasso, et al., FLUKA 99, Particle Transport Code, Version 1999.

[65] S. Biagi, Magboltz, program to compute gas transport parameters, Version 2.2, CERN.

[66] E. Gorini, Measurements of drift velocity and amplification coefficient in C2H2F4-isobutane mixtures for avalanche operated RPC, presented at the RPC 1997 - 4th Workshop on Resistive Plate Chambers and Related Detectors, October 1997, Napoli, Italy.

[67] V. Golovatyuk, Laser beam studies of RPC behaviour in avalanche mode, presented at the RPC 2001 - 6th Workshop on Resistive Plate Chambers and Related Detectors, 26-27 November 2001, Coimbra, Portugal.

[68] S. Biagi, Imonte, program to compute gas properties, Version 4.5.

[69] H. Raether, Butterworths Advanced Physics Series, Washington, (1964)

[70] W. Shockley, Journal of Applied Physics 9 (10) 635. (1938), doi:10.1063/1.1710367

[71] S. Ramo, Proceedings of the IRE 27 (9) (1939) 584 - 585, doi:10.1109/JRPROC.1939.228757

[72] T. Heubrandtner, B. Schnizer, Ch. Lippmann, W. Riegler, Nuclear Instruments and Methods in Physics Research A 489 (2002) 439 - 443

[73] D. González-Díaz, Nuclear Instruments and Methods in Physics Research A 661 (2012) 172 - 176

[74] D. González-Díaz, H. Chen, Y. Wang, Nuclear Instruments and Methods in Physics Research A 648 (2011) 52 - 72

[75] A. Blanco et al., Nuclear Instruments and Methods in Physics Research A 485 (2002) 328 - 342

[76] W. Riegler, Nuclear Instruments and Methods in Physics Research A 491 (2002) 258 - 271

[77] W. Riegler, Ch. Lippmann, Nuclear Instruments and Methods in Physics Research A 508 (2003) 14 - 18

[78] A.N.Akindinov et al., IEEE Transaction on Nuclear Science, 48(5) (2001) 1658 - 1663

[79] A.N.Akindinov et al., Nuclear Instruments and Methods in Physics Research A 533 (2004) 74 - 78

[80] W.J. Llope Nuclear Instruments and Methods in Physics Research A 661 (2012) 110 - 113

[81] J. Wang et al., Nuclear Instruments and Methods in Physics Research A 661 (2012) 125 - 128

[82] M. Petriş et al., Nuclear Instruments and Methods in Physics Research A 661 (2012) 129 - 133

[83] Y. Wang et al., Nuclear Instruments and Methods in Physics Research A 661 (2012) 134 - 136

[84] S. An et al., Nuclear Instruments and Methods in Physics Research A 594 (2008) 39 - 43

[85] http://www.awrcorp.com/products/innovative-technologies/aplac

[86] D. González-Díaz, P. Fonte, J.A. Garzón, A. Mangiarotti, Nuclear Physics B (Proc. Suppl.) 158 (2006) 111 - 117

[87] C. Gustavino et al., Nuclear Instruments and Methods in Physics Research A 527 (2004) 471 - 477

[88] A. Akindinov et al., Nuclear Instruments and Methods in Physics Research A 572 (2007) 676 - 681

[89] J. Wang et al., Nuclear Instruments and Methods in Physics Research A 621 (2010) 151 - 156

[90] L. Lopes et al., Nuclear Physics B (Proc. Suppl.) 158 (2006) 66 - 70

[91] I. Deppner et al., Nuclear Instruments and Methods in Physics Research A 661 Sup. 1 (2012) 121 - 124

[92] Ammosov, Beam test of pad tRPCs with ultra thin glass, talk at XIII CBM collaboration meeting, Darmstadt, 2009

[93] D. González-Díaz al., Nuclear Instruments and Methods in Physics Research A 555 (2005) 72 - 79

[94] L. Naumann, R. Kotte, D. Stach, J. Wüstenfeld, Nuclear Instruments and Methods in Physics Research A 635 (2011) 113 - 116

[95] Y. Leifels for the FOPI Collaboration, Journal of Physics: Conference Series 230 (2010) 012002, doi:10.1088/1742-6596/230/1/012002

[96] Y. Leifels for the FOPI Collaboration, Journal of Physics: Conference Series 420 (2013) 012019, doi:10.1088/1742-6596/420/1/012019

[97] J.L. Ritman and the FOPI collaboration: Z.Phys. A352 (1995) 355 - 357

[98] M. Eskef et al., Eur.Phys.J. A3 (1998) 335-349

[99] A. Mangiarotti et al., Nucl.Phys. A714 (2003) 89 - 123

[100] B. Hong et al., Phys. Rev. C 71, (2005) 034902

[101] W. Reisdorf et al.,Nucl.Phys. A781 (2007) 459 - 508

[102] M. Merschmeyer and the FOPI collaboration.,Physical Review C 76, (2007) 024906

[103] X. Lopez and the FOPI collaboration: Phys. Rev. C 75, (2007) 011901(R)

[104] X. Lopez and the FOPI collaboration: Phys. Rev. C 76 (2007) 052203

[105] X. Lopez and the FOPI collaboration:Phys. Rev. C 81 (2010) 061902

[106] Y. Leifels for the LAND/FOPI Collaboration, Phys. Rev. Lett. 71, (1993) 963 - 966

[107] S. C. Jeong et al., Phys. Rev. Lett. 72, (1994) 3468 - 3471

[108] R. Kotte et al., Phys. Rev. C 51, (1995) 2686 - 2699

[109] P. Crochet et al., Phys.Lett. B486 (2000) 6-12

[110] A. Andronic et al., Phys. Rev. C 64, (2001) 041604

[111] A. Andronic et al., Phys. Rev. C 67, (2003) 034907

[112] G. Stoicea and the FOPI collaboration: Phys. Rev. Lett. 92 (2004) 072303

[113] A. Andronic et al., Phys.Lett. B 612 (2005) 173-180

[114] T.I. Kang Ph.D. thesis, Korea University (2010)

[115] V. Zinyuk, Diploma thesis, Heidelberg University (2011)

[116] B. Hong et al., Phys. Rev. C 57, (1998) 244 - 253

[117] B. Hong et al., Phys. Rev. C 66, (2002) 034901

[118] W. Reisdorf et al., Phys.Rev.Lett. 92 (2004) 232301

[119] K. Wisniewski et,al., Eur.Phys.J. A9 (2000) 515 - 519

[120] M. L. Benabderrahmane and the FOPI collaboration: Phys. Rev. Lett. 102 (2009) 182501

[121] L. Fabbietti For the FOPI Collaboration, Int. J. Mod. Phys. E, 19, (2010) 2606

[122] Y. Zhang, Ph.D. thesis, Heidelberg University (2010)

[123] J. Ritman et al., Nucl.Phys.Proc.Suppl. 44 (1995) 708 - 715

[124] A. Devismes et al., Nuclear Instruments and Methods in Physics Research A 482 (2002) 179 - 191

[125] Yu.N. Pestov, G.V. Fedotovich, SLAC-TRANS-0184, IYF-77-78 (1978)

[126] Yu.N. Pestov, Nuclear Instruments and Methods in Physics Research A 196 (1982) 45 - 47

[127] Yu.N. Pestov, Nuclear Instruments and Methods in Physics Research A 265 (1988) 150 - 156

[128] E. Badura et al., Nuclear Instruments and Methods in Physics Research A 372 (1996) 352 - 358

[129] E. Badura et al., Nuclear Instruments and Methods in Physics Research A 379 (1996) 468 - 471

[130] A. Mangiarotti, A. Gobbi, Nuclear Instruments and Methods in Physics Research A 482 (2002) 192 - 215

[131] M. Petrovici et al., Nuclear Instruments and Methods in Physics Research A 487 (2002) 337 - 345

[132] M. Petrovici et al., Nuclear Instruments and Methods in Physics Research A 508 (2003) 75 - 78

[133] A. Schüttauf, Nuclear Instruments and Methods in Physics Research A 533 (2004) 65 - 68

[134] A. Schüttauf et al., Nuclear Physics B (Proc. Suppl.) 158 (2006) 52 - 55

[135] A. Schüttauf et al., Nuclear Instruments and Methods in Physics Research A 602 (2009) 679 - 681

[136] M. Kiš et al., Nuclear Instruments and Methods in Physics Research A 646 (2011) 27 - 34

[137] N. Herrmann, CBM collaboration meeting, March 2012

[138] P.Senger, EPJ Web of Conferences 7 (2010) 74

[139] P.Senger, Central European Journal of Physics 10, Issue 6 (2012) 1289-1294

[140] FAIR Baseline Technical Report 2006, http://www.gsi.de/fair/reports/btr.html

[141] Norbert Herrmann, Johannes P. Wessels and Thomas Wienold, Annu. Rev. Nucl. Part. Sci. 49 (1999) 581 - 632

[142] H. Stöcker, J. Hofmann, J. A. Maruhn and W.Greiner, Progress in Particle and Nuclear Physics, 4, (1980) 133

[143] Technical Design Report for the CBM, Silicon Tracking System (STS), rnc.lbl.gov/ xdong/SoftHadron/CBM-STS-TDR-2012-12-03.pdf

[144] V. Friese and P. Senger, Nuclear matter physics at SIS-100, CBM Report 2012-01, https://www.gsi.de/documents/DOC-2011-Aug-29-1.pdf

[145] V. Koch, arXiv:0810.2520v1 [nucl-th] (2008)

[146] M.Doering and V. Koch, arXiv:nucl-th/0204009 (2002)

[147] H. Heiselberg and A. D. Jackson, arXiv:nucl-th/0006021v3 (2001)

[148] S. Jeon and V. Koch, arXiv:hep-ph/0304012v1 (2003)

[149] G.F. Smoot, Rev. Mod. Phys. 79 (2007) 1349 - 1379

[150] S. Jeon and V. Koch, Phys. Rev. Lett. 83 (1999) 5435

[151] G. Baym and H. Heiselbergr, Physics Letters B 469 (1999) 7 - 11

[152] S. V. Afanasiev et al. Phys. Rev. Lett. 86, (2001) 1965 - 1969

[153] C. Alt et al,. arXiv:0808.1237v3 [nucl-ex] (2009)

[154] M. Bleicher et al., J. Phys. G: Nucl. Part. Phys. 25 (1999) 1859 - 1896

[155] S. V. Afanasiev et al. Phys. Rev. C 66, (2002) 054902

[156] B. I. Abelev et al., Phys. Rev. Lett. 103 (2009) 092301

[157] T. Tarnowsky, arXiv:1101.3351v1 [nucl-ex] (2011)

[158] T. Tarnowsky, arXiv:1110.2222v1 [nucl-ex] (2001)

[159] W. Ehehalt and W. Cassing, Nucl. Phys. A 602 (1996) 449 - 486

[160] J. Geiss, W. Cassing and C. Greiner, Nucl. Phys. A 644 (1998) 107 - 138

[161] J. Gosset er al., Phys.Rev. C 16 (1977) 629 - 657

[162] M. Deveaux, Journal of Physics: Conference Series 426 (2013) 012020, doi:10.1088/1742-6596/426/1/012020

[163] M. Deveaux et al., arXiv:0906.1301v1

[164] M. Deveaux et al., Nuclear Instruments and Methods In Physics Research A (2012), http://dx.doi.org/10.1016/j.nima.2012.10.013

[165] J.M. Heuser et al., Nuclear Instruments and Methods in Physics Research A 568 (2006) 258 - 262

[166] J.M. Heuser, Nuclear Instruments and Methods in Physics Research A 582 (2007) 910 - 915

[167] I. Sorokin, Nuclear Instruments and Methods In Physics Research A (2012), http://dx.doi.org/10.1016/j.nima.2012.10.118

[168] Frankenfeld et al., CBM Progress Report 2012

[169] C. Höhne et al., Nuclear Instruments and Methods in Physics Research A 553 (2005) 91 - 95

[170] C. Höhne et al., Nuclear Instruments and Methods in Physics Research A 595 (2008) 187 - 189

[171] C. Höhne et al., Nuclear Instruments and Methods in Physics Research A 639 (2011) 294 - 297

[172] Yu. Ryabov et al., CBM Progress Report 2012

[173] A. Kiseleva et al., Indian Journal of Physics Volume 85, Issue 1, (2011) 211 - 216

[174] V. Akishina, I. Kisel, Journal of Physics: Conference Series 426 (2013) 012024, doi:10.1088/1742-6596/426/1/012024

[175] P. P. Bahaduri, A. Prakash, S. Chattopadhyay, CBM Progress Report 2010

[176] S. Biswas et al., CBM Progress Report 2012

[177] V. Peshekhonov et al., CBM Progress Report 2012

[178] A. Andronic, Nuclear Instruments and Methods in Physics Research A 563 (2006) 349 - 354

[179] D. Emschermann and C. Bergmann, CBM Progress Report 2011

[180] I. E. Korolko and M. S. Prokudin, Physics of Atomic Nuclei, Volume 72, Issue 2, (2009) 293 - 299

[181] CbmRoot, http://cbmroot.gsi.de (2006)

[182] R. Brun, GEANT - detector description and simulation tool, CERN Program Library Long Writeup W5013

[183] D. Kresan, Ph.D. thesis, Johann Wolfgang Goethe University (2010)

[184] Christian Simon, privat comunication

[185] http://www.techspray.com/d-5-licron-crystal.aspx

[186] http://www.awrcorp.com/products/innovative-technologies/aplac

[187] datasheed, www3.imperial.ac.uk/pls/portallive/docs/1/7293022.PDF

[188] silicon strips detectors

[189] M. Ciobanu, N. Herrmann, K. D. Hildenbrand, M. Kiš, A. Schüttauf, IEEE NSS Conf. Rec., N30-18 (2008) 2018 - 2024

[190] M. Ciobanu, I. Deppner, D. Gonzalez-Diaz, N. Herrmann, K. D. Hildenbrand, M. Kiš, A. Schüttauf, GSI SCIENTIFIC REPORT 2008

[191] M. Ciobanu, N. Herrmann, K. D. Hildenbrand, M. Kiš, A. Schüttauf, IEEE NSS Conf. Rec., N13-44 (2009) 401 - 406,

[192] I. Deppner, Diploma thesis, Heidelberg University (2008)

[193] C. Grupen, Particle Detectors, Cambridge University Press, 1996.

[194] http://en.wikipedia.org/wiki/Copper

[195] I. Deppner et al. JINST 7 P10008 (2012), doi:10.1088/1748-0221/7/10/P10008

[196] J. Wang et al., Nuclear Instruments and Methods in Physics Research A 621 (2010) 151 - 156

[197] M. Petriş et al., Nuclear Instruments and Methods in Physics Research A 661 (2012) S129 - S133

[198] M. Petrovici et al., JINST 7 P11003 (2012), doi:10.1088/1748-0221/7/11/P11003

[199] M. Abbrescia et al., Nuclear Instruments and Methods in Physics Research A 359 (1995) 603 - 609

[200] H.Flemming and H.Deppe, IEEE NSS, Conf. Rec., N15-25 (2007) 322 - 325

[201] J. Beringer et al. (Particle Data Group), Phys. Rev. D86, 010001 (2012)

[202] Bronstein, Semendjajew, Musiol, Muhlig, Taschenbuch der Mathematik, Harri Deutsch Verlag, Nachdruck der 5 Auflage, (2001)

[203] K. Koch, H. Hardel, R. Schulze, and J. Hoffmann, Nuclear Science Symposium Conference Record, 3 (16 - 22) (2004) 1357 - 1359

[204] http://www.gsi.de/en/work/organisation/scientific_technological_divisions/experiment_elektronik\/digitalelektronik/digitalelektronik/module/vme/env/env1.htm

[205] https://www.gsi.de/work/organisation/wissenschaftlich_technologische_abteilungen\/experiment_elektronik/digitalelektronik/digitalelektronik/module/vme/vulom\/vulom3.htm

[206] F. Anghinolfi, P. Jarron, F. Krummenacher, E. Usenko, and M. C. S. Williams, IEEE TRANSACTIONS ON NUCLEAR SCIENCE, VOL. 51, NO. 5, (2004)

[207] et al., GSI SCIENTIFIC REPORT 2012

[208] Technical Design Report for the CBM, Time-of-Flight System (TOF), not published yet

[209] http://en.wikipedia.org/wiki/LVDS

[210] http://en.wikipedia.org/wiki/Nuclear_Instrument_Module

[211] http://en.wikipedia.org/wiki/VMEbus

[212] http://www.wiener-d.com/sc/powered-crates/vme/

[213] http://en.wikipedia.org/wiki/I^{2}C

[214] http://en.wikipedia.org/wiki/Serial_Peripheral_Interface

[215] http://www.caen.it/csite/CaenProd.jsp?parent=11\&idmod=789

[216] Technical Information Manual, Revision n. 10, 6 October 2009

[217] E. Bayer and M. Traxler, IEEE Transactions on Nuclear Science, Vol. 58, No. 4, (2011)

Curriculum Vitae

Personal Information

Name	Ingo Martin Deppner
Date of birth	02.06.1974
Place of birth	Hermannstadt (Sibiu)/Rumania
Citizenship	german
Marital status	married

School Education

1980 - 1984	Primary school, Reussen/Ruşi
1984 - 1987	Secondary school, Hermannstadt
09/1987 - 06/1991	Realschule, Leimen
08/1994 - 06/1995	Fachhochschulreife, Wiesloch

Professional Education

10/1991 - 06/1994	Apprenticeship as chemical laboratory assistant, Uni. Heidelberg

Military Service

10/1995 - 07/1996	Bruchsal

Academic Studies

09/1996 - 04/2001	University of applied science, Mannheim
04/2001	Diplom, engineer in technical chemistry
10/2002 - 04/2008	Heidelberg University, major in physics
04/2008	Diplom, major in physics

Graduate School

since 05/2008	PhD student at the Physicalisches Intitut der Uni. Heidelberg Supervisor: Prof. Norbert Herrmann

October 9, 2013

Danksagung

An dieser Stelle möchte ich allen Personen danken, die mich bei der Fertigstellung dieser Doktorarbeit unterstützt bzw. diese erst ermöglicht haben.
Ganz besonders möchte ich mich bei Herrn Prof. Dr. Norbert Herrmann für die hochinteressante und herausfordernde Aufgabenstellung, die sehr gute Betreuung und die vielen inspirierenden Anregungen während dieser Doktorarbeit bedanken.
Bei Herrn Prof. Dr. Hans-Christian Schultz-Coulon möchte ich mich ganz herzlich für die bereiwillige Übernahme des Zweitgutachtens bedanken.
Prof. Dr. Matthias Bartelmann und Prof. Dr. Peter Fischer danke ich für die Mitwirkung an der Disputation.
Meinen Kollegen und Zimmergenossen Pierre-Alain Loizeau und Christian Simon möchte ich ganz herzlich für das Gegenlesen der Dissertation und für die hervorragende Unterstützung und Zusammenarbeit danken.
Ein ganz herzliches Dankeschön gilt auch Dr. M. Ciobanu, Jochen Frühauf, Dr. Yvonne Leifels, Dr. M. Kis und Dr. K. Hildenbrand, die mir immer mit Rat und Tat zur Seite gestanden haben.
Bedanken möchte ich mich auch bei Dr. Changzhou Xiang, Dr. Yapeng Zhang, Dr. Krzysztof Wisniewski, Victoria Zinyuk und vielen anderen für die gute Zusammenarbeit.
Mein Dank gilt auch all den Mitglieder der FOPI- und der CBM-Kollaboration und insbesondere der CBM-ToF Gruppe mit denen ich viele schöne Stunden erlebt habe. Den mechanischen und elektrischen Werkstätten danke ich für die gewissenhafte Bearbeitung meiner Aufträge.
Auch bedanken möchte ich mich bei Dr. Christian Schmidt und seinen Mitarbeiter für die Bereitstellung des Reinraums an der GSI.
Bedanken möchte ich mich auch bei meinen Freunden, die stets an mich gedacht und es mir nicht übel genommen haben, dass ich während dieser Arbeit weniger Zeit mit ihnen verbringen konnte.
Insbesondere möchte ich meinem Freund Dr. Henning Soller für die unzähligen Gespräche über die verschiedensten Themen der Physik und darüber hinaus danken.
Ein großer Dank gilt meiner Familie, die mir das Physikstudium und erst recht diese Arbeit ermöglicht hatten.
Der wohl größte Dank gebührt meiner Frau Xuefeng für die vielen, mit Geduld ertragenen Entbehrungen während meiner Doktorarbeit. Daher widme ich diese Doktorarbeit meiner geliebten Frau Xuefeng Deppner.